Algorithms and Architectures for UWB Receiver Design

by

Jihad Ibrahim

Dissertation submitted to the Faculty of
Virginia Polytechnic Institute and State University
in partial fulfillment of the requirements for the degree of

DOCTOR OF PHILOSOPHY
in
Electrical Engineering

Committee Members:
Dr. R. Michael Buehrer (Chair)
Dr. Jeffrey Reed
Dr. Claudio da Silva
Dr. Thomas Hou
Dr. Michael Taaffe

January 25, 2007
Blacksburg, Virginia

Keywords: Ultra wideband, multipath channel, synchronization, narrowband interference (NBI).

Algorithms and Architectures for UWB Receiver Design

Jihad Ibrahim

Abstract

Impulse-based Ultra Wideband (UWB) radio technology has recently gained significant research attention for various indoor ranging, sensing and communications applications due to the large amount of allocated bandwidth and desirable properties of UWB signals (e.g., improved timing resolution or multipath fading mitigation). However, most of the applications have focused on indoor environments where the UWB channel is characterized by tens to hundreds of resolvable multipath components. Such environments introduce tremendous complexity challenges to traditional radio designs in terms of signal detection and synchronization. Additionally, the extremely wide bandwidth and shared nature of the medium means that UWB receivers must contend with a variety of interference sources. Traditional interference mitigation techniques are not amenable to UWB due to the complexity of straight-forward translations to UWB bandwidths. Thus, signal detection, synchronization and interference mitigation are open research issues that must be met in order to exploit the potential benefits of UWB systems. This thesis seeks to address each of these three challenges by first examining and accurately characterizing common approaches borrowed from spread spectrum and then proposing new methods which provide an improved trade-off between complexity and performance.

Acknowledgments

I would like to express my gratitude for my advisor Dr. R. Michael Buehrer. His guidance and encouragement have been instrumental in the completion of this dissertation. His insights and his patience over the few last years have been invaluable.

I would like to thank my committee members Dr. Jeffrey Reed, Dr. Claudio Da Silva, Dr. Thomas Hou and Dr. Michael Taaffe for providing valuable advice. I would also like to thank Dr. Annamalai Annamalai for his insights while serving on my committee.

Special thanks to Swaroop Venkatesh, Rekha Menon, Ramesh Chembil-Palat and Chris Anderson, with whom I worked on multiple projects which helped shape parts of this work.

I would finally like to thank the staff of MPRG (particularly Shelby Smith and Hilda Reynolds) for their assistance.

Contents

List of Tables

List of Figures

List of Acronyms

iid – independent identically distributed

nsec – nanoseconds

psec – picoseconds

ASK – amplitude shift keying

AWGN – additive white Gaussian noise

CDF – cumulative density function

CDMA – code division multiple access

DC – direct sequence

EGC – equal gain combining

FEC – forward error correction

FSK – frequency shift keying

ISI – inter symbol interference

LDPC – low density parity check

LOS – line of sight

MAI – multiple access interference

MMSE – minimum mean square error

MRC – maximum gain combining

NBI – narrowband interference

NLOS – Non-line of sight

PAM – pulse amplitude modulation

PDF – probability density function

PN – pseudo-noise

PPM – pulse position modulation

PSD – power spectral density

PSK – phase shift keying

SC – selection combining

SD – selection diversity

SS – spread spectrum

SINR – signal to interference and noise ratio

SIR – signal to interference ratio

SNR – signal to noise ratio

SS – spread spectrum

SV– saleh-valenzuela

TH – time-hopping

TR – transmitted-reference

UWB – ultra wideband

Chapter 1

Introduction

1.1 Research Motivation and Scope

Impulse-radio ultra wideband (UWB) technology has been attracting a great deal of research attention in recent years as a candidate for various communication and position-location applications. Attractive properties of UWB include fine time resolution, high penetrability, low probability of intercept, and low fading margin in dense multipath. Additionally, in 2002, the FCC issued a first report and order allowing the unlicensed use of UWB devices, overlaid with existing devices, subject to a power spectral mask in a 7.5 GHz swath of spectrum. This has generated wide interest in potential UWB applications, and led to a rapid increase in the number of companies and governmental agencies working in UWB.

Many investigated applications for UWB are designed to operate in indoor environments. Indoor UWB systems must contend with dense multipath channels, which are characterized by tens or even hundreds of resolvable multipath components, and delay spreads typically orders of magnitude larger than the UWB pulse duration. Additionally, due to stringent FCC regulations, UWB systems are required to operate at a very low power emission level. These facts have led to several challenges pertaining to UWB transceiver design. Specifically, there are open challenges to be met in the areas of (a) UWB signal detection, (b) synchronization, and (c) interference mitigation.

The objective of this research effort is to characterize the design difficulties in these three fields, study

their causes, identify the shortcomings of traditional proposed solutions, and investigate the design of new algorithms, specifically tailored for efficient performance in dense multipath environments at low transmit power. Summarizing the challenges in each of the three areas of interest:

(1) Signal detection: Recent research has mainly concentrated on the Rake receiver and variants of the transmitted reference receiver as candidates for UWB detectors in dense multipath. However, both receivers have severe performance limitations. Specifically, the energy capture of the Rake receiver is relatively low for a moderate number of fingers, making its implementation impractical for UWB systems. Transmitted reference receivers suffer from a "noise-cross-noise" term, caused by the use of a noisy signal as a correlation or matched filter template. Consequently, a prohibitively large number of pilot symbols are required to overcome this limitation.

(2) Synchronization: Traditional synchronization techniques applied to UWB result in prohibitively long acquisition times due to the extremely large search space caused by the use of the very short UWB pulse. Additionally, in dense multipath environments there exist a larger number of cells within the uncertainty region that can lead to acquisition lock. Locking to an arbitrary multipath component may result in unacceptable performance for many applications (large range error in positioning systems for example).

(3) Interference mitigation: UWB systems must co-exist with narrowband systems. Even though UWB systems may enjoy a high spreading gain due to their large bandwidth, stringent FCC power restrictions make them susceptible to strong narrow band interference (NBI), which can severely degrade performance. The subject of NBI mitigation has only received limited research interest until recently. Some NBI mitigation methods have been proposed for UWB, primarily relying on classic techniques used in spread spectrum. However, the implementation of most of these methods is problematic, because they require prohibitive complexity, need prior knowledge of the interferer's spectral content, and/or assume synchronization prior to interference mitigation, which might be infeasible in the presence of strong NBI.

1.2 Thesis Statement

The goal of this thesis is to address each of these open research areas. To state the goals of this research succinctly, we provide the following thesis statement:

The goal of this thesis is to develop receiver architectures and algorithms for UWB impulse radio including signal detection, synchronization and interference mitigation techniques in order that we might improve the complexity-performance trade-off of UWB receivers in dense multipath channels.

1.3 Dissertation Organization

The rest of this dissertation is organized as follows. Chapter 2 presents a brief overview of UWB systems and signals, and provides background information. Multiple access, modulation types and pulses shapes are discussed. Since the communication channel plays a fundamental role in defining the framework of this research, an overview of the channel measurements and the channel models on which analytical and simulation results in this work are based is also included.

Traditional signal detection is discussed in Chapter 3. The well-known Rake and pilot-assisted receivers are analyzed, and expressions for their probability of bit error are derived. It is shown that both techniques are inadequate when applied to UWB in dense multipath: On one hand, Rake receivers are hindered by unacceptably low energy capture for a moderate number of fingers. On the other hand, pilot-assisted receivers suffer from the use of a noisy template, and an unacceptably heavy training load is required to hinder its effect. These shortcomings are discussed, mathematically formulated and then validated through simulations.

Two new signal detection algorithms specifically tailored for UWB in dense multipath are presented in chapter 4. First, an iterative data-aided, pilot-assisted receiver is discussed. In this receiver, the heavy training load required by traditional TR systems is reduced by incorporating the data symbols into channel estimation. The convergence of the iterative process at low SNR is guaranteed by the use of forward error correction. The system jointly exploits the improved channel estimation and coding gains to yield good performance at light pilot overhead. Then, a receiver based on sequence optimization is proposed and

analyzed, where the transmit pulse sequence and the receiver template are jointly optimized to maximize SNR at the correlator output. The system achieves very high energy capture by forcing the multipath components to add up coherently, or interfere constructively, at the receiver. This receiver is also applied to a multi-user application and to a NBI mitigation scenario, where the objective is maximizing SINR rather than SNR. The implementation complexity of the above UWB receivers is also discussed, and a comparison is provided, stressing the tradeoff between system resources and performance for each.

Chapter 5 deals with synchronization. Acquisition (or coarse synchronization) is first studied, then tracking (or fine synchronization) is discussed. The problem of UWB acquisition in dense multipath is clearly defined, and previous research work is summarized. The rationale behind the need for a two-stage algorithm is explained. A mathematical framework for the analysis of acquisition systems which incorporates multipath into the analysis is described. Then, the proposed two-stage system is discussed. The first stage (coarse acquisition) consists of a fast version of traditional serial search, termed *jump-phase* search, where acquisition time is drastically reduced by uniformly spreading the cells corresponding to multipath components over the uncertainty region. Jump-phase search is shown to yield an order of magnitude reduction in the mean acquisition times compared to traditional serial search. The second stage (fine acquisition) is then mathematically described using the UWB IEEE P802.15 channel model. Fine acquisition takes advantage of coarse acquisition to calculate a more "intelligent" threshold, then robustly detects the LOS path, by taking advantage of the clustered nature of multipath. Two case studies are included which illustrate the performance of the proposed acquisition algorithm for ranging and communications applications. It is shown that the introduction of fine acquisition leads to drastic reduction in range error. The expression for probability of error of a pilot-assisted receiver in the presence of timing error is derived, and then the improvement brought by two-stage acquisition is verified through simulation.

Tracking for UWB systems is then analyzed. The inefficiency of traditional tracking algorithms applied to UWB, most notably for generalized pilot-assisted receivers, is stressed. Then, a proposed tracking algorithm for pilot-assisted receivers, loosely based on the popular early-late gate approach, is presented. Contrary to classical tracking which employs the transmit pulse shape as a template, the proposed tracking circuit achieves robust continuous estimation of the LOS component by fully exploiting the received pulse shape.

The tracking system is statistically analyzed, and its effect on the probability of error is derived. Simulation results validate the theoretical expressions and illustrate the algorithm's performance.

NBI mitigation is discussed in Chapter 6. The detrimental effect of NBI on UWB systems and the need for new, simple front-end NBI mitigation techniques are first presented, then previous work in NBI mitigation applied to UWB is summarized. The proposed scheme, based on selection diversity (SD) in a multiple-receiver antenna system, is then described and mathematically formulated. The proposed method achieves interference diversity gains by exploiting the low spatial fading of UWB signals compared to NBI signals. This method is attractive, because it does not assume signal synchronization or knowledge of the NBI's spectral content prior to interference mitigation. The system is analyzed for Rayleigh and Ricean NBI fading, and probability of bit error expressions are derived for both scenarios. Two other combining methods (EGC and MRC) are also investigated. It is shown that doubling the number of antennas potentially yields a 3-dB performance gain for SD and EGC under NBI Rayleigh fading. Smaller gains are observed for Ricean fading in general, although EGC outperforms SD. MRC only provides limited additional gains at the expense of increased complexity.

This dissertation is finally concluded in Chapter 7, where a synthesis of the research is presented, and future work is recommended.

Chapter 2

Overview of UWB Signals and Systems

2.1 Introduction

UWB communication systems can be defined as wireless communication systems whose instantaneous bandwidth is much larger than their information bandwidth, *i.e.*, the minimum bandwidth required to deliver information.

UWB systems are commonly characterized by a very large fractional bandwidth. Fractional bandwidth is defined as the ratio of the bandwidth occupied by the signal to the center frequency of the signal:

$$BW = \frac{2\,(f_h - f_l)}{f_l + f_h} \tag{2.1}$$

where f_l and f_h are the lower and upper frequency components in the signal measured at the -10 dB level, respectively. Traditional communication systems have a fractional bandwidth of the order of 0.01. Wideband CDMA (W-CDMA) has a fractional bandwidth of about 0.02. According to a DARPA report which coined the term "ultra wideband", a UWB system is a system with fractional bandwidth exceeding 0.25 [1] (Figure 2.1). In its first report and order allowing and regulating the commercial use of UWB, the FCC

defined UWB systems as any system with fractional bandwidth exceeding 0.20, or any system with a -10 dB bandwidth exceeding 500 MHz [2].

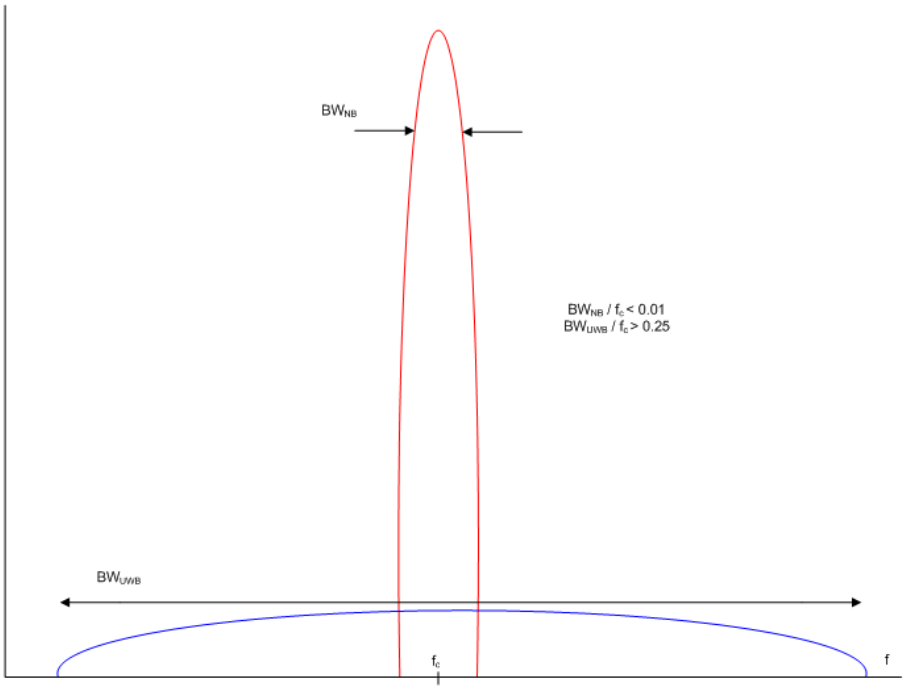

Figure 2.1: Fractional bandwidth comparison of narrowband and UWB signals.

The FCC's UWB classifications and specifications do not specify a particular technology to be used in the implementation of UWB systems. One investigated technology is multi-band orthogonal frequency division multiplexing (OFDM), which is being considered for UWB devices in wireless personal area networks. However, the term UWB in the research literature has been practically synonymous with impulse-radio technology, which is based on the transmission of very short duration (sub-nsec) pulses, as opposed to sinusoidal based signals. The sharp rise and fall of the pulse causes the pulse's energy to be spread over a large bandwidth (in the gigahertz range). This work concentrates on performance aspects of impulse-radio UWB, and thus, unless otherwise specified, the use of the term UWB will also imply impulse-radio.

A general overview of UWB systems is presented in this chapter. Various operational aspects, such as pulse shapes, modulation schemes and multiple access methods commonly used in UWB are introduced. An overview of the channel measurements and the channel models on which analytical and simulation results in

this work are based is also included.

2.2 Attractive Features of UWB Systems

The key potential of UWB systems lies in a fundamental result from information theory, which may be formulated as:

$$C = Wlog_2\left(1 + \frac{P_0}{N_0}\right) \tag{2.2}$$

where C is the system's channel capacity in bits/seconds, W is the system bandwidth in Hz, P_0 is the signal power spectral density in watts/ Hz, and N_0 is the noise power spectral density in watts/Hz. Since UWB is characterized by a very large bandwidth, UWB system can potentially achieve very high data rates at moderate signal-to-noise ratio (SNR, $SNR = \frac{P_0}{N_0}$). Alternatively, medium and low data rate may be achieved at relatively very low SNR.

Since energy is spread over a large bandwidth, the system's power spectral density is low, often of the same order as the noise spectral density. Thus, a narrowband system operating in a band that overlaps a small portion of a band within which an UWB device is operating will only suffer negligible interference, since UWB interference will only slightly raise the noise level.

With a low PSD, UWB systems are less vulnerable to covert interceptors or detectors. This Low Probability of Intercept (LPI) characteristic is especially attractive for a host of military applications.

In radar, the achievable resolution (and ranging accuracy) is proportional to the signal's bandwidth. UWB's large instantaneous bandwidth enables fine time resolution, which offers fine position location and radar capabilities.

In traditional spread spectrum systems operating in dense multipath, the energy from different multipath components may be coherently harnessed, typically through the use of a Rake receiver. However, any two paths that are separated by less than a chip duration may not be resolved. For UWB systems, paths that are separated by more than a pulse duration may be resolved. Since the pulse duration is typically very short (on the order of the inverse of the bandwidth), UWB can resolve a large number of multipath components, making it robust against multipath fading compared to narrowband systems.

Finally, an advantage of UWB system is the low cost of UWB communication hardware components. In fact, since the generated pulses are transmitted directly, the need for oscillators, mixers and other costly RF components is eliminated.

These key properties make UWB an attractive candidate for wireless systems where any combination of data communication, high precision position location, and radar applications is desirable. Moreover, in 2002, the FCC issued a first report and order [2], allowing the unlicensed use of UWB devices, overlaid with existing devices, subject to a spectral power mask (see Figure 2.2). For example, unlicensed UWB indoor communications and sensor systems are allowed to operate in the 3.1-10.6 GHz with an emission limit of -41.3 dBm/MHz. This has generated wide interest in potential UWB applications, and led to a rapid expansion of private companies and governmental agencies working in UWB. Currently investigated UWB systems include wireless personal area networks, sensor networks, imaging systems, and vehicular radar systems (for a more thorough discussion of these applications, see [3] and the references therein).

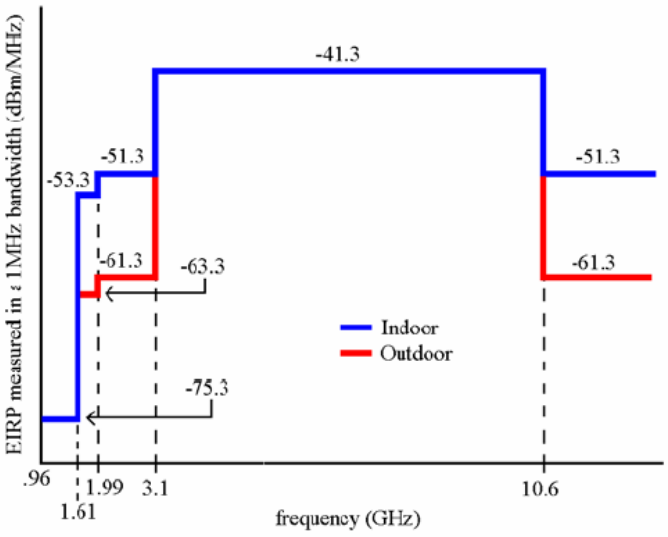

Figure 2.2: FCC spectral mask for communications and measurements applications.

2.3 General UWB System Model

A multi-user impulse-radio system based on time-hopping (TH) and pulse position modulation (PPM) was introduced in the seminal reference by Scholtz [4] in 1993. Consider a system with U users, and let $s_k(t)$ be the transmit signal of the k-th user. Then:

$$s_k(t) = \sum_j \sqrt{E_p} w\left(t - jT_f - c_j^{(k)} T_c - \Delta d_{\lfloor j/N_p \rfloor}^{(k)}\right) \tag{2.3}$$

where:

- $w(t)$ is the unit-energy transmit UWB pulse, of duration T_w.
- E_p is the pulse energy.
- N_p is the pulse repetition number, or the number of pulses used to represent one data symbol.
- Δ is the PPM time delay parameter.
- $d_i^{(k)}$ is related to the i-th data element of the k-th user (In case of binary PPM, $d_i^{(k)} = \{0, 1\}$).
- $c_j^{(k)}$ is the j-th chip of user k's TH sequence.
- T_f is the frame repetition time.
- T_c is the chip duration ($T_c << T_f$).
- $\lfloor . \rfloor$ is the floor operator.

The overall transmit signal can then be written as:

$$s(t) = \sum_{k=1}^{U} s_k(t). \tag{2.4}$$

The system is illustrated for binary PPM in an arbitrary frame in Figures 2.3 and 2.4, respectively. In this example, $T_f = 5T_c$. Therefore, each frame contains five chips, and there are five possible hop positions ($c_j^{(k)} = \{0, 1, 2, 3, 4\}$). Assume $c_j^{(k)} = 2$. If the information bit $d_{\lfloor j/N_s \rfloor}^{(k)}$ is equal to zero, no extra delay is

inserted, and the pulse $w(t)$ is placed at the start of the third chip (Figure 2.3). If $d^{(k)}_{\lfloor j/N_s \rfloor} = 1$, an extra delay Δ is inserted (Figure 2.4). The information is thus modulated through the delay of the pulse inside the TH chip.

TH codes are used to allow multiple access. This is illustrated for a simple 3-user system in Figures 2.5 and

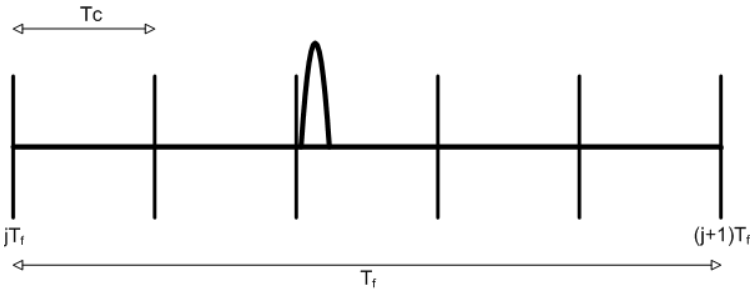

Figure 2.3: TH-PPM example, $d^{(k)}_{\lfloor j/N_s \rfloor} = 0$, $c^{(k)}_j = 2$. Pulse shifted to the third hop position in a frame with 5 hop positions. No extra delay Δ.

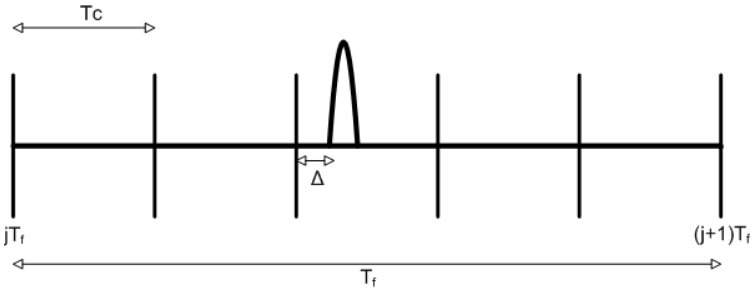

Figure 2.4: TH-PPM example, $d^{(k)}_{\lfloor j/N_s \rfloor} = 1$, $c^{(k)}_j = 2$. Pulse shifted to the third hop position in a frame with 5 hop positions, plus extra delay Δ.

2.6. Two consecutive frames are displayed for each user. In the absence of TH codes, pulses of different users are transmitted at the same time, and collisions occur (Figure 2.5). Collisions may be prevented by assigning judiciously selected TH codes to each user, so that simultaneous pulse transmissions do not occur within the same chip (Figure 2.6). The hopping codes could be based on pseudo-noise (PN) sequences or sequences designed to minimize interference between users. TH sequences are also used in UWB systems to remove spectral components from the UWB spectrum, and smoothen the PSD, therefore reducing interference caused by UWB on other systems operating in the same frequency range, and reducing its probability of intercept

[5]. Other multiple access or spreading methods may be used instead of TH sequences. For example, the use of SS-DS has been proposed for UWB in [6] [7] [8].

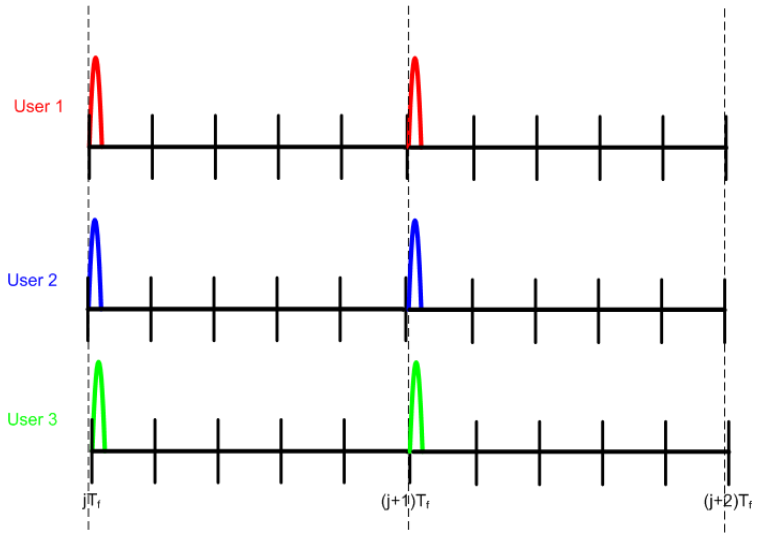

Figure 2.5: 3-user system with no TH. Collisions occur between different users.

Other variations of this PPM system are also possible. For example, modulation based on block waveforms with desired cross-correlation properties is proposed in [9][10][11], where Δ is no longer necessarily a constant. Other modulation types are also possible, such as on-off keying (OOK, Figure 2.7) and pulse amplitude modulation (PAM, Figure 2.8). Higher order ($M-$ary) modulation is possible, as well as combinations of different modulation techniques. For example, PPM and PAM may be combined to create biorthogonal modulation.

2.4 Pulse Shapes

The most commonly used family of pulses to model $w(t)$ is the Gaussian pulse and its derivatives. Gaussian pulses are easy to analyze and manipulate, because they are based on the well known Gaussian PDF. The

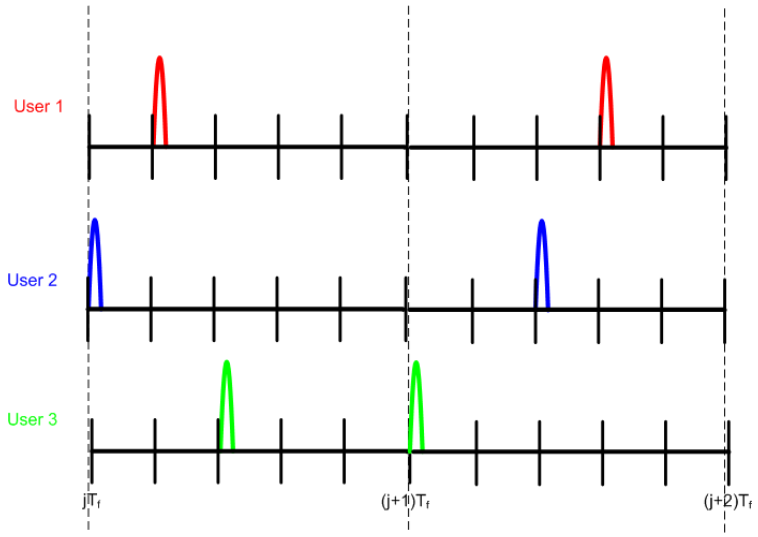

Figure 2.6: 3-user system with TH. No collisions occur.

Gaussian pulse (Figure 2.9) is defined as:

$$w(t) = \frac{1}{\sqrt{2\pi\sigma^2}} e^{-\frac{(t-\mu)^2}{2\sigma^2}} \tag{2.5}$$

where σ is the standard deviation of the pulse in seconds, and μ is the location in time of the midpoint of the Gaussian pulse in seconds [5]. The pulse width, and thus the pulse bandwidth, is controlled by σ. The pulse width is usually approximated by $T_w = 2\pi\sigma$. The pulse may be written in a slightly different form by letting $k = \frac{1}{\sqrt{2\sigma^2}}$. Then:

$$w(t) = \frac{k}{\sqrt{\pi}} e^{-k^2(t-\mu)^2} \tag{2.6}$$

and $T_w = \frac{\pi\sqrt{2}}{k}$.

The first derivative of the Gaussian pulse (Figure 2.10) is also widely used, since the transmit antenna is commonly assumed to differentiate the original pulse shape (assumed to be Gaussian). It may be written as:

$$w(t) = \left(\frac{32k^6}{\pi}\right) te^{-(kt)^2}. \tag{2.7}$$

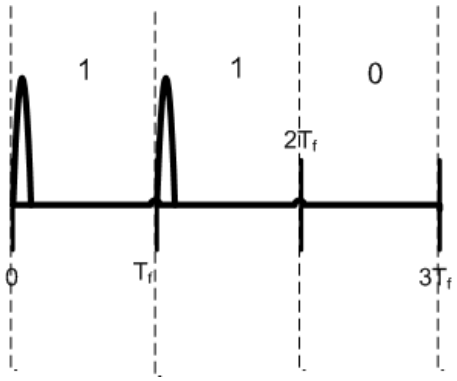

Figure 2.7: Example of binary OOK. Data sequence = $\{1, 1, 0\}$. No pulse for zero-bit.

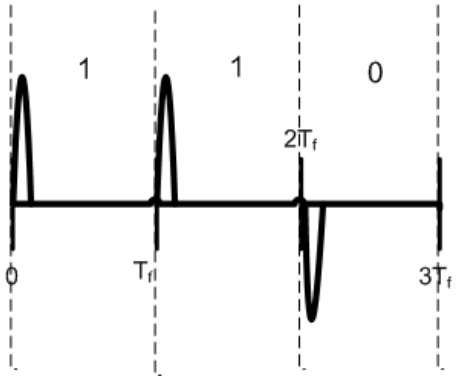

Figure 2.8: Example of binary PAM. Data sequence = $\{1, 1, 0\}$. Pulse is inverted for zero-bit.

The second derivative of a Gaussian pulse (Figure 2.11) is also used, and incorporates the differentiating effect of both transmit and receive antennas (when the generated pulse is Gaussian). It is expressed as:

$$w(t) = \left(\frac{32k^2}{9\pi}\right)^{\frac{1}{4}} \left(1 - 2\,(kt)^2\right) e^{-(kt)^2}. \tag{2.8}$$

Note that the spectrum of these three pulses extends to DC, which does not confirm with the FCC power mask. The pulses may be passed through a bandpass filter, or modulated by a sine wave, to move their

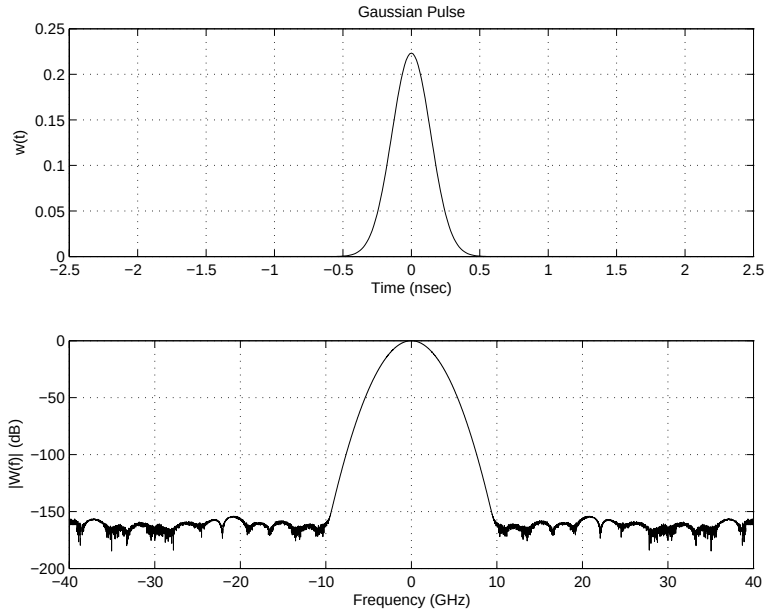

Figure 2.9: Gaussian pulse in the time domain (above) and its frequency spectrum (below). $k = 5e9\ sec^{-1}$.

spectrum to the allowable band. The modulated wave (Figure 2.12) may be expressed as:

$$w(t) = \left(\frac{8k}{\pi}\right)^{\frac{1}{4}} \frac{1}{\sqrt{1 + e^{\frac{2\pi^2 f_c^2}{k}}}} e^{-(kt)^2} cos\left(2\pi f_c t\right) \tag{2.9}$$

where f_c is the desired center frequency of the pulse.

2.5 The UWB Channel

Classical analysis of single-user communication systems in AWGN assumes that the received signal is an attenuated, delayed and *undistorted* version of the transmitted signal, plus noise and (possibly) interference. Assuming pulse $w(t)$ was transmitted, and ignoring any interference sources, the received signal may be written as:

$$r(t) = \sqrt{E_p} w(t - \tau_0) + n(t) \tag{2.10}$$

where τ_0 is the propagation delay (proportional to the distance between transmit and receive antennas), and $n(t)$ is an AWGN process. Note that no spreading or data modulation are considered. The loss in received signal power versus distance (and possibly frequency), usually referred to as large scale fading, is subsumed

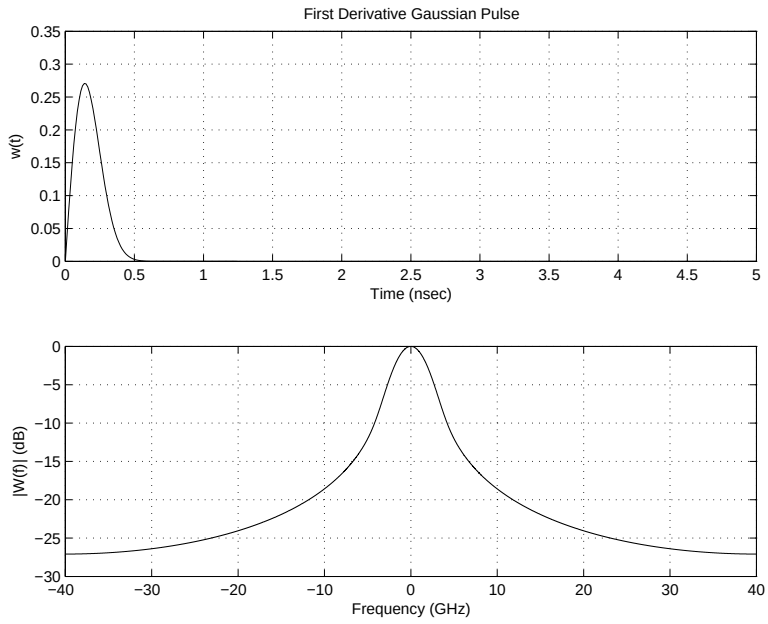

Figure 2.10: First derivative Gaussian pulse in the time domain (above) and its frequency spectrum (below). $k = 5e9\ sec^{-1}$.

into $\sqrt{E_p}$.

This simplistic model does not hold in most wireless communication applications, which are the focus of this work. In fact, due to the presence of reflectors, diffractors and scatterers in the environment, the received pulse shape is the sum of attenuated, delayed, and possibly overlapping versions (or multipath components) of the transmit pulse $w(t)$. These multipath components combine vectorially at the receiver, and may result in signal distortion, or small scale fading [12]. Assuming a realistic channel model, the received signal is then written as:

$$r(t) = v(t) + n(t) \tag{2.11}$$

where $v(t)$ is given by:

$$v(t) = w(t) * h(t, \tau) \tag{2.12}$$

where $*$ is the convolution operator, and $h(t, \tau)$ represents the time-varying communication channel impulse response between the transmitter and receiver antennas. The channel may vary in time due to the motion of the transmitter and/or the receiver, or to changes in the environment. Since the received signal in a multipath channel consists of a sum of delayed, attenuated and phase-shifted replicas of the transmitted

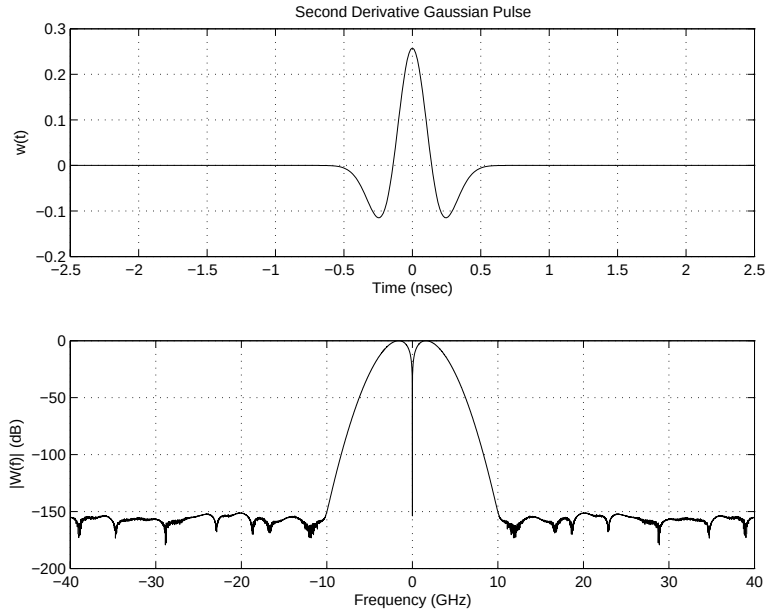

Figure 2.11: Second derivative Gaussian pulse in the time domain (above) and its frequency spectrum (below). $k = 5e9\ sec^{-1}$.

signal, the communication channel impulse response is typically modeled using a tap-delay model, and is generally expressed as [12, 13, 14, 15, 16]:

$$h(t,\tau) = \sum_{l=0}^{L(t)-1} \beta_l(t) p_l(t) \delta(\tau - \tau_l(t)) \tag{2.13}$$

where $\delta(t)$ is the Dirac-Delta function, $L(t)$ is the (time-varying) number of multipath components, and $\beta_l(t)$, $p_l(t) = \pm 1$ and $\tau_l(t)$ are the real amplitude, polarity and delay of the l^{th} multipath component, respectively. The varying nature of the multipath amplitude and delay is due to time-dependent changes in the channel, such as relative motion between the transmitter and receiver, or motion of foreign objects in the environment. If the transmit and receive antennas are stationary, and changes in the environment occur at a slow rate compared to the data rate, then the channel is assumed to be "quasi-static". That is, the channel impulse response is assumed to be time-invariant over a particular time interval of interest. This quasi-static assumption plays an important role in simplifying analytical and simulation models [17]. The time-invariant channel model is widely used in the analysis of UWB systems [5], and will also be adopted in this research.

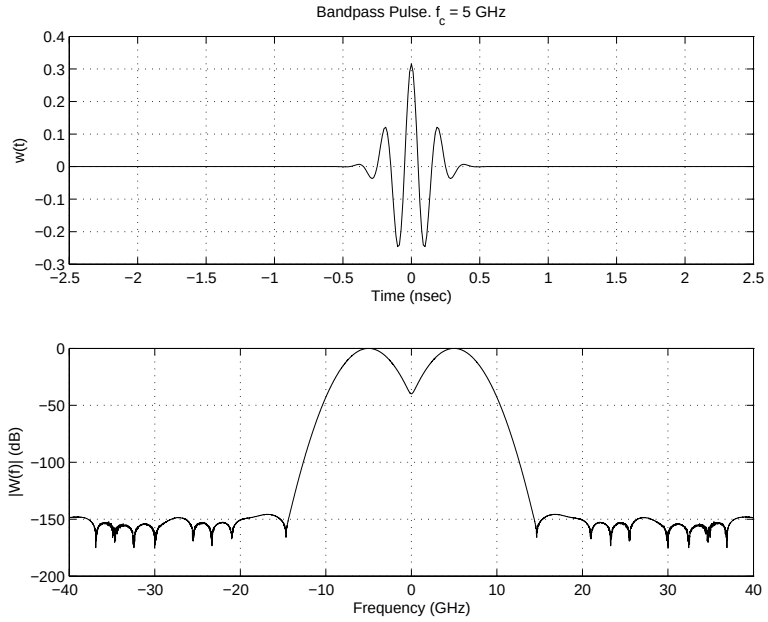

Figure 2.12: Bandpass Gaussian pulse in the time domain (above) and its frequency spectrum (below). $k = 5e9\ sec^{-1}$, $f_c = 5\ GHz$.

The time-invariant channel impulse response may then be written as:

$$h(\tau) = \sum_{l=0}^{L-1} \beta_l p_l \delta(\tau - \tau_l). \tag{2.14}$$

Let $\alpha_l = \beta_l p_l$. Then:

$$h(\tau) = \sum_{l=0}^{L-1} \alpha_l \delta(\tau - \tau_l) \tag{2.15}$$

and the received pulse may then be written as:

$$v(t) = \sum_{l=0}^{L-1} \alpha_l w(t - \tau_l). \tag{2.16}$$

2.5.1 Small Scale Channel Statistics

The communication channel can be characterized by coarse statistics, such as mean excess delay, RMS delay spread, maximum excess delay and number of paths. Although these statistics do not completely define the paths' amplitude and delay statistical distributions, they provide a useful tool for the analysis and

comparison of different channel environments [12].

The mean excess delay is the first moment of the power delay profile and is given by:

$$\tau_m = \frac{\sum_{l=0}^{L-1} \alpha_l^2 \tau_l}{\sum_{l=0}^{L-1} \alpha_l^2}. \tag{2.17}$$

The RMS delay spread is given by the square root of the second central moment of the power delay profile, and can be written as:

$$\tau_{RMS} = \sqrt{\frac{\sum_{l=0}^{L-1} \alpha_l^2 \tau_k^2}{\sum_{l=0}^{L-1} \alpha_l^2} - \tau_m^2}. \tag{2.18}$$

The maximum excess delay is defined as the delay of the last occurring multipath component. The number of paths is the number of significant multipath components. A "significant" component is one whose absolute amplitude is attenuated by less than X dB compared to the strongest available path. X is a design parameter, and depends on the required system precision. Typical values of X are 10, 15 or 20.

2.5.2 Channel Measurements Used in this Work

Most of the simulation results in this work are based on real measured indoor channel models. It is therefore essential to provide a precise characterization of these measurements. A large set of indoor (as well as outdoor) measurements was taken by Virginia Tech as part of the DARPA NETEX (NETworking in EXtreme environments) program [18][19][20]. The indoor measurement data analyzed represents various indoor line-of-sight (LOS) and non-line-of-sight (NLOS) environments. Measurements were taken with two different antennas, a wideband biconical and a TEM horn antenna. For a complete description of the measurement procedure and locations, the reader is referred to Chapter 3 of [19]. The generated pulse used to probe the channel is plotted with its corresponding spectrum in Figure 2.13. The pulse is Gaussian in shape with a pulse width of approximately of 200 psec.

By pooling together all the indoor time domain data (which consists of 800 time domain profiles), time dispersion statistics were calculated for the indoor UWB channel. Specifically mean excess delay, maximum excess delay, RMS delay spread, and the number of paths were calculated. Also of interest were the number of inverted paths and the amount of inverted energy. These two statistics are of interest to the pulse-based

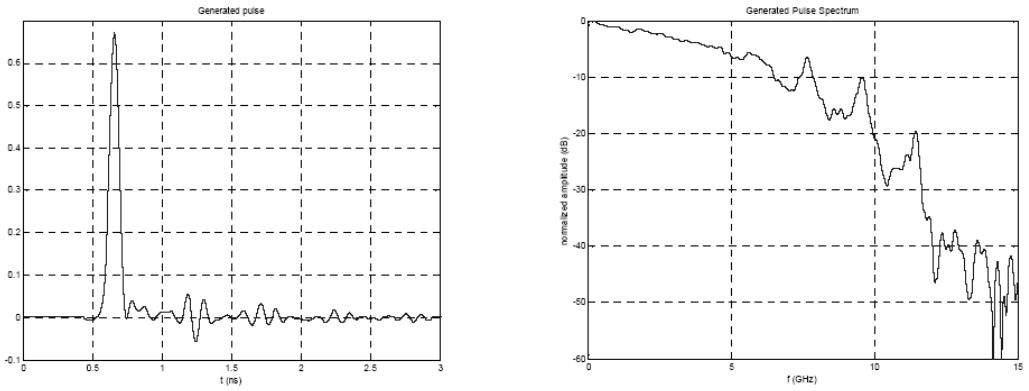

Figure 2.13: Generated time-domain pulse (left), and corresponding spectrum (right). Source: [5] (R.M. Buehrer, Chapter 3, *Channel Modeling*).

	Bicone					TEM			
	15		20			15		20	
	NLOS	LOS	NLOS	LOS		NLOS	LOS	NLOS	LOS
Mean Excess Delay (nsec)	16	5.19	20.1	10.5		2.36	0.552	5.59	1.22
Max Excess Delay (nsec)	65.7	28.4	78.6	56.8		16.1	2.65	43.1	12.4
RMS Delay Spread (nsec)	13.7	5.41	16.2	8.5		3.27	0.753	7.09	1.70
Number of Paths	72.84	24.27	153.95	64.58		28.73	6.41	99.15	15.76
Inverted Paths	49.00%	47.61%	49.30%	48.68%		50.71%	39.54%	49.81%	43.93%
Inverted Energy	44.23%	45.02%	45.36%	45.63%		34.26%	24.19%	37.67%	25.97%

Table 2.1: Small scale statistics for indoor channel measurements. CLEAN algorithm was run with 15 and 20 dB thresholds. Source: [5] (R.M. Buehrer, Chapter 3, *Channel Modeling*).

UWB systems since pulse polarity is very important in certain modulation schemes (PAM for example). The statistics were classified by the measurement environment (LOS or NLOS) and by the particular antenna used (TEM or Bicone). In order to calculate these statistics, an impulse response was first extracted from each received signal, and then the pool of impulse response profiles was statistically studied. The impulse response extraction process was based on the CLEAN algorithm, which is an iterative deconvolution technique in which a template LOS pulse is used to extract the channel impulse response from a received signal. For a detailed analysis of the CLEAN algorithm, the reader is referred to [21] or [22].

The measured channel small scale statistics are summarized in Table 2.1.

2.5.3 Common Channel Models

The main goal of small-scale channel modeling is to provide robust statistical characterization of the amplitudes and delays of the channel multipath components. Accurate channel models are extremely important for the design of communication systems, since they provide the engineer with a valuable testing and analysis tool. Understanding and modeling the channel characteristics are especially paramount within the context of this work, since the statistical properties of the channel provide information about small-scale fading, signal distortion and correlation, and energy dispersion, which should be taken into account in the design of detection, synchronization, and interference mitigation algorithms. Although actual channel measurements may be sufficient to conduct computer simulations, mathematical channel models are required to derive analytical expressions which more accurately predict system performance. This section briefly introduces the most common statistical models for indoor UWB systems.

The Saleh-Valenzuela Model

The Saleh-Valenzuela (SV) model [23] is one of the most commonly used indoor channel models. The SV model was originally designed for NLOS channels. The channel impulse response is given by a double -clustered tapped delay line, and may be written as:

$$h(t) = \sum_{k=1}^{K} \sum_{l=1}^{L} \alpha_{k,l} \delta(t - T_k - \tau_{k,l}). \tag{2.19}$$

The arriving paths are grouped into K clusters, with L paths each. $\alpha_{k,l}$ and $\tau_{k,l}$ are the amplitude and delay of the $l-th$ path in the $k-th$ cluster, respectively. The cluster arrivals are modeled by a Poisson process, and thus, the cluster inter-arrival times T_k are modeled by exponential random variables, such that:

$$p\left(T_k | T_{k-1}\right) = \Lambda exp\left[-\Lambda\left(T_k - T_{k-1}\right)\right], \quad k > 0 \tag{2.20}$$

where Λ is the mean cluster arrival rate. Within a particular cluster, the path arrival times $\tau_{k,l}$ are also modeled with a Poisson process. The distribution of the inter-arrival times is given by:

$$p\left(\tau_{k,l}|\tau_{k,l-1}\right) = \lambda exp\left[-\lambda\left(\tau_{k,l} - \tau_{k,l-1}\right)\right], \quad l > 0 \tag{2.21}$$

where λ is the mean path arrival rate. The average power of both the clusters and the multipath components within the clusters are assumed to decay exponentially, such that the average power of a multipath component at delay $T_k + \tau_{k,l}$ is given by:

$$\bar{\alpha^2_{k,l}} = \bar{\alpha^2_{0,0}} e^{-\frac{T_l}{\Gamma}} e^{-\frac{\tau_{k,l}}{\gamma}} \tag{2.22}$$

where $\bar{\alpha^2_{0,0}}$ is the expected value of the power of the first arriving multipath component, Γ is the decay exponent of the clusters and γ is the decay exponent of the rays within a cluster. In the original model, the path amplitudes $\alpha_{k,l}$ are assumed to follow a Rayleigh distribution about the expected value given in the equation above. However, research shows that the Rayleigh assumption is not suitable for UWB signals, and log-normal fading is rather used to provide a better model. When lognormal fading is used [24], the amplitudes may be expressed as:

$$\alpha_{k,l} = p_{k,l} 10^{\frac{\mu_{k,l} + X_{\sigma,k,l}}{20}} \tag{2.23}$$

where $p_{k,l} = \pm 1$ is an equi-probable binary random variable (modeling the path polarity), and:

$$\mu_{k,l} = \frac{20ln\left(\left|\bar{\alpha}\right|_{0,0} - 10\frac{T_l}{\Gamma} - 10\frac{\tau_k}{\gamma}\right)}{ln(10)} - \frac{\sigma^2 ln(10)}{20} \tag{2.24}$$

$$X_{\sigma,k,l} = N\left(0, \sigma^2\right) \quad (\sigma \ in \ dB). \tag{2.25}$$

The SV model parameters which provided the best fit (in terms of the CDF of mean excess delay, RMS delay spread, and number of paths) to the Virginia Tech indoor Bicone NLOS channel measurements are shown in Table 2.2. The parameters which fit the remaining measurements (Bicone LOS, TEM NLOS, and TEM LOS) may be found in [19].

Parameter	Value
$\frac{1}{\Lambda}$	0.4 nsec
$\frac{1}{\lambda}$	0.04 nsec
Γ	1250 nsec
γ	25 nsec
σ	9.2

Table 2.2: SV model parameters for indoor Bicone NLOS channel measurements.

The $\Delta - K$ Model

The Δ-K model has also been used to model mobile and indoor wideband channels and like the SV model, assumes that multipath components arrive in clusters. In this model, the probability that a path arrives at any given delay is higher by a factor of K if a path has arrived within the past Δ seconds. The arrival times thus follow a modified, two-state Poisson process and the inter-arrival times follow an exponential distribution where the arrival rate is based on a state model. When in state 1, $(S-1)$, the mean arrival rate is given by λ. Transition to state 2, $(S-2)$, is triggered when a path occurs. In $(S-2)$, the mean arrival rate is given by $K\lambda$. If after Δ seconds, a path has not arrived, transition back to $(S-1)$ occurs. Exponential energy decay is assumed here to describe the expected value of the energy in a path at a given delay. The polarity is assumed to be ± 1 with equal likelihood, and amplitude fading is assumed to be lognormal such that the amplitude of a path is given by the same equations as the SV model.

The Δ-K model parameters which provided the best fit to the Virginia Tech indoor Bicone NLOS channel measurements are shown in Table 2.3.

Parameter	Value
K	2.3
$\frac{1}{\lambda}$	2.5 nsec
Δ	0.7 nsec
γ	19 nsec
σ	2.5

Table 2.3: $\Delta - K$ model parameters for indoor Bicone NLOS channel measurements.

The Single-Poisson Model

The single-Poisson model a simplistic version of both of the previously introduced models and assumes that only one cluster is present in the impulse response (or equivalently, no clustering of paths). The arrivals of paths are treated as a Poisson process with arrival rate λ. Also, the decay of the paths is assumed to be

exponential, with a decay time constant of γ. The amplitudes of the paths are modeled as a log-normal random variable with parameter σ.

The single-Poisson model parameters which provided the best fit to the Virginia Tech indoor Bicone NLOS channel measurements are shown in Table 2.4.

Parameter	**Value**
$\frac{1}{\lambda}$	0.9 nsec
γ	20 nsec
σ	4

Table 2.4: Single-Poisson model parameters for indoor Bicone NLOS channel measurements.

The Split-Poisson Model

The SV model is based on the generation of multiple exponentially decaying clusters. However, processing of Virginia Tech channel measurements indicates that the average channel impulse response basically consists of two clusters, where the first short cluster contains a limited number of relatively strong, fast decaying components, and the second longer cluster contains relatively attenuated paths that decay at a slower rate. Based on these observations, the Split-Poisson model was proposed in [25][26]. This model assumes two clusters of Poisson arrivals, one delayed by τ_1 seconds relative to the other. The clusters are generated based on the parameter sets $(\lambda_1, \gamma_1, \sigma_1)$ and $(\lambda_2, \gamma_2, \sigma_2)$, respectively. Also, in order to maintain continuity in the energy decay in the overall impulse response, the first cluster is weighted higher than the second cluster by a factor α.

The split-Poisson model parameters which provided the best fit to the Virginia Tech indoor Bicone NLOS channel measurements are shown in Table 2.5.

Parameter	**Value**
t_1	0
$\frac{1}{\lambda_1}$	0.4 nsec
γ_1	17 nsec
σ_1	4.3
t_2	20 nsec
$\frac{1}{\lambda_2}$	0.8 nsec
γ_2	21 nsec
σ_2	5.7
α	3

Table 2.5: Split-Poisson model parameters for indoor Bicone NLOS channel measurements.

2.6 Note on Monte Carlo Simulations

Throughout this work, traditional and proposed algorithms are mathematically analyzed and theoretical expressions quantifying their performance are derived. The validity of these expressions is then checked by standard Monte Carlo simulations [17]. Monte Carlo simulations are also used to illustrate system performance when theoretical results are not available. This section presents a brief overview of the simulation methodology used in this work. Specifically, a derivation of the corresponding confidence intervals is included.

Most of the Monte Carlo simulations in this work estimate bit error probabilities (note that the same approach is used for the estimation of other metrics). The procedure is as follows. The simulation is run for N bits*. The estimate of the probability of error P_e is then:

$$\hat{P}_e = \frac{N_e}{N} \tag{2.26}$$

where N_e is the number of independent bit errors. Note that N_e may be written as:

$$N_e = \sum_{i=1}^{N} X_i \tag{2.27}$$

where X_i, $1 \leq i \leq N$ are independent binary random variables ($Pr(X_i = 1) = P_e$ and $Pr(X_i = 0) = 1 - P_e$ $\forall i$) . The expected value of N_e is easily found to be:

$$E[N_e] = NP_e. \tag{2.28}$$

Then:

$$E\left[\hat{P}_e\right] = P_e \tag{2.29}$$

and the estimator is unbiased.

The variance σ_e^2 of $\hat{P}_e$ is now derived. Note that:

$$E\left[N_e^2\right] = NP_e + N(N-1)P_e^2. \tag{2.30}$$

*The independence of error events is guaranteed by the use of independent noise and fading samples across bits.

Then:

$$E\left[\hat{P}_e^2\right] = \frac{P_e}{N} + \frac{(N-1)\,P_e^2}{N}. \tag{2.31}$$

Thus:

$$\sigma_e^2 = \frac{P_e\,(1-P_e)}{N}. \tag{2.32}$$

Note that the estimator $\hat{P}_e$ is consistent. The quality of $\hat{P}_e$ is traditionally expressed in terms of its confidence interval [17], defined as:

$$Pr\left(P_e - \beta\sigma_e \leq \hat{P}_e \leq P_e + \beta\sigma_e\right) = 1 - \alpha. \tag{2.33}$$

Note that based on the Gaussian approximation (for large N), $\hat{P}_e$ may be expressed as a Gaussian random variable with mean P_e and variance σ_e^2. Then, β may be expressed as[17]:

$$\beta = Q^{-1}\left(\frac{\alpha}{2}\right) \tag{2.34}$$

where $Q(.)$ is the standard Q-function, defined as:

$$Q(x) = \frac{1}{\sqrt{2\pi}}\int_x^\infty e^{-\frac{-t^2}{2}}dt. \tag{2.35}$$

In this work, N is set to $\frac{100}{P_{e,min}}$, where $P_{e,min}$ is the minimum simulated probability of error (corresponding to the highest signal-to-noise or signal-to-noise-plus-interference ratio). In this work, $P_{e,min}$ is set to 10^{-4}. N is then equal to 10^6, and the confidence interval may be written as:

$$P_e - Q^{-1}\left(\frac{\alpha}{2}\right)\sqrt{\frac{P_e\,(1-P_e)}{10^6}} \leq \hat{P}_e \leq P_e + Q^{-1}\left(\frac{\alpha}{2}\right)\sqrt{\frac{P_e\,(1-P_e)}{10^6}} \tag{2.36}$$

At $P_e = 10^{-4}$, the 95% confidence interval ($\alpha = 0.05$) is:

$$8.040 \times 10^{-5} \leq \hat{P}_e \leq\ 1.1960 \times 10^{-4}. \tag{2.37}$$

Confidence intervals for other values of P_e are shown in Table 2.6.

P_e	**Confidence Interval**
10^{-1}	$0.0994 \leq \hat{P}_e \leq 0.1006$
10^{-2}	$0.0098 \leq \hat{P}_e \leq 0.0102$
10^{-3}	$9.3805 \times 10^{-4} \leq \hat{P}_e \leq 0.0011$
10^{-4}	$8.040 \times 10^{-5} \leq \hat{P}_e \leq 1.1960 \times 10^{-4}$

Table 2.6: 95% confidence interval. $N = 10^6$.

Chapter 3

UWB Signal Detection in Dense Multipath: Traditional Approaches

3.1 Introduction and Motivation

Indoor UWB systems have to contend with extremely frequency-selective communication channels. As seen in section 2.5, the channel delay spread is typically orders of magnitude larger than the UWB transmit pulse width. Moreover, due to UWB's fine time resolution, the received signal is very rich in resolvable multipath; the signal energy is usually spread over tens or even hundreds of multipath components. Figure 3.1 illustrates the effect of the communication channel on the UWB pulse. The transmit pulse (left hand side plot) has a time duration of 500 psec, whereas the multipath components of the received pulse (right hand side plot) extend to about 80 nsec. The received pulse shape is severely distorted compared to the transmit pulse shape. From a matched filter point of view, a simple correlator receiver matched to the transmit pulse shape is highly inefficient, since such a receiver would only capture a small fraction of the available signal energy. The optimal receiver in the matched filter sense is the correlator where the template is matched to the *received* pulse shape. However, such a receiver requires perfect channel knowledge, which is not readily available.

The main challenge of UWB signal detection in dense multipath is therefore to design simple (low-cost,

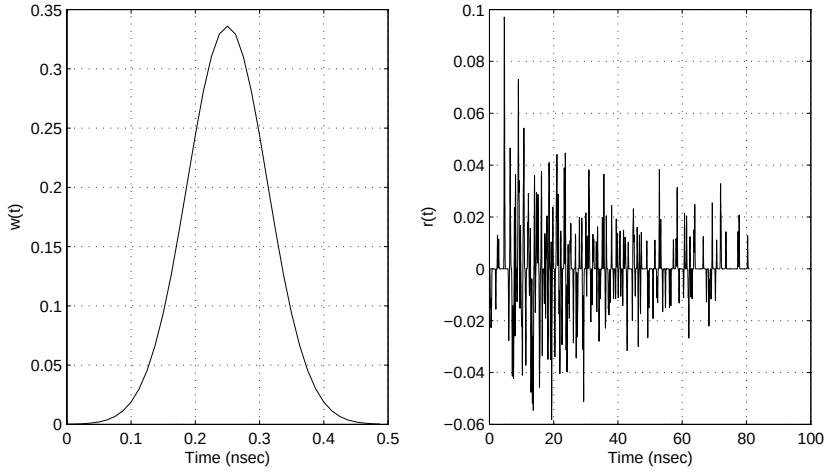

Figure 3.1: Transmit pulse shape (left) and received pulse shape (right).

low-complexity) receivers that can achieve high energy capture (and thus good performance).

Research has mainly concentrated on Rake receivers as candidates for efficient UWB detectors, because of the inherent fine time resolution of the UWB pulse [27]-[38] and their use in SS systems. However, because of the large number of available resolvable paths, the Rake energy capture is relatively low for a moderate number of fingers. Tens of fingers might be needed for acceptable energy capture, making the implementation of a Rake receiver impractical for UWB systems.

Another popular investigated receiver structure is the generalized autocorrelation, or transmit-reference (TR) receiver (also named pilot-assisted receiver in this report), which aims at gathering all the signal energy by using the received pulse shape itself as a correlation template [35],[39]-[48]. TR receivers achieve complete energy capture, but suffer from a "noise-cross-noise" term, caused by the use of a noisy signal as a correlation or matched filter template. Consequently, a prohibitively large number of pilots is required to overcome this limitation.

The main objective of this chapter is to analyze traditional signal detection techniques for UWB systems in dense multipath channels. The limitation of Rake and TR receivers are mathematically analyzed and characterized . New receiver structures that overcome those limitations are proposed and studied in Chapter 4.

3.2 List of Contributions

The two main contributions of this chapter are:

- An accurate characterization of existing/traditional signal detection approaches for UWB systems in dense multipath channels.
- An analysis of the probability of error of Rake receivers in dense multipath taking channel estimation error (which is usually ignored in the literature) into account.

3.3 Chapter Organization

The rest of this chapter is organized as follows. The general signal detection system model is introduced in section 3.4. Throughout this chapter analysis is performed for both binary PAM and binary PPM modulation. The perfect matched filter receiver, where the receiver template is matched to the received pulse shape, is analyzed in section 3.5. Although this is an idealized receiver, since it requires perfect channel knowledge, it provides a useful performance benchmark for the other UWB receivers. A simple matched filter where the template is matched to the transmit pulse shape is investigated in section 3.6. This receiver achieves very low energy capture, and illustrates the inefficiency of traditional detection algorithms applied to UWB in dense multipath. Traditional Rake receivers are analyzed in section 3.7. Previous work in UWB Rake receivers is first summarized. Then, the probability of error of a UWB Rake receiver employing maximum ratio combining (MRC) is mathematically derived. Moreover, the effect of channel estimation on Rake receivers, which is usually neglected in the literature, is analyzed. Simulation results based on real indoor channels illustrating the limited energy capture of Rake receivers are also provided. Then, generalized TR receivers are analyzed both theoretically and through simulations in section 3.8. The effect of the noise-cross-noise term is emphasized. The expression for the probability of error of a TR system utilizing a front-end bandpass filter is derived. Simulation results illustrate the heavy training overhead required by TR receivers. This chapter is finally concluded in section 3.9.

3.4 General System Model

We assume a single-user UWB impulse-radio system [55][56] operating in an indoor multipath channel corrupted by AWGN. The analysis is applied to two modulation techniques: binary PAM (2-PAM), and binary PPM (2-PPM). Note that this work may be easily extended to other modulation techniques, as well as multilevel (M-ary) modulation. Since TH (which generally provides interference mitigation) does not play a role in the analysis, the TH sequence which is traditionally included in UWB systems is omitted. Note that TH may be inserted with no significant change in the derivation of performance. For 2-PAM, we write the transmitted signal as:

$$s_{PAM}(t) = \sqrt{E_p} \sum_{j=-\infty}^{\infty} b_j w(t - jT_f) \tag{3.1}$$

where $b_j = \pm 1$ is the j^{th} data bit, $w(t)$ is the unit-energy UWB transmit pulse, of duration T_w, and E_p is the transmit pulse energy. The transmitter and receiver antenna transfer functions are assumed to be included in $w(t)$. T_f is the symbol duration time ($T_f >> T_w$).

The transmitted signal for 2-PPM is given by:

$$s_{PPM}(t) = \sqrt{E_p} \sum_{j=-\infty}^{\infty} w(t - jT_f - \frac{b_j + 1}{2}\Delta) \tag{3.2}$$

where $\Delta << T_f$ is the delay associated with PPM.

The shape of the transmit pulse $w(t)$ does not affect the analysis. However, note that, for all simulations, a Gaussian pulse is used as the transmit pulse, and is given by:

$$w(t) = \frac{k}{\sqrt{\pi}} e^{-k^2 t^2} \tag{3.3}$$

where k is a parameter controlling the pulse width. It is usually assumed that $T_w \approx \frac{\pi\sqrt{2}}{k}$ (see section 2.4). For all simulations, a pulse of length 500 psec is used. The normalized autocorrelation function of $w(t)$ is given by:

$$R(\tau) = \int_{-\infty}^{\infty} w(t) w(t - \tau) dt. \tag{3.4}$$

For the pulse used in the simulations, $R(\tau)$ is:

$$R(\tau) = \frac{k^2}{\pi} \int_{-\infty}^{\infty} e^{-k^2 t^2} e^{-k^2 (t-\tau)^2} dt. \tag{3.5}$$

Further calculations show that:

$$\begin{aligned}
R(\tau) &= \frac{k^2}{\pi} \int_{-\infty}^{\infty} e^{-2k^2 \left(t^2 - t\tau + \frac{\tau^2}{2} \right)} dt \\
R(\tau) &= \frac{k^2}{\pi} \int_{-\infty}^{\infty} e^{-2k^2 \left[\left(t - \frac{\tau}{2} \right)^2 + \frac{\tau^2}{4} \right]} dt \\
R(\tau) &= \frac{k^2}{\pi} e^{-\frac{k^2 \tau^2}{2}} \int_{-\infty}^{\infty} e^{-2k^2 \left(t - \frac{\tau}{2} \right)^2} dt = \frac{k^2}{\pi} e^{-\frac{k^2 \tau^2}{2}} \int_{-\infty}^{\infty} e^{-2k^2 t^2} dt.
\end{aligned}$$

Thus:

$$R(\tau) = \sqrt{\frac{\pi}{2k^2}} \frac{k^2}{\pi} e^{-\frac{k^2 \tau^2}{2}} = \frac{k}{\sqrt{2\pi}} e^{-\frac{k^2 \tau^2}{2}}.$$

$R(\tau)$ is plotted versus time for $k = 5\text{e}9\ sec^{-1}$ (which corresponds to $T_w \approx 880$ psec) in Figure 3.2. Note that $R(\tau) \approx 0$ for $|\tau| > T_w$.

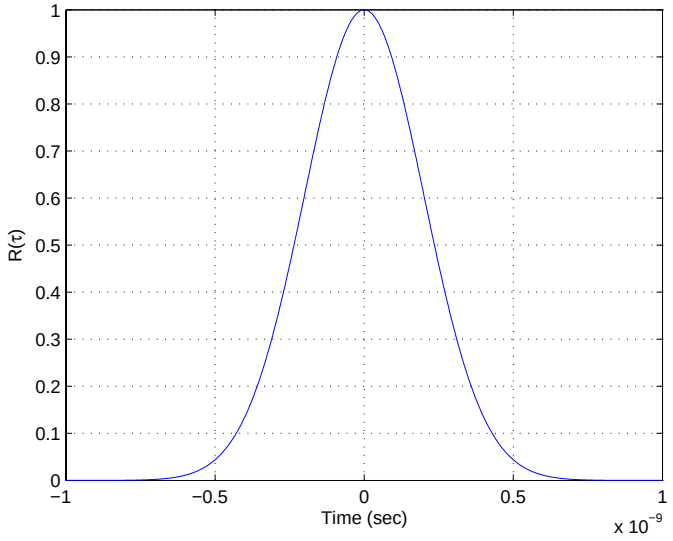

Figure 3.2: Autocorrelation function $R(\tau)$. $k = 5\text{e}9$. Energy in pulse normalized to unity.

The indoor multipath channel is given by a linear tap-delay model. The channel impulse response is

defined as:

$$h(\tau) = \sum_{l=0}^{L-1} \alpha_l \delta(\tau - \tau_l) \tag{3.6}$$

where $\delta(t)$ is the Dirac-delta function, and α_l and τ_l are the magnitude and delay of the l^{th} path, respectively. Note that, since the channel is spatially-varying, α_l and τ_l are random variables whose respective distributions depend on the channel's statistical properties. However, for slowly fading (or quasi-static) channels, the channel may be assumed to be stationary over the analysis, *i.e.* α_l and τ_l may be treated as constants. The received signals for 2-PAM and 2-PPM are written as:

$$r_{PAM}(t) = \sqrt{E_p} \sum_{j=-\infty}^{\infty} b_j v(t - jT_f) + n(t) \tag{3.7}$$

$$r_{PPM}(t) = \sqrt{E_p} \sum_{j=-\infty}^{\infty} v\left(t - jT_f - \frac{b_j + 1}{2}\Delta\right) + n(t) \tag{3.8}$$

respectively, where:

$$v(t) = \sum_{l=0}^{L-1} \alpha_l w(t - \tau_l) \tag{3.9}$$

and $n(t)$ is a zero-mean AWGN random process, with double sided PSD equal to $\frac{N_o}{2}$. We assume that T_f is longer than the channel maximum delay spread τ_{L-1}, so that any ISI effects may be ignored.

3.5 Optimal Matched Filter Receiver

If a signal $v(t)$ is corrupted by AWGN, the filter (or receiver) with impulse response matched to $v(t)$ maximizes the output SNR at the optimal sampling time [57]. Thus, from a matched filter perspective, the optimal receiver is simply a correlator template is matched to the *received* pulse shape $v(t)$. Knowledge of $v(t)$ assumes perfect knowledge of the channel $h(t)$, which is not usually readily available, making this receiver practically infeasible. However, it provides a performance benchmark, and thus provides a good reference against which we can test the performance of other UWB receivers. In this section, we derive an expression for the bit error probability performance of an optimal matched filter receiver. Note that such a receiver is studied in [58] for PPM modulation, where, by averaging performance over multiple indoor channel realizations, it

is shown that UWB achieves a low fading margin, due to the ability of the UWB pulse to resolve a large number of multipath components. UWB's strong immunity to multipath fading will also be illustrated in this section's simulation results.

3.5.1 2-PAM Performance

Assuming 2-PAM, the decision statistic for the j^th transmitted bit may be written as:

$$g_j = \int_{jT_f}^{(j+1)T_f} r(t)v(t - jT_f)dt \tag{3.10}$$

which can be expressed as:

$$g_j = \sqrt{E_p}b_j d_{PAM} + n_j \tag{3.11}$$

where:

$$d_{PAM} = \sum_{l_1=0}^{L-1}\sum_{l_2=0}^{L-1} \alpha_{l1}\alpha_{l2}R\left(\tau_{l1} - \tau_{l2}\right) \tag{3.12}$$

and n_j is a zero-mean Gaussian random variable with variance σ_n^2:

$$\sigma_n^2 = \frac{N_0}{2}\sum_{l_1=0}^{L-1}\sum_{l_2=0}^{L-1} \alpha_{l1}\alpha_{l2}R\left(\tau_{l1} - \tau_{l2}\right) = \frac{N_0}{2}d_{PAM}. \tag{3.13}$$

The decision is based on the sign of g_j. If $g_j > 0$, then the estimated bit is $\hat{b}_j = 1$. Else, $\hat{b}_j = -1$. Since g_j is a Gaussian random variable, then, based on classical error probability analysis in AWGN [57], the probability of error is given by:

$$P_{e|h(t)} = Q\left(\frac{\sqrt{E_p}d_{PAM}}{\sqrt{\sigma_n^2}}\right). \tag{3.14}$$

After some basic manipulations, we get:

$$P_{e|h(t)} = Q\left(\sqrt{\frac{2E_p d_{PAM}}{N_0}}\right). \tag{3.15}$$

Note that $P_{e|h(t)}$ is the probability of error conditioned on a specific channel realization, *i.e.* by treating $h(t)$ as a constant. In order to obtain a more precise error probability expression, $P_{e|h(t)}$ must be integrated

over the channel's statistical distribution. Analytical expressions for this distribution depend on the specific channel characteristics, and are not readily available. However, the integration operation may be approximated by averaging $P_{e|h(t)}$ over multiple channel impulse response profiles obtained from measurements (*i.e.* Monte Carlo integration).

Note that, in the case where $d_{PAM} = 1$, performance is equivalent to classical performance of binary phase shift keying (BPSK) corrupted by AWGN [57]. For a specific channel realization, d_{PAM} may be greater or smaller than 1, depending on how the various multipath channel components add up. For example, Figure 3.3 shows the performance of the 2-PAM optimal receiver for a specific Bicone NLOS indoor channel, taken from measurements. The theoretical curve is obtained by numerically evaluating Equation (3.14) (d_{PAM} for the specific channel profile is calculated and used in the equation). First, notice that the simulated and theoretical performance curves are practically identical. Second, Note that the proposed system's performance is about 1 dB better than the AWGN BPSK bound. This can be explained by the fact that the multipath components added up coherently, resulting in a boost in the signal energy level. However, when performance is averaged over ten NLOS channel realizations (Figure 3.4), the probability of error of the studied system approaches the classical BPSK bound.

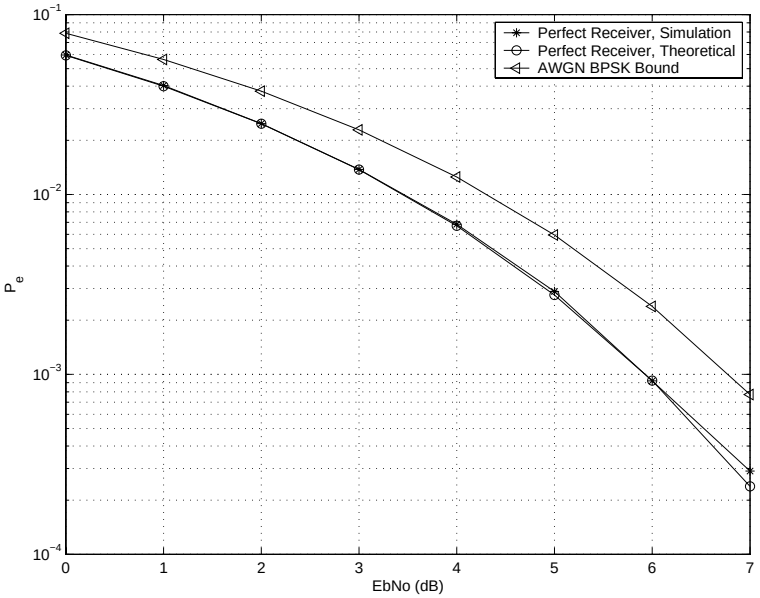

Figure 3.3: Optimal receiver performance for a specific Bicone NLOS indoor channel profile. 2-PAM.

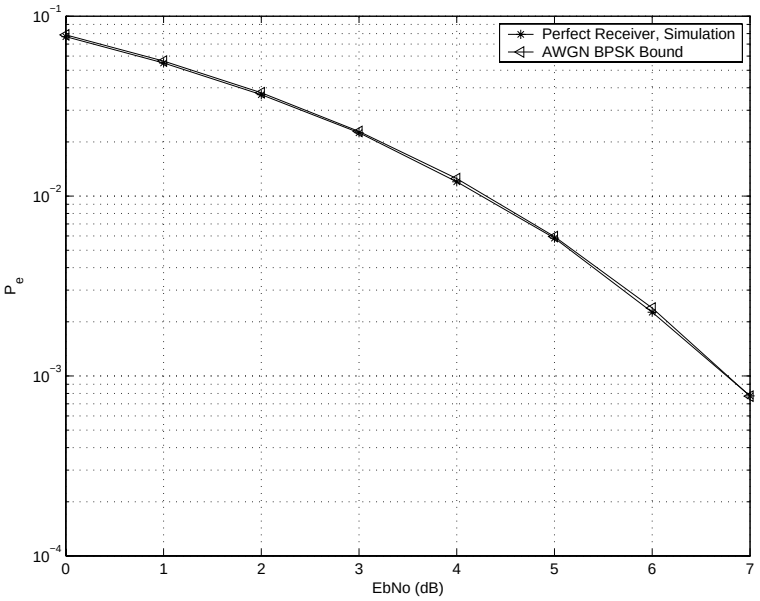

Figure 3.4: Optimal receiver performance averaged over 10 Bicone NLOS indoor channel profiles. 2-PAM.

3.5.2 2-PPM Performance

We now look at the performance of the optimal receiver for 2-PPM. Since information is conveyed through the position of the pulse, the template is formed of a linear combination of two shifted versions of $v(t)$, and may be written as:

$$v_{PPM}(t) = v(t - \Delta) - v(t). \tag{3.16}$$

The decision statistic for the j^th bit is:

$$g_j = \int_{jT_f}^{(j+1)T_f} r(t) v_{PPM}(t - jT_f) dt. \tag{3.17}$$

The decision is based on the sign of g_j. If $g_j > 0$, then the estimated bit is $\hat{b}_j = 1$. Else, $\hat{b}_j = -1$. We assume $b_j = 1$ for ease of notation. Then, g_j can be written as:

$$g_j = \sqrt{E_p} d_{PPM} + n_j \tag{3.18}$$

where:

$$d_{PPM} = \sum_{l_1=0}^{L-1} \sum_{l_2=0}^{L-1} \alpha_{l1} \alpha_{l2} \left(R(\tau_{l1} - \tau_{l2}) - R(\tau_{l1} - \tau_{l2} + \Delta) \right) \tag{3.19}$$

and n_j is a zero-mean Gaussian random variable, given by:

$$n_j = \int_0^{T_f} n(t + jT_f) \left[v(t - \Delta) - v(t) \right] dt. \tag{3.20}$$

The variance σ_n^2 of n_j may be calculated as follows:

$$\begin{aligned}
\sigma_n^2 &= \int_0^{T_f} \int_0^{T_f} E\left[n(t + jT_f) n(\lambda + jT_f) \right] \left(v(t - \Delta) - v(t) \right) . \left(v(\lambda - \Delta) - v(\lambda) \right) dt d\lambda \\
\sigma_n^2 &= \frac{N_0}{2} \int_0^{T_f} \left(v(t - \Delta) - v(t) \right)^2 dt \\
\sigma_n^2 &= N_0 |d_{PPM}|
\end{aligned} \tag{3.21}$$

where $E[.]$ is the expectance operator.

Thus, g_j conditioned on $b_j = 1$ is a Gaussian random variable with mean $\sqrt{E_p} d_{PPM}$ and variance $N_0 |d_{PPM}|$. Calculations are identical for $b_j = -1$. By symmetry, and along the lines of the previous section, the error probability is then given by:

$$P_{e|h(t)} = Q\left(\sqrt{\frac{E_p |d_{PPM}|}{N_0}}\right). \tag{3.22}$$

Note that, in the case where $d_{PPM} = 1$, performance is equivalent to classical performance of any binary orthogonal modulation corrupted by AWGN, such as binary FSK, or binary ASK [57].

Figure 3.5 tests the validity of Equation (3.22), and compares performance to the binary orthogonal bound, for a specific NLOS indoor channel, where Δ is set to T_w. Notice that the theoretical and simulated curves match, and that performance is slightly better than the AWGN bound. Performance is averaged over ten Bicone NLOS channel realizations in Figure 3.6, and is practically identical to the AWGN bound, as expected.

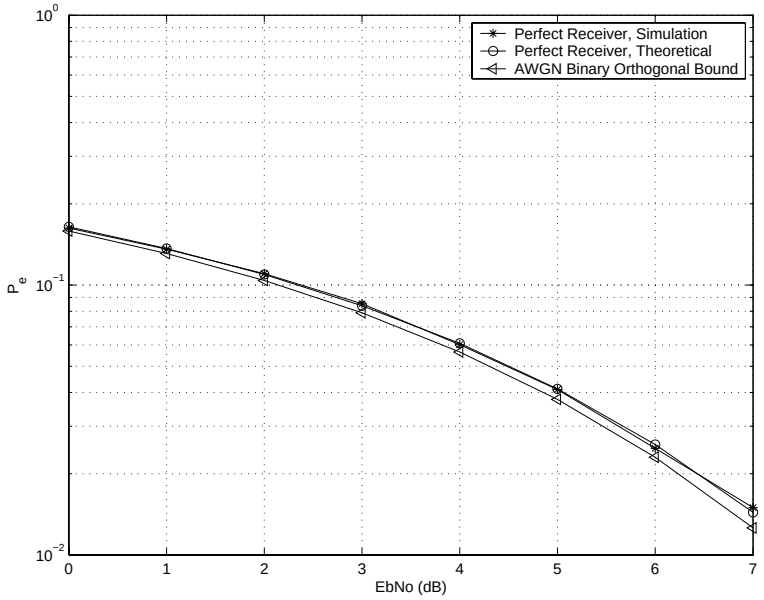

Figure 3.5: Optimal receiver performance for a specific Bicone NLOS indoor channel profile. 2-PPM. $\Delta = T_w$.

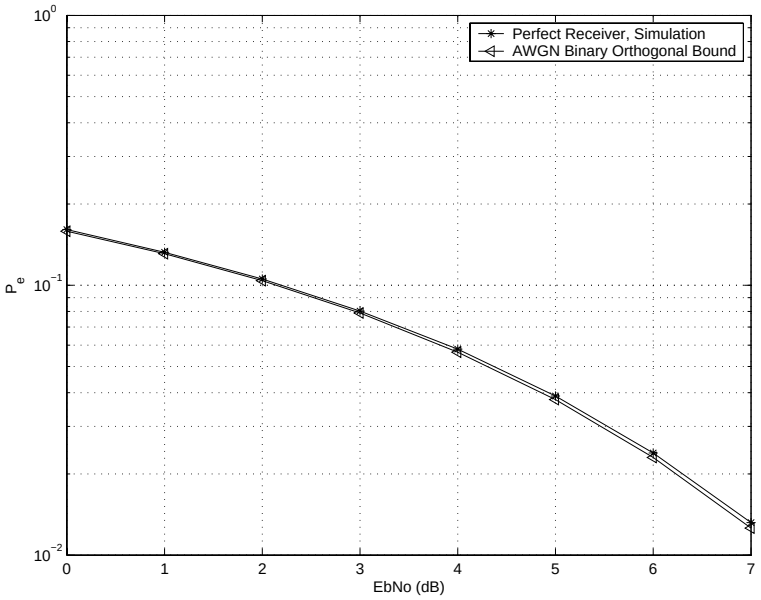

Figure 3.6: Optimal receiver performance averaged over 10 Bicone NLOS indoor channel profiles. 2-PPM. $\Delta = T_w$.

3.6 Simple Pulse-Matched Filter Receiver

Traditional analysis of narrowband systems in AWGN assumes that the received pulse shape is identical to the transmitted pulse shape, or that they are at least highly correlated. Indeed, assuming a multipath-free, pure AWGN channel, a matched filter employing the *transmitted* pulse shape $w(t)$ as a template would achieve the theoretical operational lower bound (such a system is studied in [59]). However, since the indoor UWB communication channel is extremely frequency selective, the received signal is very rich in resolvable multipath, which makes a simple correlator matched to the transmit pulse shape highly inefficient from an energy capture perspective. The limitation of such a simple matched filter is mathematically formulated for both 2-PAM and 2-PPM in this section (a study for the PPM case may also be found in [60]).

3.6.1 2-PAM Performance

Assuming 2-PAM, the decision statistic for the j^{th} bit is:

$$g_j = \int_{jT_f}^{(j+1)T_f} r(t)w(t - jT_f)dt \tag{3.23}$$

where the decision is based on the sign of g_j. g_j can be written as:

$$g_j = \sqrt{E_p} b_j d_{PAM} + n_j \tag{3.24}$$

where:

$$d_{PAM} = \sum_{l=0}^{L-1} \alpha_l R(\tau_l) \tag{3.25}$$

and n_j is a zero-mean Gaussian random variable of variance $\sigma_n^2 = \frac{N_0}{2}$. Then, along the lines set in the previous section, the probability of error conditioned on a specific channel realization is:

$$P_{e|h(t)} = Q\left(\frac{\sqrt{E_p d_{PAM}^2}}{\sqrt{\sigma_n^2}}\right) \tag{3.26}$$

which can be written as:

$$P_{e|h(t)} = Q\left(\sqrt{\frac{2E_p d_{PAM}^2}{N_0}}\right). \tag{3.27}$$

The limitation of such a receiver may be observed by considering the factor d_{PAM}, which is a measure of the system's energy capture. In fact, recall that, for any delay τ_l larger than the pulse width T_w, $R(\tau_l) = 0$. Since the channel delay spread is typically much larger than the pulse width, the energy in almost all the multipath components is lost. Figure 3.7 shows the performance of the simple matched filter for a specific channel realization. First, notice that the error between theoretical (obtained by evaluating Equation (3.27)) and simulated error curves is negligible. Moreover, performance is highly suboptimal, as can be seen by comparison with the BPSK lower bound. Figure 3.8 shows performance averaged over 10 different channel realizations, demonstrating that such a receiver wastes almost all of the available signal energy.

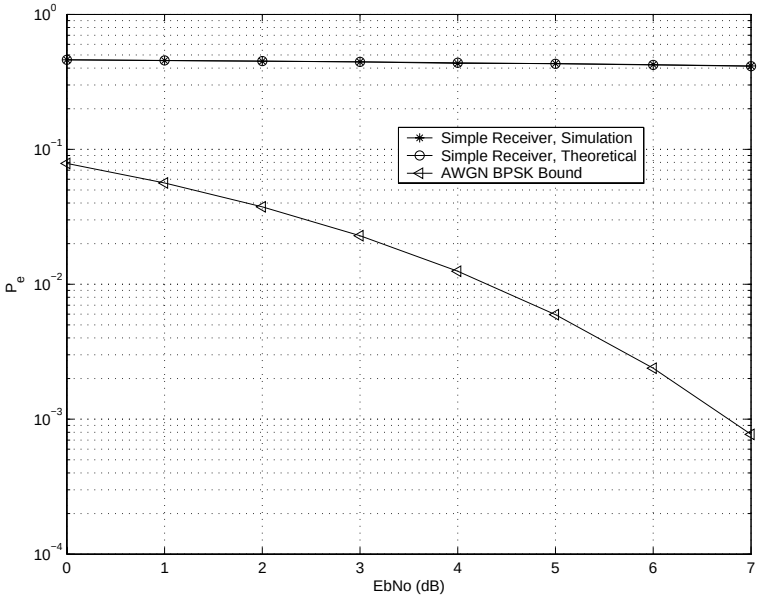

Figure 3.7: Simple receiver performance for a specific Bicone NLOS indoor channel profile. 2-PPM.

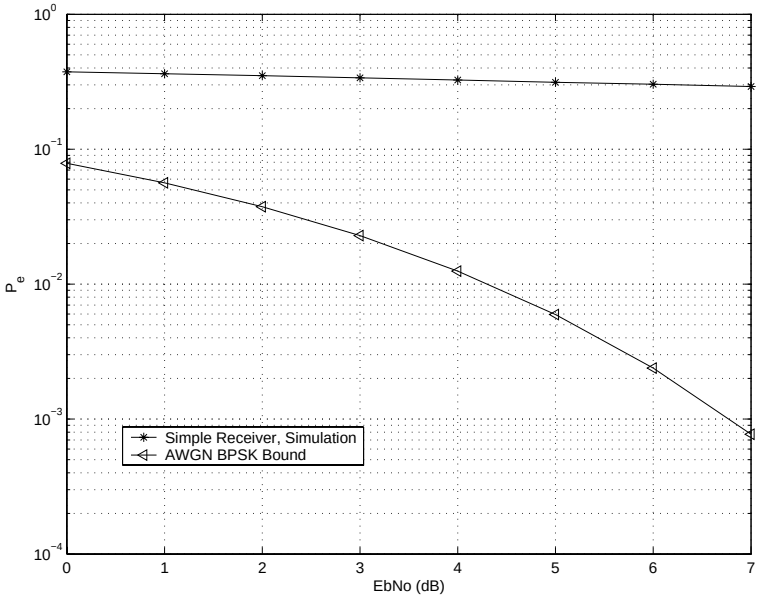

Figure 3.8: Simple receiver performance averaged over 10 Bicone NLOS indoor channel profiles. 2-PPM.

3.6.2 2-PPM Performance

The decision statistic for the $j-th$ bit, assuming 2-PPM, can be written as:

$$g_j = \int_{jT_f}^{(j+1)T_f} r(t)\left[w(t-jT_f-\Delta)-w(t-jT_f)\right]dt. \tag{3.28}$$

g_j is a Gaussian random variable, whose mean depends on the transmitted bit. Let $\sqrt{E_p}d_{PPM,1}$ and $\sqrt{E_p}d_{PPM,-1}$ be the mean values of g_j for $b_j = 1$ and $b_j = -1$, respectively. We can write:

$$g_j = \sqrt{E_p}d_{PPM,b_j} + n_j \tag{3.29}$$

where

$$d_{PPM,1} = \sum_{l_1=0}^{L-1} \alpha_{l1}\left[R\left(\tau_{l1}\right) - R\left(\tau_{l1}+\Delta\right)\right] \tag{3.30}$$

$$d_{PPM,-1} = \sum_{l_1=0}^{L-1} \alpha_{l1}\left[R\left(\tau_{l1}-\Delta\right) - R\left(\tau_{l1}\right)\right] \tag{3.31}$$

and n_j is a zero-mean Gaussian random variable, whose variance is found to be $\sigma_n^2 = N_0\left[1-R\left(\Delta\right)\right]$. Then, the performance is given by:

$$P_e = \frac{1}{2}\left[Q\left(\frac{\sqrt{E_p}d_{PPM,1}}{\sqrt{N_0\left[1-R\left(\Delta\right)\right]}}\right) + Q\left(\frac{\sqrt{E_p}d_{PPM,-1}}{\sqrt{N_0\left[1-R\left(\Delta\right)\right]}}\right)\right]. \tag{3.32}$$

Again, most of the signal energy will be lost due to $w(t)$ autocorrelation properties, and the multipath channel's large delay spread. Simulation for an individual channel profile is shown in Figure 3.9. Figure 3.10 shows performance averaged over 10 different channel realizations. The same observations made for 2-PAM apply.

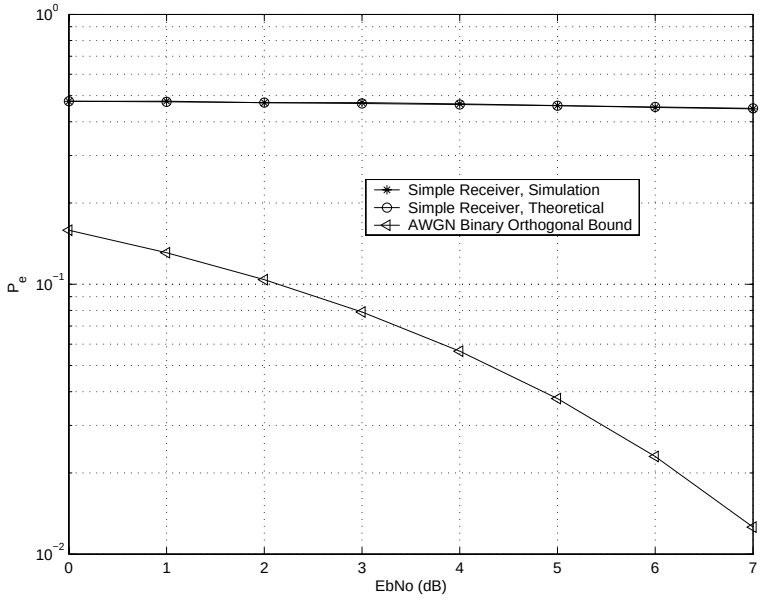

Figure 3.9: Simple receiver performance for a specific Bicone NLOS indoor channel profile. 2-PPM. $\Delta = T_w$.

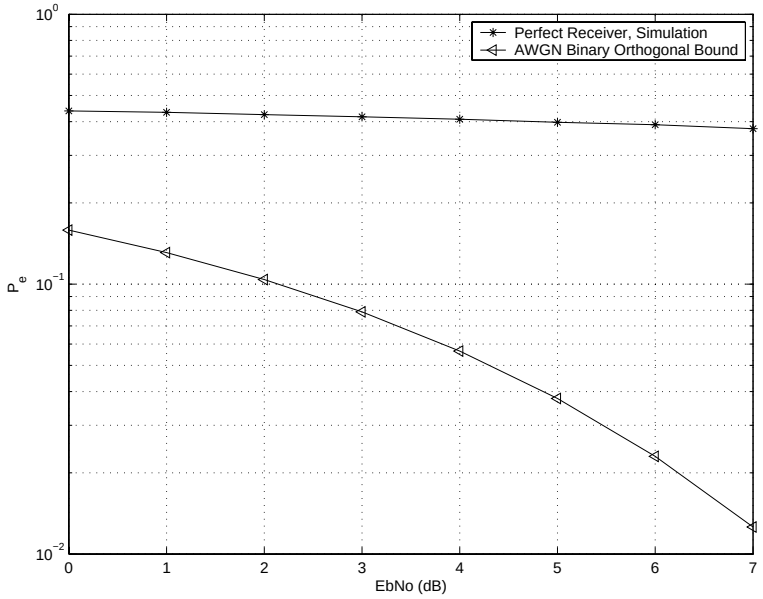

Figure 3.10: Simple receiver performance averaged over 10 Bicone NLOS indoor channel profiles. 2-PPM. $\Delta = T_w$.

3.7 The Rake Receiver

3.7.1 Introduction

Research in UWB signal detection has mainly concentrated on Rake receivers as candidates for efficient UWB detectors, because of the inherent fine time resolution of the UWB pulse, and its potential to resolve a large number of multipath components. Rake receivers are widely used in SS communication systems to accumulate the energy content of the signal replicas corresponding to the different received multipath components. A Rake receiver consists of a bank of correlators, where each correlator (or finger) is synchronized to a multipath component. Multipath energy may be coherently added at the receiver using different finger combining techniques. In equal gain combining (EGC), for example, the signals from different fingers are equally weighted and added. Selection combining (SC) consists of choosing the finger with maximum SNR. Maximum ratio combining (MRC) weights each finger corresponding to its SNR (or the strength of its corresponding multipath). For a detailed analysis of Rake receivers for traditional communication systems, the reader is referred to [57] or [62].

UWB Rake receivers suffer from two major drawbacks. First, the signal energy is spread over tens, even hundreds of multipath components, which leads to a low energy capture when a moderate number of fingers is used. Second, because of the low energy level per path, estimation of the fingers delays and weights is a challenging task at low SNR [27, 28, 29, 30, 31, 32].

Several papers have focused on UWB Rake receivers in recent years. In [33], the performance of an MRC Rake receiver in an indoor multipath environment based on the $\Delta - K$ channel model is studied. The finger delays are uniformly spread over the symbol duration, and the MRC weights are assumed to be known. In [34], a semi-analytical study of three types of MRC Rake receivers is presented, based on indoor office channel measurements: a partial Rake receiver, where the first F arriving multipath components are combined, an improved, selective Rake receiver, where the F strongest paths are selected, and an all-Rake receiver, where all the available paths are combined perfectly. Rake receivers based on square law combining (SLC), where the signals from different Rake fingers are first squared then added, are compared to MRC Rake receivers in [35]. Indoor channel measurements are used, and perfect channel estimation is assumed, *i.e.*, the MRC

weights are known. An analysis of the probability of error of MRC Rake receivers based on tap-delay channel models is presented in [36], assuming perfect channel estimation. It is shown that the increase in energy capture becomes negligible for diversity orders exceeding 100. The impact of imperfect channel estimation is studied in [37]. However, the path delays are assumed to be known, and only the path amplitudes (or the finger weights) are estimated. The impact of the UWB pulse width on Rake receiver performance is investigated in [38]. It is found that shortening the pulse width drastically increases the number of resolvable multipath components, therefore enhancing the energy capture, if enough fingers are used.

In this section, the performance limitation of Rake receivers is mathematically formulated for 2-PAM. Performance for 2-PPM is also included for completeness. Specifically, the effect of channel estimation on Rake receivers, which is usually neglected, is analyzed. Simulation results, based on real indoor channel measurements, are also included to validate the analysis.

3.7.2 Channel Estimation

Since no *a priori* channel information is available, the Rake receiver must first estimate the delays and weights of the fingers before forming the decision statistic. We assume channel estimation is performed using N_p unmodulated pulses, or pilots. The received training sequence can be written as:

$$r_{tr}(t) = \sqrt{E_p} \sum_{k=0}^{N_p-1} v(t - kT_f) + n_p(t) \tag{3.33}$$

where $n_p(t)$ is zero-mean AWGN, with PSD $\frac{N_o}{2}$. In the channel estimation stage, the Rake receiver estimates the correlations, or weights, $\hat{\alpha_f}$, between the received pilot signal and a stored transmit pulse shape delayed by τ_f, $1 \leq f \leq F_{max}$. The F fingers are then selected based on the F strongest weights among the F_{max} available weights. Moreover, any two fingers are separated by at least T_w, to ensure time diversity.
The estimated, normalized weight at delay τ_f can be written as:

$$\hat{\alpha}_f = \frac{1}{N_p\sqrt{E_p}} \sum_{n=0}^{N_p-1} \int_{nT_f}^{nT_f+T_w} r_{tr}(t).w(t - nT_f - \tau_f)dt \tag{3.34}$$

which evaluates to:

$$\hat{\alpha}_f = \sum_{l=0}^{L-1} \alpha_l R(\tau_l - \tau_f) + n_f \tag{3.35}$$

where n_f is a zero mean Gaussian random variable with variance $\frac{N_o}{2N_p E_p}$. Note that, due to the noise and the paths cross-correlations components, there is no guarantee that the F strongest weights will strictly correspond to the F strongest multipath components.

Let $\hat{\alpha}_{f_i}$ be the weight of the i^{th} selected finger at delay τ_{fi}, and $\alpha'_{f_i} = \sum_{l=0}^{L-1} \alpha_l R(\tau_l - \tau_{fi})$. Then, the template constructed by an F- finger Rake receiver is:

$$\hat{v}(t) = \sum_{i=0}^{F-1} \left[\alpha'_{f_i} + n_{f_i}\right] w(t - \tau_{f_i}), \tag{3.36}$$

where $n_{fi},\ \forall i$ is a zero mean Gaussian random variable with variance $\frac{N_o}{2N_p E_p}$.

3.7.3 2-PAM Performance

The decision statistic for the j^{th} bit, formed by the Rake receiver based on MRC, can be written as:

$$g_j = \int_{jT_f}^{(j+1)T_f} r(t).\hat{v}(t - jT_f)dt. \tag{3.37}$$

The bit decision is made based on the sign of g_j. Assuming $b_j = 1$, without loss in generality, we write g_j as:

$$g_j = \sqrt{E_p}U + X_1 + X_2 + X_3 \tag{3.38}$$

where:

$$U = \sum_{i=0}^{F-1}\sum_{j=0}^{L-1} \alpha_j \alpha_{f_i}^{'} R(\tau_j - \tau_{f_i}) \tag{3.39}$$

$$X_1 = \int_{jT_f}^{(j+1)T_f} n(t).\sum_{i=0}^{F-1} \alpha_{f_i}^{'} w(t-\tau_{f_i}-jT_f)dt \tag{3.40}$$

$$X_2 = \int_{jT_f}^{(j+1)T_f} n(t).\sum_{i=0}^{F-1} n_{f_i} w(t-\tau_{f_i}-jT_f)dt \tag{3.41}$$

$$X_3 = \sqrt{E_p}\int_0^{T_f}\sum_{l=0}^{L-1} \alpha_l w(t-\tau_l).\sum_{i=0}^{F-1} n_{f_i} w(t-\tau_{f_i})dt \tag{3.42}$$

where X_1, X_2 and X_3 are zero-mean Gaussian random variables. The variance of g_j is given by $E(X_1^2) + E(X_2^2) + E(X_3^2)$. The calculations are listed below:

$$\begin{aligned}
E(X_1^2) &= E\left[\int_0^{T_f}\int_0^{T_f} n(t).n(\lambda)\sum_{i=0}^{F-1}\alpha_{f_i}^{'} w(t-\tau_{f_i}).\sum_{j=0}^{F-1}\alpha_{f_j}^{'} w(\lambda-\tau_{f_j})dtd\lambda\right] \\
&= \int_0^{T_f}\int_0^{T_f} E\left[n(t).n(\lambda)\right]\sum_{i=0}^{F-1}\alpha_{f_i}^{'} w(t-\tau_{f_i}).\sum_{j=0}^{F-1}\alpha_{f_j}^{'} w(\lambda-\tau_{f_j})dtd\lambda \\
&= \frac{N_o}{2}\int_0^{T_f}\sum_{i=0}^{F-1}\alpha_{f_i}^{'} w(t-\tau_{f_i}).\sum_{j=0}^{F-1}\alpha_{f_j}^{'} w(t-\tau_{f_j})dt \\
&= \frac{N_o}{2}\left[\sum_{i=0}^{F-1}\alpha_{f_i}^{'2} + \sum_{i=0}^{F-1}\sum_{j=0,i\neq j}^{F-1}\alpha_{f_i}^{'}\alpha_{f_j}^{'} R(\tau_{f_i}-\tau_{f_j})\right].
\end{aligned} \tag{3.43}$$

$$\begin{aligned}
E(X_2^2) &= E\left[\int_0^{T_f}\int_0^{T_f} n(t).n(\lambda)\sum_{i=0}^{F-1}.\sum_{j=0}^{F-1} n_{f_i}n_{f_j} w(t-\tau_{f_i})w(\lambda-\tau_{f_j})dtd\lambda\right] \\
&= \sum_{i=0}^{F-1}.\sum_{j=0}^{F-1}\int_0^{T_f}\int_0^{T_f} E\left[n(t).n(\lambda)n_{f_i}n_{f_j}\right] w(t-\tau_{f_i})w(\lambda-\tau_{f_j})dtd\lambda \\
&= \sum_{i=0}^{F-1}\int_0^{T_f}\int_0^{T_f} E\left[n(t).n(\lambda)n_{f_i}^2\right] w(t-\tau_{f_i})w(\lambda-\tau_{f_i})dtd\lambda \\
&= \frac{N_o^2}{4E_pN_p}\sum_{i=0}^{F-1}\int_0^{T_f} w^2(t-\tau_{f_i})dt = F.\frac{N_o^2}{4E_pN_p}.
\end{aligned} \tag{3.44}$$

$$
\begin{aligned}
E\left(X_3^2\right) &= \frac{N_o}{2N_p}\int_0^{T_f}\int_0^{T_f}\sum_{l_1=0}^{L-1}\sum_{l_2=0}^{L-1}\sum_{i=0}^{F-1}\alpha_{l_1}\alpha_{l_2}w(t-\tau_{l1})w(\lambda-\tau_{l2})w(t-\tau_{f_i})w(\lambda-\tau_{f_i})dtd\lambda \\
&= \frac{N_o}{2N_p}\int_0^{T_f}\sum_{l_1=0}^{L-1}\sum_{l_2=0}^{L-1}\sum_{i=0}^{F-1}\alpha_{l_1}\alpha_{l_2}R(\tau_{l_1}-\tau_{f_i})w(\lambda-\tau_{l2})w(\lambda-\tau_{f_i})d\lambda \\
&= \frac{N_o}{2N_p}\sum_{l_1=0}^{L-1}\sum_{l_2=0}^{L-1}\sum_{i=0}^{F-1}\alpha_{l_1}\alpha_{l_2}R(\tau_{l_1}-\tau_{f_i})R(\tau_{l2}-\tau_{f_i}). \qquad (3.45)
\end{aligned}
$$

We get the following expression for the probability of bit error:

$$
P_e = Q\left(\sqrt{\frac{2E_p}{N_o}.\frac{U^2}{Y_1+\frac{Y_2}{N_p}+\left(\frac{2N_p}{F}\frac{E_p}{N_o}\right)^{-1}}}\right) \qquad (3.46)
$$

where:

$$
Y_1 = \sum_{k=0}^{F-1}\alpha_{f_k}^{'2}+\sum_{i=0}^{F-1}\sum_{j=0,j\neq i}^{F-1}\alpha_{f_i}^{'}\alpha_{f_j}^{'}R(\tau_{f_i}-\tau_{f_j}) \qquad (3.47)
$$

$$
Y_2 = \sum_{l_1=0}^{L-1}\sum_{l_2=0}^{L-1}\sum_{i=0}^{F-1}\alpha_{l_1}\alpha_{l_2}R(\tau_{l_1}-\tau_{f_i})R(\tau_{l2}-\tau_{f_i}). \qquad (3.48)
$$

Let:

$$
Z_F = \frac{U^2}{Y_1+\frac{Y_2}{N_p}+\left(\frac{2N_p}{F}\frac{E_p}{N_o}\right)^{-1}}. \qquad (3.49)
$$

Z_F represents the effective receiver energy capture. Z_F increases as more fingers are added. However, it has been shown that a typical indoor NLOS channel may have hundreds of resolvable dominant specular components (see Table 2.1). Even if a Rake receiver with so many fingers is realizable, it would only be able to capture part of the signal energy [27][28]. Also, in the absence of *a priori* channel information, estimation of the fingers' delays and weights is a challenging task in dense multipath. In fact, the term $\frac{Y_2}{N_p}+\left(\frac{2N_p}{F}\frac{E_p}{N_o}\right)^{-1}$ degrades performance for a small number of pilots at low SNR values, which are the typical operating conditions for an UWB system.

3.7.4 2-PPM Performance

Derivation of the 2-PPM Rake receiver performance is straightforward, and is similar to the derivation in the 2-PAM. It is somewhat cumbersome, and results in more complex notations, but does not provide any additional insight compared to 2-PAM. Nonetheless, the analysis is included here for completeness. The decision statistic for the j^{th} bit can be written as:

$$g_j = \int_{jT_f}^{(j+1)T_f} r(t).\left[\hat{v}(t - jT_f - \Delta) - \hat{v}(t - jT_f)\right] dt. \tag{3.50}$$

Let $g_{j,1}$ and $g_{j,-1}$ be the decision statistics corresponding to $b_j = 1$ and $b_j = -1$, respectively. Then:

$$g_{j,1} = \sqrt{E_p}U_1 + X_1 + X_2 + X_{3,1} \tag{3.51}$$

$$g_{j,-1} = \sqrt{E_p}U_{-1} + X_1 + X_2 + X_{3,-1} \tag{3.52}$$

where:

$$\begin{aligned}
U_1 &= \sum_{i=0}^{F-1}\sum_{j=0}^{L-1} \alpha_j \alpha_{f_i}^{'} \left[R(\tau_j - \tau_{f_i}) - R(\tau_j - \tau_{f_i} + \Delta)\right] \\
U_{-1} &= \sum_{i=0}^{F-1}\sum_{j=0}^{L-1} \alpha_j \alpha_{f_i}^{'} \left[R(\tau_j - \tau_{f_i} - \Delta) - R(\tau_j - \tau_{f_i})\right] \\
X_1 &= \int_{jT_f}^{(j+1)T_f} n(t).\sum_{i=0}^{F-1} \alpha_{f_i}^{'} \left[w(t - \tau_{f_i} - jT_f - \Delta) - w(t - \tau_{f_i} - jT_f)\right] dt \\
X_2 &= \int_{jT_f}^{(j+1)T_f} n(t).\sum_{i=0}^{F-1} n_{f_i} \left[w(t - \tau_{f_i} - jT_f - \Delta) - w(t - \tau_{f_i} - jT_f)\right] dt \\
X_{3,1} &= \sqrt{E_p}\int_0^{T_f} \sum_{l=0}^{L-1} \alpha_l w(t - \tau_l - \Delta).\sum_{i=0}^{F-1} n_{f_i} \left[w(t - \tau_{f_i} - \Delta) - w(t - \tau_{f_i})\right] dt \\
X_{3,-1} &= \sqrt{E_p}\int_0^{T_f} \sum_{l=0}^{L-1} \alpha_l w(t - \tau_l).\sum_{i=0}^{F-1} n_{f_i} \left[w(t - \tau_{f_i} - \Delta) - w(t - \tau_{f_i})\right] dt.
\end{aligned}$$

X_1, X_2, $X_{3,1}$ and $X_{3,-1}$ are zero-mean Gaussian random variables. The calculations for their second moments are listed below:

$$\begin{aligned}
E(X_1^2) &= E\left[\int_0^{T_f}\int_0^{T_f} n(t).n(\lambda)\sum_{i=0}^{F-1}\alpha_{f_i}^{'}\left[w(t-\tau_{f_i}-\Delta)-w(t-\tau_{f_i})\right].\sum_{j=0}^{F-1}\alpha_{f_j}^{'}\left[w(\lambda-\tau_{f_j}-\Delta)-w(\lambda-\tau_{f_j})\right]dtd\lambda\right] \\
&= \frac{N_o}{2}\int_0^{T_f}\sum_{i=0}^{F-1}\alpha_{f_i}^{'}\left[w(t-\tau_{f_i}-\Delta)-w(t-\tau_{f_i})\right].\sum_{j=0}^{F-1}\alpha_{f_j}^{'}\left[w(t-\tau_{f_j}-\Delta)-w(t-\tau_{f_j})\right]dt, \\
&= \frac{N_o}{2}\left[\sum_{i=0}^{F-1}\sum_{j=0}^{F-1}\alpha_{f_i}^{'}\alpha_{f_j}^{'}\left[2R(\tau_{f_i}-\tau_{f_j})-R(\tau_{f_j}-\tau_{f_i}-\Delta)-R(\tau_{f_j}-\tau_{f_i}+\Delta)\right]\right].
\end{aligned}$$

$$\begin{aligned}
E(X_2^2) &= E[\int_0^{T_f}\int_0^{T_f} n(t).n(\lambda)\sum_{i=0}^{F-1}.\sum_{j=0}^{F-1}n_{f_i}n_{f_j}\left[w(t-\tau_{f_i}-\Delta)-w(t-\tau_{f_i}+\Delta)\right].\left[w(\lambda-\tau_{f_j}-\Delta)-w(\lambda-\tau_{f_j})\right] \\
&= \sum_{i=0}^{F-1}.\sum_{j=0}^{F-1}\int_0^{T_f}\int_0^{T_f}E[n(t).n(\lambda)n_{f_i}n_{f_j}\left[w(t-\tau_{f_i}-\Delta)-w(t-\tau_{f_i}\right].\left[w(\lambda-\tau_{f_j}-\Delta)-w(\lambda-\tau_{f_j})\right]]dtd\lambda \\
&= \sum_{i=0}^{F-1}\int_0^{T_f}\int_0^{T_f}E[n(t).n(\lambda)n_{f_i}^2\left[w(t-\tau_{f_i}-\Delta)-w(t-\tau_{f_i})\right].\left[w(\lambda-\tau_{f_i}-\Delta)-w(\lambda-\tau_{f_i})\right]]dtd\lambda \\
&= \frac{N_o^2}{4E_pN_p}\sum_{i=0}^{F-1}\int_0^{T_f}\left[w(t-\tau_{f_i}-\Delta)-w(t-\tau_{f_i})\right]^2dt \\
&= \left[F-R\left(\Delta\right)\right].\frac{N_o^2}{2E_pN_p}.
\end{aligned}$$

$$\begin{aligned}
E\left(X_{3,1}^2\right) &= \frac{N_o}{2N_p}\int_0^{T_f}\int_0^{T_f}\sum_{l_1=0}^{L-1}\sum_{l_2=0}^{L-1}\sum_{i=0}^{F-1}\alpha_{l_1}\alpha_{l_2}w(t-\tau_{l1}-\Delta)w(\lambda-\tau_{l2}-\Delta) \\
&\quad \left[w(t-\tau_{f_i}-\Delta)-w(t-\tau_{f_i})\right]\left[w(\lambda-\tau_{f_i}-\Delta)-w(\lambda-\tau_{f_i})\right]dtd\lambda \\
&= \frac{N_o}{2N_p}\int_0^{T_f}\sum_{l_1=0}^{L-1}\sum_{l_2=0}^{L-1}\sum_{i=0}^{F-1}\alpha_{l_1}\alpha_{l_2}\left(R(\tau_{l_1}-\tau_{f_i})-R(\tau_{l_1}-\tau_{f_i}+\Delta)\right)w(\lambda-\tau_{l2}-\Delta) \\
&\quad \left[w(\lambda-\tau_{f_i}-\Delta)-w(\lambda-\tau_{f_i})\right]d\lambda \\
&= \frac{N_o}{2N_p}\sum_{l_1=0}^{L-1}\sum_{l_2=0}^{L-1}\sum_{i=0}^{F-1}\alpha_{l_1}\alpha_{l_2}.\left[R(\tau_{l_1}-\tau_{f_i})-R(\tau_{l_1}-\tau_{f_i}+\Delta)\right].\left[R(\tau_{l_2}-\tau_{f_i})-R(\tau_{l_2}-\tau_{f_i}+\Delta)\right].
\end{aligned}$$

$$
\begin{aligned}
E\left(X_{3,-1}^2\right) &= \frac{N_o}{2N_p}\int_0^{T_f}\int_0^{T_f}\sum_{l_1=0}^{L-1}\sum_{l_2=0}^{L-1}\sum_{i=0}^{F-1}\alpha_{l_1}\alpha_{l_2}w(t-\tau_{l1})w(\lambda-\tau_{l2}) \\
&\quad \left[w(t-\tau_{f_i}-\Delta)-w(t-\tau_{f_i}+\Delta)\right]\left[w(\lambda-\tau_{f_i}-\Delta)-w(\lambda-\tau_{f_i})\right]dtd\lambda \\
&= \frac{N_o}{2N_p}\int_0^{T_f}\sum_{l_1=0}^{L-1}\sum_{l_2=0}^{L-1}\sum_{i=0}^{F-1}\alpha_{l_1}\alpha_{l_2}\left(R(\tau_{l_1}-\tau_{f_i}-\Delta)-R(\tau_{l_1}-\tau_{f_i})\right)w(\lambda-\tau_{l2}) \\
&\quad \left[w(\lambda-\tau_{f_i}-\Delta)-w(\lambda-\tau_{f_i})\right]d\lambda \\
&= \frac{N_o}{2N_p}\sum_{l_1=0}^{L-1}\sum_{l_2=0}^{L-1}\sum_{i=0}^{F-1}\alpha_{l_1}\alpha_{l_2}.\left[R(\tau_{l_1}-\tau_{f_i}-\Delta)-R(\tau_{l_1}-\tau_{f_i})\right].\left[R(\tau_{l_2}-\tau_{f_i}-\Delta)-R(\tau_{l_2}-\tau_{f_i})\right].
\end{aligned}
$$

We get the following expression for the probability of bit error:

$$
P_e = \frac{1}{2}\left[Q\left(\sqrt{\frac{E_pU_1^2}{E\left(X_1^2\right)+E\left(X_2^2\right)+E\left(X_{3,1}^2\right)}}\right)+Q\left(\sqrt{\frac{E_pU_{-1}^2}{E\left(X_1^2\right)+E\left(X_2^2\right)+E\left(X_{3,-1}^2\right)}}\right)\right].
$$

3.7.5 Simulation Results

The performance of MRC Rake receivers using 2-PAM is analyzed through simulation in this section. Recall that a Gaussian pulse of length 500 psec is used.

Figure 3.11 validates the theoretical 10-finger Rake performance (Equation (3.46)) for an arbitrary Bicone channel profile by simulation. Perfect channel knowledge is assumed (*i.e.* N_p is infinite). When numerically evaluating Equation (3.46), it is assumed that the ten strongest resolvable paths are selected. First, note that the theoretical and simulated curves match with negligible error. Second, note that performance is about 3 dB worse than the theoretical lower bound (BPSK performance in AWGN). The robustness of the theoretical expression is tested for imperfect channel estimation in Figures 3.12 ($N_p = 100$) and 3.13 ($N_p = 10$). Notice the performance degradation brought by errors in channel estimation. Moreover, note that the error between simulated and theoretical curves grows as N_p decreases, because the assumption that the 10 strongest paths are selected no longer holds. In fact, in the presence of estimation errors, the fingers are no longer set at delays strictly corresponding to specular components. At the limit of the system's operation (very low SNR, very low N_p), the multipath components are completely covered by noise, and fingers are chosen randomly.

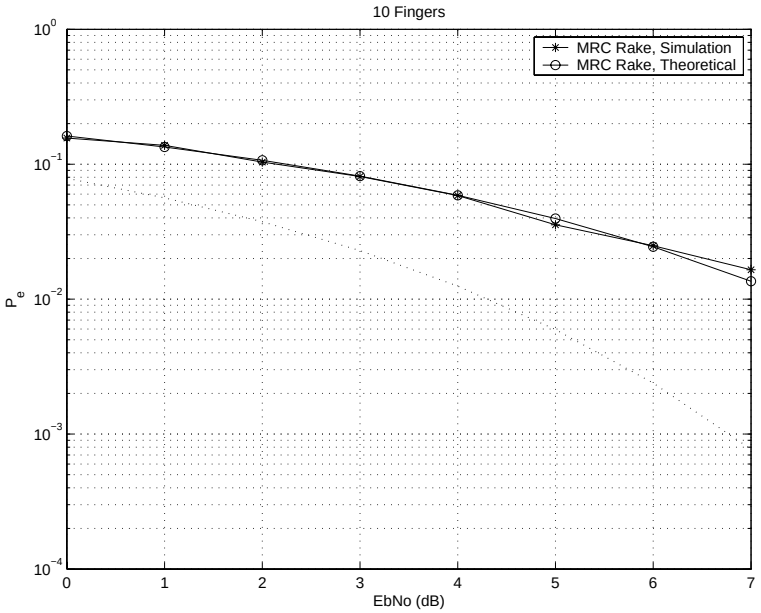

Figure 3.11: MRC-Rake Performance. 2-PAM. 10 Fingers. Perfect channel estimation. Dotted line represents BPSK performance in AWGN.

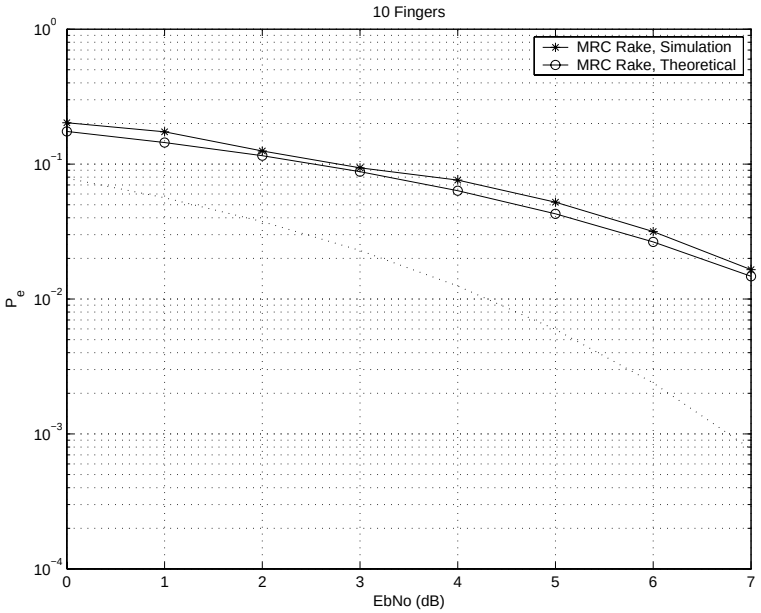

Figure 3.12: MRC-Rake Performance. 2-PAM. 10 Fingers. 100 pilot-channel estimation. Dotted line represents BPSK performance in AWGN.

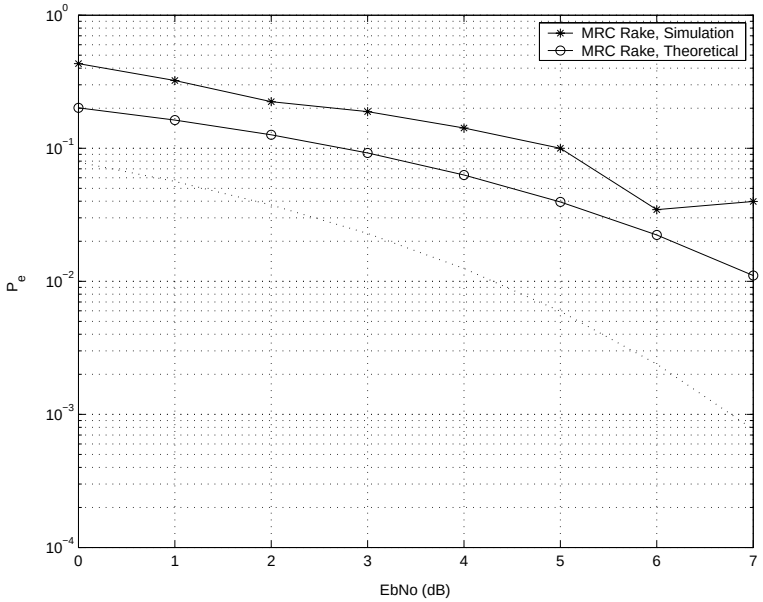

Figure 3.13: MRC-Rake Performance. 2-PAM. 10 Fingers. 10 pilot-channel estimation. Dotted line represents BPSK performance in AWGN.

Figures 3.14 and 3.15 compare theoretical and simulated performance for 20 fingers (perfect channel estimation and $N_p = 100$, respectively), for the same channel profile. Note a gain of about 1 dB compared to the 10-finger case. Moreover, the error between theory and simulation is negligible for 100-pilot channel estimation.

Figure 3.16 compares performance of 10, 20 and 50-finger Rake receivers for $N_p = 100$. Notice the diminishing returns when increasing the number of fingers from 10 to 20, and from 20 to 50, respectively. 50 fingers yield a performance that is about 1.5 dB worse than the BPSK lower bound. The effect of the training load for 10, 20 and 50 fingers is investigated in Figure 3.17. Note that the error probability is high for all three receivers for low training; performance improves with increasing N_p, until it reaches a floor (which is the perfect estimation case). The floor is determined by the achievable finger energy capture. The receiver with less fingers reaches the floor for a smaller N_p (45 pilots for 10 fingers, 80 pilots for 20 fingers, 100 pilots for 50 fingers), because fingers corresponding to low amplitude paths require more averaging to surpass the noise level. Finally, Figure 3.18 shows the energy capture (the energy in the selected paths) versus the number of Rake fingers. Notice that 70 fingers are required to achieve 90% energy capture. 10 fingers achieve less than 50% energy capture.

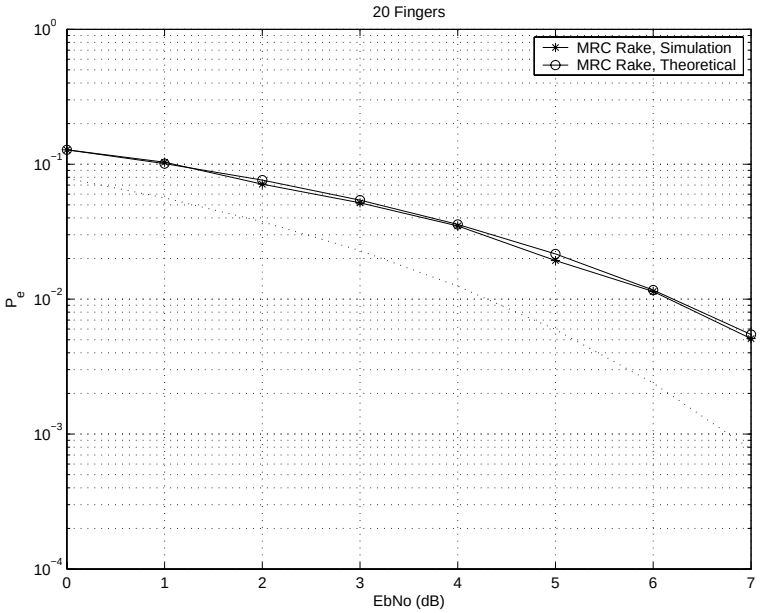

Figure 3.14: MRC-Rake Performance. 2-PAM. 20 Fingers. Perfect channel estimation. Dotted line represents BPSK performance in AWGN.

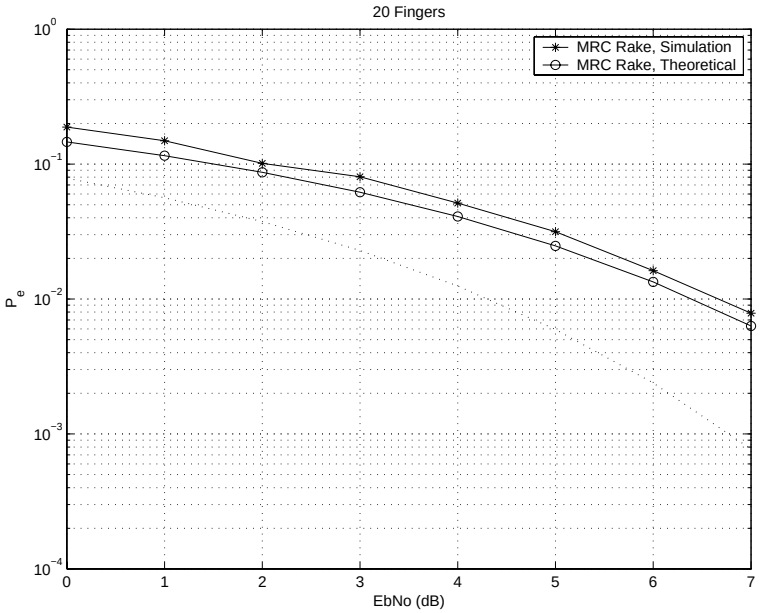

Figure 3.15: MRC-Rake Performance. 2-PAM. 20 Fingers. 100 pilot-channel estimation. Dotted line represents BPSK performance in AWGN.

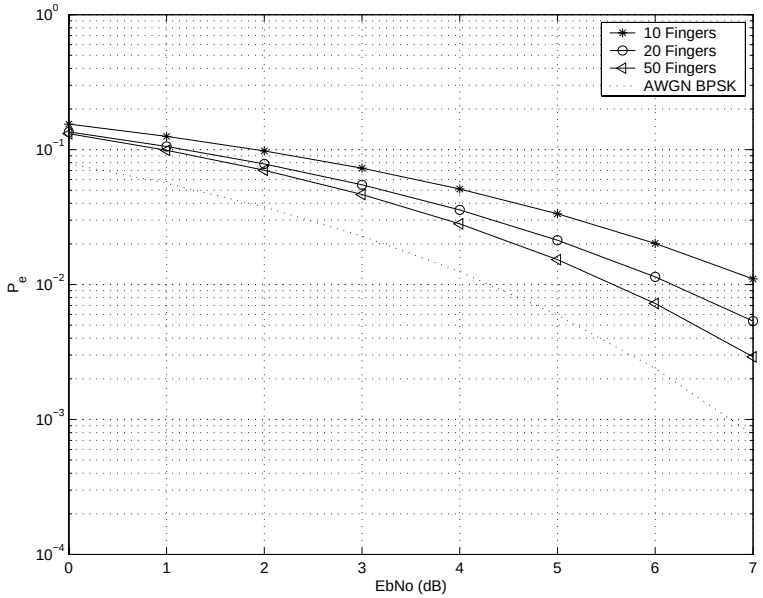

Figure 3.16: Performance of 10, 20 and 50 finger-Rake, averaged over 10 Bicone NLOS realizations. 2-PAM. 100 pilot-channel estimation.

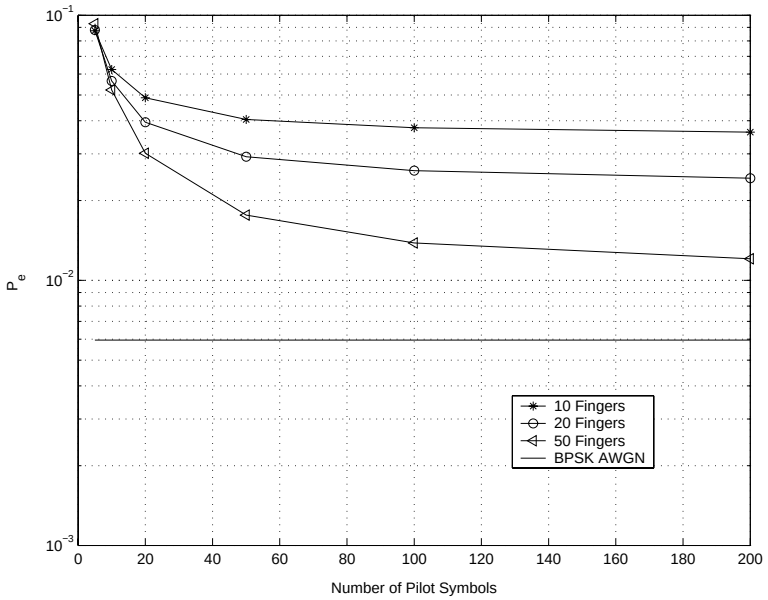

Figure 3.17: Performance versus number of pilot symbols for 10, 20 and 50 finger-Rake, averaged over 10 Bicone NLOS realizations. 2-PAM. $\frac{E_b}{N_0} = 5\ dB$.

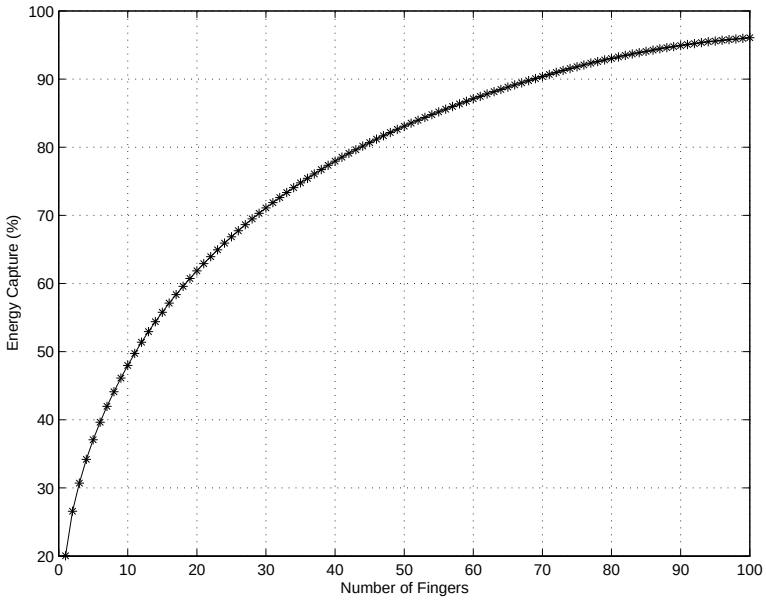

Figure 3.18: Energy capture versus number of fingers, averaged over 30 Bicone NLOS channel realizations.

3.8 The Pilot-Assisted Receiver

3.8.1 Introduction

The pilot-assisted receiver is a widely studied type of receiver which aims at gathering all the signal energy by using the received pulse shape itself as a correlation template. This system can be thought of as a generalization of traditional autocorrelation, or TR receivers. In the original form of a TR system, a pair of unmodulated and modulated signals is transmitted, and the former is employed to demodulate the latter. This receiver can capture the entire signal energy for a slowly varying channel without requiring channel estimation. However, it suffers from the use of a noisy received signal as a template for demodulation (the noise-cross-noise term).

TR systems were first proposed in the 1920s [35]. However, fundamental system weaknesses, such as bandwidth inefficiency and high noise vulnerability, coupled with the advent of stored reference and matched filter implementations in the 1950s and 1960s largely diminished research interest in TR schemes [61]. Research in UWB autocorrelation receivers has been relatively active recently, fueled by the need for receivers that can achieve high energy capture in dense multipath. A delay-hopped, TR Communications system was recently built by the research and development center in GE. Experiments show the viability of such a system in an indoor multipath environment [39][40]. An analytical characterization of the performance of an UWB autocorrelation TR system can be found in [41]. Experimental results comparing the TR receiver with Rake receiver structures can be found in [35]. It is shown that the TR receiver performs slightly better than a single finger Rake receiver with MRC. The effect of the noise-cross-noise term is also illustrated. A general framework for the analysis of TR systems in arbitrary fading channels is presented in [42]. A general pilot waveform assisted modulation (PWAM) scheme, which subsumes TR as a special case, is introduced in [43]. The values of the systems parameters are derived to minimize the channel′s MSE and maximize the average capacity. The circumstances under which the UWB autocorrelation-TR system is optimal are also analyzed. In [44], the performance of a TR system is derived with and without averaging many pilot signals. A differential TR system is also proposed. However, it is difficult to average many signals when differential modulation is used. In [45], an improved TR template is introduced, where both pilot and data symbols are

used to reconstruct the template, based on a generalized likelihood ratio test. A combination of differential and traditional TR systems, coupled with the use of linear block codes instead of the standard repetition code, in suggested in [46], in order to reduce the training load. The effect of the integration time on system performance is investigated in [47]. It is shown that excessive integration time, which introduces more noise to the system, is less harmful than short integration times, which results in reduced energy capture. A generalization of TR systems, where the correlator template is multiplied by weighting functions, obtained based on the average likelihood test, is suggested in [48].

In this section, a general pilot-assisted system is mathematically analyzed. Analysis is performed based on an arbitrary number of pilot symbols N_p. Note that the system degenerates into a standard TR system for $N_p = 1$. The detrimental effect of the noise-cross-noise term is emphasized. The need for a noise bandlimiting filter at the receiver front end is demonstrated. The section is concluded by simulation results, which illustrate various performance aspects of pilot-assisted systems. A proposed improvement on this system is proposed in the following section.

3.8.2 Receiver Template

We assume a frame structure comprising a preamble of N_p unmodulated pilot symbols, followed by N_d data symbols. The N_p pilots are processed to generate a template estimate. This estimate is then used to demodulate the N_d data symbols. Assuming the pilot structure of Equation (3.33), the estimated, normalized template is:

$$\hat{v}(t) = \frac{1}{\sqrt{E_p} N_p} \sum_{k=0}^{N_p - 1} r_{tr}\left(t + kT_f\right), \; 0 \leq t \leq T_f \tag{3.53}$$

which can be written as:

$$\hat{v}(t) = v(t) + n_{tr}(t) \tag{3.54}$$

where $n_{tr}(t)$ is a zero-mean AWGN process with PSD $\frac{N_0}{2N_p E_p}$.

3.8.3 Signal Detection in the Absence of a Bandlimiting Filter

In this section we show that the correlation operation results in a noise term with infinite power in the absence of a front-end bandlimiting filter. Assuming 2-PAM, the decision statistic for the j^{th} bit is:

$$g_j = \int_{jT_f}^{jT_f+T_{int}} \hat{v}(t)r(t)dt \tag{3.55}$$

where $T_{int} \leq T_f$ is the integration time. The expression may be written as:

$$\begin{aligned} g_j = \sqrt{E_p}\int_0^{T_{int}} v^2(t)dt + \int_{jT_f}^{jT_f+T_{int}} v(t-jTf)n(t)dt + \\ \sqrt{E_p}\int_{jT_f}^{jT_f+T_{int}} v(t-jTf)n_{tr}(t)dt + \int_{jT_f}^{jT_f+T_{int}} n(t)n_{tr}(t)dt. \end{aligned} \tag{3.56}$$

Let g_n be the problematic noise-cross-noise term:

$$g_n = \int_{jT_f}^{jT_f+T_{int}} n(t)n_{tr}(t)dt. \tag{3.57}$$

The variance σ_g^2 of this zero-mean term is calculated as follows:

$$\begin{aligned} \sigma_g^2 &= \int_0^{T_{int}}\int_0^{T_{int}} E\left[n(t).n_{tr}(t)n(\lambda).n_{tr}(\lambda)\right]dtd\lambda \\ \sigma_g^2 &= \int_0^{T_{int}}\int_0^{T_{int}} R_n(t-\lambda).R_{n_{tr}}(t-\lambda)dtd\lambda \end{aligned} \tag{3.58}$$

where $R_n(\tau)$ and $R_{n_{tr}}(\tau)$ are the autocorrelation functions of $n(t)$ and $n_{tr}(t)$, respectively, and are given by:

$$R_n(\tau) = \frac{N_o}{2}\delta(\tau) \tag{3.59}$$

$$R_{n_{tr}}(\tau) = \frac{N_o}{2N_p}\delta(\tau) \tag{3.60}$$

where $\delta(\tau)$ is defined as:

$$\begin{aligned} \delta(0) &= \infty && (3.61) \\ \delta(\tau) &= 0,\ \tau \neq 0 && (3.62) \\ \int_{-\infty}^{\infty} \delta(t)dt &= 1 && (3.63) \end{aligned}$$

where ∞ represents infinity. Therefore:

$$\begin{aligned} \sigma_g^2 &= \int_0^{T_{int}} \int_0^{T_{int}} \frac{N_o}{2}\delta(t-\lambda).\frac{N_o}{2N_p}\delta(t-\lambda)dtd\lambda \\ \sigma_g^2 &= \frac{N_o^2}{4N_p} \int_0^{T_{int}} \int_0^{T_{int}} \delta(t-\lambda).\delta(t-\lambda)dtd\lambda. \end{aligned}$$

Then, using the sifting property [65],

$$\int_0^{T_{int}} \delta(t-\lambda).\delta(t-\lambda)dt = \int_{-\lambda}^{T_{int}-\lambda} \delta(x).\delta(x)dx = \delta(0) = \infty$$

Therefore, $\sigma_g^2 = \infty$, and the noise-cross-noise term's power overwhelms performance.

3.8.4 2-PAM Performance in the Presence of Band-Limiting

In order to control the power in the noise-cross-noise, we assume that all received signals are processed by a bandpass filter of bandwidth W and center frequency f_c [5]. We also assume that W is large enough such that negligible inter pulse and inter-symbol interference occur. The decision statistic for the j^{th} bit is then:

$$g_j = \int_{jT_f}^{jT_f+T_{int}} r^{'}(t).\hat{v}^{'}(t-jT_f)dt. \tag{3.64}$$

Assuming $b_j = 1$, g_j can be written as:

$$g_j = \sqrt{E_p}U + X_1 + X_2 + X_3 \tag{3.65}$$

where:

$$U = \int_0^{T_{int}} v^{'2}(t)dt \tag{3.66}$$

$$\begin{aligned} X_1 &= \int_{jT_f}^{jT_f+T_{int}} v^{'}(t-jT_f)n^{'}(t)dt & (3.67)\\ X_2 &= \sqrt{E_p}\int_{jT_f}^{jT_f+T_{int}} v^{'}(t-jT_f)n_{tr}^{'}(t)dt & (3.68)\\ X_3 &= \int_{jT_f}^{jT_f+T_{int}} n^{'}(t)n_{tr}^{'}(t)dt & (3.69) \end{aligned}$$

and $r^{'}(t)$,$v^{'}(t)$, $\hat{v}^{'}(t)$, $n^{'}(t)$ and $n_{tr}^{'}(t)$ are the filtered versions of $r(t)$,$v(t)$, $\hat{v}(t)$, $n(t)$ and $n_{tr}(t)$, respectively. Note that the autocorrelation functions of $n^{'}(t)$ and $n_{tr}^{'}(t)$ are now given by [5]:

$$\begin{aligned} R_n^{'}(\tau) &= N_o W sinc(W\tau)cos(2\pi f_c\tau) & (3.70)\\ R_{n_{tr}}^{'}(\tau) &= \frac{N_o}{N_p} W sinc(W\tau)cos(2\pi f_c\tau) & (3.71) \end{aligned}$$

where $sinc(x) = \frac{sin(\pi x)}{\pi x}$.

Calculation of the second moments of X_1, X_2 and X_3 are listed below:

$$E\left(X_1^2\right) = E\left(\int_{jT_f}^{jT_f+T_{int}} \int_{jT_f}^{jT_f+T_{int}} v^{'}(t-jT_f)n^{'}(t)v^{'}(\lambda-jT_f)n^{'}(\lambda)dtd\lambda\right)$$

$$E\left(X_1^2\right) = N_0 W \int_0^{T_{int}} \int_0^{T_{int}} v^{'}(t)v^{'}(\lambda)sinc(W(t-\lambda)).cos(2\pi f_c(t-\lambda))dtd\lambda.$$

$$E\left(X_2^2\right) = E\left(\int_{jT_f}^{jT_f+T_{int}} \int_{jT_f}^{jT_f+T_{int}} v^{'}(t-jT_f)n_{tr}^{'}(t)v^{'}(\lambda-jT_f)n_{tr}^{'}(\lambda)dtd\lambda\right)$$

$$E\left(X_2^2\right) = \frac{N_0 W}{N_p} \int_0^{T_{int}} \int_0^{T_{int}} v^{'}(t)v^{'}(\lambda)sinc(W(t-\lambda)).cos(2\pi f_c(t-\lambda))dtd\lambda.$$

$$E\left(X_3^2\right) = E\left(\int_{jT_f}^{jT_f+T_{int}} \int_{jT_f}^{jT_f+T_{int}} n^{'}(t-jT_f)n_{tr}^{'}(t)n^{'}(\lambda-jT_f)n_{tr}^{'}(\lambda)dtd\lambda\right)$$

$$E\left(X_3^2\right) = \frac{N_0^2W^2}{N_pE_p}\int_0^{T_{int}}\int_0^{T_{int}} sinc^2(W(t-\lambda)).cos^2(2\pi f_c(t-\lambda))dtd\lambda.$$

Then, since g_j is a Gaussian random variable, the probability of error is given by:

$$P_e = Q\left(\sqrt{\frac{E_p}{N_o}.\frac{U^2}{\frac{N_p+1}{N_p}Z_2+\left(\frac{N_pE_p}{N_oZ_1}\right)^{-1}}}\right). \tag{3.72}$$

where

$$Z_1 = W^2\int_0^{T_{int}}\int_0^{T_{int}} sinc^2(W(t-\lambda)).cos^2(2\pi f_c(t-\lambda))dtd\lambda \tag{3.73}$$

$$Z_2 = W\int_0^{T_{int}}\int_0^{T_{int}} v^{'}(t)v^{'}(\lambda)sinc(W(t-\lambda)).cos(2\pi f_c(t-\lambda))dtd\lambda. \tag{3.74}$$

The degradation caused by the noise-cross-noise term is mathematically represented by $\left(\frac{N_pE_p}{N_oZ_1}\right)^{-1}$. Simulation results will show that a large number of pilots is required to hinder its effects.

3.8.5 2-PPM Performance

Similar to the Rake receiver case, derivation of performance for 2-PPM is straightforward, but leads to cumbersome equations and calculations, without significant added insight. Although simulation results will be solely based on 2-PAM, the steps of the 2-PPM analysis are included for completeness.

The decision statistic for the j^{th} bit is given by:

$$g_j = \int_{jT_f}^{jT_f+T_{int}} r^{'}(t).\left[\hat{v}^{'}(t-jT_f-\Delta)-\hat{v}^{'}(t-jT_f)\right]dt \tag{3.75}$$

which can be written as:

$$g_j = \int_0^{T_{int}} r^{'}(t+jT_f).\left[v^{'}(t-\Delta)-v^{'}(t)+n_{tr}^{'}(t-\Delta)-n_{tr}^{'}(t)\right]dt. \tag{3.76}$$

Assuming $b_j = 1$, g_j can be written as:

$$g_j = \sqrt{E_p}U + X_1 + X_2 + X_3 \tag{3.77}$$

where:

$$\begin{aligned}
U &= \int_0^{T_{int}} v^{'2}(t)dt - \int_0^{T_{int}} v^{'}(t-\Delta).v^{'}(t)dt && (3.78)\\
X_1 &= \int_0^{T_{int}} v^{'}(t)\left[n_{tr}^{'}(t-\Delta) - n_{tr}^{'}(t)\right]dt && (3.79)\\
X_2 &= \int_0^{T_{int}} n^{'}(t).\left[v^{'}(t-\Delta) - v^{'}(t)\right]dt && (3.80)\\
X_3 &= \int_0^{T_{int}} n^{'}(t).\left[n_{tr}^{'}(t-\Delta) - n_{tr}^{'}(t)\right]dt. && (3.81)
\end{aligned}$$

Moments calculation are listed below:

$$\begin{aligned}
E\left(X_1^2\right) &= E\left(\int_0^{T_{int}}\int_0^{T_{int}} v^{'}(t)v^{'}(\lambda)\left[n_{tr}^{'}(t-\Delta) - n_{tr}^{'}(t)\right]\left[n_{tr}^{'}(\lambda-\Delta) - n_{tr}^{'}(\lambda)\right]dtd\lambda\right)\\
E\left(X_1^2\right) &= \frac{N_0W}{N_p}\int_0^{T_{int}}\int_0^{T_{int}} v^{'}(t)v^{'}(\lambda)[2sinc(W(t-\lambda)).cos(2\pi f_c(t-\lambda)) -\\
&\quad sinc(W(t-\lambda-\Delta)).cos(2\pi f_c(t-\lambda-\Delta)) - sinc(W(t-\lambda+\Delta)).cos(2\pi f_c(t-\lambda+\Delta))]dtd\lambda
\end{aligned}$$

$$\begin{aligned}
E\left(X_2^2\right) &= E\left(\int_0^{T_{int}}\int_0^{T_{int}} n^{'}(t)n^{'}(\lambda)\left[v^{'}(t-\Delta) - v^{'}(t)\right]\left[v^{'}(\lambda-\Delta) - v^{'}(\lambda)\right]dtd\lambda\right)\\
E\left(X_2^2\right) &= N_0W\int_0^{T_{int}}\int_0^{T_{int}}\left[v^{'}(t-\Delta) - v^{'}(t)\right]\left[v^{'}(\lambda-\Delta) - v^{'}(\lambda)\right].sinc(W(t-\lambda)).cos(2\pi f_c(t-\lambda))dtd\lambda
\end{aligned}$$

$$\begin{aligned}
E\left(X_3^2\right) &= E\left(\int_0^{T_{int}}\int_0^{T_{int}} n^{'}(t)n^{'}(\lambda)\left[n_{tr}^{'}(t-\Delta) - n_{tr}^{'}(t)\right]\left[n_{tr}^{'}(\lambda-\Delta) - n_{tr}^{'}(\lambda)\right]dtd\lambda\right)\\
E\left(X_3^2\right) &= \frac{N_0^2W^2}{N_pE_p}\int_0^{T_{int}}\int_0^{T_{int}} sinc(W(t-\lambda)).cos(2\pi f_c(t-\lambda))[2sinc(W(t-\lambda)).cos(2\pi f_c(t-\lambda)) - sinc(W(t-\lambda-\Delta))\\
&\quad .cos(2\pi f_c(t-\lambda-\Delta)) - sinc(W(t-\lambda+\Delta)).cos(2\pi f_c(t-\lambda+\Delta))]dtd\lambda.
\end{aligned}$$

Although the terms are correlated because of the use of two delayed versions of the same noisy template, it can be shown that g_j may be approximated by a Gaussian random variable [35]. Then, by symmetry, the

error probability is given by:

$$P_e = Q\left(\sqrt{\frac{E_p U^2}{E\left(X_1^2\right)+E\left(X_2^2\right)+E\left(X_3^2\right)}}\right). \tag{3.82}$$

3.8.6 Simulation Results

The performance of pilot-assisted receivers using 2-PAM is analyzed through simulation in this section. For all cases, the front-end bandpass filter parameters are set to $W = 7$ GHz and $f_c = 3.5$ GHz. A Gaussian transmit pulse (T_w=500 psec) is employed.

Figure 3.19 compares the simulated and theoretical (Equation (3.72)) error probability performances for a specific Bicone NLOS channel profile, for $N_p = 10$, 50 and 100, respectively, and an integration time T_{int} equal to T_f. First, note that the error between analysis and simulation is negligible. Moreover, diminishing gains are observed as the number of pilot increases: a gain of about 3 dB when passing from 10 to 50 pilots, and a gain of about 1 dB when passing from 50 to 100 pilots. Performance for $N_p = 100$ is about 2 dB worse than the BPSK lower bound in AWGN. Figure 3.20 illustrates performance averaged over 30 different

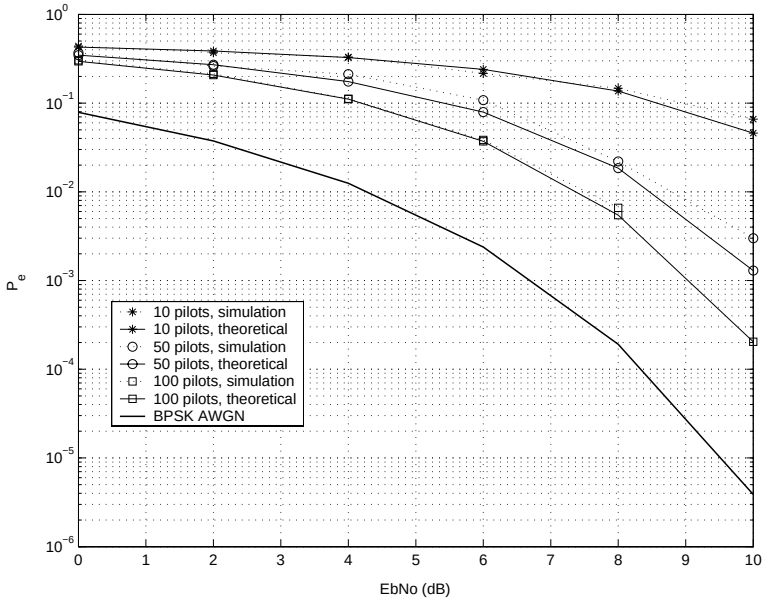

Figure 3.19: Pilot-assisted receiver performance for an arbitrary NLOS channel profile. 2-PAM. $N_p = \{10, 50, 100\}$.

NLOS channel profiles for varying N_p between 10 and 1000. Notice that a load of 1000 pilots is about 0.5 dB

worse than the lower bound. Figure 3.21 studies performance versus the integration time T_{int} (taken as a fraction of the symbol time T_f), for $N_p = 100$ and $\frac{E_p}{N_0}$=5 dB. Notice that the error probability decreases with increasing T_{int}, up to an optimal time (about $0.5T_f$), after which performance deteriorates. In fact, short integration times waste a significant fraction of the symbol energy, whereas long integration times introduce more noise to the system while only capturing the energy in low amplitude paths. Moreover, note that short integration times are more harmful than long integration times.

Figures 3.22, 3.23 and 3.24 plot the bit error probability versus N_p and $T_{int} = 0.5T_f$, for $\frac{E_b}{N_0} = 0$ dB, 5 dB,

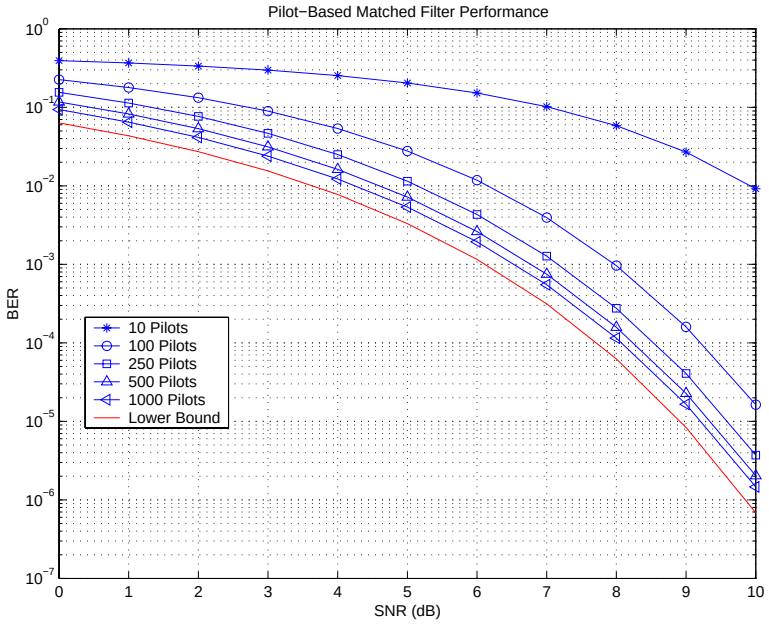

Figure 3.20: Pilot-assisted receiver performance for different N_p. 2-PAM. T_{int}=50 nsec.

and 10 dB, respectively. Note that performance converges to the lower bound faster for higher $\frac{E_b}{N_0}$, because of the use of a cleaner template. Performance is especially unacceptable for low $\frac{E_b}{N_0}$ and low training.

Figure 3.25 compares the performance of the pilot-assisted receiver to a 20-finger Rake receiver using MRC. The number of training symbols used to set the Rake fingers is varied. Note that the Rake probability of error reaches a floor for 100 pilot-training, at which performance is about 3 dB away from AWGN reception, whereas the pilot-assisted receiver performance keeps improving with more training symbols. The Rake receiver is inherently limited by its low energy capture, whereas the pilot-assisted receiver can only achieve good performance by using a heavy training load.

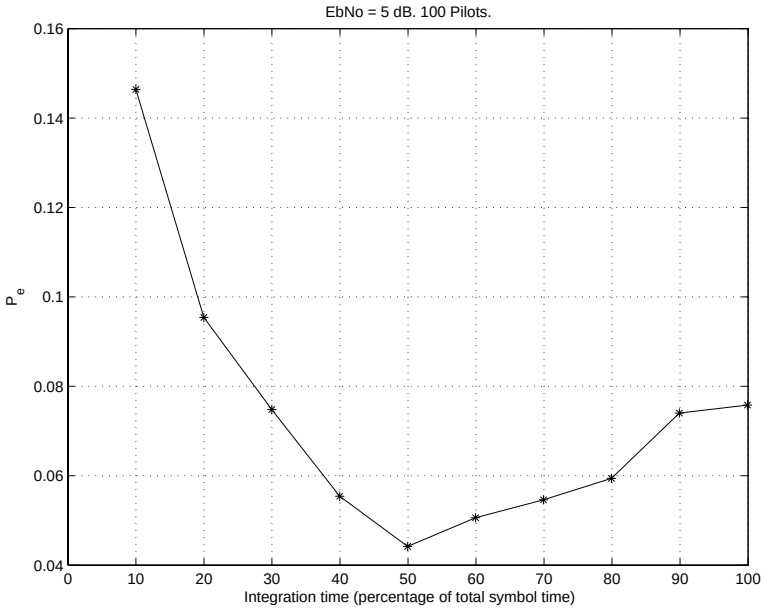

Figure 3.21: Pilot-assisted receiver performance for different T_{int}. 2-PAM. $N_p = 100$.

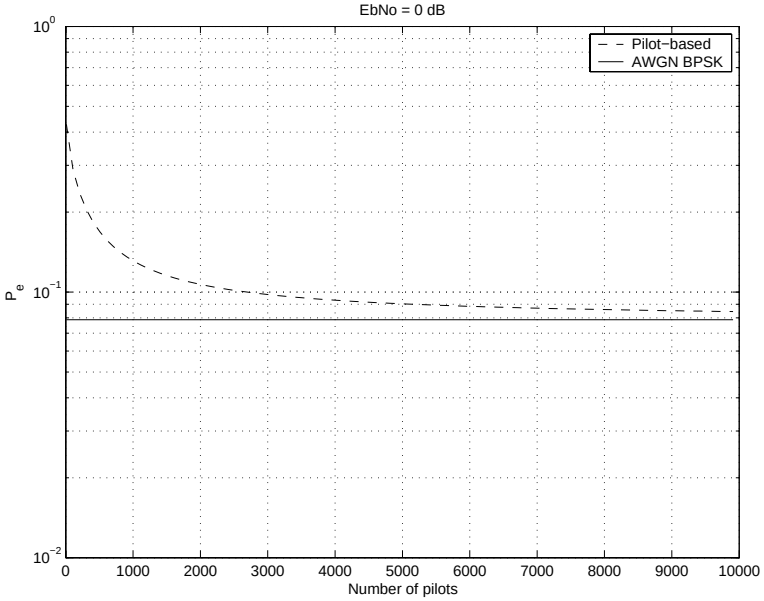

Figure 3.22: Pilot-assisted receiver performance versus number of pilots. $\frac{E_p}{N_0} = 0\ dB$.

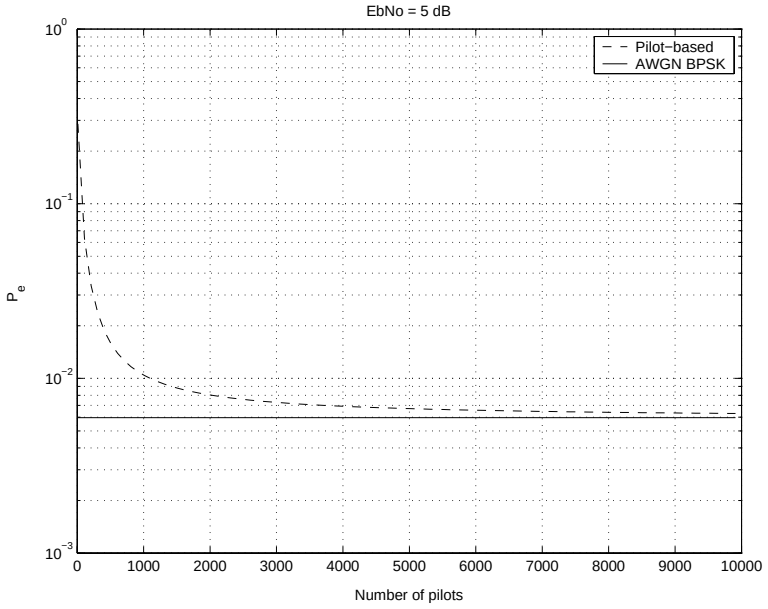

Figure 3.23: Pilot-assisted receiver performance versus number of pilots. $\frac{E_p}{N_0} = 5\ dB$.

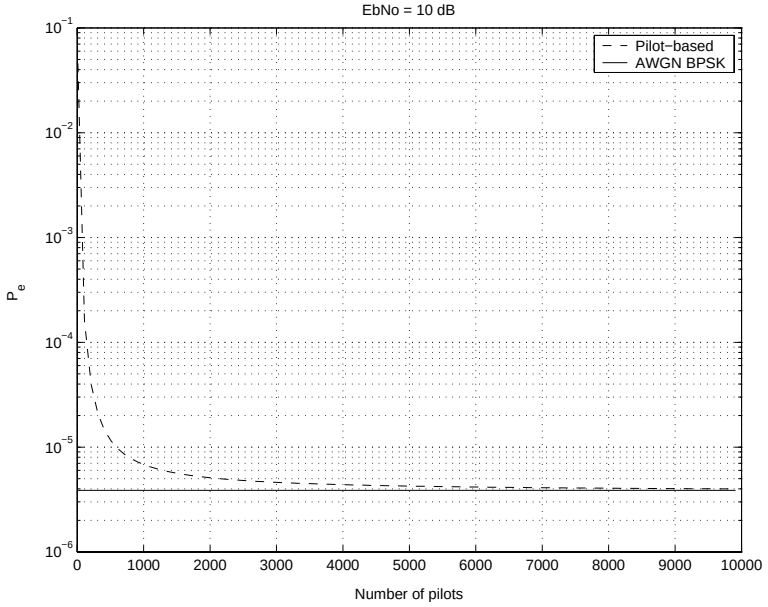

Figure 3.24: Pilot-assisted receiver performance versus number of pilots. $\frac{E_p}{N_0} = 10\ dB$.

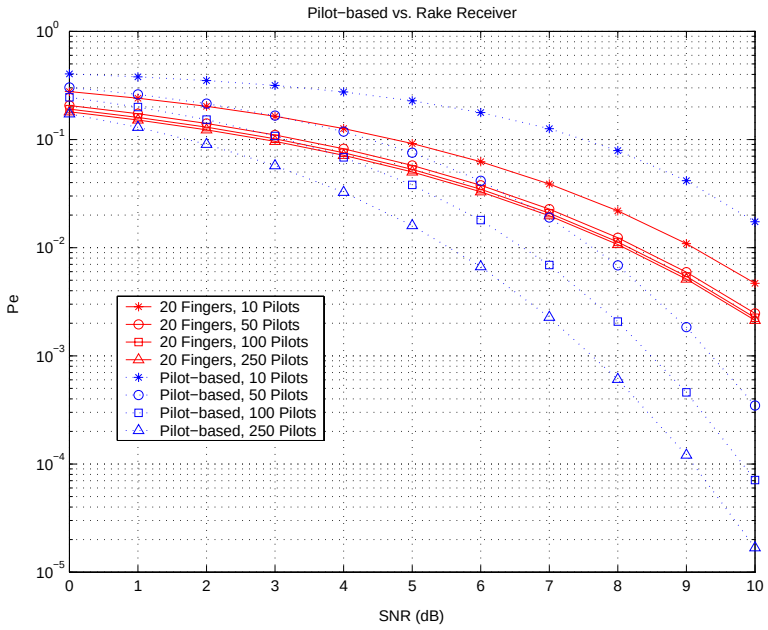

Figure 3.25: Comparing Rake and pilot-assisted receivers for different number of pilots.

3.9 Conclusions

This chapter presents a discussion of traditional signal detection for UWB in dense multipath. The fundamental weaknesses of TR and Rake receivers are mathematically formulated, and illustrated through analysis. TR receivers suffer from the detrimental noise-cross-noise term, which requires an unacceptable training load to limit its effects. Rake receivers are inherently impeded by the limited energy capture for a moderate number of fingers.

Due to the inadequacy of traditional signal detection algorithms applied to UWB in dense multipath, new and improved algorithms which circumvent those limitations are required. Two such modified systems are discussed in the next chapter.

Chapter 4

UWB Signal Detection in Dense Multipath: New and Proposed Approaches

4.1 Introduction

The limitations of Rake and pilot-assisted receivers were discussed in chapter 3. In this chapter, new receiver structures which overcome these limitations are analyzed. Specifically, two new receivers are proposed:

First, an **iterative data-aided TR receiver** with low parity density check (LDPC) coding [49] is introduced, where the training overhead traditionally required by TR systems is reduced by iteratively extracting channel information from both the training and data signals. Convergence of the iterative algorithm is ensured by using a strong forward error correction code (FEC). Error correction coding is especially attractive for systems employing low-duty cycle pulses, since coding can be added while maintaining the data rate by reducing the symbol repetition time. This receiver exploits the synergy between error correction coding, improved channel estimation and large available UWB bandwidth to yield large performance gains with reduced training overhead.

Second, **a receiver based on sequence optimization** [50][51][52] is proposed, where the transmit waveform and receiver template are designed to force the channel multipath components to add up coherently at the output of the receiver. The transmit waveform is made up of a train of delayed and scaled pulses, the amplitudes of which can be represented by a real-valued sequence. The receiver template is modeled by another real-valued sequence. The transmitter and receiver sequences are chosen such that the correlation of the received signal (the sequence convolved with the multipath channel) with the receive template is maximized. Contrary to a traditional Rake receiver, where performance is limited by the low energy capture from a limited number of paths, the proposed technique results in constructive inter-path interference at the receiver output. A transmit beamforming effect is achieved, resulting in very high energy capture with the use of a relatively simple receiver.

4.2 List of Contributions and Publications

The main contributions of this chapter are:

- An accurate characterization of existing/traditional signal detection approaches for UWB systems in dense multipath channels.
- A proposed iterative data-aided pilot-assisted receiver with LDPC, which reduces the training overhead required by traditional TR receivers, and yet achieves high performance gains.
- A proposed sequence optimization receiver, which exploits the dense multipath structure and achieves very high energy capture by forcing coherent combining of the multipath components in the channel and at the output of the receiver. Performance is studied for single-user, multi-user and NBI scenarios.

Other contributions include:

- An analysis of the probability of error of Rake receivers in dense multipath taking channel estimation error (which is usually ignored in the literature) into account.
- An analysis of the probability of error for generalized TR receivers (with an arbitrary number of pilot symbols) for both binary PAM and PPM modulation.

- A comparison of implementation complexity for key UWB receivers, with emphasis on the required number of operations for channel estimation and signal detection. Specifically, we show that the proposed receiver structures provide a better tradeoff between performance and complexity.

A list of relevant publications is included for reference:

- Co-author, *An Introduction to Ultra Wideband Communication Systems,* Chapter 6, Receiver Design Principles, edited by Jeffrey H. Reed, Prentice Hall, 2005.
- J. Ibrahim, R. Menon, and R.M. Buehrer, "UWB Signal Detection Based on Sequence Optimization," *IEEE Communications Letters,* vol.10, issue 4, pp. 228-230, April 2006.
- R. Menon, J. Ibrahim, and R.M. Buehrer, "UWB Signal Detection Based on Sequence Optimization," in *Proc. 2005 WirelessComm,* vol.2, pp. 1231-1236, June 2005.
- J. Ibrahim and R.M. Buehrer, "A Data-Aided Iterative UWB Receiver with LDPC," in *Proc. 2005 VTC Fall,* vol. 1, pp. 33-37, June 2005.
- J. Ibrahim, R. Menon, and R.M. Buehrer, "UWB Sequence Optimization for Enhanced Energy Capture and Interference Mitigation," in *Proc. 2005 MILCOM,* vol.4, pp. 2086-2092, October 2005

4.3 Chapter Organization

The proposed iterative data-aided pilot-assisted receiver is introduced in section 4.4. The improvement brought by data-aided channel estimation is explained. The role of FEC is also discussed. Simulation results show that the proposed model outperforms Rake and TR receivers, while reducing the required overhead. The proposed sequence optimization receiver is discussed in section 4.5. The design mechanism for the transmit and receive sequences is derived. The application of this method to a multi-user application as well as a NBI mitigation scenario is also provided. Comparison with time-reversal, a popular method which also incorporates the channel's rich structure into the transmit pulse, is included as well. Simulation results show that the proposed scheme yields significant improvement over traditional receiver structures with substantially less complexity. It is also shown that this method may be further simplified (by reducing

the feedback overhead), while still yielding good performance. A comparison between the design complexity of the above studied receivers is then provided in section 4.6, and the tradeoff between system resources and probability of error performance is also discussed. The chapter is concluded in section 4.7.

4.4 Proposed UWB Receiver: Iterative Data-aided Pilot-Assisted Receiver with FEC

4.4.1 Introduction

Although its energy capture is significantly higher than that of a Rake receiver, the large number of pilots required for the pilot-assisted detector makes it unattractive from a practical standpoint. Specific methods must be devised to reduce its training overhead. A potential solution is developed by noting that the modulated received signals contain information about the channel and can be used to construct an improved estimate for the received pulse shape. A data-aided UWB pilot-assisted system is studied in [45], where the template is estimated using all modulated (data) and unmodulated (pilot) symbols. The optimal strategy to form the template is derived based on a generalized likelihood ratio test. This test is computationally complex, which makes its implementation problematic. Moreover, in order for the algorithm to converge to a satisfactory performance point, a good starting point for the iterative process is required (that is, a clean initial template), which is not guaranteed. At low SNR, a heavy training load would then still be required. We propose a modified, simplified model here, where a good starting point is provided through the use of FEC, while maintaining a relatively small training overhead.

4.4.2 Iterative Data-Aided Template Estimation

We aim for a receiver where the entire received energy is captured, while maintaining a "clean" template for a limited number of pilots. Since both pilot and data signals contain information about the channel, the training overhead can be reduced by incorporating both into an iterative template construction algorithm. The receiver works as follows. First, an initial template is generated using a training frame of N_p pilots

signals, based on the model in Equation (3.33):

$$\hat{v}_0(t) = \frac{1}{\sqrt{E_p}N_p} \sum_{k=0}^{N_p-1} r_{tr}\left(t + kT_f\right),\ 0 \le t \le T_f. \tag{4.1}$$

Then, the data bits are iteratively estimated and used to construct an improved estimate. Assume a data frame consisting of N_d data symbols, and let $r_d(t)$ be the data signal, written as:

$$r_d(t) = \sqrt{E_p} \sum_{m=0}^{N_d-1} b_m v(t - mT_f) + n(t).$$

Note $\hat{b}_{i,n}$ as the estimated i^{th} bit at the n^{th} iteration. $\hat{b}_{i,n}$ may be written as:

$$\hat{b}_{i,n} = sign\left[\int_{iT_f}^{iT_f+T_{int}} r_d(t)\hat{v}_{n-1}(t - iT_f)dt\right]$$

where $\hat{v}_{n-1}(t)$ is the $(n-1)$-th template. The template at the n^{th} iteration is then defined as:

$$\hat{v}_n(t) = \frac{1}{\sqrt{E_p}N_d} \sum_{k=0}^{N_d-1} \hat{b}_{k,n} r_d\left(t + kT_f\right),\ 0 \le t \le T_f.$$

Notice that each incorrectly decoded bit will "cancel out" a correctly decoded bit. Then, if N_d is large enough, $\hat{v}_n(t)$ may be approximated as:

$$\hat{v}_n(t) \approx \left(1 - 2p_{n-1}\right) v(t) + n_d(t)$$

where p_{n-1} is the probability of bit error for the $(n-1)$-th stage, and $n_d(t)$ has PSD $\frac{N_0}{2N_dE_p}$.

4.4.3 System Performance

Assuming $b_j = 1$, the decision statistic for the j^{th} bit at the $n-th$ iteration can be written as:

$$g_{j,n} = \int_{jT_f}^{jT_f+T_{int}} [\sqrt{E_p}v^{'}(t) + n^{'}(t)][(1 - 2p_{n-1})v^{'}(t + jT_f) + n_d^{'}(t + jT_f))]dt, \tag{4.2}$$

where $v^{'}(t)$, $n^{'}(t)$ and $n_d^{'}(t)$ are the filtered versions of $v(t)$, $n(t)$ and $n_d(t)$, respectively.

$g_{j,n}$ can be broken down into four components:

$$\begin{aligned} g_{j,n} &= (1-2p_{n-1})\sqrt{E_p}\int_0^{T_{int}} v^{'2}(t)dt \\ &+ \sqrt{E_p}\int_0^{T_{int}} v^{'}(t)n_d^{'}(t)dt \\ &+ (1-2p_{n-1})\int_0^{T_{int}} v^{'}(t)n^{'}(t+jT_f)dt \\ &+ \int_0^{T_{int}} n^{'}(t+jT_f)n_d^{'}(t)dt \\ &= \mu_{g_n} + z_1 + z_2 + z_3. \end{aligned} \tag{4.3}$$

The variance of the three zero-mean terms z_1, z_2 and z_3 is calculated as follows:

$$\begin{aligned} E\left[z_1^2\right] &= W\frac{N_o}{N_d}\int_0^{T_{int}}\int_0^{T_{int}} v^{'}(t)v^{'}(\lambda)sinc(W(t-\lambda))cos(2\pi f_c(t-\lambda))dtd\lambda \\ E\left[z_2^2\right] &= (1-2p_{n-1})^2WN_o\int_0^{T_{int}}\int_0^{T_{int}} v^{'}(t)v^{'}(\lambda)sinc(W(t-\lambda))cos(2\pi f_c(t-\lambda))dtd\lambda \\ E\left[z_3^2\right] &= W^2\frac{N_o^2}{E_pN_d}\int_0^{T_{int}}\int_0^{T_{int}} sinc^2(W(t-\lambda))cos^2(2\pi f_c(t-\lambda))dtd\lambda. \end{aligned}$$

The total noise variance is then:

$$\sigma_z^2 = E\left[z_1^2\right] + E\left[z_2^2\right] + E\left[z_3^2\right]. \tag{4.4}$$

We write:

$$\sigma_z^2 = \frac{N_o^2}{E_pN_d}Z_1 + N_oZ_2\left[\frac{1}{N_d} + (1-2p_{n-1})^2\right]. \tag{4.5}$$

where Z_1 and Z_2 are given by Equations (3.73) and (3.74), respectively. The probability of error is then given by:

$$p_n = Q\left(\frac{(1-2p_{n-1})\sqrt{E_p}U}{\sqrt{\frac{N_o^2}{E_pN_d}Z_1 + N_oZ_2\left[\frac{1}{N_d} + (1-2p_{n-1})^2\right]}}\right)$$

where U is given by 3.66. Moreover:

$$p_n = Q\left(\frac{\sqrt{(1-2p_{n-1})^2 E_p U^2}}{\sqrt{\frac{N_o^2}{E_p N_d} Z_1 + N_o Z_2 \left[\frac{1}{N_d} + (1-2p_{n-1})^2\right]}}\right)$$

$$p_n = Q\left(\sqrt{\frac{E_p}{N_0}} \frac{\sqrt{(1-2p_{n-1})^2 U^2}}{\sqrt{\frac{N_o}{E_p N_d} Z_1 + Z_2 \left[\frac{1}{N_d} + (1-2p_{n-1})^2\right]}}\right).$$

Let $w_n = 1 - 2p_{n-1}$. Then:

$$p_n = Q\left(\sqrt{w_n^2 \frac{E_p}{N_0} . \frac{U^2}{(w_n^2 + \frac{1}{N_d}) Z_2 + \left(\frac{N_d E_p}{N_o Z_1}\right)^{-1}}}\right), \tag{4.6}$$

The expression for the "starting-point" probability of error p_1 is similar to the expression obtained for traditional pilot-assisted receivers:

$$p_1 = Q\left(\sqrt{\frac{E_p}{N_o} . \frac{U^2}{\frac{N_p+1}{N_p} Z_2 + \left(\frac{N_p E_p}{N_o Z_1}\right)^{-1}}}\right). \tag{4.7}$$

Assume there are N iterations. Then, N template estimates are generated before the final bit decision is made. In other words, the effective system probability of error is p_N. Subject to a good starting point, each iteration results in an improved template. This leads to more bits being detected correctly, which in turn produces a cleaner template. Note that, if $N = 1$, the system degenerates into the pilot-assisted receiver studied in the previous section.

4.4.4 Error Correction Coding

For the proposed scheme to operate efficiently, a good starting point is required. The quality of the initial template $\hat{v}_0(t)$ is limited by the low instantaneous signal energy due to the dispersive channel. This can be solved by adding a strong error correcting code that guarantees good coding gains at low SNR. Note that error correction coding has already been suggested for UWB in the literature. For example, application of convolutional codes to 2-PPM and M-ary PPM is investigated in [83] and [84], respectively. FEC is shown

to be an attractive option for UWB, since it does not require additional reduction in the data rate, because of UWBs very large spreading gain. However, this characteristic is not exclusively specific to UWB, and is indeed also valid for traditional SS systems. In this work, we use LDPC codes, which are linear block codes based on a large, sparse parity check matrices. LDPC decoding is based on the iterative belief propagation algorithm. LDPC codes have generated much interest lately, and have been shown to potentially outperform turbo codes [63]. The proposed receiver uses an iterative decoding approach which takes advantage of the systematic bits in the decoded message to re-estimate the template. Figure 4.1 illustrates the proposed system. The incoming data signals are demodulated and decoded, and then the hard bit estimates are used to construct a new template, as formulated in the equations above. If a systematic code is used, there is no need for an encoder at the receiver, since the position of the signals corresponding to the data bits is known. However, note that the hard estimates corresponding to the redundant bits introduced by coding are not used in the template estimation in that case. The potential efficiency of the proposed system lies in the following synergy: in order to yield significant coding gain, the decoding scheme requires an adequate energy capture level, which is provided by the improved template. Moreover, the coding gains lead to more bits being decoded correctly, thus forming a cleaner template.

It is important to note that the choice of LDPC codes is rather arbitrary. In fact, it is possible to use any other systematic code, provided it yields sufficient coding gains and is useful at low SNR.

The effect of error correction coding on system performance is further illustrated with an example. Suppose

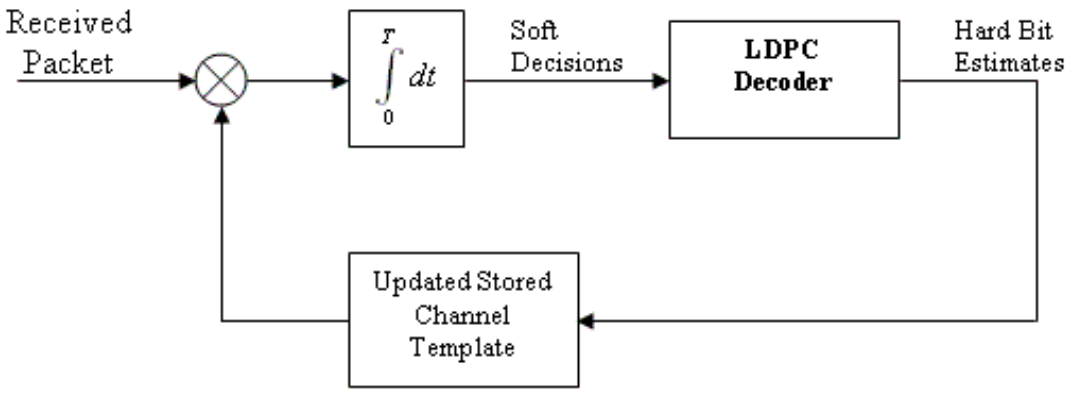

Figure 4.1: Data-aided, pilot-assisted LDPC receiver model.

a rate $\frac{1}{2}$ constraint length-4 convolutional code is used (Figure 4.2). The weight enumerator of this code can be shown to be (see [64]):

$$T(X,Y) = \frac{X^6Y^3 - X^{10}Y^3 + X^6Y}{1 - 2X^2Y^3 - 3X^2Y + 2X^6Y^3}. \tag{4.8}$$

Assuming hard decision decoding, the bit error rate for this code over a binary symmetric channel with

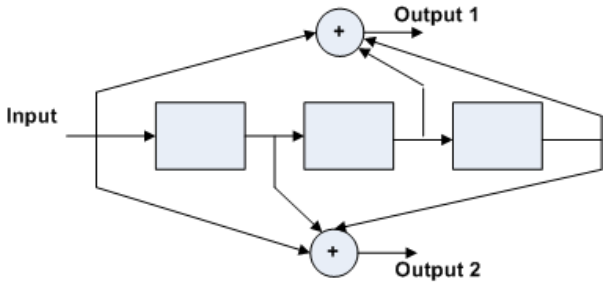

Figure 4.2: Rate 1/2, constraint-length-4 convolutional encoder.

crossover probability p may be upper-bounded as follows:

$$P_b < \left.\frac{\partial T(X,Y)}{\partial Y}\right|_{X=2\sqrt{p(1-p)},Y=1}. \tag{4.9}$$

A lower bound for the code is given by:

$$P_b \geq 10p^3(1-p)^3 + 15p^4(1-p)^2 + 6p^5(1-p) + p^6. \tag{4.10}$$

An estimate of performance which falls between both bounds is [64]:

$$P_b \approx 256\left(p(1-p)\right)^3. \tag{4.11}$$

Consider the uncoded "starting-point" system probability of bit error p_1 in (4.7). The equivalent coded bit probability $p_{1,c}$ at the output of the convolutional decoder may approximated by:

$$p_{1,c} \approx 256\left(p_1(1-p_1)\right)^3. \tag{4.12}$$

Based on (4.6), the probability of error for the second iteration at the input of the error-correction decoder is then:

$$p_2 \approx Q\left(\sqrt{w_{2,c}^2 \frac{E_p}{N_0} . \frac{U^2}{(w_{2,c}^2 + \frac{1}{N_d}) Z_2 + \left(\frac{N_d E_p}{N_o Z_1}\right)^{-1}}}\right) \tag{4.13}$$

where $w_{2,c} = 1 - 2p_{1,c}$. When coding gains are observed, $p_{1,c} < p_1$, and consequently the noise in the template used to estimate bits in the second iteration is further mitigated, leading to lower probability of bit error. The probability of error at the output of the decoder is then $p_{2,c} \approx 256 \left(p_2 \left(1 - p_2\right)\right)^3$. After n iterations, the output probability of error is given by $p_{n,c}$.

The gains brought by FEC (in other words, the difference between uncoded p_n given by (4.6) and $p_{n,c}$) will be shortly illustrated through simulation.

4.4.5 Simulation Results

The gains brought by the iterative approach are illustrated in Figure 4.3. A NLOS channel profile is used. The initial template is based on 30 pilot symbols. The data frame holds 1000 data symbols. The integration time is equal to the symbol duration T_f. Three iterations are performed, and the probability of error is evaluated after each iteration. First, note that the theoretical curves (based on (4.6)) match the simulated results. Also, note that performance based on the template obtained after one extra iteration yields more than 4 dB gain compared to the performance based on the initial template. The gains seen after two iterations are less substantial. Thus, a single iteration seems sufficient to limit the number of required pilots.

The performance of uncoded and coded data-aided pilot-assisted receiver are compared to the traditional pilot-assisted receiver in Figure 4.4. The coded system employs a rate 1/2 systematic LDPC code. There are 541 data bits per frame, and it is assumed that the initial template is constructed using a preamble of 50 pilots. There are 5 iterations per frame, that is, for each set of 541 bits, the template is iteratively estimated 5 times, before a final bit decision is made. First, notice that incorporating the data signals into the template estimation, even in the absence of coding, yields significant gains. Second, at SNR values less than 2.5 dB, the coding gain is not large enough to compensate for the energy lost due to redundancy, and the uncoded scheme outperforms the coded scheme. However, as the SNR increases, the coded system becomes largely superior to the uncoded system. Note that the probability of error is 10^{-4} at an SNR of 5

dB, which represents a gain of about 3.5 dB over optimal uncoded detection (matched filter) in AWGN. The effect of FEC is displayed in Figure 4.5. A rate $\frac{1}{2}$, constraint-length 4 convolutional code is assumed, and the approximation from (4.11) is used. Notice that (4.11) is an extremely loose bound at low SNR, and does not give insight into true system behavior. However, note that the improvement brought by coding is apparent for higher values of SNR, both for one and three iterations. For three iterations, a probability of bit error of 10^{-8} is achieved for an SNR of 8 dB. It is important to stress here that the observed improvement is not solely due to error correction coding, but rather to the simultaneous use of coding and the data-aided estimation method. In fact, note that performance of the coded system after one iteration is equivalent to the expected performance of a conventional TR system (which does not use the data-aided iterative method) employing error correction coding. Performance is very poor in that case because the template is too dirty to yield any coding gains. The combination of FEC and data-aided estimation guarantees a clean template and substantial coding gains for a small number of iterations.

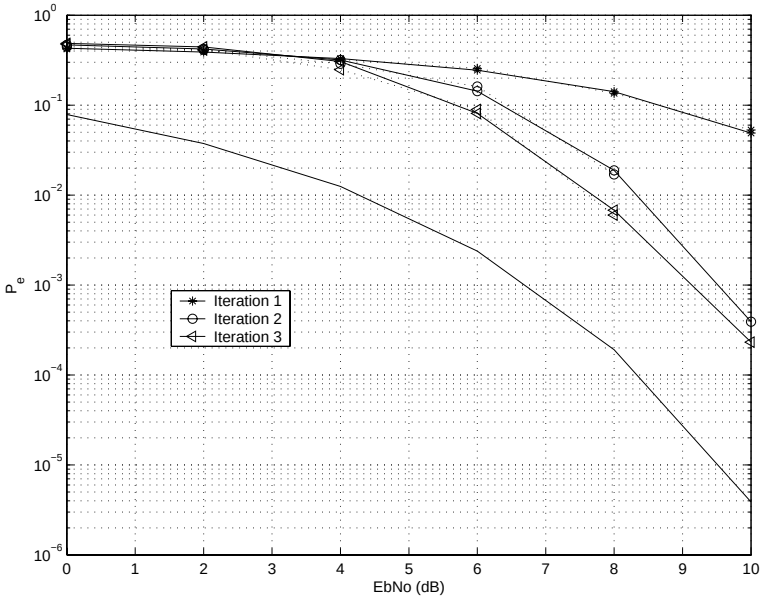

Figure 4.3: Data-aided iterative receiver. $N_p = 10$, $N_d = 100$, $T_{int} = T_f$.

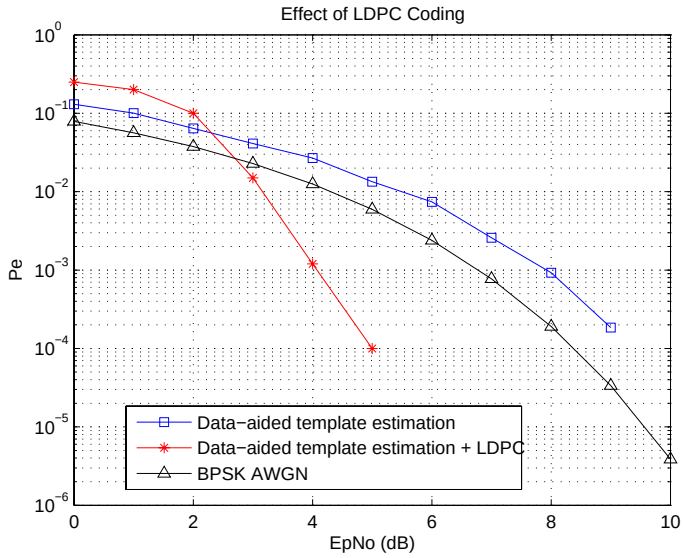

Figure 4.4: Performance of proposed data-aided model with LDPC. Curves averaged for multiple NLOS channel profiles.

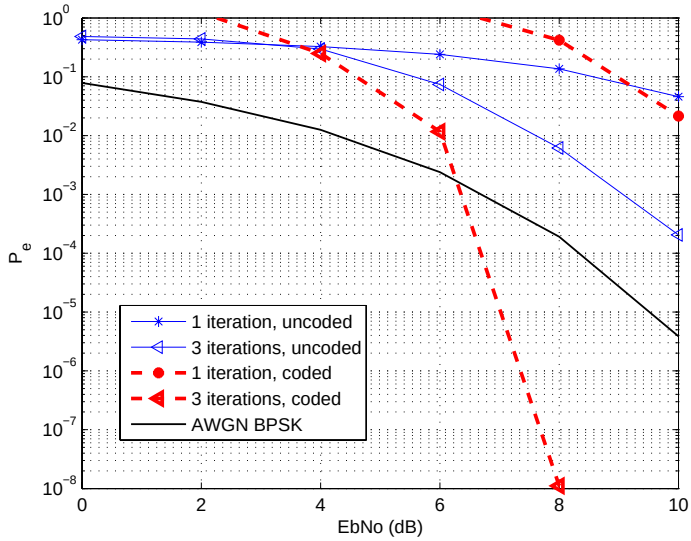

Figure 4.5: Coded versus uncoded system. One and three iterations. Curves averaged for multiple NLOS channel profiles.

4.5 Proposed UWB Receiver: The Sequence Optimization Receiver

4.5.1 Introduction

As was demonstrated in section 3.7, the Rake receiver suffers from a low energy capture for a moderate number of fingers, making its implementation impractical for UWB systems. An alternative strategy that is conceptually similar to Rake receivers, but offers significant complexity reduction, is pre-Rake diversity combining, first studied for SS systems [66, 67, 68, 69, 70, 71], which achieves performance equivalent to Rake diversity combining without increasing the receiver complexity. In this method, Rake combining is performed before transmission, by delaying and scaling the transmitted signals accordingly to the delay and amplitude of the channel multipath components. This assumes channel knowledge is available at the transmitter. An alternative approach is to precode the transmit signal using a time inverse of the channel impulse response [72]. This technique, called time-reversal, has the potential to perform like the perfect Rake receiver (a Rake receiver with an infinite number of fingers) if perfect channel knowledge at the transmitter is available. A different approach is suggested in [73], where a spreading sequence is transmitted, and signal detection at the correlator-receiver is based on a fixed spreading sequence. The transmitted spreading sequence is optimized in order to maximize the energy output after correlation. A multipath beamforming effect is achieved, where the energy from several multipath components is coherently added at the receiver. However, the energy capture in this method is limited by the use of a fixed sequence at the receiver. In [74] and [75], the receiver and transmitter sequences are jointly optimized to maximize the output SNR in a SS system. However, it does not apply directly to UWB, since it assumes a small number of paths, as well as perfect channel estimation.

In this section, we propose an extension of the above sequence optimization technique for UWB systems, which takes the effect of channel estimation into account. This work has been published in [50], [51] and [52]. In [50], sequence optimization for the single user scenario is analyzed. The proposed technique results in coherent combining of a substantial number of the multipath components at the receiver, resulting in very high energy capture with the use of a simple receiver. The transmit waveform is made up of a train of delayed

and scaled pulses, the amplitudes of which can be represented by a real-valued sequence. The transmitter and receiver sequences are chosen such that the correlation of the received signal (the sequence convolved with the multipath channel) with the receive template is maximized. The work in [50] is generalized in [51] to a multi-user scenario, where the SINR for a particular user is maximized. Additionally, the applicability of this method to signal detection in the presence of a high power NBI is analyzed.

The rest of this section is organized as follows. First, since the proposed method is derived from classical transmit-pulse shaping techniques, previous work on time-reversal and pre-Rake combining is presented. The general single user system model for the proposed system is then formulated. The transmitted signal-sequence and the decision statistic after correlation are mathematically defined. The sequence optimization scheme and the effect of channel estimation are described. A qualitative comparison between sequence optimization and time-reversal is then included. Sequence optimization is then generalized to the multi-user scenario. Application of the proposed scheme to NBI mitigation is also provided. Then, simulation results, based on real measured indoor NLOS channel profiles, are presented. It is shown that the proposed method leads to significant improvement in terms of effective energy capture and interference mitigation over traditional receiver structures, with less complexity. Also, it is shown that quantizing the real-valued sequence to reduce system complexity only leads to a slight degradation in performance even for a small number of quantization bits.

4.5.2 Previous Work in Transmit-Pulse Shaping: Time-Reversal and Pre-Rake Combining

Time-reversal is one of the most popular transmit-pulse shaping methods, and provides a valuable benchmark against which the proposed sequence optimization receiver can be compared. Time-reversal was first applied in the field of under-water acoustics and has recently attracted research interest in wireless communication, particularly for UWB signal detection (see [72] and the references therein). Time-reversal solves the problem of limited energy capture of UWB Rake receivers by pre-filtering the transmit pulse shape with the reversed channel impulse response. Focusing of temporal energy ensues, and high energy capture can be obtained with only a small number of taps. Note that feedback capability is required if channel estimation is performed

at the receiver. Alternatively, in a time-duplexed system, channel estimation may be performed at the transmitter, and the design complexity is then transferred from the receiver to the transmitter. Examples of UWB receivers employing the time-reversal approach may be found in [53] and [54].

In order to fully appreciate the potential of time-reversal, the effect of channel estimation errors are first neglected, and an idealized time-reversal receiver (where perfect channel knowledge is assumed) is discussed. The effect of channel estimation on more realistic time-reversal structures is then presented.

The main assumption for idealized time-reversal is that the transmitter has infinite channel estimation resolution. That is, a perfect copy of the channel impulse response is available at the transmitter. This requires that the amplitudes and delays of all the multipath components are known, even if paths occur within a fraction of a transmit pulse width. Moreover, ideal time-reversal assumes that the transmitter is capable of applying an exact copy of the impulse response as a filter to the transmitted pulse shape. Any realistic channel estimation algorithm would have to operate at a finite resolution and would not be capable of estimating all paths metrics regardless of their respective delays. Nonetheless, this ideal assumption allows us to assess the full potential of the algorithm.

Assuming the same channel model used in previous sections of this chapter, the time-reversed channel impulse response may be written as:

$$h(-\tau) = \sum_{l=0}^{L-1} \alpha_l \delta\left(\tau_{L-1} - \tau_l\right). \tag{4.14}$$

The transmit pulse $w(t)$ is pre-filtered using $h(-\tau)$. Assuming a data bit equal to one, the transmitted pulse of the time-reversal scheme is given by:

$$s(t) = \sqrt{\frac{E_p}{R_0}} \sum_{l=0}^{L-1} \alpha_l w\left(t - \tau_{L-1} + \tau_l\right). \tag{4.15}$$

where R_0 is a normalizing constant applied to ensure the transmit energy is equal to unity:

$$R_0 = \sum_{l=0}^{L-1} \alpha_l^2 + \sqrt{E_p} \sum_{l1=0}^{L-1} \sum_{l2 \neq l1}^{L-1} \alpha_{l1} \alpha_{l2} R\left(\tau_{l2} - \tau_{l1}\right). \tag{4.16}$$

Consider the filter $h(-\tau)$. When $s(t)$ is transmitted, $h(-\tau)$ is effectively convolved with $h(\tau)$. A correlation effect is thus obtained. The output of the convolution $h(\tau) \star h(-\tau)$ is evaluated for a particular real measured impulse response and shown in Figure 4.6. A peak value is observed due to the channel's autocorrelation properties. A similar effect is observed in classical matched filter analysis, where full energy capture is obtained by applying the inverse of the received pulse shape as a filter at the receiver. In the context of time-reversal, the communication channel thus plays the role of the matched filter. A low-complexity receiver, which simply samples the output signal at its peak point, is therefore capable of harnessing a high percentage of the available energy.

We now provide an example showcasing the energy capture boost brought by time-reversal. Consider the

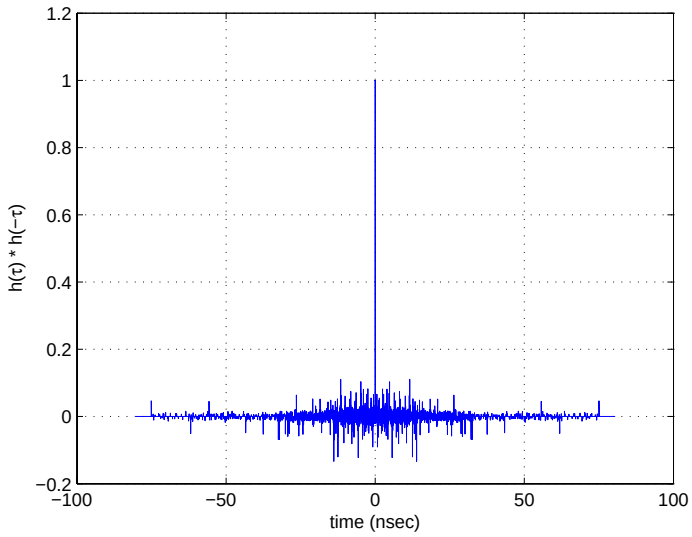

Figure 4.6: $h(\tau) \star h(-\tau)$ versus τ. Notice the large peak corresponding to all the multipath components aligning.

simple 3-path CIR in Figure 4.7. Assuming the transmit pulse width is shorter than the path inter-arrival time, the energy gathered by the perfect matched filter of section 3.5 (which in this case is a Rake receiver with 3 fingers) is equal to $1 + 0.5^2 + (-0.5)^2 = 1.5$.

The reversed CIR is shown in Figure 4.8. When the unit-energy transmit pulse is pre-filtered by the inverted CIR, the received pulse shape is equivalent to the sum of three scaled and delayed versions of the signal in Figure 4.8, as shown in Figure 4.9. Note that the pulse shape used is irrelevant for this discussion as long as the transmit pulse is short enough to perfectly resolve all multipath components. The resulting received

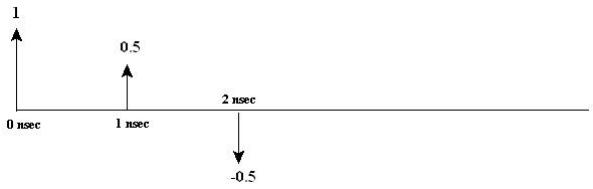

Figure 4.7: Simple 3-path CIR.

time-reversal signal is shown in Figure 4.10. Notice the presence of 2 additional multipath components compared to the conventional perfect matched filter case. Now, assuming that the transmitted pulses for time-reversal and the conventional Rake system have equal energy, the received time-reversal energy is equal to $\frac{(-0.5)^2+0.25^2+1.5^2+0.25^2+0.5^2}{1.5} = 1.916$. Notice the increase in captured energy due to the constructive multipath combination. Moreover, note that if only the main received multipath component is captured (*i.e.* single-tap time reversal is used), the energy capture is then equal to 1.5 and thus equivalent to that of the perfect matched filter.

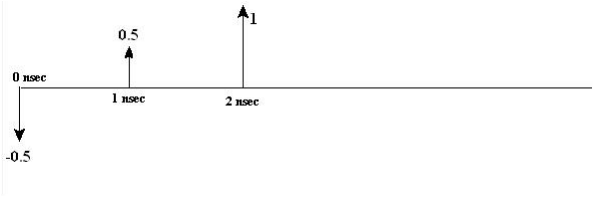

Figure 4.8: Reversed CIR.

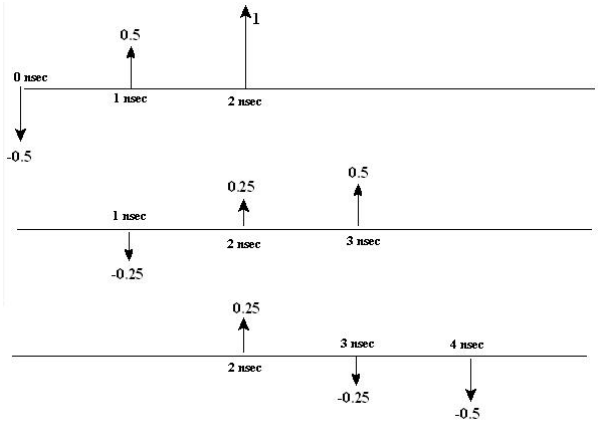

Figure 4.9: Three delayed and scaled versions of the reversed CIR are added at the receiver.

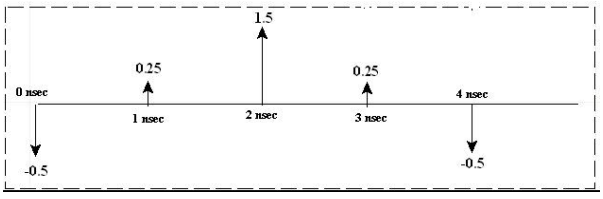

Figure 4.10: Equivalent time-reversal received pulse shape.

We now present a mathematical formulation of the above example. Assuming binary PAM modulation and a transmit bit of 1, the received signal is:

$$r(t) = \sqrt{\frac{E_p}{R_0}} \sum_{l1=0}^{L-1} \sum_{l2=0}^{L-1} \alpha_{l1}\alpha_{l2} w\left(t - \tau_{L-1} + \tau_{l2} - \tau_{l1}\right) + n(t). \tag{4.17}$$

Notice that R_0 is equal to the desired signal component d_{PAM} (given by (3.12)) for the optimal matched filter receiver in section 3.5.

The output of a single tap at delay t_0 is given by:

$$g(t_0) = \int_{t=-\infty}^{\infty} r(t)w(t - t_0)dt = d(t_0) + n(t_0) \tag{4.18}$$

where

$$d(t_0) = \sqrt{\frac{E_p}{d_{PAM}}} \sum_{l1=0}^{L-1} \sum_{l2=0}^{L-1} \alpha_{l1}\alpha_{l2} R\left(t_0 - \tau_{L-1} + \tau_{l2} - \tau_{l1}\right) \tag{4.19}$$

and the noise metric $n(t_0)$ is zero-mean Gaussian with variance $\frac{N_0}{2}$.

Setting $t_0 = \tau_{L-1}$, we get:

$$d(\tau_{L-1}) = \sqrt{\frac{E_p}{d_{PAM}}} \sum_{l1=0}^{L-1} \sum_{l2=0}^{L-1} \alpha_{l1}\alpha_{l2} R\left(\tau_{l2} - \tau_{l1}\right). \tag{4.20}$$

$$d(\tau_{L-1}) = \sqrt{E_p d_{PAM}}. \tag{4.21}$$

Then probability of error of a single-tap time-reversal system is then:

$$P_e = Q\left(\frac{\sqrt{E_p d_{PAM}}}{\frac{N_0}{2}}\right) = Q\left(\sqrt{\frac{2E_p d_{PAM}}{N_0}}\right). \tag{4.22}$$

Note that the probability of error is equal to that of the perfect matched filter receiver given by (3.15). A single-tap time-reversal system is thus equivalent to a perfect conventional Rake receiver capable of resolving all multipath components. All the energy available for the conventional perfect matched filter may thus be harnessed through a single-tap receiver using time-reversal. Also note that despite the fact that it captures

the same amount of energy as the "optimal" matched filter, the single-tap time-reversal receiver captures only part of the available energy. More energy may be gathered by including more taps (at the expense of increased receiver complexity). In fact, it can be shown that the peak tap holds about 50% of the available energy (see [72]). Thus we can achieve a potential 3-dB performance improvement if the energy in the other taps is harnessed. The decision statistic for time-reversal employing N taps may be written as:

$$d_N = \sum_{n=0}^{N-1} \gamma_n g(t_n) \tag{4.23}$$

where γ_n and t_n are the weight and delay of the n^{th} tap, respectively.

Figure 4.11 shows the time-reversal energy capture (averaged over multiple measured channels) as a percentage of the total available energy versus the number of taps used at the receiver. Notice that the energy capture grows slowly with the number of taps beyond the main tap. With 40 taps, only half of the remaining energy is captured (equivalently, 75% of the total energy is captured). Note that the position of these 40 taps is not known *a priori* and must be estimated based on channel knowledge at the receiver, which increases the design complexity. Figure 4.12 shows the temporal compression ratio (the inverse of the ratio of the power in the main tap to the power in the remaining taps) averaged over multiple channel measurements. Notice the absence of any strong tap beyond the main tap.

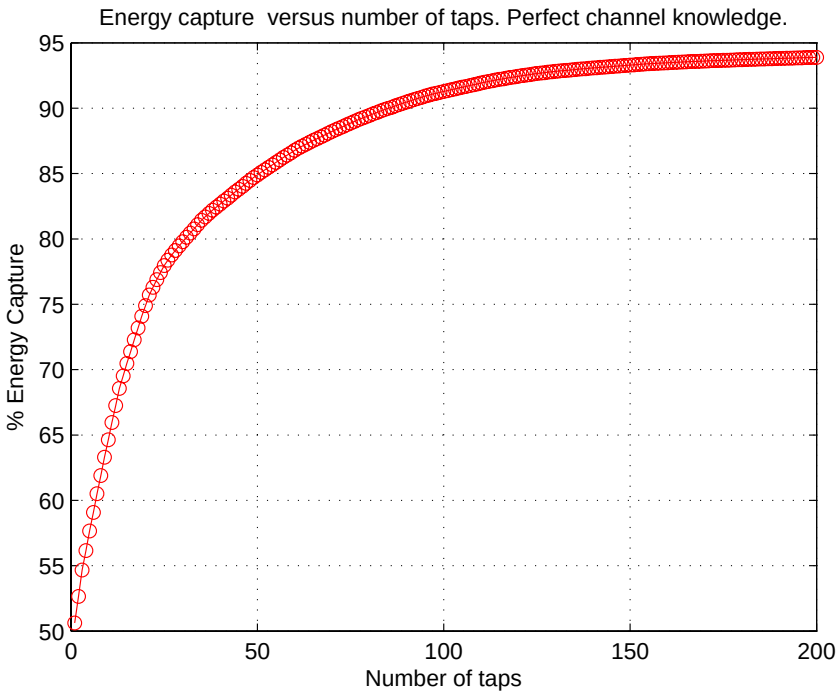

Figure 4.11: Energy capture (as percentage of total available energy) versus number of taps. Perfect channel knowledge. Real measured channel profiles used.

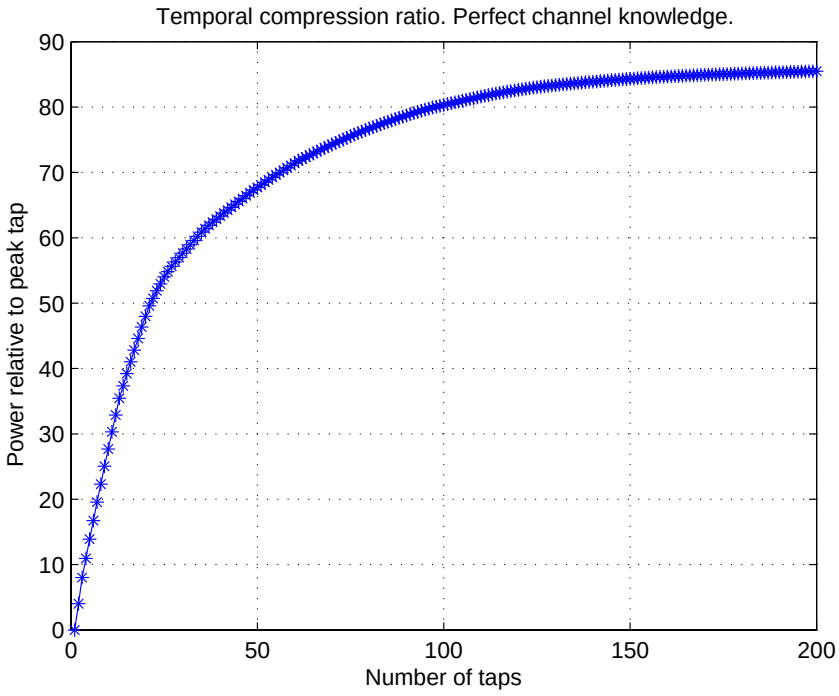

Figure 4.12: Temporal compression ratio versus number of taps. Perfect channel knowledge. Real measured channel profiles used.

Time-reversal may be thought of as a generalization of the pre-Rake receiver. In the pre-Rake scheme, the transmitted pulse is pre-coded with the F strongest available multipath components, rather than the entire impulse response. Assuming the delays and amplitudes of the F strongest paths are known, the transmitted signal is given by:

$$s(t) = \sum_{i=0}^{F-1} \alpha_{f_i} w\left(t - \tau_{L-1} + \tau_{f_i}\right) \tag{4.24}$$

where α_{f_i} and τ_{f_i} are the amplitude and delay of the i^{th} strongest path, respectively, and energy normalization is skipped for clarity. In the absence of channel knowledge, the complexity of channel estimation for this method is identical to the complexity of channel estimation for a conventional Rake receiver with F fingers employing MRC. Moreover, it can be easily shown that the performance of a single-tap Pre-Rake receiver is identical to that of a conventional Rake receiver with F fingers employing MRC given by (3.46). Improvement in performance is obtained if more taps are used at the receiver.

Performance with Channel Estimation

Perfect channel knowledge is an unrealistic assumption. We now study the performance of time-reversal when channel estimation is performed. The objective is to estimate the channel $h(\tau)$. We assume that estimation is performed at the transmitter*. Assume a training sequence of length N_p. The received training sequence can be written as:

$$r_{ts}(t) = \sqrt{E_p} \sum_{j=0}^{N_p-1} \sum_{l=0}^{L-1} \alpha_l w(t - \tau_l - jT_f) + n(t). \tag{4.25}$$

Since the transmitter has finite estimation resolution, channel coefficients cannot be feasibly estimated at random delays. We assume that the transmitter estimates an equivalent channel coefficient every δt seconds (where δt is defined as the estimation's resolution). With $\delta t = T_w$, channel estimation constructs the following CIR:

$$\hat{h}\left(\tau\right) = \sum_{l=0}^{L-1} \hat{\beta}_l \delta(lT_w) \tag{4.26}$$

*Note that for multi-tap time-reversal, additional channel estimation is required at the receiver in order to set the taps' weights and delays.

where the k^{th} path amplitude is estimated as:

$$\hat{\beta}_k = \frac{1}{\sqrt{E_p}} \frac{1}{N_p} \sum_{j=0}^{N_p-1} \int_{kT_w+jT_f}^{(k+1)T_w+jT_f} r_{ts}(t) w(t - kT_w - jT_f) dt \tag{4.27}$$

which gives

$$\hat{\beta}_k = \sum_{l=0}^{L-1} \alpha_l R\left(\tau_l - kT_w\right) + n_k \tag{4.28}$$

where n_k is a zero-mean Gaussian random variable with variance $\frac{N_0}{2E_pN_p}$.

The transmitted signal is then:

$$s_{Np}(t) = \sqrt{E_p} \sum_{l=0}^{L-1} \hat{\beta}_l w\left(t - \tau_{L-1} + lT_w\right) \tag{4.29}$$

where energy normalization is skipped for brevity.

Assuming a data bit equal to one, the received signal is then:

$$r_{Np}(t) = \sqrt{E_p} \sum_{l1=0}^{L-1} \sum_{l2=0}^{L-1} \alpha_{l1} \hat{\beta}_{l2} w\left(t - \tau_{L-1} + l_2T_w - \tau_{l1}\right) + n(t). \tag{4.30}$$

The output of a single tap (at delay t_0) of the receiver is then:

$$g(t_0) = \int_{t=-\infty}^{\infty} r_{Np}(t) w(t - t_0) dt = d(t_0) + n(t_0). \tag{4.31}$$

At $t_0 = \tau_{L-1}$:

$$g(\tau_{L-1}) = \sqrt{E_p} \sum_{l1=0}^{L-1} \sum_{l2=0}^{L-1} \alpha_{l1} \hat{\beta}_{l2} R\left(l_2T_w - \tau_{l1}\right) + n \tag{4.32}$$

$$g(\tau_{L-1}) = \sqrt{E_p} \left[\sum_{l1=0}^{L-1} \sum_{l2} \alpha_{l1} \sum_{l3=0}^{L-1} \alpha_{l3} R\left(\tau_{l3} - l_2T_w\right) R\left(l_2T_w - \tau_{l1}\right) + \sum_{l1=0}^{L-1} \sum_{l2} \alpha_{l1} n_{l2} R\left(l_2T_w - \tau_{l1}\right) \right] + n \tag{4.33}$$

where n is a zero-mean Gaussian random variable with variance $\frac{N_0}{2}$.

Let:

$$Y = \sqrt{E_p} \sum_{l1=0}^{L-1} \sum_{l2} \alpha_{l1} n_{l2} R\left(l_2 T_w - \tau_{l1}\right). \tag{4.34}$$

It is easy to show that the variance v of Y is given by:

$$v = \frac{N_0}{2N_p} \sum_{l2} \left(\sum_{l1=0}^{L-1} \alpha_{l1} R\left(l_2 T_w - \tau_{l1}\right) \right)^2. \tag{4.35}$$

The probability of error is then given by:

$$P_e = Q\left(\sqrt{ \frac{E_p \left[\sum_{l1=0}^{L-1} \sum_{l2} \alpha_{l1} \sum_{l3=0}^{L-1} \alpha_{l3} R\left(\tau_{l3} - l_2 T_w\right) R\left(l_2 T_w - \tau_{l1}\right) \right]^2}{\frac{N_0}{2} \left[1 + \frac{1}{N_p} \sum_{l2} \left(\sum_{l1=0}^{L-1} \alpha_{l1} R\left(l_2 T_w - \tau_{l1}\right) \right)^2 \right]} } \right) \tag{4.36}$$

As the number of pilots approaches infinity, the expression becomes:

$$P_e = Q\left(\sqrt{ \frac{2E_p \left[\sum_{l1=0}^{L-1} \sum_{l2} \alpha_{l1} \sum_{l3=0}^{L-1} \alpha_{l3} R\left(\tau_{l3} - l_2 T_w\right) R\left(l_2 T_w - \tau_{l1}\right) \right]^2}{N_0} } \right) \tag{4.37}$$

where the term in the numerator represents the energy loss due to the mismatch between the adopted channel model in (4.26) and the real channel.

In the case of idealized channels where the multipath delays are exact multiples of T_w, (4.26) faithfully models the channel. Let:

$$A = \sum_{l1=0}^{L-1} \sum_{l2} \alpha_{l1} \sum_{l3=0}^{L-1} \alpha_{l3} R\left(\tau_{l3} - l_2 T_w\right) R\left(l_2 T_w - \tau_{l1}\right) \tag{4.38}$$

$$B = \sum_{l2} \left(\sum_{l1=0}^{L-1} \alpha_{l1} R\left(l_2 T_w - \tau_{l1}\right) \right)^2. \tag{4.39}$$

Since the autocorrelation function is only evaluated at multiple of T_w, and since $R(\tau) \approx 0$ for $\tau > T_w$, we get:

$$A = \sum_{l1=0}^{L-1} \sum_{l2} \alpha_{l1}\alpha_{l2} R\left(l_2 T_w - \tau_{l1}\right) = \sum_{l1=0}^{L-1} \alpha_{l1}^2 \tag{4.40}$$

$$B = \sum_{l2} \alpha_{l2}^2. \tag{4.41}$$

Assuming $\sum_l \alpha_l^2 = 1$, the expression collapses to:

$$P_e = Q\left(\sqrt{\frac{2E_p}{N_0\left(1+\frac{1}{N_p}\right)}}\right). \tag{4.42}$$

Notice that at high N_p we get the probability of error of the perfect matched filter obtained for idealized time-reversal.

A qualitative comparison between time-reversal and the proposed sequence optimization method is later provided in this section, along with simulation results.

4.5.3 Single User Sequence Optimization

Time-reversal achieves high concentrated energy capture by incorporating the channel impulse response into the transmit pulse shape. We now propose a more generalized approach, which jointly optimizes the transmit pulse and the receiver template for maximal energy capture.

Consider a single user system where the transmit waveform of the user consists of a real-valued sequence. The transmitted signal has the form:

$$s(t) = \sqrt{E_p} \sum_{i=-\infty}^{\infty} b_i \sum_{n=0}^{N_x-1} x_n w\left(t - nT_w - iT_f\right) \tag{4.43}$$

where $X = [x_0\ x_1\ ...\ x_{N_x-1}]^T$ is the real-valued transmit signal sequence. For mathematical simplicity, it is assumed that T_f is an integer multiple of T_w.

Let τ_{max} be the maximum channel spread (the maximum multipath delay). It is assumed that $T_f >$

$N_x T_w + \tau_{max}$, eliminating any ISI effects at the receiver. The signal sequence is normalized, that is:

$$X^T X = \sum_{n=0}^{N_x-1} x_n^2 = 1. \tag{4.44}$$

We assume the same channel model used in the previous sections of this chapter. Then, without loss in generality, the received signal in the time interval $[0, T_f]$ can then be written as:

$$r(t) = \sqrt{E_p} b_0 \sum_{l=1}^{L} \alpha_l \sum_{n=0}^{N_x-1} x_n w\left(t - nT_w - \tau_l\right) + n(t) \tag{4.45}$$

where $n(t)$ is a zero-mean AWGN process with PSD $\frac{N_0}{2}$.

The unit-energy template for the receiver correlator is:

$$s_0(t) = \sum_{m=0}^{N_y-1} y_m w(t - mT_w), \tag{4.46}$$

where $Y = \begin{bmatrix} y_0 & y_1 & ... & y_{N_y-1} \end{bmatrix}^T$ is the normalized receiver template sequence, and $N_y = \frac{T_f}{T_w}$. The decision statistic for bit b_0 can be written as:

$$r_0 = \int_0^{T_f} r(t) s_0(t) dt = \sqrt{E_p} b_0 d + n \tag{4.47}$$

where:

$$d = \int_0^{T_f} \sum_{l=1}^{L} \alpha_l \sum_{n=0}^{N_x-1} x_n w\left(t - nT_w - \tau_l\right) s_0(t) dt \tag{4.48}$$

$$n = \int_0^{T_f} n(t) s_0(t) dt. \tag{4.49}$$

It can be easily shown that n is a zero-mean Gaussian random variable with variance $\frac{N_0}{2}$. d can be rearranged as:

$$d = \sum_{l=1}^{L} \alpha_l \sum_{n=0}^{N_x-1} \sum_{m=0}^{N_y-1} x_n y_m R\left(nT_w - mT_w + \tau_l\right). \tag{4.50}$$

The SNR of the received signal is given by

$$SNR = \frac{2E_p d^2}{N_0}. \tag{4.51}$$

The probability of error conditioned on X and Y can then be expressed as:

$$P_e = Q\left(\frac{\sqrt{E_p}d}{\sqrt{\frac{N_0}{2}}}\right). \tag{4.52}$$

Therefore:

$$P_e = Q\left(\sqrt{\frac{2E_p d^2}{N_0}}\right). \tag{4.53}$$

Consider the case where $X = [1\ 0\ 0\ ...\ 0]^T$ and $Y = [1\ 0\ 0\ ...\ 0]^T$, which corresponds to a simple matched filter receiver where the correlator template is matched to $w(t)$. Then, $d = \sum_{l=1}^{L} \alpha_l R(\tau_l)$. Since $R(\tau) = 0$ for $\tau > T_p$, the receiver only captures the energy contained in the interval $[0, T_w]$, and the energy in the subsequent multipath components is lost, resulting in poor performance (this receiver was studied in section 3.6).

Note that SNR depends directly on the value of d. d may be increased by choosing sequences X and Y such that the energy from the different multipath components add up coherently at the receiver. This sequence optimization technique is quite similar to a beamformer in which transmissions from different antennas are weighted such that they coherently combine at the receiver.

The decision statistic d can be rearranged in the following form:

$$d = \sum_{m=0}^{N_y-1} y_m \sum_{n=0}^{N_x-1} \sum_{l=1}^{L} x_n \alpha_l R(nT_p - mT_w + \tau_l). \tag{4.54}$$

Since $R(\tau) = 0$ for $\tau > T_w$, the above equation can also be re-written as,

$$d = \sum_{m=0}^{N_y-1} y_m \sum_{k=max(0,m-N_x+1)}^{m} h_k x_{m-k} \tag{4.55}$$

where,

$$h_k = \sum_{l=1}^{L} \alpha_l R\left(\tau_l - kT_w\right). \tag{4.56}$$

Here, h_k can be interpreted as the equivalent channel coefficient obtained by transmitting $w(t)$ and binning the received signal after correlation with $w(t)$, every T_w seconds.

In order to exploit *all* the channel multipath components, let $N_x = 1 + \lceil \frac{T_c}{T_w} \rceil$ (where $\lceil . \rceil$ is the ceil operator) and $N_y = 2N_x - 1$. An intuitive interpretation for this choice is that the available degrees of freedom are uniformly distributed over the channel spread. The expression for d can be more conveniently represented using matrix notation as

$$d = Y^T H X, \tag{4.57}$$

where

$$H = \begin{bmatrix} h_0 & 0 & ... & 0 \\ h_1 & h_0 & ... & 0 \\ \vdots & \vdots & \ddots & \vdots \\ h_{N_x-1} & h_{N_x-2} & ... & h_0 \\ 0 & h_{N_x-1} & ... & h_1 \\ \vdots & \vdots & \ddots & \vdots \\ 0 & 0 & ... & h_{N_x-1} \end{bmatrix}. \tag{4.58}$$

From a matched filter perspective, the optimal sequence used at the receiver is matched to the transmit sequence convolved with the channel [74][75]. Hence $Y = HX$. d can now be written as,

$$d = X^T H^T H X. \tag{4.59}$$

The sequence optimization process, which keeps the sequence normalized to one, can be formulated as the following optimization problem.

$$P1 : \max_X f(X) = \max_X \frac{X^T H^T H X}{X^T X}. \tag{4.60}$$

The channel correlation matrix $H^T H$ is symmetric and positive semi-definite. Hence, $H^T H$ can be diagonalized as,

$$H^T H = U D U^T \tag{4.61}$$

where U is a unitary matrix whose columns are formed by the orthonormal eigenvectors of $H^T H$, $\{u_1, \ldots, u_{N_x}\}$, and D is a diagonal matrix whose diagonal elements are the eigenvalues of $H^T H$, $\{\lambda_1, \ldots, \lambda_{N_x}\}$. Without loss of generality, we assume that $\lambda_1 \geq \lambda_2 \geq \ldots, \geq \lambda_{N_x}$. Since the eigenvectors of $H^T H$ form a complete basis, there exists a set of coefficients $\beta_i,\ i \in \{1, \ldots, N_x\}$ for any vector X such that $X = \beta_1 u_1 + \beta_2 u_2 + \ldots + \beta_{N_x} u_{N_x}$. Then, $f(X)$ can be expressed as,

$$f(X) = \frac{X^T H^T H X}{X^T X} = \frac{\sum_{n=1}^{N_x} \lambda_n |\beta_n|^2}{\sum_{n=1}^{N_x} |\beta_n|^2}. \tag{4.62}$$

Since $\lambda_1 \geq \lambda_i$ for $i \in \{2, \ldots, N_x\}$, we may write:

$$f(X) = \frac{\sum_{n=1}^{N_x} \lambda_n |\beta_n|^2}{\sum_{n=1}^{N_x} |\beta_n|^2} \leq \frac{\lambda_1 \sum_{n=1}^{N_x} |\beta_n|^2}{\sum_{n=1}^{N_x} |\beta_n|^2} = \lambda_1. \tag{4.63}$$

Note that $f(X) = \lambda_1$ for $X = \beta_1 u_1$. Hence, $f(X)$ is maximized by u_1, the eigenvector corresponding to the maximum eigenvalue of $H^T H$. This is also a well known result in linear algebra. $f(X)$ is the Rayleigh quotient for matrix $H^T H$. The Rayleigh quotient is maximized by the eigenvector corresponding to the maximum eigenvalue of $H^T H$ [76] [77].

4.5.4 Channel Estimation

Note that since channel knowledge is not readily available, a channel estimation procedure is required in order to estimate H. After channel estimation is performed at the receiver, the optimal sequence is determined and then fed back to the transmitter. It is assumed that the sequence is re-estimated periodically to account for the time-varying channel.

The channel estimation procedure used for time-reversal is again used for sequence optimization. A training sequence of length N_p (given by (4.25)) is transmitted. Recall that the channel coefficients $\hat{h}_i$ are estimated

as:

$$\hat{h}_i = \frac{1}{N_p} \sum_{j=0}^{N_p-1} \int_{iT_p+jT_f}^{(i+1)T_w+jT_f} r_{ts}(t) w\left(t - iT_w - jT_f\right) dt \tag{4.64}$$

for $0 \leq i \leq N_x - 1$. These estimates are used to construct the matrix H at the receiver. It must be noted that the channel estimation described above can be done in the analog domain with simple integrators and does not require increased sampling rates. Also, notice that the same channel estimation technique was applied for the time-reversal receiver.

In the presence of channel estimation errors, the calculated sequence is not the maximum eigenvector of H, but the maximum eigenvector of $H + N$, where,

$$N = \begin{bmatrix} n_0 & 0 & ... & 0 \\ n_1 & n_0 & ... & 0 \\ \vdots & \vdots & \ddots & \vdots \\ n_{N_x-1} & n_{N_x-2} & ... & n_0 \\ 0 & n_{N_x-1} & ... & n_1 \\ \vdots & \vdots & \ddots & \vdots \\ 0 & 0 & ... & n_{N_x-1} \end{bmatrix}. \tag{4.65}$$

Here, $n_i, \ \forall i$ is a zero mean Gaussian random variable with variance $\frac{N_0}{2N_p}$. This eigenvector mismatch adversely affects the performance of the system. The effect of the number of pilots on performance will now be studied, based on traditional eigenvector perturbation theory [78] [79].

Let $V = [V_1 \ V_2 \ ... \ V_n]$ be the matrix formed of the eigenvectors of $H^T H$. Then,

$$V^{-1} H^T H V = diag\left(\lambda_1, \lambda_2, ..., \lambda_n\right) \tag{4.66}$$

where $\lambda_1, \lambda_2, ..., \lambda_n$ are the eigenvalues of $H^T H$, and $diag(Z)$ is the diagonal matrix with Z as the diagonal. V_i is the eigenvector corresponding to λ_i. Let $A = H^T H$. Assume that A is perturbed by an error Δ_A:

$$\hat{A} = A + \Delta_A. \tag{4.67}$$

Note that, in our system, H is perturbed by the noise matrix N and consequently, matrix $H^T H$ is perturbed by,

$$\Delta_A = H^T N + N^T H + N^T N. \tag{4.68}$$

The perturbed eigenvector $\hat{V}_i$ can be written as:

$$\hat{V}_i = V_i + \delta_{V_i}. \tag{4.69}$$

Without loss in generality, assume V_1 is the desired eigenvector (the same analysis can be performed for any eigenvector). Let ϵ be the greatest absolute value in the perturbation matrix, Δ_A. Then it can be shown that [79]:

$$\delta_{V_1} = \epsilon Y g_1 + \epsilon^2 Y g_2 + \epsilon^3 Y g_3 + ... \tag{4.70}$$

where $Y = [V_2\ V_3\ ...V_n]$ and g_i is an $(n-1)$-dimensional vector.

The first order perturbation term is:

$$p_1 = \epsilon Y g_1. \tag{4.71}$$

It can be shown that p_1 can be written as:

$$p_1 = V \Delta V^T \Delta_A V_1 \tag{4.72}$$

where $\Delta = diag\left(0, (\lambda_1 - \lambda_2)^{-1}, ... (\lambda_1 - \lambda_n)^{-1}\right)$. The mean of this term is given by

$$E[p_1] = N_x \sigma^2 V \Delta V^T V_1 \tag{4.73}$$

and:

$$\sigma^2 = \frac{N_0}{2N_p}. \tag{4.74}$$

Since the eigenvalue of $V \Delta V^T$ corresponding to eigenvector V_1 is zero, $E[p_1] = 0$. In most applications, the first order perturbation is sufficient to characterize the error. However, simulation results do not show a zero

mean for the perturbation error. Hence, the second order term for the perturbation error is considered here. The second order perturbation can be written as [78]:

$$\begin{aligned} p_2 &= V\Delta V^T \Delta_A V \Delta V^T \Delta_A V_1 \\ &- \left(V\Delta V^T\right)^2 \Delta_A V_1 V_1^T \Delta_A V_1 \\ &- \frac{1}{2} V_1 V_1^T \Delta_A \left(V\Delta V^T\right)^2 \Delta_A V_1. \end{aligned} \tag{4.75}$$

Equations (4.72) and (4.75) can be used to calculate the resultant perturbation of the eigenvector of $H^T H$. The mean and variance of this perturbation may be expressed in the following form:

$$\mu_p = E\left[p_1 + p_2\right] = A_1\sigma^2 + A_2\sigma^4 \tag{4.76}$$

$$\sigma_p^2 = E\left[\left(p_1 + p_2\right)^2\right] - \mu_p^2 = A_3\sigma^2 + A_4\sigma^4 + A_5\sigma^6 + A_6\sigma^8. \tag{4.77}$$

A_1 and A_2 are $(N_x \times 1)$ matrices and A_3, A_4 and A_5 are $(N_x \times N_x)$ matrices, that solely depend on the channel. The variance of noise, σ^2 is inversely proportional to the number of pilots used in the system. Hence, it is expected that the effect of A_2, A_4, A_5 and A_6 will be significantly reduced even for a small number of pilots. Also, it will be shown by simulation that the overall perturbation of the sequence (eigenvector of $H^T H$) is successfully limited for moderate values of training.

The perturbation error is simulated and compared to the theoretical error obtained with the first and second order perturbations. Including the second order perturbation gives a good estimate of the mean (Figure 4.13) and an improved estimate of the variance (Figure 4.14) of the transmit sequence error. In this example, a sequence of length 50 was used.

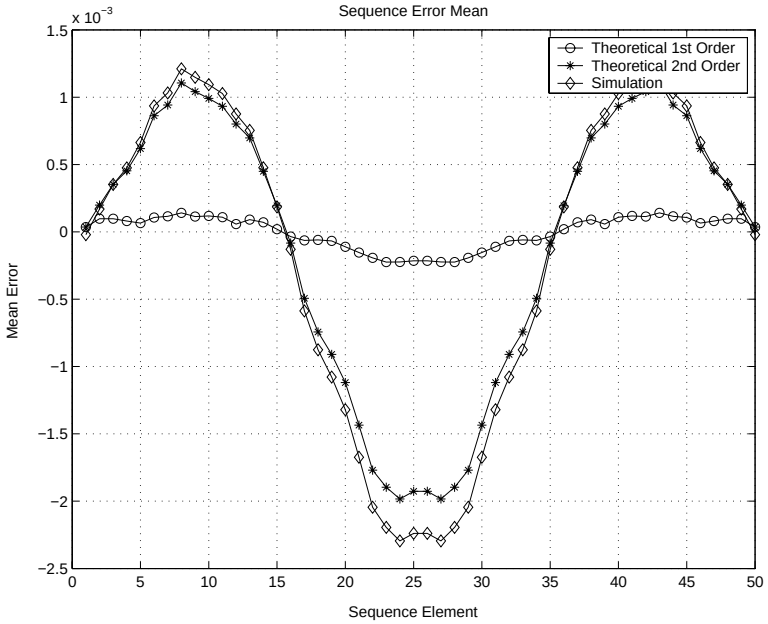

Figure 4.13: Mean of sequence error. $\frac{E_p}{N_0} = 5$ dB. $N_p = 100$.

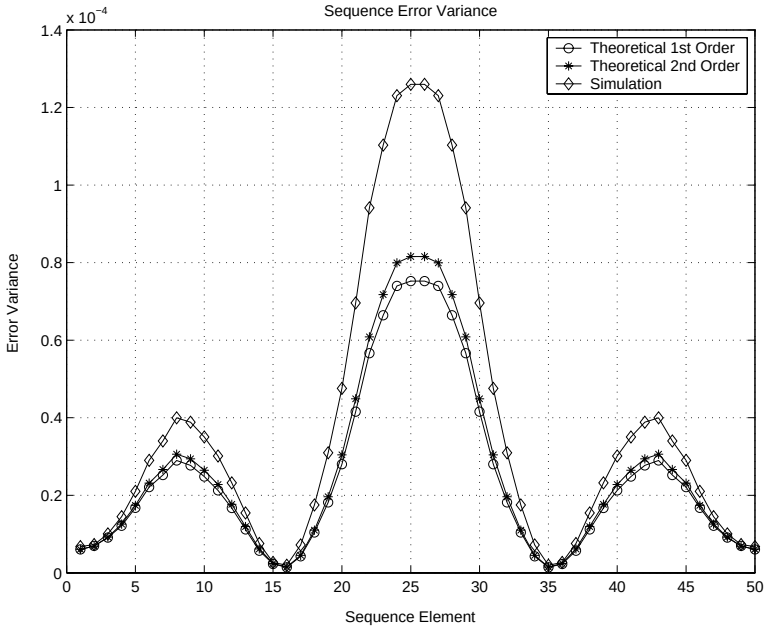

Figure 4.14: Variance of sequence error. $\frac{E_p}{N_0} = 5$ dB. $N_p = 100$.

4.5.5 Sequence Optimization versus Time-Reversal

We now present a theoretical comparison between sequence optimization and time-reversal. First consider idealized time-reversal, which is characterized by a probability of error given by (4.22). Recall that the transmitted signal and receiver template for sequence optimization are formed of a stream of scaled Gaussian pulses spaced by one pulse width. In the case of infinite channel resolution, the transmitted time-reversal signal has a richer structure, since it pre-codes multipath components that occur at random times (potentially within a pulse duration). The transmit time-reversal signal may be written as the sum of scaled and delayed Gaussian pulses which need not be separated by multiples of a pulse width. The equivalent time-reversal sequence thus does not belong to the group of sequences over which our proposed method optimizes its sequence. Therefore, it is theoretically possible for the idealized time-reversal receiver to outperform the sequence optimization receiver for a specific number of taps[†].

As stated earlier, idealized time-reversal is infeasible, and finite-resolution channel estimation must be applied. Assume the same channel estimation process (consisting of estimating one channel coefficient every transmit pulse width) is applied for both methods with the same estimation resolution. In the sequence optimization approach, the transmit sequence and receiver template are designed such that the received energy capture is maximized. Denote the group of all possible transmit sequences and all possible receiver templates constrained by a specific channel estimation resolution by G_T and G_R, respectively. The optimal transmit sequence and receiver template are optimized over these two groups (in the maximal energy capture sense). Since the time-reversal transmit sequence also belongs to G_T, time-reversal employing a single tap cannot outperform sequence optimization (since a single tap receiver may be modeled by a sequence belonging to G_R). Sequence optimization thus presents a lower bound on single-tap time-reversal performance. However, multi-tap time reversal where taps are separated by random intervals (rather than multiples of a pulse width) can potentially outperform sequence optimization, since the equivalent template of such a receiver does not belong to G_R.

[†]Note that although sequence optimization in this work is based on the design of sequences where pulses are separated by multiples of a pulse width, the method may be extended to a finer resolution, where pulses are separated by sub-pulse width durations. Higher energy capture levels are then possible.

4.5.6 Multiple User Sequence Optimization

The sequence optimization scheme for the multipath channel is now extended to a multi-user UWB system. Consider K users communicating with a centralized receiver. The transmission of each user is assumed to be sequence-based. For simplicity of notation, the users' received signals are assumed to be synchronized. Following the notation in the previous section, let H_k be the channel matrix from the k^{th} user to the receiver, p_k be the signal power of the k^{th} user, X_k be the transmit sequence vector of the k^{th} user and b_k be the data bit transmitted by the k^{th} user. The signal vector at the receiver, R, in a single symbol interval is given by,

$$R = \sum_{k=1}^{K} \sqrt{p_k} H_k X_k b_k + N \tag{4.78}$$

where N is a vector of zero-mean Gaussian random variables with variance $\sigma^2 = \frac{N_0}{2}$. Let Y_i be the unit-energy correlation template vector at the receiver for the i^{th} user. The signal after correlation is given by,

$$Y_i^T R = Y_i^T \sum_{i=k}^{K} \sqrt{p_k} H_k X_k b_k + Y_i^T N. \tag{4.79}$$

The signal-to-interference-plus-noise ratio of the i^{th} user at the receiver can be written as,

$$SINR_i = \frac{p_i \left(Y_i^T H_i X_i\right)^2}{Y_i^T Z_i Y_i} \tag{4.80}$$

where Z_i is the interference-plus-noise correlation matrix defined as $Z_i = \sum_{j \neq i} p_j H_j X_j X_j^T H_j^T + \sigma^2$. The optimal sequence Y_i (that corresponds to the optimal receiver), which maximizes $SINR_i$ is the solution to the following maximization problem:

$$P2 : \max_{Y_i \neq 0} SINR_i = \max_{Y_i \neq 0} p_i \frac{Y_i^T H_i X_i X_i^T H_i^T Y_i}{Y_i^T Z_i Y_i}. \tag{4.81}$$

Since Z_i is a Hermitian matrix, it can be diagonalized as $Z_i = U_i \Lambda_i U_i^T$, where U_i is a unitary matrix and Λ_i is a diagonal matrix. Let $W_i = \Lambda_i^{\frac{1}{2}} U_i^T Y_i$. Then,

$$SINR_i = p_i \frac{W_i^T \Lambda_i^{-\frac{1}{2}} U_i^T H_i X_i X_i^T H_i^T U_i \Lambda_i^{-\frac{1}{2}} W_i}{W_i^T W_i}. \tag{4.82}$$

The sequence W_i that maximizes $SINR_i$ is given by,

$$W_i = \Lambda_i^{-\frac{1}{2}} U_i^T H_i X_i. \tag{4.83}$$

The optimal Y_i is therefore given by,

$$Y_i = U_i \Lambda_i^{-1} U_i^T H_i X_i = Z_i^{-1} H_i X_i. \tag{4.84}$$

The correlator output now becomes,

$$Y_i^T R = X_i^T H_i^T Z_i^{-1} H_i X_i b_i + Y_i^T \sum_{j \neq i} H_j X_j b_j + Y_i^T N. \tag{4.85}$$

The decision statistic d is given by

$$d = X_i^T H_i^T Z_i^{-1} H_i X_i. \tag{4.86}$$

Matrix $H_i^T Z_i^{-1} H_i$ is symmetric and positive definite. Hence d is maximized if X_i is the eigenvector corresponding to the maximum eigenvalue of $H_i^T Z_i^{-1} H_i$.

Note that $Z_i = E\left[RR^T\right] - p_i H_i X_i X_i^T H_i^T$, assuming bit transmissions from multiple users are uncorrelated. Hence, in the absence of transmissions from the i^{th} user, Z_i can be estimated by computing and averaging the received correlation matrices, with no additional load on the system.

4.5.7 Sequence Optimization in Presence of NBI

The above sequence optimization technique for the UWB system with multi-user interference can be applied to reject narrowband interference. In this framework, the interferer is modeled by a sinusoidal wave.

Moreover, the interferer's period is assumed to be an integer multiple B of the symbol duration of the UWB user. B is assumed to be known at the receiver. Note that the interference in these B symbol intervals can be viewed as transmissions from B separate interferers, where only one interferer transmits in each interval. Let I_j, $j \in \{1, ..., B\}$ be the interference vector in the j^{th} symbol interval and r_j be the received signal in that interval. The interference-plus-noise correlation matrix Z can be written as,

$$Z = \sum_{j=1}^{B} I_j I_j^T + \sigma^2. \tag{4.87}$$

From the analysis from the previous section, the optimal transmit sequence X is the maximum eigenvector of $H^T Z^{-1} H$ and the optimal receiver correlation template Y is $Z^{-1} H X$, where H is the UWB user's channel matrix. Again, Z may be estimated at the receiver with no additional overhead.

4.5.8 Simulation Results

The performance of the proposed single-user scheme is compared to other signal detection methods in Figure 4.15. Performance is averaged over multiple NLOS profiles. The training overhead is equal to 250 pilots for the proposed method. First, note that the simple matched filter ($X = Y = [1\ 0\ 0 ...\ 0]$, employing $w(t)$ as a correlation template) leads to poor performance, since only the energy in the first arriving path is captured. Using a non-optimized, random sequence also leads to similar performance, because the multipath energy adds noncoherently, thus leading to a very low energy capture. A Rake receiver with 10 fingers (where it is assumed that the energy in the strongest 10 paths is perfectly captured) gathers only a fraction of the total received energy, and yields a performance that is about 4.5 dB worse than the perfect Rake case (Rake receiver with an infinite number of fingers with perfect channel estimation). A pilot-assisted receiver with 250 pilots only achieves performance that is within 2 dB of the perfect Rake. The proposed receiver based on the optimal sequence outperforms the perfect Rake by about 2 dB. The large performance gain brought by the optimized sequence might seem counter-intuitive, since the perfect Rake captures *all* the received energy, and one might think that it provides a limit on performance. However, the optimized sequence leads to a boost in the received power level due to coherent multipath energy combining (d in Equation (4.50) may be greater than one). Thus, there is essentially more energy available for the receiver to gather. This

effect is similar to the gains seen when using transmit beamforming, or error correction coding.

The required training load for the proposed method is examined in Figure 4.16. Note that increasing the

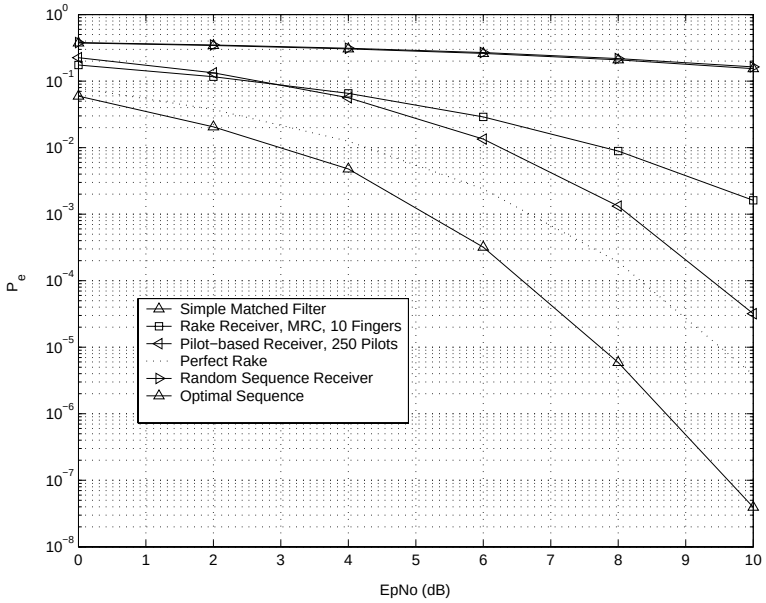

Figure 4.15: Performance of sequence adaptation receiver with $N_p = 250$. Proposed scheme outperforms a 10-Finger RAKE receiver, and a pilot-assisted receiver with 250 pilots. Performance is averaged over multiple NLOS measured channel profiles.

training load from 50 to 100 pilots leads to significant gains (around 2 dB). Increasing the load from 100 to 250 pilots only leads to about 0.5 dB gain. The proposed method with 100 pilots therefore gives a good tradeoff between training load and performance. Figure 4.17 compares the performance of the proposed receiver with a 10-finger Rake receiver and a pilot-assisted receiver for different number of training pilots with a constant $\frac{E_b}{N_0} = 6$ dB (where E_b is the bit energy). Notice that all three methods perform similarly for a very light load, but the proposed method shows drastic gains as the number of pilots increases. The proposed receiver outperforms the perfect Rake receiver with perfect channel knowledge for a training load greater than 80 pilots.

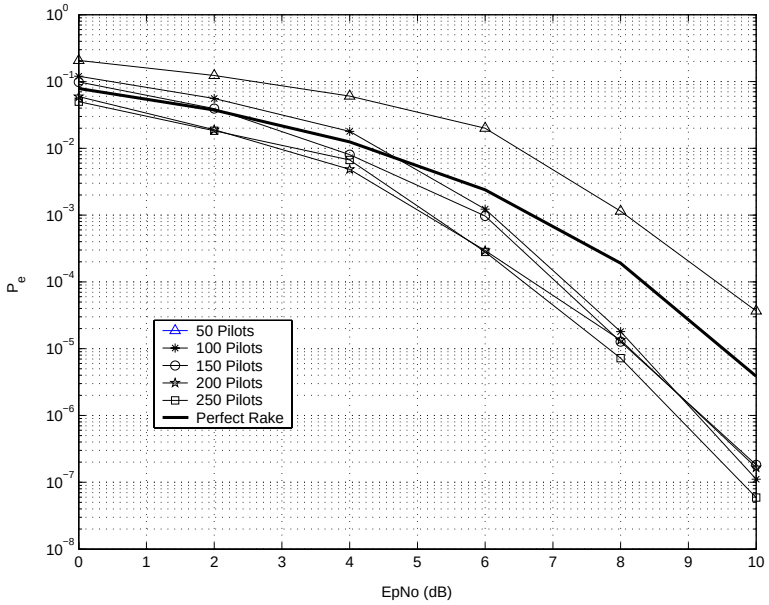

Figure 4.16: Performance of proposed method for different number of pilots. Performance is averaged over multiple NLOS measured channel profiles.

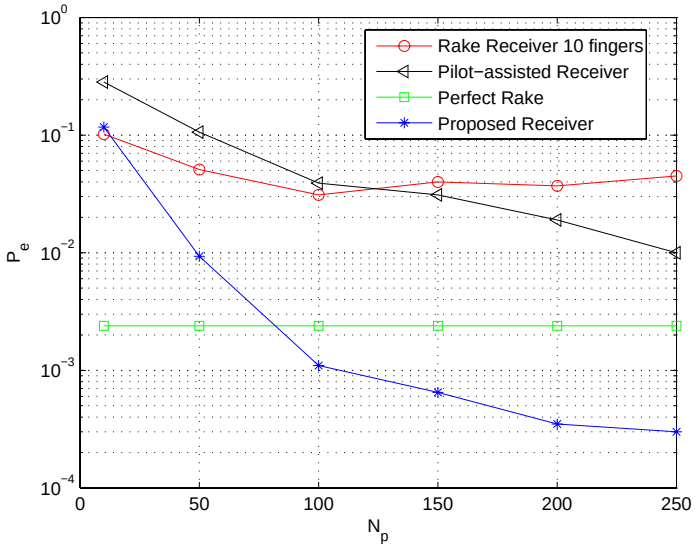

Figure 4.17: Performance comparison of proposed method with 10-finger Rake receiver and pilot-assisted receiver for varying number of pilots. $\frac{E_b}{N_0} = 6$ dB. Perfect Rake assumes perfect channel knowledge.

Note that one limitation of the proposed method is the need to feedback the real-valued sequence from the receiver to the transmitter. This additional overhead required by the feedback is now studied in terms of the number of bits that could be used to quantize the sequence without significantly affecting the performance of the system (Figure 4.18). In addition to quantization levels of 3, 5, 9 and 11 bits, a ternary code is also used, where three levels, -1, 0 and 1, are used to quantify the sequence. It is seen that performance improvement over the perfect Rake can be achieved even while using the simple ternary code. Note that 9-bit quantization achieves a performance close to the perfect quantization case.

An additional way to reduce the feedback overload in the system is by the use of transmit sequences with

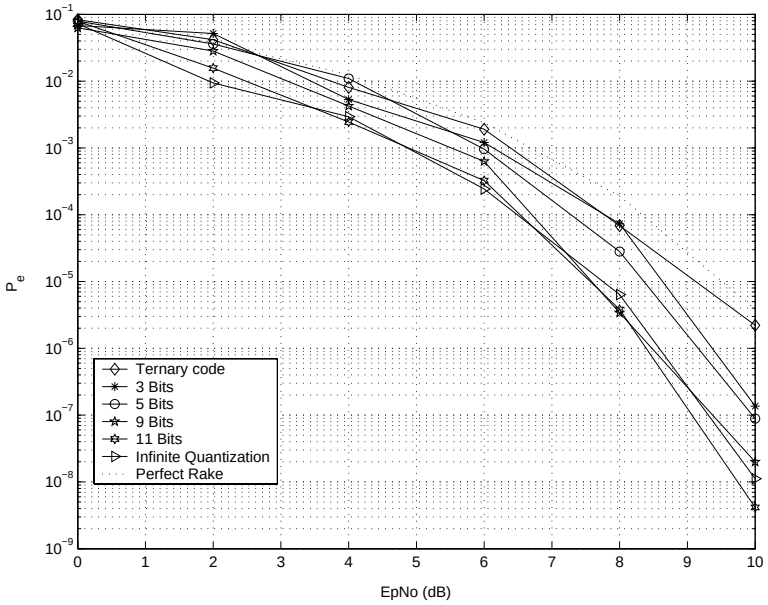

Figure 4.18: System performance with quantized sequence at the transmitter.

length smaller than $1 + \lceil \frac{T_c}{T_w} \rceil$. These reduced length sequences can be constructed by uniformly spacing the sequence over the delay spread T_c or by clustering them at the beginning. Figure 4.19 shows the performance of the system with different reduced length sequences. It is seen that clustering the sequence at the beginning gives improved performance over equally spacing the sequence. This is intuitive since most of the energy of the channel is concentrated at the beginning of the impulse response. The delay spread considered in the simulation is equal to $160T_w$. It is seen that a performance gain over the perfect Rake can be obtained by a sub-optimal sequence of length 40.

Note that the proposed scheme finds a sequence of length $1 + \lceil \frac{T_c}{T_p} \rceil$ optimized for the channel. We now

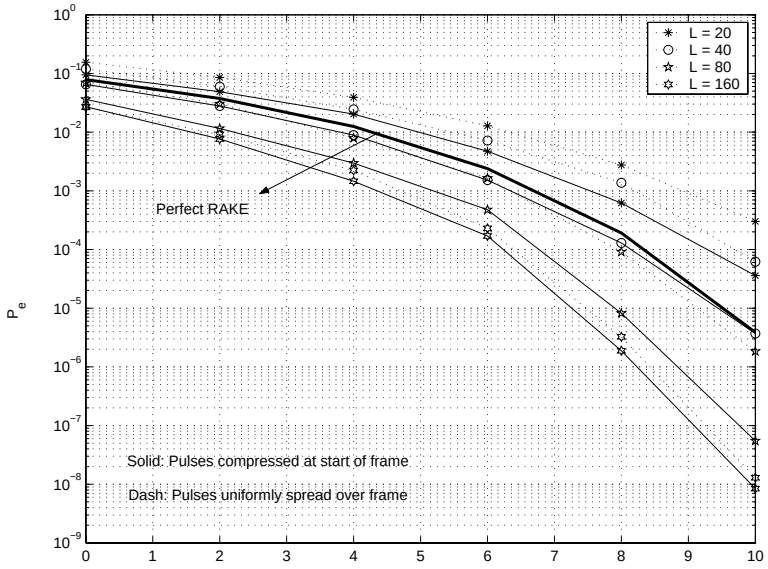

Figure 4.19: Performance with reduced-length sub-optimal sequences.

consider using sequence lengths greater than $1 + \lceil \frac{T_c}{T_p} \rceil$. It is seen in Figure 4.20 that increasing the sequence length only leads to marginal improvements in performance. Also to be noted is the fact that increasing the sequence length necessitates an increased guard interval between successive symbol transmissions.

Sequence optimization is next compared to time-reversal. The same channel estimation method (where one channel coefficient is estimated every one transmit pulse duration) is applied to both methods. A single tap is first used for time-reversal. Performance is averaged over multiple channel realizations for different training loads and results are plotted in Figure 4.21. Notice that the time-reversal error probability does not improve with increasing training length, whereas sequence optimization does considerably. A channel estimation resolution of one pulse width does not faithfully approximate the real channel behavior, which results in unacceptably low energy capture for time-reversal[‡]. Figure 4.22 presents the performance of time-reversal when lower channel estimation resolution is used and infinite training is assumed. Notice that the performance lower bound (BPSK in AWGN) is approached for a resolution of $\frac{T_w}{4}$, beyond which only negligible improvement is observed. Performance of time-reversal with 10 taps for different resolutions is shown in Figure 4.23. Notice the same pattern in probability of error improvement as the resolution

[‡]Notice that we would obtain similarly unacceptable performance for a Rake receiver employing the same channel estimation resolution (*i.e.* generating channel metrics every transmit pulse width and then selecting the F strongest metrics). Sub-pulse resolutions are required for adequate performance. This is also the case for time-reversal.

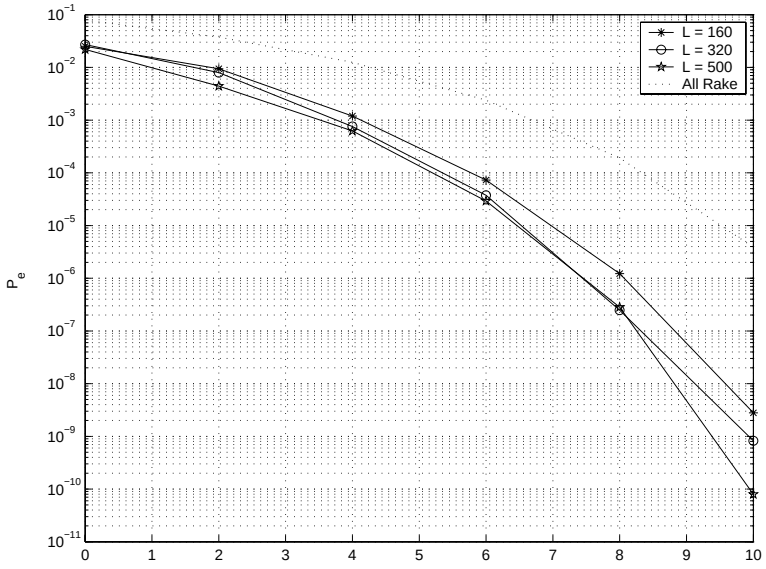

Figure 4.20: Performance with increased-length sequences.

decreases. Also, note that a 10-tap time-reversal with a resolution of $\frac{T_w}{8}$ still performs worse than sequence optimization with a resolution of only T_w. The performance of 1-tap time-reversal for different resolutions and $N_p = 200$ is shown in Figure 4.24. Results are similar but slightly worse than the ones in Figure 4.22 because of the error ensuing from finite training.

Performance of a time-reversal scheme using a channel estimation resolution of $\frac{T_w}{8}$ and 50 taps is compared to sequence optimization with a resolution T_w in Figure 4.25. Notice that the probability of error of the time-reversal receiver approaches that of the sequence optimization receiver and outperforms it at high SNR. However, note that this comes at the expense of a channel estimation process which is 8 times more complex. Moreover, the estimation of the position of the 50 strongest taps in the received signal[§] also increases complexity.

Performance of Pre-Rake combining is displayed in Figures 4.26, 4.27, and 4.28 for 1, 10 and 50 taps respectively, and a varying number of fingers F (F is the number of multipath components used to pre-code the transmit pulse shape). Notice that the probability of error decreases with increasing number of fingers and taps, because of the enhanced energy capture at the receiver. Also note that for a sufficient high number of taps and fingers, time-reversal can outperform the proposed sequence optimization method (time-reversal

[§]The complexity of this operation is equivalent to channel estimation for a Rake receiver employing MRC and 50 fingers.

with 100 fingers with 20 taps for example, or with 50 fingers and 50 taps).

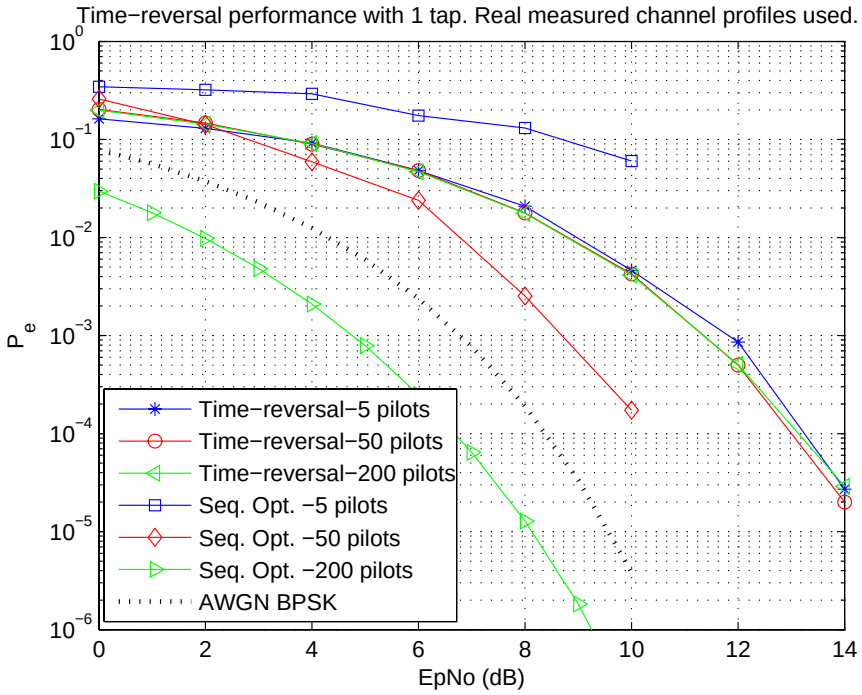

Figure 4.21: Time-reversal versus sequence optimization. Estimation resolution=T_w. $N_p = 5$, 50, 200.

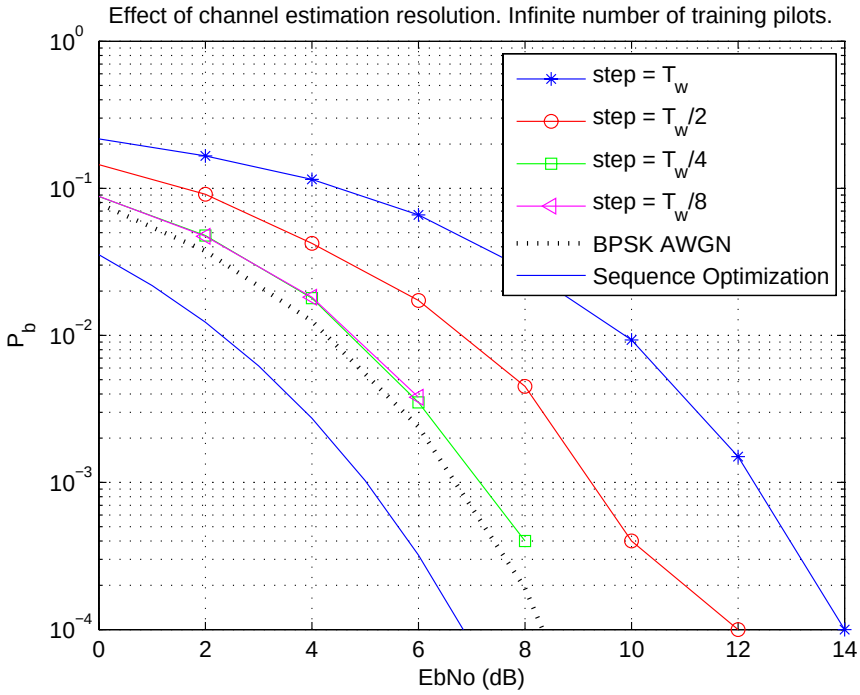

Figure 4.22: Effect of channel estimation resolution on time-reversal performance. 1 tap. Infinite training.

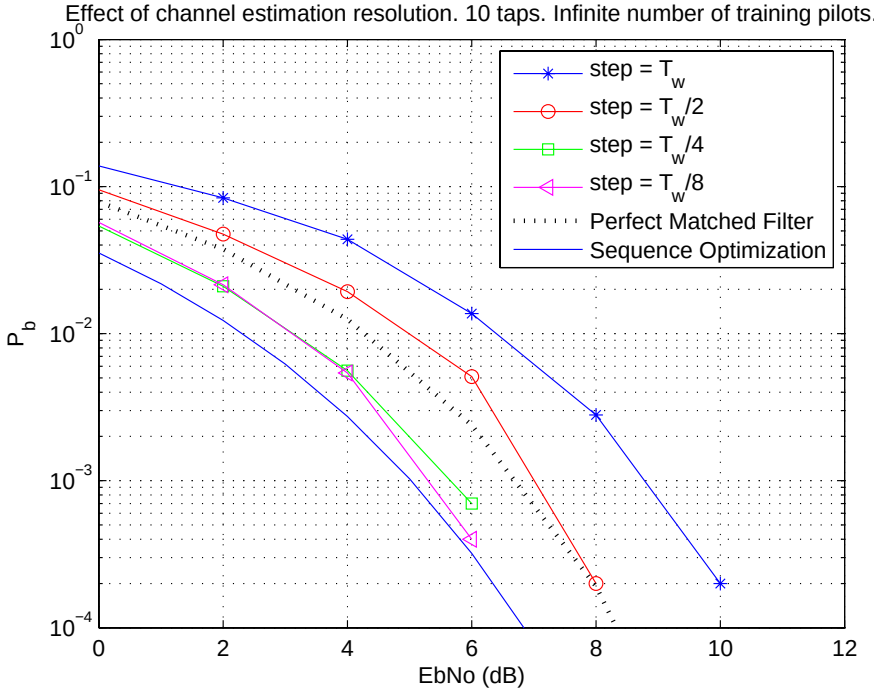

Figure 4.23: Effect of channel estimation resolution on time-reversal performance. 10 taps. Infinite training.

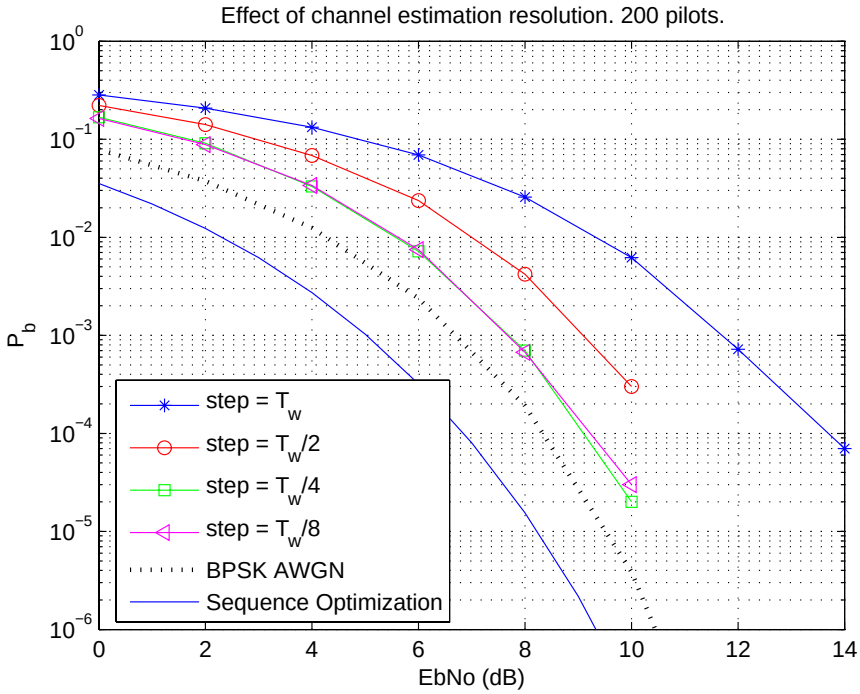

Figure 4.24: Effect of channel estimation resolution on time-reversal performance. 1 tap. $N_p = 200$.

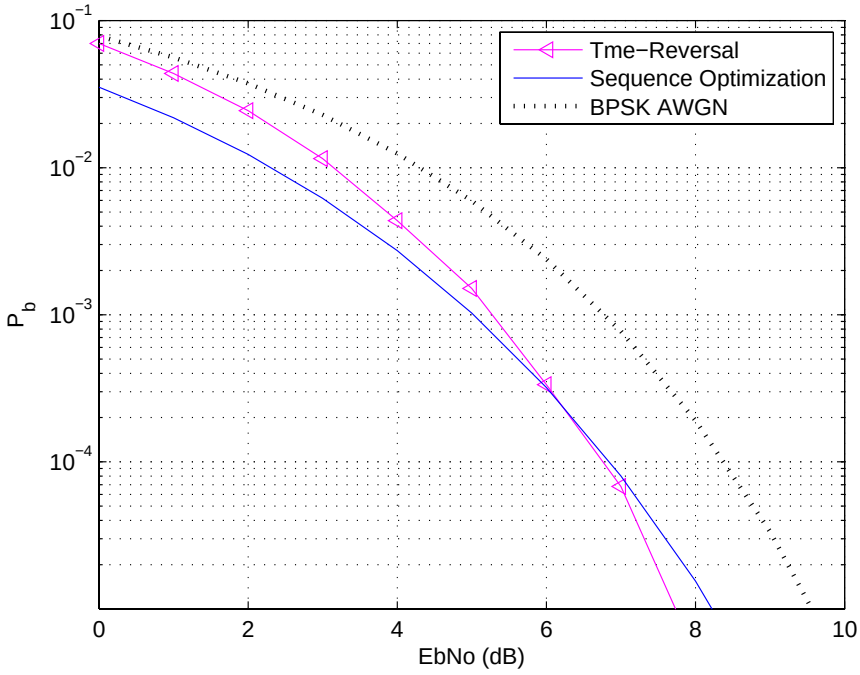

Figure 4.25: Time-Reversal versus sequence optimization. Channel resolution for time-reversal receiver is $\frac{T_w}{8}$. 50 taps. $N_p = 200$.

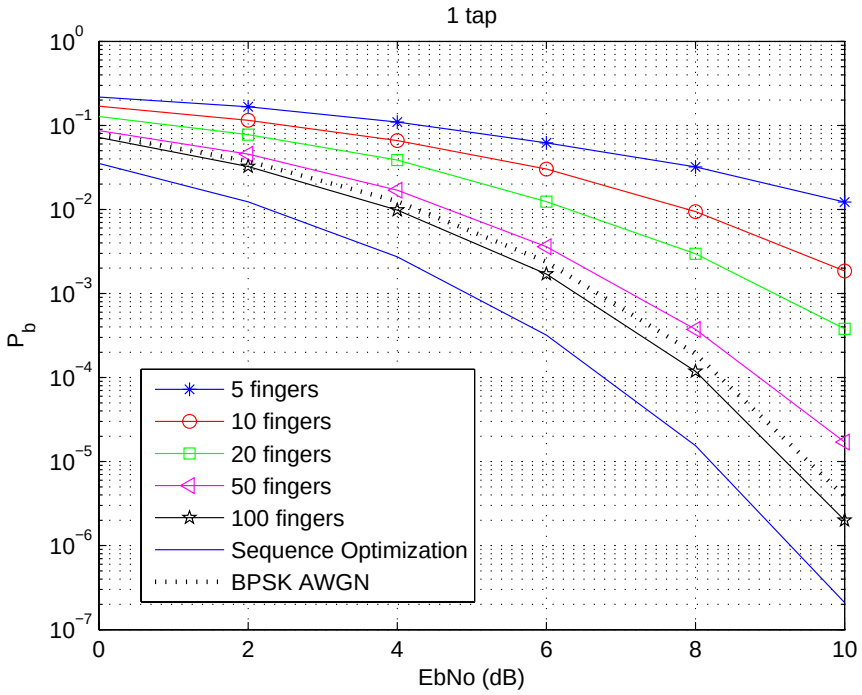

Figure 4.26: Time-Reversal versus sequence optimization. 1-tap receiver. Infinite training.

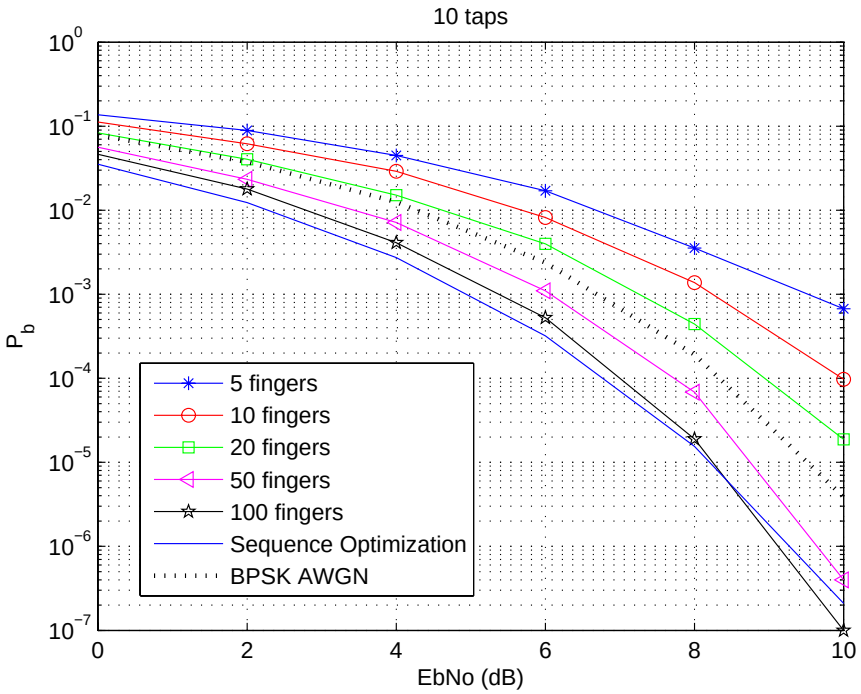

Figure 4.27: Time-Reversal versus sequence optimization. 10-tap receiver. Infinite training.

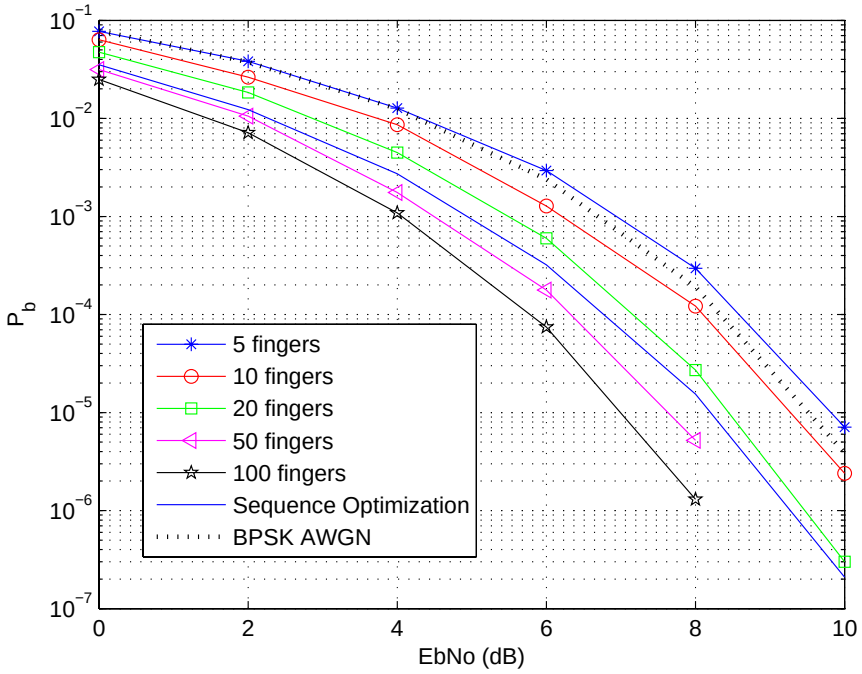

Figure 4.28: Time-Reversal versus sequence optimization. 50-tap receiver. Infinite training.

The performance of the optimization process for multiple users is illustrated in Figure 4.29. A load of 160 equal-power users using 160-length transmit sequences (obtained based on the single user optimization procedure) is assumed. The single-user optimization procedure fails, because performance is dominated by the high cross-correlation between the desired users and some other users channels. The process optimized for multiple users (Section 3) effectively mitigates interference. Performance is close to that of a single-user system with a perfect all-Rake receiver. The proposed system also outperforms a CDMA-like scheme where each user is assigned a length-160 random spreading sequence. Note that the latter system increases the effective symbol length by a factor of 160, whereas the proposed system does not require such an overhead. Performance in the presence of NBI with data modulation, $B = 5$, and whose received power is 100 dB above that of the UWB user, is shown in Figure 4.30. NBI is effectively avoided, and the performance of the system is similar to that of the single user system with no interference in Figure 4.15.

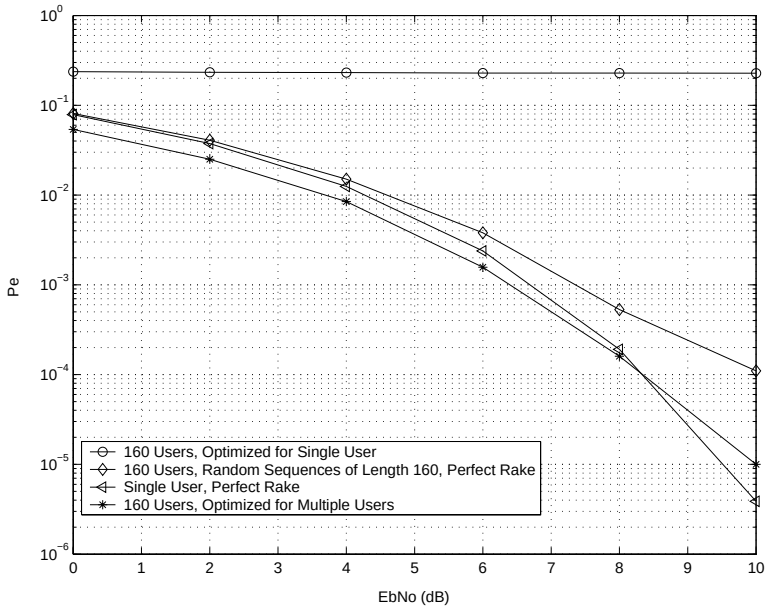

Figure 4.29: Performance of sequence adaptation optimized for multiple-users. 160 equal-power users. Performance is averaged over multiple NLOS measured channel profiles.

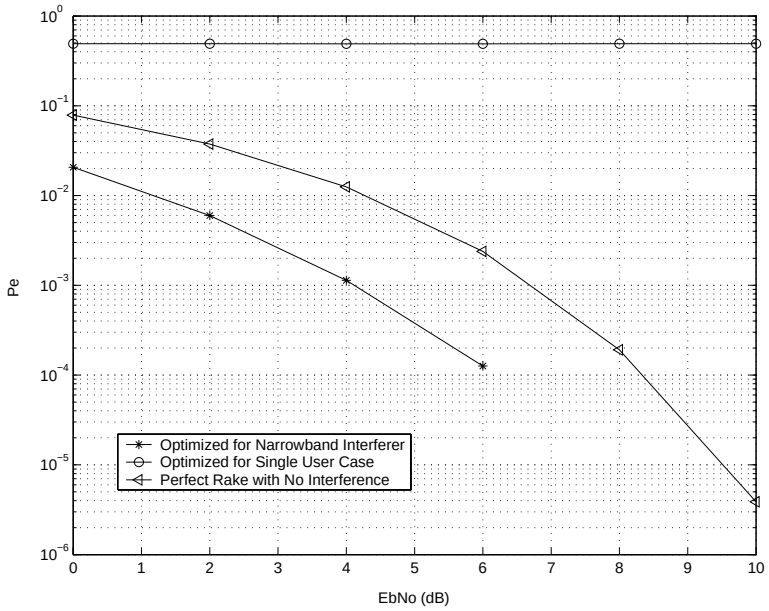

Figure 4.30: Performance of sequence optimization in presence of narrowband interferer. Interferer power is 100 dB above signal power. Performance is averaged over multiple NLOS measured channel profiles.

4.6 Complexity Analysis

The previous sections of this chapter have mainly studied performance of key UWB receiver structures from a probability of error perspective. The implementation complexity of these receivers is discussed in this section. Note that a study of the hardware implementation of UWB receivers is beyond the scope of this research effort[¶]. Emphasis is rather put on the number of operations (multiply-and-add) required for channel estimation and signal detection for each receiver. The compromise between increased complexity and improved performance (in terms of probability of bit error) is also tackled.

Since the studied UWB receivers cover a relatively wide range of detection and estimation algorithms, complexity analysis calls for a unified receiver structure framework, within which comparison of implementation requirements is feasible. A generalized digital receiver structure, which encompasses all relevant signal detection algorithms, is thus presented. The receiver is shown in Figure 4.31. This receiver comprises a stored reference signal vector $\mathbf{s}$ of length L_s and a stored vector of coefficients $\mathbf{c}$ of length L_c. Vectors $\mathbf{s}$ and $\mathbf{c}$ are used to process the received signal vector $\mathbf{r}$. The decision statistic is expressed as:

$$r = \sum_{n=0}^{L_c-1} c_n \sum_{m=0}^{Ls-1} s_m r_{m+t_n} \tag{4.88}$$

where t_n is the delay (in number of samples) corresponding to c_n.

It will be shown that the decision statistics of the key studied UWB receivers may be expressed using (4.88).

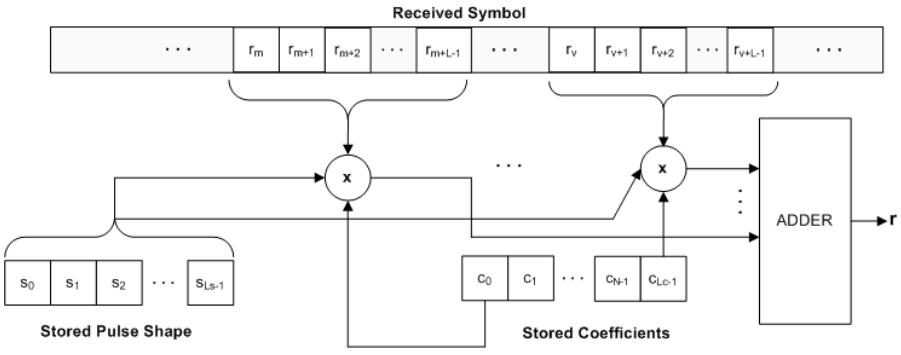

Figure 4.31: General Digital Receiver Circuit.

[¶]The reader is referred to [80] for an exhaustive discussion of hardware implementation of UWB systems

The rest of this section is organized as follows. First, the complexity of the different UWB receiver structures (Rake, time-reversal, pilot-assisted, and sequence-optimization receivers) is studied within the framework defined above. Expressions for the required number of operations for channel estimation and signal detection are derived. The compromise between increased complexity and enhanced performance is discussed and illustrated through simulations. The section is then concluded by a brief qualitative complexity comparison of the different receivers.

4.6.1 The Rake Receiver

We first discuss the implementation complexity of the general F-finger Rake receiver presented in section 3.7, where channel estimation is based on the training sequence given by (3.33).

Recall that the Rake receiver decision statistic may be written as:

$$r = \int_{T_f} r(t) \sum_f \alpha_f w(t - \tau_f) dt \tag{4.89}$$

where $r(t)$ is the received signal, T_f is the symbol duration, and α_f and τ_f are the amplitude and delay of the f^{th} finger, respectively. Simple inspection of Figure 4.31 in the context of the Rake receiver reveals that the stored reference vector $\mathbf{s}$ corresponds to the sampled version of the transmit pulse shape $w(t)$, and $L_s = T_w F_s$, where T_w is the duration of the transmit pulse, and F_s is the sampling frequency. Moreover, the stored coefficients correspond to the weights of the F fingers, and L_c is equal to F.

Recall from (3.34) that channel estimation for the Rake receiver is based on generating channel coefficients at multiple symbols delays, and then selecting the F largest coefficients. Assuming N_p pilots, the number of multiply-accumulate operations required for the computation of one channel coefficient is equal to $N_p T_w F_s$. Assuming such a coefficient is computed every δt seconds (defined as the estimation's resolution), the average number of multiply-accumulate operations required for Rake channel estimation is then equal to:

$$M_{Rake,est} = N_p \frac{T_f}{\delta t} T_w F_s. \tag{4.90}$$

As an example, let $N_p = 50$, $T_w = 1$ nsec, $T_f = 50$ nsec, $F_s = 15$ GHz and $\delta t = 0.2$ nsec. Then, $M_{Rake,est} = 187,500$.

Note that in addition to the multiply-accumulate operations, at least F *find-max* and *memory read-write* operations are required to select and store the F strongest components.

Signal detection for the Rake receiver is equivalent to applying F correlations with the transmit pulse used as template at F different delays. Since each correlation requires $T_w F_s$ operations, the total number of multiply-add operations per data frame is then:

$$M_{Rake,detect} = N_d F T_w F_s \tag{4.91}$$

where N_d is the number of information bits per frame. For example, if $N_d = 500$ and $F = 20$, we get $M_{Rake,detect} = 150,000$.

The probability of error and complexity (in number of required operations) are plotted versus N_p and F in Figure 4.32. The system parameters are $F_s = 8$ GHz, $T_w = 500$ psec, δt =125 psec, $N_d = 5000$ and $\frac{Eb}{No} = 7$ dB. First, note that the probability of error for a fixed number of fingers reaches a floor for a relatively low number of training symbols, beyond which any increase in N_p only causes detrimental increased complexity. Little improvement is also eventually seen beyond 40 fingers, and only negligible additional energy is harnessed by increasing F, at the expense of a more taxing signal detection process.

In order to assess the system operating point at which the best performance/complexity balance is achieved, a joint metric reflecting both complexity and error probability must be devised. In this work, the metric is simply set to:

$$m = \frac{P_e}{\bar{P}_e} \frac{Comp}{\bar{Comp}} \tag{4.92}$$

where *comp* is the system complexity (in number of operations), P_e is the probability of error, and $\bar{comp}$ and $\bar{P}_e$ are the average complexity and probability of error, computed over all parameter realizations, respectively. Note that a small metric is desired. The joint metric is plotted versus system parameters N_p and F in Figure 4.33. Notice that for low F and large N_p, the metric m is largest, since system resources are wasted on channel estimation, and performance is limited by a small energy capture which does not improve with

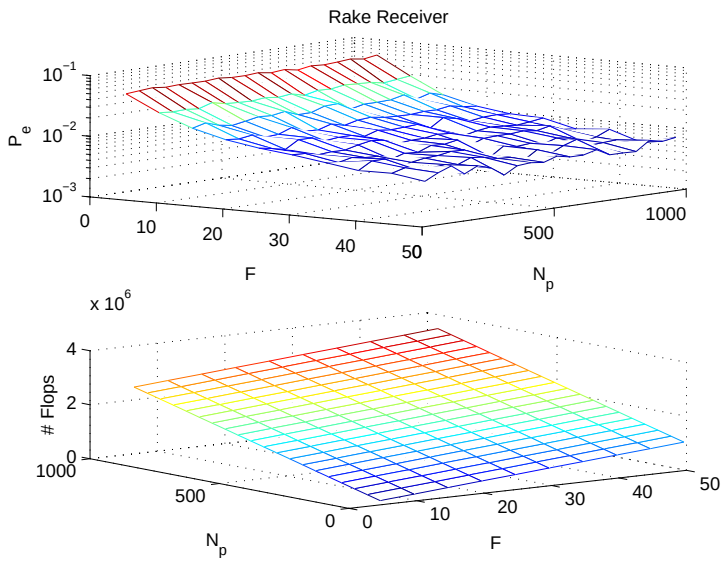

Figure 4.32: Complexity and probability of error versus system parameters N_p and F. Rake receiver. $F_s = 8$ GHz, $T_w = 500$ psec, δt =125 psec, $N_d = 5000$, $\frac{Eb}{No} = 7$ dB.

increased training. Also, m improves with decreasing N_p for all values of F, which suggests that a relatively light training load is required to render channel estimation errors negligible. Finally, notice that m decreases substantially with increasing number of fingers for the range $F < 40$. Beyond 40 fingers, increased energy capture is offset by added signal detection complexity, and the joint metric reaches a floor.

It is important to note that the above complexity analysis does not encompass the critical issue of synchronization for Rake receivers. In fact, synchronization for a Rake receiver with tens of fingers is a daunting task. Synchronization management of the different fingers is highly problematic. Initial synchronization of each finger to a particular multipath component is required. Due to time jitter and slow changes in the channel, subsequent tracking is required as well, where each finger must continuously adapt to the drifting of the multipath component to which it is assigned. Moreover, due to timing errors, two fingers might lock to the same multipath component, which affects time diversity. Some sort of super-structure, or finger management unit, is therefore needed to organize the way fingers search for paths. If the number of fingers is large, these requirements become too stringent. Fingers locked to low-power specular components will especially prove challenging to maintain, since they might operate at very low SNR (a very reasonable assumption for UWB in dense multipath). The energy capture gains will then be negated by the increasing parameter estimation error, as suggested in [81] and [82].

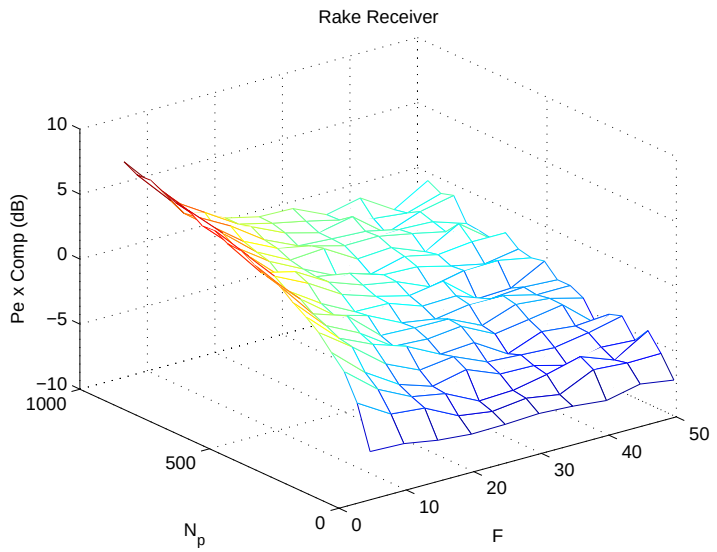

Figure 4.33: *comp* $\times P_e$ versus system parameters N_p and F. Rake receiver. Parameters are same as those in Figure 4.32.

4.6.2 Time-Reversal and Pre-Rake Combining

The complexity of time-reversal and Pre-Rake combining is now discussed. Multiple received taps are assumed for both receivers. Similar to the Rake receiver, by examining Figure 4.31, it is easy to show that the vector $\mathbf{s}$ stores the transmit pulse shape ($L_s = T_w F_s$), and $\mathbf{c}$ holds the tap coefficients (L_c is equal to the number of taps used).

Recall that multi-tap time-reversal requires channel estimation both at the transmitter and receiver. The channel is estimated at the transmitter in order to set the transmit pulse shape. The delays and multiplicative coefficients of the taps then have to be estimated at the receiver. Both estimation processes are similar to the one used for the Rake receiver and are based on the computation of a channel metric every δt seconds, where δt depends on the estimation's resolution. Let N_{p1} and N_{p2} be the number of training symbols used for the transmit and receiver channel estimation, respectively. Also let δt_1 and δt_2 be the resolutions used for the estimation stages[‖]. Then, the overall number of operations required for channel estimation may be expressed as:

$$M_{TRev,est} = N_{p1}\frac{T_f}{\delta t_1}T_w F_s + N_{p2}\frac{T_f}{\delta t_2}T_w F_s. \tag{4.93}$$

[‖]Equivalently, it is possible that both estimation stages are performed at the transmitter (with the same resolution). The tap metrics then have to be fed to the receiver.

The number of operations required for signal detection of one data frame is:

$$M_{TRev,detect} = N_d L_c T_w F_s. \tag{4.94}$$

Note that the analysis also holds for pre-Rake combining.

The system parameters δt_2 and L_c are varied and the corresponding probability of error and complexity are evaluated and plotted in Figure 4.34. As δt_2 decreases, the estimated channel coefficients approximate the multipath channel more faithfully, and more signal energy is available at the receiver, leading to a lower P_e. This comes at the expense of more complex channel estimation, since more channel coefficients are computed. The same observations hold when increasing the number of receiver taps L_c. Note however that P_e reaches a floor after a few dozen taps beyond which any additional taps would only yield marginal extra energy capture and necessary additional channel estimation and signal detection operations.

The joint metric m is shown in Figure 4.35. Notice that m is the largest (or worst) for high δt_2 and low L_c

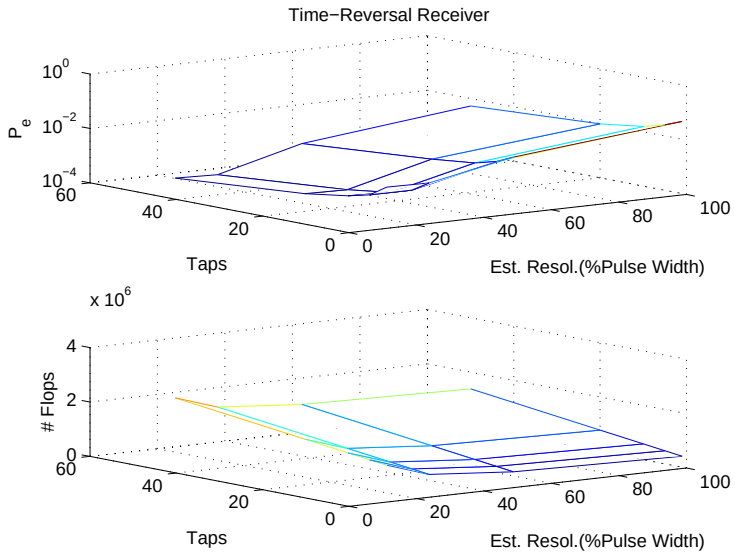

Figure 4.34: Complexity and probability of error versus system parameters δt_2 and L_c. Time-Reversal. $F_s = 8$ GHz, $T_w = 500$ psec, T_f =80 nsec, $N_d = 5000$, $\frac{E_b}{N_o} = 7$ dB., Np_1=200, N_{p2}=100.

due to the unacceptably high probability of error in that region. m decreases as the estimation resolution and number of taps increases. Notice that decreasing resolution from $\frac{T_w}{4}$ to $\frac{T_w}{8}$ leads to higher m, because the marginal drop in P_e is nullified by the more substantial increase in complexity.

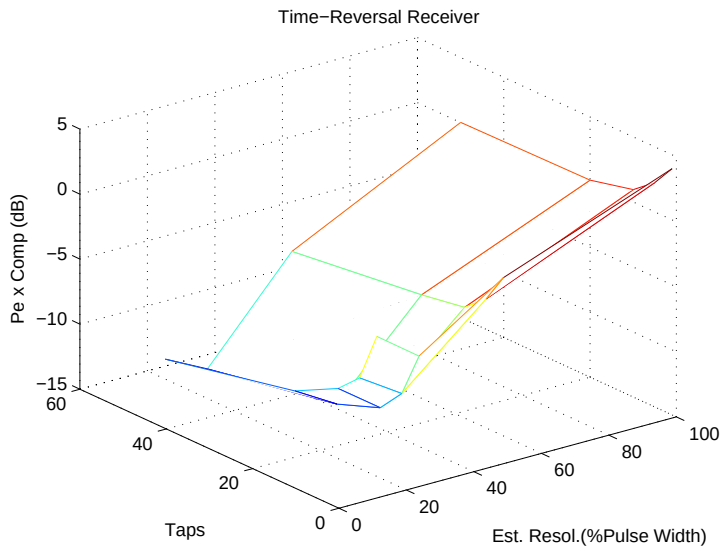

Figure 4.35: *comp* $\times P_e$ versus system parameters δt_2 and L_c. Time-Reversal. Parameters are same as those in Figure 4.34.

4.6.3 The Pilot-Assisted Receiver

Consider the pilot-assisted receiver discussed in section 3.8. We restrict complexity analysis to the simple pilot-assisted receiver, where the correlation template is obtained by averaging N_p training symbols. Then, in the context of the general digital receiver in Figure 4.31, vector $\mathbf{s}$ is set to the received pulse shape, and $L_s = T_f F_s$. Note that the stored reference is much longer than the ones used for the other receivers, since signal detection is based on the received pulse shape rather than the transmit pulse shape. The coefficient vector $\mathbf{c}$ is redundant for the pilot-assisted receiver and need not be stored.

Recall that no explicit channel estimation is required for the pilot-assisted receiver, and the template is rather obtained by simple averaging. Assuming the template length is T seconds ($T \leq T_f$), the number of operations required to generate the template is approximated by:

$$M_{PA,est} = N_p T F_s. \tag{4.95}$$

For example, let $N_p = 250$, $T = 60$ nsec and $F_s = 15$ GHz. Then, $M_{PA,est} = 225,000$.

The decision statistic is generated by directly multiplying the stored reference by the received signal (vector $\mathbf{c}$ is all-ones). Then, the number of multiply-accumulate operations for signal detection over a frame of N_d

bits is:

$$M_{PA,detect} = N_d T F_s. \tag{4.96}$$

As an example, for $N_d = 500$, $M_{PA,detect} = 450,000$.

The probability of error and complexity versus N_p and T (as a fraction of T_f) are plotted in Figure 4.36. Notice that P_e decreases with increasing T due to enhanced energy capture (as seen in section 3.8). If T is increased beyond about half of T_f, negligible additional energy is captured, and considerable increased complexity does not yield any performance improvement (performance in fact slightly deteriorates because further noise is included in the template). Also, P_e only reaches a floor beyond a few hundred pilot symbols. The joint complexity/error probability metric is displayed in Figure 4.37. As expected, the worst system

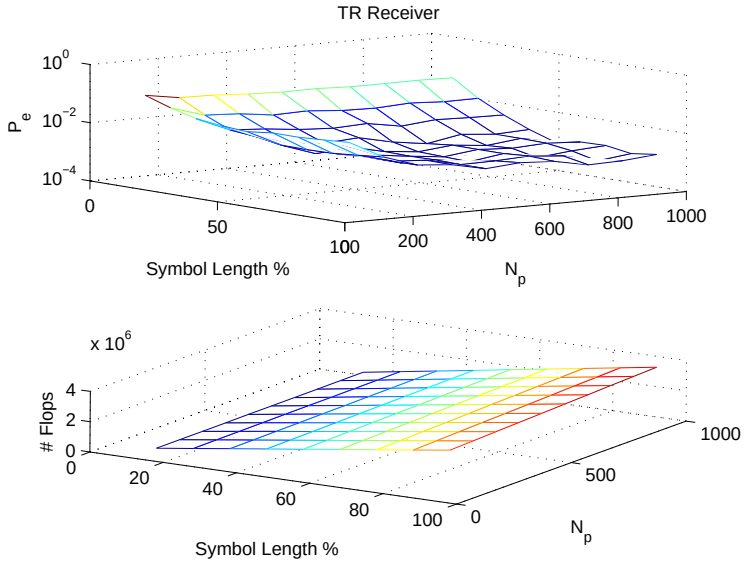

Figure 4.36: Complexity and probability of error versus system parameters N_p and T. Pilot-assisted receiver. $F_s =$ 8 GHz, $T_w = 500$ psec, $T_f =$80 nsec, $N_d = 5000$, $\frac{E_b}{N_o} = 7$ dB.

operating points occur at very low values of T coupled with high N_p, since complex channel estimation is nullified by extremely low energy capture. Moreover, at low training ($N_p < 300$), the noise power in the dirty template overwhelms performance regardless of energy capture. The optimal operating point is achieved for relatively high training and long enough integration time. The concave shape is caused by the slight increase of P_e at extremely high T.

Note that the main complexity burden for sophisticated TR systems (where multiple unmodulated signals

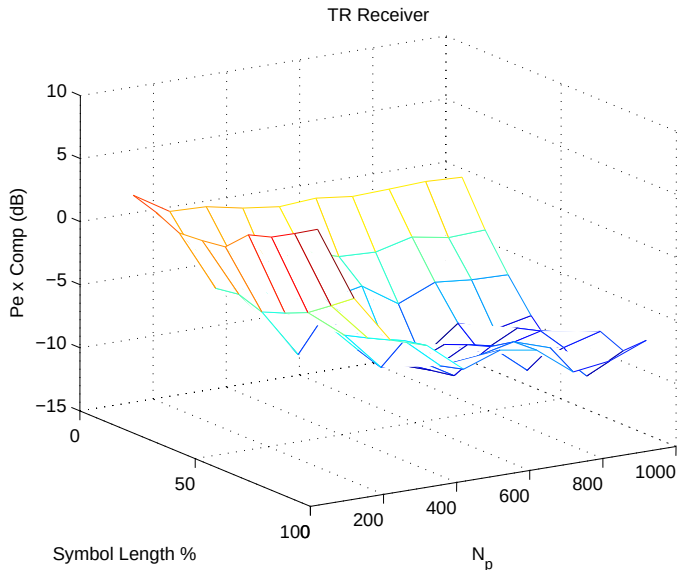

Figure 4.37: *comp* $\times P_e$ versus system parameters N_p and T. Pilot-assisted receiver. Parameters are same as those in Figure 4.36.

are averaged to produce a cleaner template) is the required storage of a potentially long signal**. In this research, simulation results were obtained based on a stored template composed of 6400 real numbers. Storing and processing this large real sequence may result in a highly power-hungry device, with heavy memory requirements.

4.6.4 Sequence Optimization Receiver

Recall that the computation of the transmit sequence X and template sequence Y for the sequence optimization†† receiver require estimation of the channel matrix H. The channel estimation procedure is mathematically defined by (4.64), where a channel coefficient is computed every T_w seconds. Assuming N_p training symbols, the corresponding number of operations may be expressed as:

$$M_{SO,est} = N_p N_x T_w F_s + M_{eig}. \tag{4.97}$$

**The same problem applies for the proposed data-aided pilot-assisted system.

††Here, considering the general structure from Figure 4.31, $\mathbf{s}$ corresponds to $w(t)$, and $\mathbf{c}$ is set to the template sequence Y.

where M_{eig} represents the overhead due to the eigenvector computation performed on H.

The complexity of the signal detection stage is found to be:

$$M_{SO,detect} = N_d N_y T_w \tag{4.98}$$

where N_y is the length of vector Y.

The transmit sequence length and training load are varied, and the probability of error and complexity are evaluated and shown in Figure 4.38. The joint metric is shown in Figure 4.39. Notice the complexity increase and performance improvement as N_x and N_p grow. A performance floor is reached, beyond which adding training or increasing the sequence length is only detrimental to the overall system.

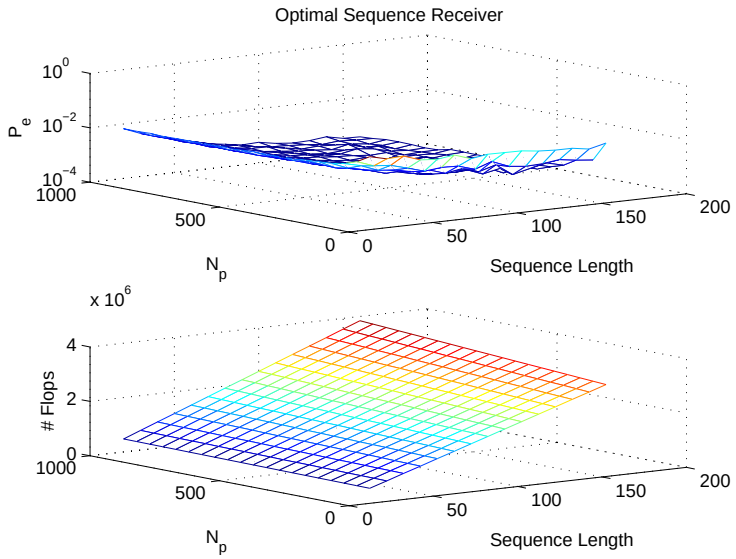

Figure 4.38: Complexity and probability of error versus system parameters N_p and N_x. Sequence-optimization receiver. $F_s = 8$ GHz, $T_w = 500$ psec, T_f =80 nsec, $N_d = 5000$, N_y =160, $\frac{E_b}{N_o} = 7$ dB.

4.6.5 Complexity Comparison

When considering the four main receiver structures studied in this section, selection of the most suitable receiver is not a straightforward task. In fact, the receiver which presents the best compromise between design complexity and probability of error performance depends on widely varying system characteristics and requirements, such as target BER, available power, and allowed circuit complexity.

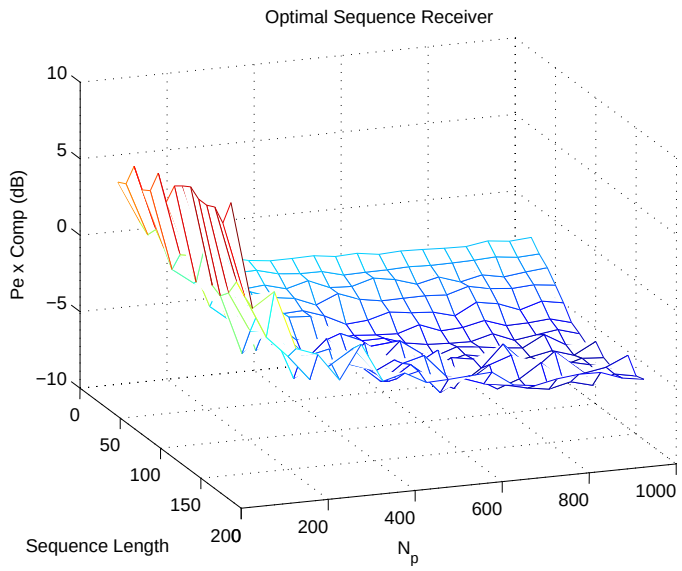

Figure 4.39: *comp* $\times P_e$ versus system parameters N_p and N_x. Sequence-optimization receiver. Parameters are same as those in Figure 4.38.

Since UWB systems are subject to stringent FCC power restrictions, receiver structures which guarantee satisfactory probability of error at relatively low signal-to-noise ratios are required. The shortcomings of traditional pilot-assisted and Rake receivers have been studied in this chapter, with emphasis on their inefficiency in dense multipath at low transmit power level. In addition to its ineffectiveness from a probability of error point of view, the pilot-assisted receiver presents a large memory and power requirement burden caused by the need to store a relatively very long template. Channel estimation is more complex for Rake receivers compared to their pilot-assisted counterparts, because of the need of generating channel coefficients at sub-pulse intervals. The management of a large number of fingers (required for adequate energy capture) is another serious design challenge.

More sophisticated receivers such as sequence optimization and time-reversal allow for higher energy capture (and consequently better probability of error) by more efficiently exploiting the available multipath structure (in fact both methods can potentially outperform the performance lower bound for Rake and pilot-assisted receivers by coherently combining multipath components). This comes at the expense of a generally more complex implementation and more stringent computational requirements.

Although both systems alleviate receiver design by shifting complexity to the transmitter, they require receiver feedback capability and thus introduce an additional design burden. Channel estimation for multi-

tap time-reversal is more complex than for sequence optimization, since two separate estimation operations (for setting the transmit filter and evaluating the receiver's taps) are required[‡‡]. Moreover, both estimation stages require sub-pulse resolutions to guarantee adequate performance, whereas sequence optimization was shown to yield satisfactory results at a resolution of one transmit pulse width. Signal detection is more complex for sequence optimization in general, because the sequence optimization template is based on a relatively long sequence (a sequence of length 160 is used in the simulation results of this chapter) compared to the number of taps used for time-reversal. This difference in complexity is however offset by the burden of management of the time-reversal taps (similar to finger management in a Rake receiver). Moreover, as was shown in section 4.5, the transmit sequence may be potentially shortened while maintaining acceptable performance, and a similar simplifying procedure may potentially be applied to the receiver template.

4.7 Conclusions

This chapter presents two new UWB signal detection algorithms which circumvent the limitations of Rake and TR receivers.

A modified system which solves the noise-cross-noise problem in TR receivers is proposed. The system reduces the training overhead by incorporating the modulated data symbols into an iterative channel estimation process. FEC is provided to achieve a good iterative starting point. It is shown that the proposed model outperforms both Rake and TR receivers, while substantially reducing the training overhead.

A proposed system based on sequence optimization solves the problem of limited energy capture in Rake receivers by more fully taking advantage of the multipath structure, and forcing the coherent addition, or "constructive interference" of the multipath components at the receiver output. The proposed system achieves very high energy capture, with a low training overhead. The effectiveness of the model is also displayed for multi-user and NBI scenarios.

[‡‡]Both channel time-reversal estimation stages may be bundled into one estimation stage performed at the transmitter. Nonetheless, that stage would still require a finer resolution than sequence optimization, and would thus be more complex.

Chapter 5

UWB Synchronization in Dense Multipath

5.1 Introduction and Motivation

In a typical wireless communication system, the receiver does not have *a priori* information about the arrival instant of the incoming signal. Prior to demodulation, the receiver must first sense the environment, and recognize the presence of an information signal. Since classical demodulation is highly dependent on the sampling instant, the receiver must accurately align any stored reference or template with the received modulated signals.

Synchronization is the process of aligning the incoming waveform with a reference signal. The reference signal might be a pulse shape or a spreading sequence in a SS system, for example. Synchronization misalignment potentially results in catastrophic performance. For example, in a typical SS system, if the spreading sequence used in demodulation is misaligned by more than a chip length from the received spreading sequence, the output receiver SNR is reduced by a factor equal to the spreading gain, due to the autocorrelation properties of the sequence.

The synchronization process is usually divided into two phases: First, the acquisition phase achieves coarse synchronization. Then, the tracking stage refines the timing estimation and achieves synchronization.

Acquisition usually occurs once during initial synchronization and gives a starting point for tracking. Tracking is an ongoing process that continuously ensures correct synchronization [61][85][86].

Acquisition and tracking for indoor UWB systems are discussed in this chapter. The specific synchronization challenges posed by UWB in dense multipath are investigated, and then solutions are proposed. Since acquisition is the stage which has generated the most interest and drawn most of the UWB synchronization research effort, emphasis is given to coarse synchronization. The application of fine synchronization to UWB is treated at the end of the chapter.

5.1.1 UWB Acquisition

The design of fast and efficient acquisition schemes is a challenging aspect of UWB. Traditional synchronization techniques used in SS systems are not suitable for UWB, mainly because they result in prohibitively long acquisition times. In fact, due to the use of extremely short, low duty cycle UWB pulses, the delay uncertainty region contains a huge number of potential timing offsets, or cells, compared to narrowband systems. Designing efficient search algorithms that efficiently process those cells has been the main focus of research in UWB acquisition to date.

In addition to the long acquisition time, the problem of UWB synchronization is further complicated in indoor dense multipath channels, where energy dispersion makes it hard to generate reliable decision metrics. Moreover, whereas traditional acquisition strategies for SS systems assume that there is a single correct cell (termed an H_1 cell [61][87]) within the uncertainty region which represents the correct signal delay, this assumption does not hold for UWB in multipath, because of the large number of resolvable paths. Instead, there will be a group of H_1 cells corresponding to the different multipath delays which can terminate the acquisition process. Previous work on indoor UWB acquisition assumes that synchronization is successful if any H_1 cell is selected. However, locking to an arbitrary multipath component may lead to unacceptable performance (large ranging error in position location applications, and large symbol energy loss for communication applications, for example). Figure 5.1 illustrates this problem for a typical indoor multipath channel profile. Correct ranging estimation based on time-of-arrival [88] is achieved by choosing, or locking to the LOS path (the first arriving path). In this particular example, an arbitrary multipath component which is

about 30 nsec away from LOS is selected. Since light travels at an approximate speed of 1 foot/nsec, this timing error translates into a ranging error of approximately 30 feet, which is unacceptable for most indoor position location applications.

The main challenge for UWB coarse synchronization in dense multipath is therefore to design acquisition

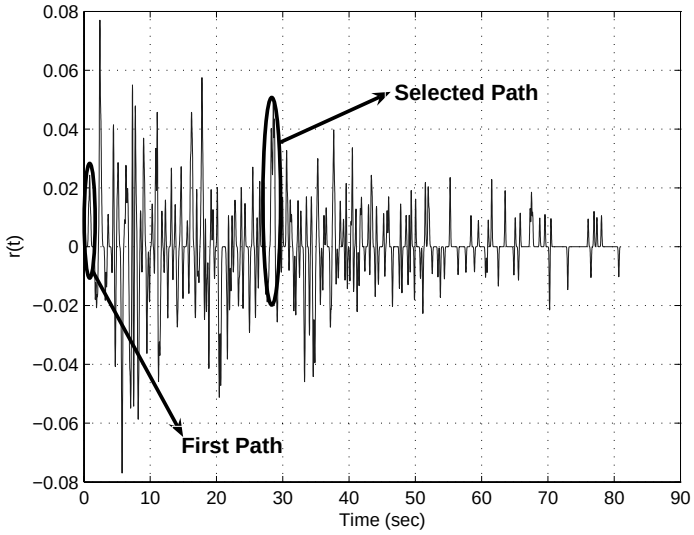

Figure 5.1: Typical acquisition scenario for UWB in dense multipath. The selected multipath component is about 30 nsec away from the LOS component.

algorithms that are able to accurately detect the first arriving multipath, while minimizing the acquisition time. One such algorithm is presented in this chapter. Specifically, a two-stage acquisition technique is proposed (Figure 5.2), where the first stage termed *coarse acquisition* simply finds any of the many multipath components (i.e., simply achieves rough symbol/code synchronization). The main requirement for this stage is that it must detect a multipath as fast as possible. In the proposed implementation, the first stage is a fast version of traditional serial threshold comparison test. Our proposed scheme is termed *jump-phase* search, where the search time is drastically reduced by performing a non-consecutive search, where the order in which cells are tested is set such that the H_1 cells are uniformly spread over the uncertainty region. The procedure does not add any significant complexity to the circuit compared to serial search, and knowledge of the number of multipath components is not needed. Although this stage might not necessarily lock to the desired path, it allows the uncertainty region (in which the desired path exists) to be reduced considerably.

The second stage, termed *fine acquisition*, searches for the first arriving path in the reduced uncertainty region. The second stage takes advantage of a robust estimate of the noise variance, obtained from the first stage, to calculate a new, more reliable threshold. Moreover, it exploits the clustered nature of the multipath to better segregate H_0 cells (cells corresponding to incorrect delays) from H_1 cells, and more reliably detect the start of the signal, even when the LOS path is severely attenuated.

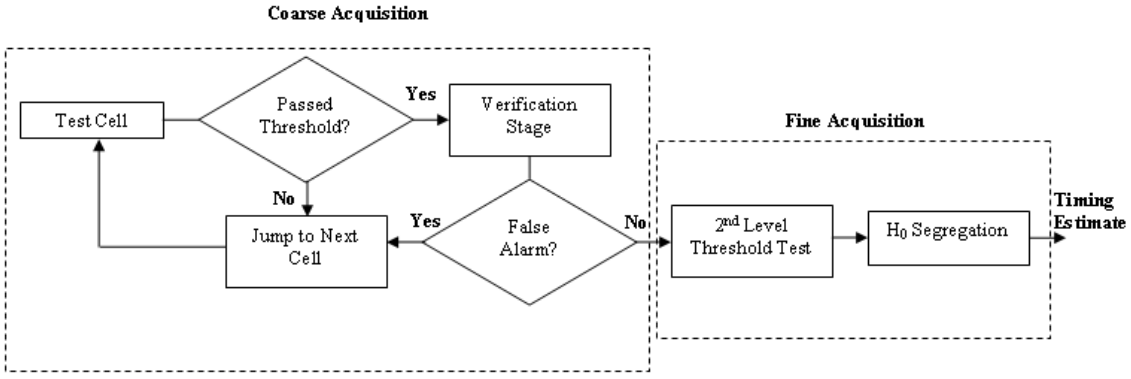

Figure 5.2: General two-stage acquisition model.

5.1.2 UWB Tracking

Research in UWB synchronization has mainly concentrated on the acquisition process. Tracking for UWB signals has received relatively little research interest, and is usually based on the application of traditional SS tracking methods [61].

In order for traditional tracking schemes to work properly, acquisition must give a reasonably good coarse estimate of the timing delay (within a fraction of a chip duration for SS systems). This assumption is suitable for a UWB Rake receiver, where a separate tracking circuit is assigned to each Rake finger, and acquisition provides a good estimate of the delay of the multipath component corresponding to each finger. However, the assumption is highly problematic for UWB pilot-based receivers in dense multipath, where the objective of synchronization is to detect the LOS component. In fact, since the UWB received energy is spread over tens or even hundreds of multipath elements, there will exist a group of delays corresponding to the different multipath components which can terminate the acquisition process. The LOS path might be

severely attenuated and need not be the strongest available path. Detection of the LOS component is thus not guaranteed. Moreover, as we have already noted, most UWB acquisition techniques assume that acquisition is successful if *any* of the available multipath components are detected, rather than the LOS component (see [98] or [101] for example). The detected multipath might be tens of nanoseconds away from the start of the signal due to the large channel delay spread. In this case, a traditional tracking algorithm would lock on that selected multipath, and would fail in correcting the large delay error, resulting in significant energy loss, and thus unacceptable performance degradation.

The main limitation of standard tracking techniques applied to UWB in dense multipath is that they are based on the correlation of the received signal with a local stored reference matched to the *transmit* pulse shape. Such circuits do not take advantage of the *received* pulse shape, and are thus unsuitable for correcting delay errors which are large compared to the transmit pulse duration. Thus, there is a need for modified fine synchronization algorithms which converge to the LOS component even when they are fed a large delay error by the acquisition stage.

A modified tracking algorithm for pilot-assisted receivers is proposed in this chapter. It is assumed that initial acquisition potentially results in the detection of an arbitrary multipath component, thus leading to a timing error much larger than the transmit pulse duration. The tracking method is based on a modified early-late gate approach [61], where the correlator uses an estimated template of the received pulse shape rather than the transmit pulse shape, thus enabling much higher energy capture during tracking. The symbol intervals preceding and succeeding the estimated delay are processed in order to measure their energy content. The symbol delay is then corrected based on the difference in energy in the two intervals. The method does not require any additional training overhead, and the algorithm is deployed iteratively, where the receiver's correlation template is re-evaluated after delay correction, and data bits are re-estimated using this new template, leading to significantly improved performance.

5.2 List of Contributions and Publications

The main contributions of this chapter are:

- A mathematical formulation for a general indoor UWB acquisition model, where the effect of dense multipath and the existence of multiple H_1 cells (which is usually neglected in the literature) is explicitly included.

- A derivation for the mean acquisition time for serial search in dense multipath (with the existence of multiple H_1 cells), using a super-cell approach.

- A new two-stage acquisition approach, which combines fast acquisition time and robust timing estimate in dense multipath, even when the LOS component is severely attenuated.

- A new coarse acquisition search pattern, termed "jump-phase" search, where mean acquisition time is drastically reduced by uniformly spreading H_1 cells over the uncertainty region.

- A new fine acquisition stage, which robustly detects the LOS component, by taking advantage of the clustered nature of the multipath components.

- A case study of the effect of timing error on the performance of a generalized TR system.

- A new tracking algorithm for generalized UWB pilot-assisted receivers, which can correct timing errors much larger than the transmit pulse duration.

- A statistical analysis of an iterative version of the tracking method, where the pilot-assisted receiver's correlation template is iteratively re-evaluated after delay correction, and data bits are re-estimated using this new template, leading to significantly improved performance.

Relevant publications are listed below for reference:

- J. Ibrahim and R.M. Buehrer, "Two-Stage Acquisition for UWB in Dense Multipath," *IEEE Journal on Selected Areas in Communication,* vol. 24, issue 4, part I, pp. 801-807, April 2006.

- J. Ibrahim and R.M Buehrer, "A Modified Tracking Algorithm for UWB Pilot-Assisted Receivers," in *Proc. 2006 ICUWB,* September 2006.

- J. Ibrahim and R.M. Buehrer, "Two-Stage Acquisition for UWB in Dense Multipath," in *Proc. 2005 MILCOM,* pp. 1898-1904, vol.3, October 2005.

5.3 Chapter Organization

The rest of this chapter is organized as follows. Since most previous work in UWB acquisition is based on traditional SS acquisition techniques, a brief introduction to SS acquisition is included in section 5.4. Relevant previous work on UWB and SS acquisition in dense multipath is summarized in section 5.5. The general acquisition model is mathematically formulated in section 5.6. The model incorporates the existence of multiple H_1 cells into the analysis. Coarse acquisition is discussed in section 5.7. Traditional serial search is first analyzed. An expression for the mean acquisition time of serial search in the presence of multiple H_1 cells is derived, using a "super-cell" approach. Then, the proposed jump-phase search is introduced, and an expression for its mean acquisition time is derived. The section is concluded by simulation results, which show that jump-phase search speeds up mean acquisition time by about an order of magnitude as compared to serial search by uniformly spreading the H_1 cells over the uncertainty region. Although jump-phase search efficiently reduces acquisition time, it nonetheless leads to a significant timing error, because it locks into an arbitrary H_1 cell, rather than the first H_1 cell (corresponding to the LOS path)*. This timing error is mitigated by the fine acquisition stage, which is presented in section 5.8. The operation of this two-step stage is mathematically described using the IEEE P802.15 model proposed for UWB, then illustrated through numerical results. A study of the performance of the proposed two-stage acquisition scheme is tested in the context of a ranging system through simulations in section 5.9. It is shown that the introduction of the fine acquisition stage leads to a drastic reduction in range error. The expression for the probability of bit error of a pilot-assisted receiver in the presence of timing error is derived in section 5.10, then the performance improvement brought by the proposed scheme is demonstrated by simulation. Section 5.11 presents previous work on tracking for UWB and discusses the limitations of traditional tracking methods applied to UWB in dense multipath. The proposed tracking model is presented in section 5.12. The algorithm is based on the construction of "early" and "late" templates, which are used to measure the energy content in the time intervals preceding and succeeding the estimated timing delay. The delay is fixed based on a comparison of these two energy values. The iterative deployment of the algorithm is also discussed. The model is statistically and mathematically analyzed in section 5.13. The first and second-order statistics of

*Note that this is the case for all coarse acquisition methods discussed in this work

the algorithm's decision metrics are derived and used to formulate a probability of bit error for the system. Simulation results which validated the theoretical expressions and illustrate the model's performance are included in section 5.14. Finally, section 5.15 concludes this chapter.

5.4 Traditional Acquisition for SS Systems

The primary function of a SS direct-sequence receiver is to despread the received spreading code. The received signal is despread by multiplying it by a locally generated replica of the code. However, since the signal's time of arrival is generally unknown, the receiver must first estimate the timing delay, then align, or synchronize, the generated and received codes. Acquisition is a part of the synchronization process that occurs (ideally) once during initial synchronization. Acquisition produces a coarse alignment of the two codes (typically less than a fraction of chip duration). The acquisition process searches a specific timing uncertainty region for the correct delay. The uncertainty region is typically divided into discrete cells, where each cell is associated with a specific delay. A training sequence or preamble is typically used to achieve acquisition. Once this preamble is aligned with the stored reference (*i.e.* the cell that contains the real delay is selected), the receiver is said to attain lock. If the correct cell is not detected, we say that the receiver "missed" acquisition. A false alarm occurs when a wrong cell is selected. We label the probabilities of a hit (or detection), false alarm and missed detection as P_d, P_{fa} and P_m respectively. The average time it takes acquisition to terminate successfully is the mean acquisition time $\bar{T}_{acq}$. The four main performance measures of a typical acquisition process are $\bar{T}_{acq}$, P_{fa}, P_m and P_d. A well designed acquisition process should ideally yield low $\bar{T}_{acq}$, low P_{fa}, low P_m and high P_d. These measures are usually inter-dependent, and their relative importance is closely related to the specifications of the application at hand. In a packet-based system, for example, where the packet is either detected or all the information is lost, maintaining a high probability of detection is paramount. In real-time applications, where high latency is damaging, special care is put into reducing $\bar{T}_{acq}$. In this section, we introduce fundamentals of acquisition theory for SS systems. For an exhaustive analysis of SS acquisition, the reader is referred to [61].

5.4.1 Classification of Detector Structures

Coherent Versus Non-Coherent Detectors

For almost all acquisition detectors, the received and local spreading sequences are multiplied to produce a measure of correlation between the two. This measure is then processed by a decision rule and search strategy, to determine whether the two codes are in synchronism, and what to do if they are not. All detectors thus make decisions based on some form of threshold comparison test [61]. Acquisition circuits fall into two basic categories, namely, coherent and non-coherent. The non-coherent detector removes any phase or frequency ambiguity before processing the metric (by squaring the metric, for example, or taking its absolute value). The non-coherent detector is the most commonly used, because the carrier phase and the frequency shifts caused by propagation delay and Doppler are usually unknown, and coherent methods applied prior to carrier and frequency estimation are inapplicable. If good estimates of the carrier phase and frequency shift are available, coherent acquisition is possible.

Fixed Versus Variable Integration Time

Another classification criterion is based upon the length of integration time in the detector. Fixed and variable integration time detectors exist. Fixed integration time detectors may be further categorized as single dwell or multiple dwell. In single dwell systems, detection of acquisition is based on a single integration. It is based on multiple integrations for multiple dwell systems. Single dwell detectors can be further categorized according to whether they use partial or full period code correlation. Multiple dwell detectors are categorized depending on the way in which the additional integrations are used to verify the decision made based on the first integration. For variable-integration detectors, the integration time required for threshold crossing is allowed to vary.

5.4.2 Acquisition Techniques

The Maximum Likelihood Algorithm

In the maximum likelihood (ML) procedure (Figure 5.3), the received signal is correlated with *all phases* of the local spreading code. In other words, assuming that the uncertainty region is divided into N cells (each

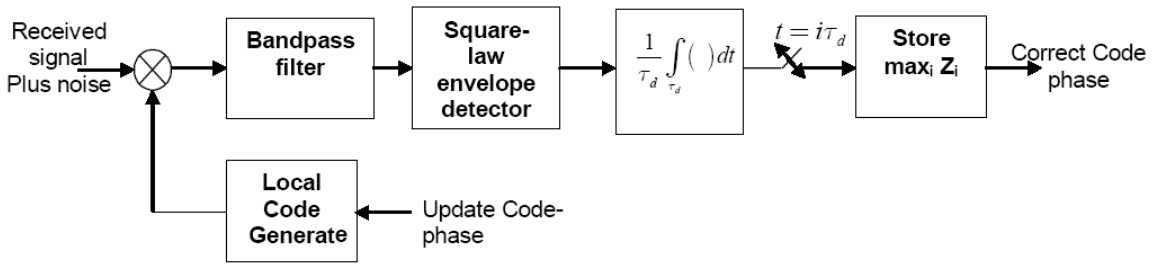

Figure 5.3: Serial realization of the ML technique.

corresponding to a code phase, or delay), all N cells are tested. The cell yielding the greatest decision statistic is selected. In a strict ML implementation, all decisions are made in parallel. In the serial implementation, cells are tested successively and their statistics are stored (this assumes that the delay does not change during the time it takes to test all the cells). A decision is only made after all cells are tested. The advantage of the ML technique is that it tests all possibilities, which leads to a relatively reliable decision. However, it suffers from an increased complexity (in the parallel implementation) or an increased search time (in the serial implementation) which makes it infeasible in most applications.

Single Dwell Serial Search

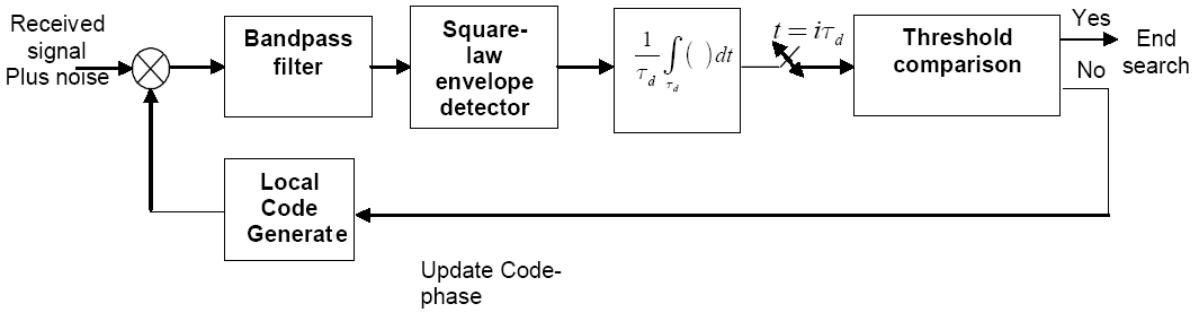

Figure 5.4: Single dwell-time, non-coherent serial search.

In the serial search technique (Figure 5.4), cells are searched consecutively. If the decision from a cell

exceeds a pre-defined threshold, acquisition terminates and switches to the verification stage. Else, the search proceeds to the next cell. Compared to the ML technique, serial search trades off accuracy for shorter acquisition time. The margin of the step (the time distance between two consecutive cells) is determined by the desired acquisition precision. It is typically set to one half or one fourth of a chip. In the absence of *a priori* information of the code phase, the sweep of the uncertainty region is uniform (i.e., the steps are equal) and unidirectional. Alternatively, if *a priori* information is available, the search starts in the region of highest certainty and expands to regions of lesser certainty. This is termed as an *expanding window* search. However, the term "serial search" usually refers to consecutive (linear) search, where cells are searched in the order in which they occur in time. The single-dwell non-coherent serial search detector is the most popular acquisition technique for practical DS systems. Its performance has been studied closely. Analysis is typically based on generating flow graph models and the use of basic Markov chain theory. Although a complete characterization of the probability distribution of the acquisition time is desirable, the literature is often content with measuring performance in terms of the first two moments, $\bar{T}_{acq}$ and σ^2_{acq}. It is assumed that a false alarm is detected in a verification stage performed after lock, and leads to a penalty time of $T_{fa} = K\tau_d$, where τ_d is the dwell time (the time required for a single integration), and K is a parameter depending on system characteristics. In traditional serial search analysis, it is commonly assumed that only one cell holds the correct phase. Although this is a valid assumption in AWGN channels, it does not hold in multipath environments, where multiple cells (corresponding to different multipath components) may legitimately achieve lock. The definition of successful acquisition is then more subtle, and depends on the particular considered application.

Multiple Dwell Serial Search

In the multiple dwell approach, the examination interval is divided into a sequence of short integration times. Integrations are performed consecutively. If, at any time, the result of a particular integration does not exceed the threshold, failure is declared, and acquisition proceeds to the next cell. Lock is only achieved if all integrations exceed the threshold. The major advantage of such a strategy is that it enables fast rejection of out-of-phase cells, therefore reducing acquisition time. However, this comes at the cost of

increased complexity.

The MAX/TC Search

One of the disadvantages of the serial search criterion is that it is highly sensitive to the fixed threshold, especially in extremely noisy environments. In fact, if the threshold is too low, many cells could terminate the search, potentially causing a false alarm. If the threshold is too high, the search cannot be terminated, and detection is missed. The threshold must therefore be optimized, which could be a complex process, since it depends on the statistical properties of the communication channel.

An alternative strategy is to choose the largest decision metric from a group of cells, and only compare that maximum value to the threshold. This is labeled the MAX/TC criterion. Since it requires fewer comparisons with the threshold, it leads to a more robust, but more complex acquisition process. The MAX/TC criterion can be performed in either a serial or parallel mode. Note that the MAX/TC approach is similar to the ML approach, except that the final decision is preceded by a threshold comparison. This blocks acquisition from making an incorrect decision in the absence of a signal (i.e. when choosing the maximum statistic among noisy statistics). In a multiple-sector MAX/TC criterion, cells are grouped into sectors. The cell with the maximum statistic is selected from a sector, and its statistic is compared to the threshold. If it exceeds the threshold, acquisition is terminated. If it does not, acquisition moves to the next sector [89]. The number of threshold comparisons is proportional to the number of sectors. A modified method is the global MAX/TC criterion, where the maximum is selected after searching the whole uncertainty region, then compared to a threshold. The global MAX/TC approach is the least sensitive to the threshold. However, it is characterized by a fixed one-round search time, since all cells have to be searched before a decision is made.

The Matched Filter Technique

The previous techniques considered active correlation, that is, the received signal was correlated with a locally generated spreading sequence, after which a decision was made. The matched filter technique (Figure 5.5) uses passive correlation; the filter is matched to a portion of the spreading sequence. Correlation is performed as the received signal slides through the filter. The matched filter produces maximum correlation when its impulse response matches the incoming sequence. A simple threshold device may be used to detect

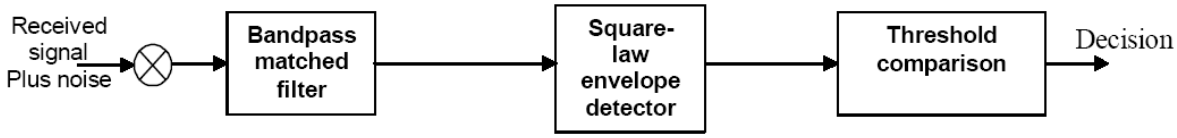

Figure 5.5: The matched filter implementation.

this peak. Since correlation is continuous in this case, the matched filter technique offers a reduced acquisition time compared to serial search. The matched filter technique is not suitable for applications where the shape of the received pulse is unknown (which is the case of UWB in dense multipath), since a unique, strong correlation maximum cannot be achieved in that case.

5.5 Previous Work on SS and UWB Acquisition in Dense Multipath

The problem of acquisition in multipath has received some attention in SS research. One of the earliest references to study the performance of an acquisition system considering multiple H_1 cells is [90], where the probability of successful acquisition is defined as the probability of detecting any multipath component. A matched-filter acquisition approach that combines two consecutive matched filter output samples in order to coherently gather multipath energy is proposed in [91]. An expression for the mean acquisition time in multipath for an SS system is derived in [92]. In [93], the effect of the order in which cells are tested is investigated. It is found that uniformly spreading the H_1 over the uncertainty region yields lower acquisition times. This idea is extended in [94], where the uncertainty region is divided into sectors, each sector containing exactly one H_1 cell. However, the number of multipath components is assumed to be known and relatively small. Acquisition for SS Rake receivers in multipath are studied in [95] and [96]. In [95], decision statistics for all cells in the uncertainty region are produced, and then the first finger tap is set to the delay corresponding to the greatest metric. The number of remaining fingers and their respective delays are set based on a ratio-threshold test. In [96], Rake acquisition is divided to two stages. Initial acquisition locks to an arbitrary multipath component, while post-initial acquisition searches the reduced uncertainty region

around the selected cell to fix the position of the remaining fingers. While insightful, this work does not directly apply to UWB due to the high energy dispersion and relatively large number of multipath components in the UWB channel.

Recent research effort has focused on acquisition methods specifically tailored for UWB. Most of the proposed solutions are based on variants of single dwell non-coherent serial search, because of its low complexity, simplicity of implementation, and ease of analysis. A threshold crossing technique based on equal gain combining to gather energy from different multipath components is proposed in [97]. The same approach is extended in [98], where two levels of signals spreading are used in order to reduce the acquisition search space. Optimal cell search patterns in multipath are investigated in [99] [100] [101]. It is found that a "bit reversal" search, that maximizes the distance between consecutive tested cells, yields significant reduction in mean acquisition time compared to a linear (serial) search where cells are searched in order, at the expense of a more complex search mechanism. Bit reversal search is employed in [102] along with a double dwell approach, which speeds up acquisition time by introducing parallelism. The use of the MAX/TC approach [89] is proposed for UWB in [103], where the maximum metric from a group of parallel correlators is chosen then compared to a threshold. The approach is more robust than serial search but introduces significant complexity to the circuit. A system where acquisition is performed by selecting the peak of the cross-correlation between consecutive pilot signals is studied in [104] and [105]. However, such a system is highly sensitive to noise because of the use of a dirty template, and suffers from the "noise-cross-noise" effect seen in transmitted-reference receivers [35]. In [106] and [107], the authors take advantage of the inherent cyclostationarity of UWB signals when spreading sequences are used, by picking the peak of a time-varying correlation to estimate the delay. Acquisition based on spectral estimation techniques is investigated in [108] and [109]. In [110], a joint channel estimation and synchronization method based on least squares is studied, where a sub-spaced method first identifies the presence of multipath clusters, before performing a finer search on the detected cluster. A two-stage acquisition approach, where a rough block search is first performed, and then the search is refined by processing the selected block, is proposed in [111].

The above mentioned references assume that acquisition is successful if any H_1 cell is detected. However, this assumption is highly unsuitable for UWB applications operating in dense multipath (unless a Rake re-

ceiver is used). In fact, for UWB ranging applications, the detected multipath might be tens of nanoseconds away from the start of the signal due to the large delay spread, resulting in ranging errors in the tens of feet. This approach is also inefficient in communication applications, since locking to an arbitrary multipath and assuming it to be the earliest arriving path might lead to a loss of a large part of the symbol energy, resulting in substantially higher symbol error probabilities. The problem is identified in the literature (see [92]), and the need for some additional sweep stage is recognized, but a specific algorithm for robustly detecting the first multipath has not yet been presented. The problem is not trivial, since the LOS path might not be the strongest path. Moreover, it might be severely attenuated, which makes its detection with high probability a challenging task.

5.6 General Acquisition System Model

The proposed acquisition model is based on a training sequence. For ranging applications, the training sequence is part of a ranging packet and is used to estimate the signal's time of flight, which is directly related to the position of the first arriving path [†]. For communication applications, the training sequence is followed by data transmission after acquisition terminates. The definition of some terms was provided in the previous chapter, and is repeated here for convenience. The training sequence $s_{ts}(t)$ is defined as:

$$s_{ts}(t) = \sqrt{E_p} \sum_{i=-\infty}^{\infty} \sum_{n=0}^{N_c-1} a_n w\left(t - nT_f - iN_cT_f\right) \tag{5.1}$$

where $a_n = \pm 1, 0 \leq n \leq N_c - 1$ is a maximal length sequence of length N_c, and $w(t)$ is a unit-energy UWB Gaussian pulse shape, which is assumed to have non-negligible amplitude over a time duration T_w. It is assumed that the effects of the transmit and receive antennas are incorporated into $w(t)$. For mathematical simplicity, it is also assumed that the symbol time $T_f >> T_w$ is longer than the channel maximum delay spread, and any ISI effects caused by the multipath channel are thus ignored[‡]. E_p is the pulse energy. $R(\tau)$

[†]The exact algorithm for range estimation is not detailed here. Rather, we will assume that the range error is directly related to the timing error.

[‡]Note that, although ISI is not included in the analysis, the system possesses inherent ISI mitigation capability, due to the use of a spreading sequence. Specifically, the impact of ISI will be reduced by a factor N_c.

is the autocorrelation function of $w(t)$ evaluated at delay τ, and is given by:

$$R(\tau) = \int_{-\infty}^{\infty} w(t)w(t-\tau)dt \tag{5.2}$$

The impulse response of the L-multipath channel is given by the following tapped delay model:

$$h(t) = \sum_{l=1}^{L} \alpha_l \delta(t - \tau_l). \tag{5.3}$$

α_l and τ_l are the real amplitude (including polarity) and delay of the l^{th} path, respectively. The channel is assumed to be time-invariant (quasi-static) over the analysis. After channel convolution, the received training sequence can be written as:

$$r_{ts}(t) = \sqrt{E_p} \sum_{i=-\infty}^{\infty} \sum_{n=0}^{N_c-1} a_n \sum_{l=1}^{L} \alpha_l w\left(t - \tau_l - nT_f - iN_cT_f\right) + n(t). \tag{5.4}$$

$n(t)$ is a zero-mean white Gaussian noise process with PSD $\frac{N_0}{2}$.

At the receiver, $r_{ts}(t)$ is correlated with a delayed version of the spreading sequence in order to detect the presence of signal components. Since the length of the spreading sequence is N_c, the timing uncertainty region is of length N_cT_f seconds. In other words, if the delay of the correlator-spreading sequence is incremented on a time interval of length N_cT_f, the received and correlator sequences are guaranteed to align at some delay. Thus, we shall assume that the true delay of the received signal is equal to 0 ($\tau_1 = 0$), and restrict our analysis to the uncertainty interval $[0, N_cT_f]$ without loss of generality. If this interval is tested and acquisition is not successful, intervals $[iN_cT_f, (i+1)N_cT_f]$, $i \geq 1$ are successively tested in a similar fashion, until acquisition is successful.

The uncertainty region is divided into discrete cells, where each cell corresponds to a specific delay. The time difference between two consecutive tested delays is given by $\Delta\tau$. A decision metric corresponding to a specific cell is generated by correlating the received training sequence by a delayed version of the unit-energy correlator template $m(t)$, where:

$$m(t) = \frac{1}{N_c} \sum_{n=0}^{N_c-1} a_n w\left(t - nT_f\right). \tag{5.5}$$

Assuming the true delay of the received signal to be 0 ($\tau_1 = 0$), and varying the delay of $m(t)$ from 0 to $N_c T_f$, the correlator output corresponding to delay $\hat{\tau}$ can be written as:

$$d_{\hat{\tau}} = \int_{\hat{\tau}}^{\hat{\tau}+N_c T_f} r_{ts}(t) m(t-\hat{\tau}) dt. \tag{5.6}$$

We can express (5.6) as:

$$d_{\hat{\tau}} = \frac{\sqrt{E_p}}{N_c} \int_{\hat{\tau}}^{\hat{\tau}+N_c T_f} \sum_{l=1}^{L} \alpha_l \sum_{i=-\infty}^{\infty} \sum_{n=0}^{N_c-1} a_n w\left(t - nT_f - iN_c T_f - \tau_l\right) \sum_{m=0}^{N_c-1} a_m w\left(t - mT_f - \hat{\tau}\right) dt + n_d \tag{5.7}$$

where n_d is a zero-mean Gaussian random variable given by:

$$n_d = \frac{1}{N_c} \int_0^{N_c T_f} n(t) \sum_{m=0}^{N_c-1} a_m w\left(t - mT_f\right) dt. \tag{5.8}$$

The variance of n_d is found to be:

$$\begin{aligned} \sigma^2 &= \frac{1}{N_c^2} \int_0^{N_c T_f} \int_0^{N_c T_f} E\left[n(t)n(\lambda)\right] \sum_{m_1=0}^{N_c-1} \sum_{m_2=0}^{N_c-1} a_{m1} a_{m2} w\left(t - m_1 T_f\right) w\left(t - m_2 T_f\right) dt d\lambda \\ &= \frac{N_0}{2N_c^2} \sum_{m_1=0}^{N_c-1} a_{m1}^2 \int_0^{N_c T_f} w^2(t) = \frac{N_0}{2N_c}. \end{aligned} \tag{5.9}$$

We can re-write $d_{\hat{\tau}}$ as:

$$\begin{aligned} d_{\hat{\tau}} &= \frac{\sqrt{E_p}}{N_c} \sum_{l=1}^{L} \alpha_l \sum_{n=0}^{N_c-1} \sum_{m=0}^{N_c-1} a_n a_m \int_{\hat{\tau}}^{N_c T_f} w\left(t - nT_f - \tau_l\right) w\left(t - mT_f - \hat{\tau}\right) dt \\ &+ \frac{\sqrt{E_p}}{N_c} \sum_{l=1}^{L} \alpha_l \sum_{n=0}^{N_c-1} \sum_{m=0}^{N_c-1} a_n a_m \int_{N_c T_f}^{\hat{\tau}+N_c T_f} w\left(t - nT_f - N_c T_f - \tau_l\right) w\left(t - mT_f - \hat{\tau}\right) dt + n_d. \end{aligned} \tag{5.10}$$

Now, if $\hat{\tau} \leq T_f$, then:

$$d_{\hat{\tau}} = \frac{\sqrt{E_p}}{N_c} \sum_{l=1}^{L} \alpha_l \sum_{n=0}^{N_c-1} a_n^2 R\left(\tau_l - \hat{\tau}\right) + n_d = \sqrt{E_p} \sum_{l=1}^{L} \alpha_l R\left(\tau_l - \hat{\tau}\right) + n_d. \tag{5.11}$$

If $T_f \leq \hat{\tau} \leq N_c T_f$, then:

$$d_{\hat{\tau}} = \frac{\sqrt{E_p}}{N_c} \sum_{l=1}^{L} \alpha_l \sum_{n=0}^{N_c-1} a_n a_{n+\lfloor \frac{\hat{\tau}}{T_f} \rfloor \ mod \ N_c} R\left(\tau_l - \hat{\tau} + \lfloor \frac{\hat{\tau}}{T_f} \rfloor T_f\right) + n_d. \tag{5.12}$$

Since a maximal length sequence is used, we can write:

$$d_{\hat{\tau}} = \frac{-\sqrt{E_p}}{N_c} \sum_{l=1}^{L} \alpha_l R\left(\tau_l - \hat{\tau} + \lfloor \frac{\hat{\tau}}{T_f} \rfloor T_f\right) + n_d. \tag{5.13}$$

For a large spreading gain N_c, the self-interference component becomes negligible, and $d_{\hat{\tau}} \approx n_d$. Indeed, the autocorrelation function of the spreading sequence is negligible if the delay between the template and received sequence is greater than T_f, because of the inherent spreading gain. Then, we can write:

$$d_{\hat{\tau}} \approx \begin{cases} \sqrt{E_p} \sum_{l=1}^{L} \alpha_l R(\tau_l - \hat{\tau}) + n_d, & 0 \leq \hat{\tau} \leq T_f. \\ n_d, & T_f \leq \hat{\tau} \leq N_c T_f \end{cases}$$

Note that traditional acquisition models assume the presence of a single H_1 cell. The inherent multipath structure is incorporated into the model by defining an H_1 cell as *any* cell which falls in the interval $[0, T_f]$ (labeled the H_1 region). An H_0 cell is any cell falling anywhere outside that interval (labeled the H_0 region). An H_0 cell does not include any signal component, and its decision statistic is therefore purely a noise component. Note that an H_1 cell *potentially* holds a signal component. In fact, an H_1 cell might fall in a region where no multipath has occurred, and in that case it would be statistically identical to an H_0 cell. We will discuss the impact of this shortly.

The coarse acquisition stage is based on the popular threshold crossing technique [112], where the decision metric of a specific cell is compared to a pre-defined threshold. If the metric exceeds the threshold, a lock is declared. If the metric does not exceed the threshold, the search moves to the next cell. The order in which cells are tested and its impact on performance will be discussed shortly. It is also assumed that a lock is followed by a verification stage, where the region in the vicinity of the selected cell is further tested. In this framework, the verification stage consists of an extra test step, where the presence of additional multipath components around the selected cell is checked. For example, the decision metrics for the M cells (M is a

positive integer) occurring before and after the selected cell might be re-generated using a longer dwell time (i.e. a more robust mechanism). If any of the M cells exceeds the threshold, the cell passes the test. If the cell fails the verification stage, that is, if no signal components are detected around it, the lock is canceled, and the search moves to the next cell. If it passes the test, the system proceeds to fine acquisition. It is important to note that, although some H_1 cells might be statistically identical to an H_0 cell, it is assumed that such a cell will pass the verification stage. This assumption holds in dense multipath scenarios. In fact, although some H_1 cell might not contain any signal component, one or more of its neighboring cells will most likely hold a signal component, because of the large number of resolvable paths. It is therefore assumed that all H_1 cells pass the verification stage, and all H_0 fail it. The rationale behind this assumption will be further clarified in section 5.8.

The probabilities of the decision metric for an H_0 and an H_1 cells exceeding the threshold are now derived. Since no information exists on the path polarity, the decision statistic is squared to remove the path sign uncertainty. Let Z_i and Y_j be the acquisition decision statistics for the i^{th} H_1 and the j^{th} H_0 cells, respectively. Then:

$$Z_i = \left(\sqrt{E_p} \sum_{l=1}^{L} \alpha_l R(\tau_l - \tau_i) + n_d \right)^2 \tag{5.14}$$

$$Y_j = n_d^2 \tag{5.15}$$

where τ_i is the delay corresponding to the i^{th} H_1 cell. Z_i is a noncentral chi-squared random variable with one degree of freedom and noncentrality parameter $\left(\sqrt{E_p} \sum_{l=1}^{L} \alpha_l R(\tau_l - \tau_i) \right)^2$. Y_j is a central chi-squared random variable with one degree of freedom. Let $f_{z_i}(z)$ and $f_y(y)$ be the probability density functions (pdf) of the i^{th} H_1 cell and any H_0 cell, respectively. Then, we can write [114]:

$$f_{z_i}(z) = \frac{1}{2\sqrt{2\pi z}\sigma} e^{-\frac{(\sqrt{z}-\mu_i)^2}{2\sigma^2}} + \frac{1}{2\sqrt{2\pi z}\sigma} e^{-\frac{(\sqrt{z}+\mu_i)^2}{2\sigma^2}}, \quad z \geq 0 \tag{5.16}$$

$$f_y(y) = \frac{1}{\sqrt{2\pi y}\sigma} e^{-\frac{y}{2\sigma^2}}, \quad y \geq 0 \tag{5.17}$$

where:

$$\mu_i = \sqrt{E_p}\sum_{l=1}^{L}\alpha_l R(\tau_l - \hat{\tau}_i). \tag{5.18}$$

Note that the delay of an H_0 cell does not play any role in its pdf definition. The respective cumulative distribution functions (CDF) are then:

$$F_{Z_i}(Z) = \frac{1}{2}\left[erf\left(\frac{\sqrt{Z}-\mu_i}{\sigma\sqrt{2}}\right) + erf\left(\frac{\sqrt{Z}+\mu_i}{\sigma\sqrt{2}}\right)\right] \tag{5.19}$$

$$F_Y(Y) = erf\left(\frac{\sqrt{Y}}{\sigma\sqrt{2}}\right) \tag{5.20}$$

where $erf(.)$ is the error function. The probability that the i^{th} H_1 cell exceeds a pre-defined threshold ζ is then:

$$p_{di} = 1 - F_{Z_i}(\zeta) = 1 - \frac{1}{2}\left[erf\left(\frac{\sqrt{\zeta}-\mu_i}{\sigma\sqrt{2}}\right) + erf\left(\frac{\sqrt{\zeta}+\mu_i}{\sigma\sqrt{2}}\right)\right]. \tag{5.21}$$

The probability that an H_0 cell exceeds ζ (a false alarm) is:

$$p_{fa} = 1 - F_Y(\zeta) = 1 - erf\left(\frac{\sqrt{\zeta}}{\sigma\sqrt{2}}\right). \tag{5.22}$$

Note that the above analysis assumes $\Delta\tau \geq T_w$, which ensures independence among cell statistics.

5.7 Coarse Acquisition

The number of H_1 cells is equal to $C_{in} = \lfloor \frac{T_f}{\Delta\tau} \rfloor$. Similarly, the number of H_0 cells is $C_{out} = \lfloor \frac{(N_c-1)T_f}{\Delta\tau} \rfloor$. The total number of cells is then $C = C_{in} + C_{out}$. The performance of the coarse acquisition scheme depends on the order in which these C cells are searched. In this section, two coarse acquisition strategies are presented. The popular serial (linear) search is first discussed. The proposed search method, termed "jump-phase" search, is then introduced. Mean acquisition time expressions for both these systems in dense multipath are derived.

5.7.1 Traditional Coarse Acquisition: Serial Search

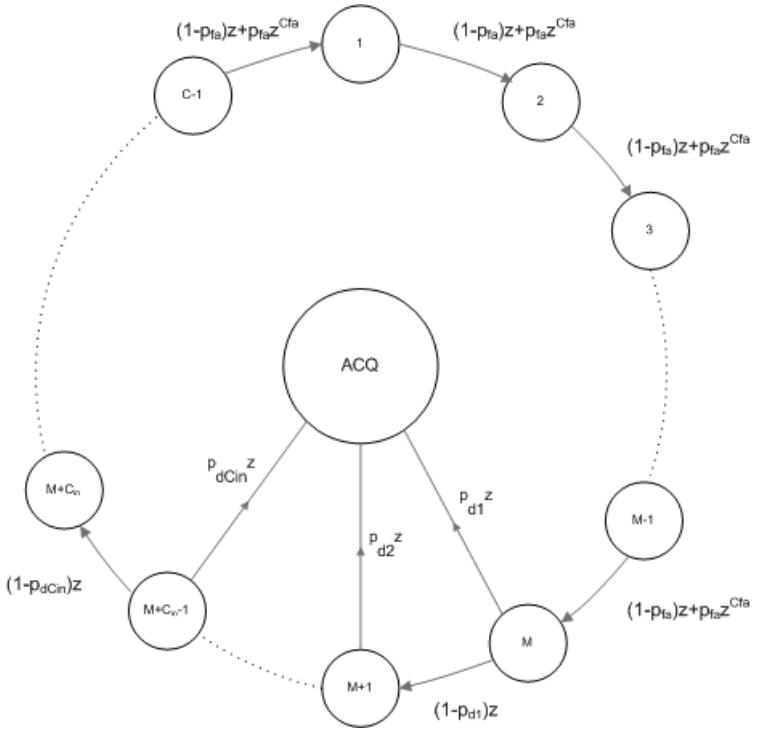

Figure 5.6: Serial Search State Diagram. H_1 cells occur consecutively in the uncertainty region.

Serial search is the most popular acquisition technique for practical systems. In serial search, the cells in the uncertainty region are searched consecutively, in the order in which they occur in time (Figure 5.6). Since no *a priori* timing information exists, it is assumed that the search start position is uniformly distributed over the uncertainty region, that is, the probability of starting the search at an arbitrary cell is equal to $\frac{1}{C}$.

The mean acquisition time $\bar{T}_{acq}$ is defined as the average effective number of cells that are tested before coarse acquisition is terminated successfully. Serial search acquisition time has been studied thoroughly for SS systems [87][61]. Analysis is typically based on generating flow graph models and basic Markov chain theory, although brute force approaches are also sometimes used. The expressions that exist in the literature usually assume the existence of a single H_1 cell, which does not apply for UWB acquisition in dense multipath. A simple method to efficiently approximate $\bar{T}_{acq}$ based on the traditional expressions is proposed

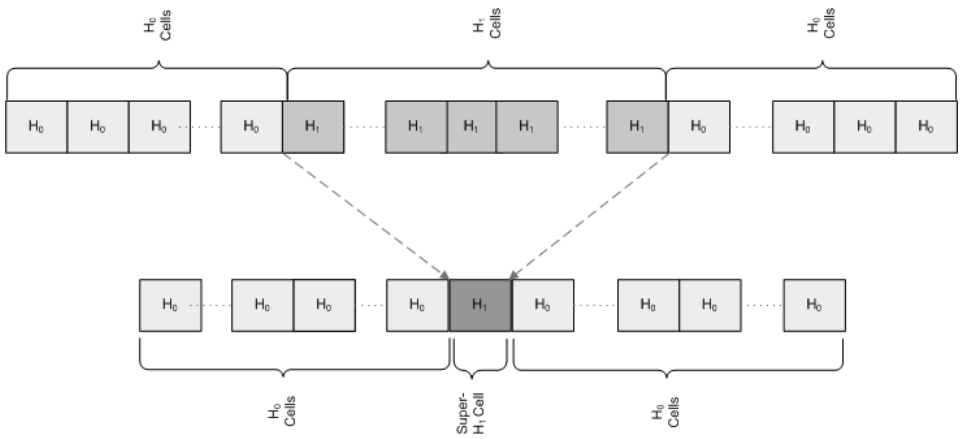

Figure 5.7: The Super Cell Approach. All H_1 cell are bundled into one super-H_1 cell.

here. In fact, since all H_1 cells, as defined in this framework, occur consecutively, an approximate expression for $\bar{T}_{acq}$ may be obtained by collapsing all H_1 cells into one super-H_1 cell (Figure 5.7). The probability of the super H_1 cell exceeding the threshold is equal to the probability that at least one H_1 cell exceeds the threshold. The problem then degenerates into the classical single H_1 scenario. Using this approach, $\bar{T}_{acq}$ can be expressed based on the key results in [112] [113], with negligible additional calculations. We get:

$$\bar{T}_{acq} = \frac{2 + (2 - P_d)\, C_{out}(1 + p_{fa} C_{fa})}{2P_d} + \frac{\bar{n}_0}{P_d} \tag{5.23}$$

where:

$$P_d = 1 - \prod_{i=1}^{C_{in}} (1 - p_{di}) \tag{5.24}$$

and C_{fa} is the penalty time associated with the verification stage. $\bar{n}_0$ is the mean position of the selected H_1 cell within the super-cell, which is approximated by:

$$\bar{n_0} = \sum_{i=1}^{C_{in}} \prod_{j=1}^{i-1} i\,(1 - p_{dj})\, p_{di}. \tag{5.25}$$

It will be shown by simulation that the error induced by the above approximations is negligible.

For high signal-to-noise (SNR) scenarios, $P_d = 1$ and $p_{fa} = 0$, and:

$$\bar{T}_{acq} = \frac{C_{out}}{2} + \bar{n}_0 + 1. \tag{5.26}$$

Therefore, at best, approximately half of the cells are searched on average, which leads to prohibitively long $\bar{T}_{acq}$, even for moderate spreading lengths. Moreover, for low SNR values, since half the H_0 cells are searched on average before reaching the H_1 region, performance will be severely limited by the high false alarm rate, especially for large values of C_{fa}. Notice that $\bar{T}_{acq}$ at high SNR is *independent* of the multipath structure. Serial search does not take advantage of the multipath channel, which is a highly suboptimal approach. In fact, serial search would result in almost the same acquisition time performance in a pure LOS channel. A search pattern that exploits the multipath structure and spreads the H_1 cells more uniformly over the uncertainty region will yield significant gains. The next section discusses such a pattern.

5.7.2 Proposed Coarse Acquisition: The Jump-Phase Search

The key to reducing $\bar{T}_{acq}$ in dense multipath is to search the multipath components in non-consecutive order. In [99], a search pattern where the jump between consecutive cells is equal to the number of multipath components is investigated. However, this assumes knowledge of the number of multipath components, which is unrealistic. A modified strategy, termed *bit reversal* search, is introduced, where the binary representation of the cell indices are 'bit-reversed' and searched in a new order. This strategy maximizes the distance between consecutively tested cells, and is shown to yield similar performance to the prior search at high SNR. However, there is an inherent added complexity involved in performing the bit reversal and modifying the delay from one cell to another, especially for a large number of cells. Moreover, the procedure is further complicated when the number of cells is not a power of two, which is usually the case. We propose a simple search algorithm, named *jump-phase* search, that does not add any significant complexity compared to serial search, and does not assume knowledge of the number of multipath components. In the jump-phase search, the jump between cells is equal to C_{in}, where C_{in} is the number of cells in one particular spreading code symbol duration T_f. Note that C_{in} is independent of the channel profile. By using this search, the H_1 cells are uniformly spread over the uncertainty region (Figure 5.8). An H_1 cell is visited every N_c cell (Figure

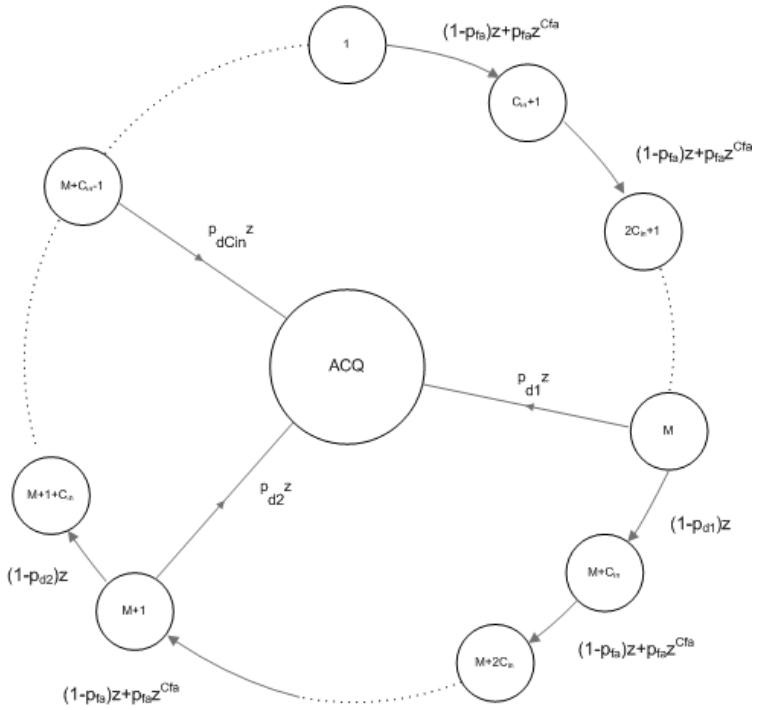

Figure 5.8: Jump-Phase Search State Diagram. H_1 cells are uniformly spread over the uncertainty region.

5.9). The search becomes more efficient as the number of resolvable multipath components increases, and more H_1 cells terminate the search. Since UWB inherently possesses a fine time resolution, we expect $\bar{T}_{acq}$ to be reduced drastically compared to serial search. However, it is important to note that, at low SNR, performance is highly sensitive to the choice of threshold. In fact, on one hand, if the threshold is too high, H_1 cells will fail the test because energy is dispersed along many multipath components. On the other hand, if the threshold is too low, the false alarm rate increases. The threshold setting should therefore strike a balance between exploiting the multipath structure and minimizing the false alarm rate. Simulation will also show that our approach results in only slight loss compared to the bit reversal search with better implementation complexity.

An exact expression for the mean acquisition time using jump-phase search may be obtained by following the general flow chart approach presented in [100] and [101]. After some basic mathematical manipulation,

direct substitution gives:

$$\bar{T}_{acq} = \frac{X_1.Y_1 - X_2.Y_2}{Y_1^2} \tag{5.27}$$

where:

$$X_1 = \frac{1}{C}\sum_{m=1}^{C_{in}}\sum_{k=1}^{C}\sum_{i=1}^{C_{in}}\prod_{j=1}^{i-1}\left(1-p_{d(j+m) \bmod C_{in}}\right).p_{d(i+m) \bmod C_{in}}\left[i+\left[iC-i-k\right]\left(1+C_{fa}p_{fa}\right)\right] \tag{5.28}$$

$$X_2 = \frac{1}{C_{in}}\sum_{k=1}^{C_{in}}\sum_{j=1}^{C_{in}} p_{d(j+k) \bmod C_{in}}\prod_{i=1}^{j-1}\left(1-p_{d(i+k) \bmod C_{in}}\right) \tag{5.29}$$

$$Y_1 = 1-\prod_{i=1}^{C_{in}}\left(1-p_{di}\right) \tag{5.30}$$

$$Y_2 = -\left(C_{in}+C_{out}\left(1+C_{fa}p_{fa}\right)\right).\prod_{j=1}^{C_{in}}\left(1-p_{dj}\right). \tag{5.31}$$

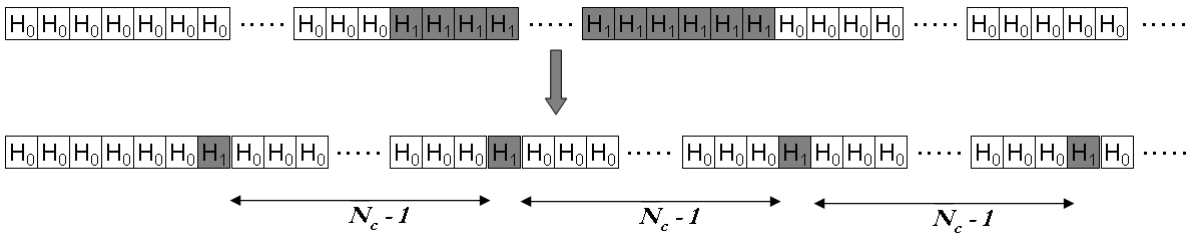

Figure 5.9: Order of tested cells in serial (top) and jump-phase search (bottom). H_1 cells uniformly spread over uncertainty region for jump-phase search.

5.7.3 Simulation Results

The theoretical expressions for serial and jump-phase search mean acquisition time (Equations (5.23) and (5.27)) are tested by simulation for a spreading code of length 32, and penalty times of 100 and 1000 cells, respectively. NLOS channel profiles are used[§]. The results are plotted in Figures 5.10 and 5.11. The threshold is set to 0.01, which corresponds to approximately one sixth of the average energy in the strongest path. Note that the error between theoretical and simulated results is negligible. Also, the jump-phase search significantly outperforms serial search. The mean acquisition time is reduced by more than an order

[§]For a detailed description of the statistical distribution of the channels used in these simulations, the reader is referred to section 2.5 and the references therein.

of magnitude.

The jump-phase search is also compared to the bit reversal search by averaging performance over 32 different channel profiles (Figures 5.12 and 5.13). Note that the bit reversal search slightly outperforms our scheme, but that the gains observed when passing from serial to jump-phase search are much more substantial than when passing from jump-phase to bit reversal search. The jump-phase search thus results in only a slight degradation in mean acquisition time performance, in exchange of a much simpler search mechanism.

The effect of the threshold ζ on the jump-phase search is illustrated in Figure 5.14. The number of H_1 cells that pass the threshold test at high SNR is plotted versus ζ. The probability of false alarm (the probability that an H_0 cell exceeds ζ, Equation (5.22) is also plotted versus ζ, assuming $N_c = 32$ and $\frac{E_p}{N_0} =$ 10 dB. Notice that the number of detectable paths drops with increasing ζ. Thus, the mean acquisition time at high SNR increases with increasing ζ, since less H_1 cells terminate the search, as shown in Figure 5.15. However, p_{fa} decreases with increasing ζ. Thus, the performance at low and moderate SNR values improves, since mean acquisition time at these energy levels is limited by the false alarm penalty time. The choice of ζ therefore depends on the system's operating point. ζ must be decreased at high SNR, and increased for low SNR. If no *a priori* SNR information is available, the choice of ζ must strike a balance between fully exploiting the multipath structure, and minimizing the false alarm rate.

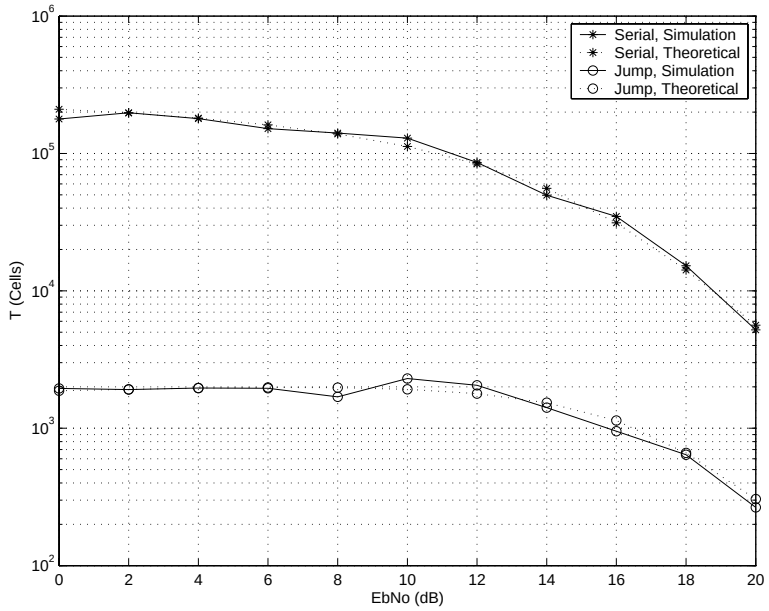

Figure 5.10: Simulation and theoretical mean acquisition time (in number of cells) for serial versus jump-phase search. $N_c = 32$. $C_{fa} = 100$. Cell separation $= T_w$. Real NLOS measured channel profile used.

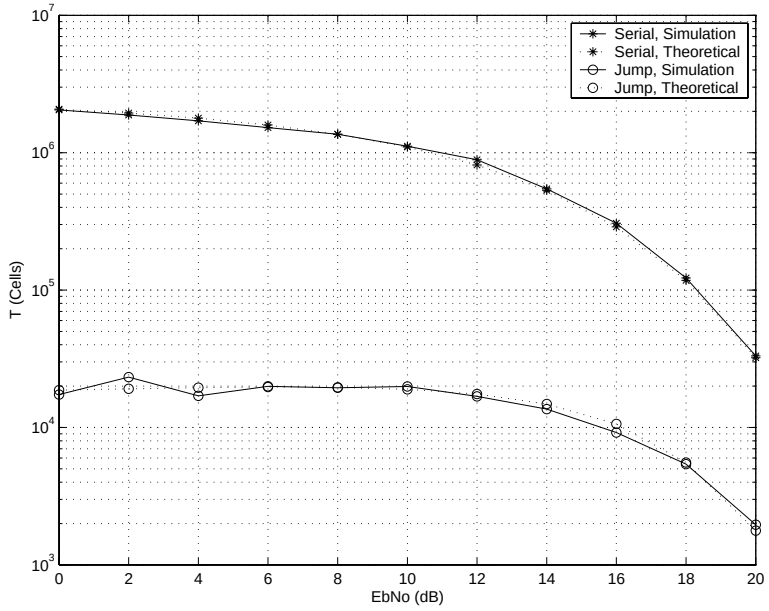

Figure 5.11: Simulation and theoretical mean acquisition time (in number of cells) for serial versus jump-phase search. $N_c = 32$. $C_{fa} = 1000$. Cell separation $= T_w$. NLOS Real measured channel profile used.

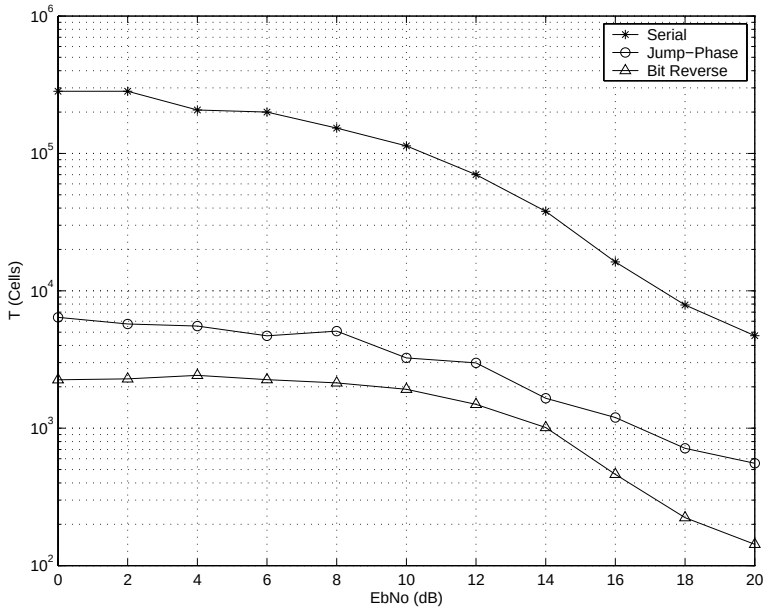

Figure 5.12: Serial, Jump-Phase, and Bit Reversal Search. N_c=32, C_{fa}=100. Real measured NLOS channel profiles used. Results are averaged over 32 different profiles.

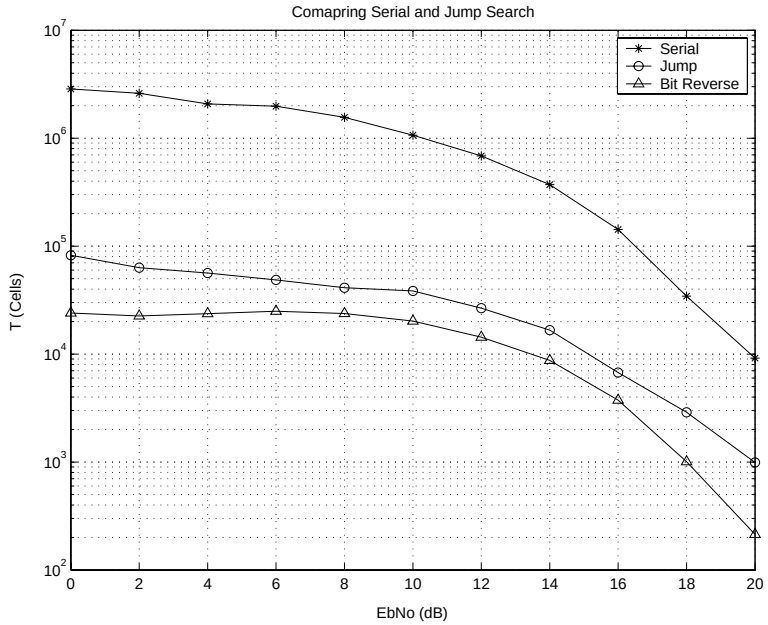

Figure 5.13: Serial, Jump-Phase, and Bit Reversal Search. N_c=32, C_{fa}=1000. Real measured NLOS channel profiles used. Results are averaged over 32 different profiles.

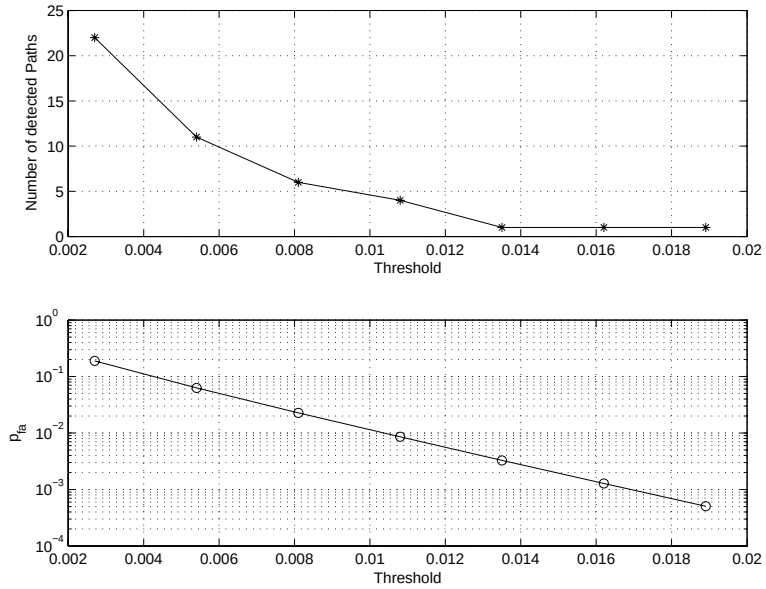

Figure 5.14: Number of detectable paths, and p_{fa} at $\frac{E_p}{N_0}$=10 dB vs. threshold. Increasing the threshold increases the average acquisition time at high SNR, but decreases the false alarm rate at low SNR.

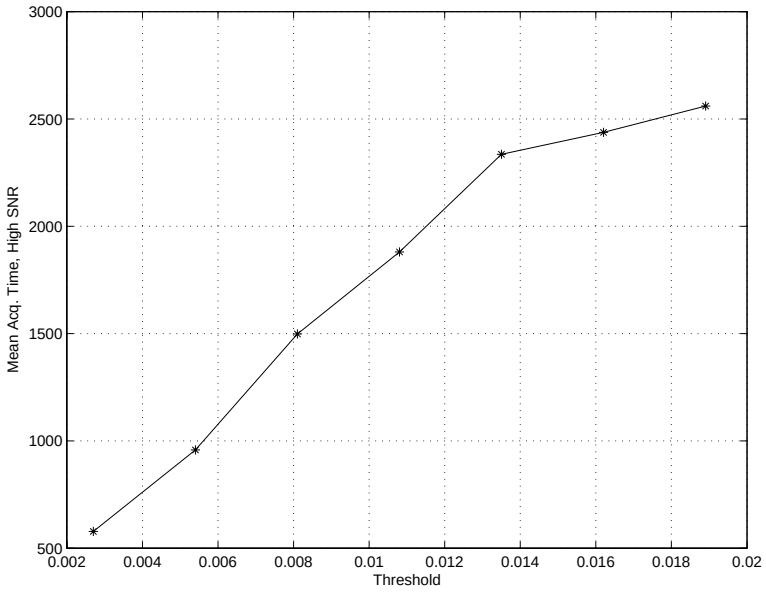

Figure 5.15: $\bar{T}_{acq}$ at high SNR versus threshold. The number of detectable paths decreases with increasing threshold, and therefore $\bar{T}_{acq}$ increases.

We now briefly discuss the mechanism used in setting the threshold ζ. As we have already noted, lower values of ζ result in more H_1 cells crossing the threshold test, thus more efficiently exploiting the channel multipath structure, but lead to an increase in the probability of false alarm. The false alarm rate drops with increasing ζ, at the expense of a longer mean acquisition time. The value of ζ should therefore be judiciously selected in order to strike a balance between fully exploiting the multipath structure and minimizing the false alarm rate. An optimal value of ζ may be derived if the noise variance (which completely defines the false alarm rate) is known, and if perfect knowledge of the amplitudes of the specular components is obtainable. In a practical system, neither is readily available. Many threshold setting strategies have been proposed for SS acquisition in AWGN. Most techniques are based on a constant false alarm rate approach, where the probability of false alarm is set to a desired value by design. This is achieved by first estimating the noise variance, or including a system training phase.

The design of threshold setting techniques specifically tailored for UWB in dense multipath is not explicitly dealt with in this work (the reader is referred to [115] and the references therein for example of thresholding setting techniques for SS systems). Nonetheless, we present sample results of a straightforward training stage, which guides the user in setting ζ. The procedure is as follows. For a specific system operating point (here defined by the transmit power and spreading width), the mean acquisition time $\bar{T}_{acq,\zeta}$ is computed over multiple realizations of the multipath channel for different values of ζ. The optimal threshold ζ_0 is the value which minimizes $\bar{T}_{aq,\zeta}$. The procedure is simulated for four key IEEE UWB multipath channel models [24], with $\frac{E_b}{N_o} = 20$ dB and $N_c = 64$. Results are averaged over 200 channel realizations. $\bar{T}_{acq,\zeta}$ is plotted versus ζ for the channel models CM1 (residential LOS), CM2 (residential NLOS), CM3 (office LOS) and CM4 (office NLOS) in figures 5.16, 5.17, 5.18 and 5.19, respectively. Notice the presence of an optimal threshold beyond which the acquisition time increases for all four cases, as expected. The optimal value is not the same for all four cases, since the channel models have different statistical properties. Also, note that the optimal value for the LOS models (CM1 and CM4) is smaller than its NLOS counterpart (CM2 and CM4, respectively). In fact, since the early arriving paths for LOS channels have more energy compared to NLOS channels, more H_1 cells pass the threshold comparison test for the same low value of ζ.

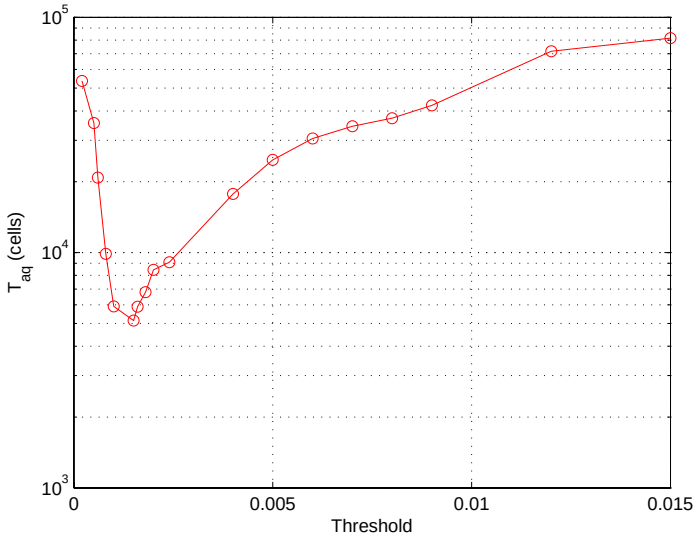

Figure 5.16: $\bar{T}_{acq}$ versus ζ. SNR = 20 dB, $N_c = 64$. CM1.

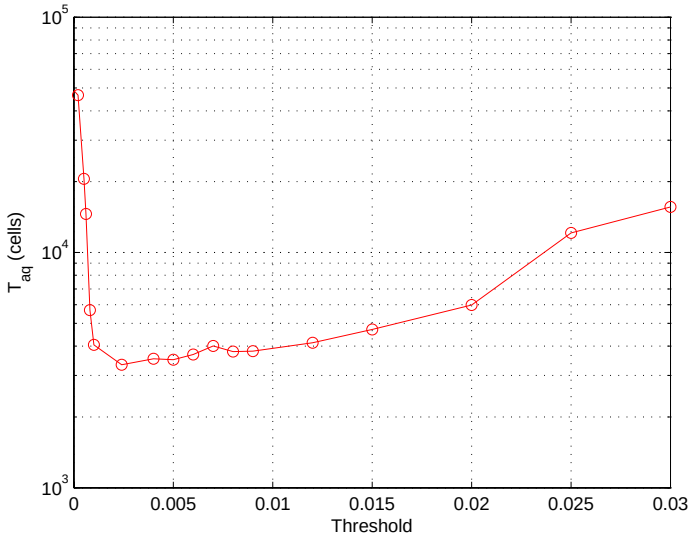

Figure 5.17: $\bar{T}_{acq}$ versus ζ. SNR = 20 dB, $N_c = 64$. CM2.

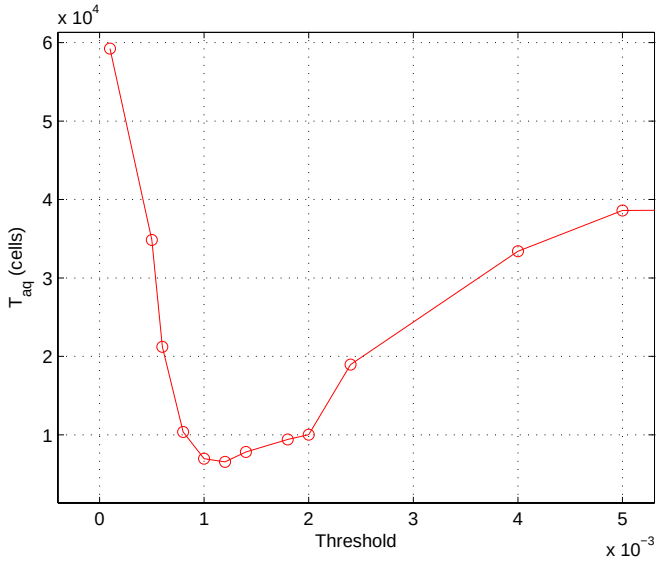

Figure 5.18: $\bar{T}_{acq}$ versus ζ. SNR = 20 dB, $N_c = 64$. CM3.

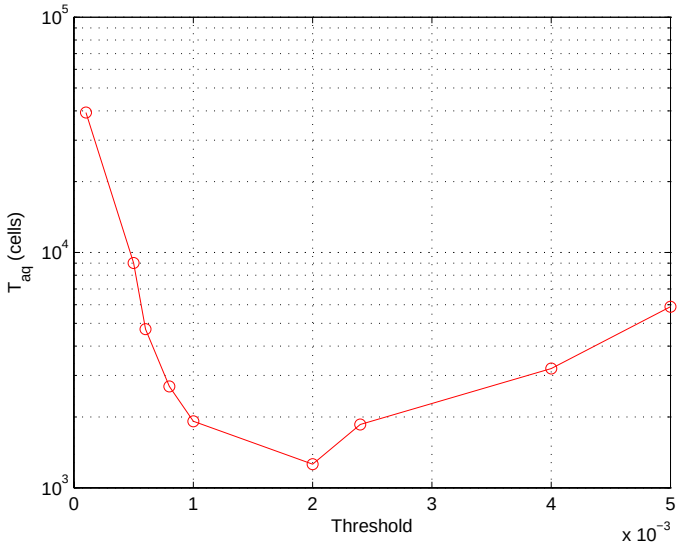

Figure 5.19: $\bar{T}_{acq}$ versus ζ. SNR = 20 dB, $N_c = 64$. CM4.

Although jump-phase search reduces acquisition time, it may lead to a large timing error, because it locks into an arbitrary H_1 cell, not the earliest H_1 cell. In Figure 5.20, jump-phase search is performed on 542 different channel profiles at very high SNR (in order to neutralize the effect of noise on the error). The computed mean timing error is 3.5057 nsec. In some severe cases, errors exceeding 20 nsec are observed. This is an unacceptable error; it would lead to a ranging error of 20 feet in a position location application, for example. An additional stage which reduces this error must be included. The next section discusses such a stage.

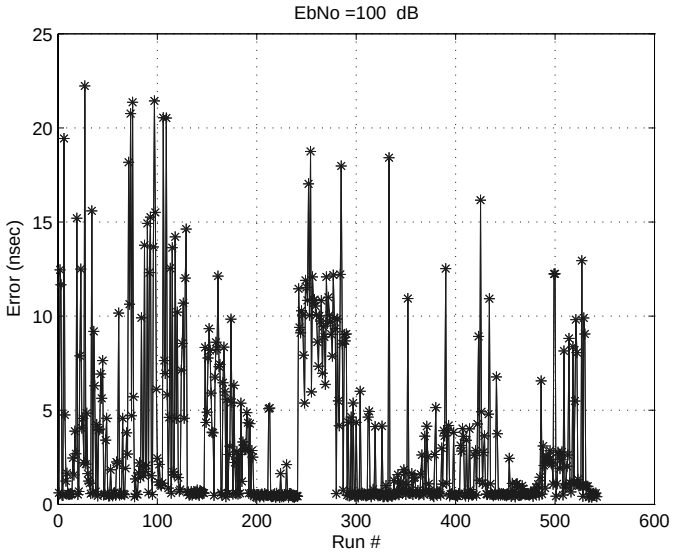

Figure 5.20: Timing error produced by jump-phase search. 542 real channel profiles. $\frac{E_p}{N_0} = 100\ dB$.

5.8 Proposed Second Stage: Fine Acquisition

The coarse acquisition stage locks onto an arbitrary multipath component. This is unsuitable for both ranging and communications applications, since it respectively leads to large ranging errors and significant loss in symbol energy capture. We propose a method to capture the earliest arriving path in this section.

Let $\hat{\tau}$ be the delay estimated by the first stage. Since the H_1 region spans T_f seconds, we know that the first arriving path delay belongs to the interval $[\hat{\tau} - T_f, \hat{\tau}]$. The fine acquisition stage performs an additional search in this reduced uncertainty region. This stage is formed of two steps. First, a threshold crossing test

is performed, using a newly calculated threshold. Then, an additional test is performed to segregate H_0 cells and detect the earliest H_1 cell, by taking advantage of the clustered nature of the multipath channel. We will discuss these two steps in the following subsections.

5.8.1 Step One: Second Level Threshold Crossing

In the coarse acquisition stage, the noise power is unknown, and the threshold setting mechanism cannot take SNR information into account with a simple procedure. However, since the H_1 region has been identified to within C_{in} cells at the end of coarse acquisition, an estimate of the noise variance can now be obtained by calculating the average of the decision statistics over the H_0 region. Any bias can be eliminated by not incorporating any cell within T_f of $\hat{\tau}$ in the averaging operation. The variance estimate is then given by:

$$\hat{\sigma}^2 = \frac{1}{\|\hat{C}\|} \sum_{c_n \in \hat{C}} d^2_{\hat{\tau}_n} \tag{5.32}$$

where $\hat{C}$ is the set of cells $c_i,\ 1 \leq i \leq \|\hat{C}\|$, tested in coarse acquisition such that $|\hat{\tau}_i - \tau| \geq T_f$, where $\hat{\tau}_i$ is the delay associated with c_i. If the set is empty, the system is reset to the coarse acquisition stage, since a reliable variance estimate may not be obtained.

Note that the large number of cells in the original uncertainty region is exploited to lead to a robust variance estimate. The new threshold $\zeta^{'}$ is set to ensure a constant false alarm rate. Assuming we require that any H_0 cell fails the test with probability P_e, we write:

$$P(d^2_\tau < \zeta^{'}) = erf\left(\frac{\sqrt{\zeta^{'}}}{\sigma\sqrt{2}}\right) = P_e \tag{5.33}$$

Then, the threshold is set as:

$$\zeta^{'} = 2\hat{\sigma^2}\left(erf^{-1}(P_e)\right)^2. \tag{5.34}$$

All cells in the reduced uncertainty region with decision statistics falling below $\zeta^{'}$ are eliminated. The second step of the fine search takes the indices of the surviving cells as input.

5.8.2 Step Two: H_0 Cell Segregation

Let C_s be the number of cells that passed the first phase of the fine acquisition stage. We denote their indices by X_j, $1 < j < C_S$. These cells are further tested as follows. For a particular cell X_k, we calculate t_k, the time difference between X_k and its closest neighboring survivor cell X_{k+1}. If t_k exceeds a predefined constant t_0, then cell X_k is eliminated. After all cells are tested, the earliest surviving cell is selected. The rationale behind this method is based on the clustered nature of multipath. Since multipath occurs in clusters, as will be clarified shortly, it is most likely that the multipath cluster will result in a group of neighboring surviving cells. If, on the other hand, an isolated cell exceeds the threshold, it is most likely an H_0 cell. Assuming $\Delta\tau = T_w$ and $t_0 = cT_w$, where c is an integer, the new false alarm probability is then:

$$p_{fa} = 1 - P_e - (1 - P_e)(P_e)^c. \tag{5.35}$$

The probability of detecting the first path will only be slightly reduced by this method, because there is most likely another path crossing the threshold in its vicinity. We shed light on the proposed algorithm by adopting a realistic indoor channel model, based on the IEEE P802.15 model proposed for UWB [24]. The model channel impulse response is given by:

$$h(t) = \sum_{u=1}^{U} \sum_{l=1}^{L} \alpha_{ul} \delta(t - T_c - \tau_{ul}) \tag{5.36}$$

The model assumes that multipath occurs in clusters. The number of clusters is U, and there are L paths in each cluster. Since we are interested in the first arriving path, we restrict our analysis to the first cluster. The path inter-arrival time in the first cluster follows an exponential distribution:

$$p(\tau_k|\tau_{k-1}) = \lambda exp[-\lambda(\tau_k - \tau_{k-1})] \tag{5.37}$$

where λ is the path arrival rate,and τ_{k-1} and τ_k are the delays associated with the $(k-1)$-th and k-th paths, respectively. Assuming the first path arrives at time zero ($\tau_1 = 0$), the probability that the second path

occurs before time T can be calculated as:

$$P_T = P\left(\tau_2 < T | \tau_1 = 0\right) = 1 - exp\left[-\lambda T\right]. \tag{5.38}$$

Moreover, the path amplitudes in the first cluster are given by:

$$\alpha_l = \pm\beta_l, \tag{5.39}$$

where β_l is a lognormal random variable, $\beta_l = 10^{\frac{n}{20}}$, where n is a Gaussian distribution with mean μ_l and standard deviation σ_L. μ_l is given by:

$$\mu_l = \frac{10ln\left(\Omega_0\right) - 10\frac{\tau_l}{\gamma}}{ln(10)} - \frac{\sigma_L^2 ln(10)}{20} \tag{5.40}$$

where γ is the ray decay factor, and Ω_0 is the average received power in the first arriving path.

The pdf of β_l can be shown to be:

$$f_{x_l}(x) = \frac{1}{r} x^{\frac{1}{r}-1} . \frac{1}{x^{\frac{1}{r}}\sqrt{2\pi\sigma_L^2}} exp\left[-\frac{\left(20log_{10}x - \mu\right)^2}{2\sigma_L^2}\right] \tag{5.41}$$

where $r = \frac{ln(10)}{20}$.

By integrating Equation (5.21) over the PDF in Equation (5.41), the probability of the l^{th} path exceeding the threshold can be expressed as:

$$P_{Dl} = \int_0^\infty f_{x_l}(x) . \left[1 - \frac{1}{2}\left[erf\left(\frac{\sqrt{\zeta} - x}{\sigma\sqrt{2}}\right) + erf\left(\frac{\sqrt{\zeta} + x}{\sigma\sqrt{2}}\right)\right]\right] dx \tag{5.42}$$

The first path passes the fine acquisition test if its associated metric exceeds $\zeta^{'}$ and another path occurs before time $T = cT_w$ and also exceeds $\zeta^{'}$. We simplify the expression by assuming that at most one path occurs before time T. Then, the new probability of detection is:

$$P_D \approx P_T . P_{D1} . P_{D2}. \tag{5.43}$$

The delay of the second path is set to T when calculating P_{D2}, ensuring the expression is an upper bound for performance. Simulation will show that the probability of detecting the LOS path is only marginally decreased, while the probability of false alarm falls substantially.

Finally, note that the optimal value of c depends on the multipath channel's statistical properties. The setting mechanism of this parameter must exploit any available *a priori* information. If no such information is available, a training phase is required, where the statistical characteristics of the clustered multipath is analyzed.

5.8.3 Numerical Results

The performance of the acquisition stage is tested through numerical evaluation. Parameter c for the fine acquisition stage is equal to 7, and $P_e = 0.999$. The channel's main characteristics matched to the 802.15 channel model are $\gamma = 17$ nsec, $\lambda^{-1} = 0.5$ nsec, $\sigma_L = 5$ dB, and Ω_0 is 6% of the total received power.

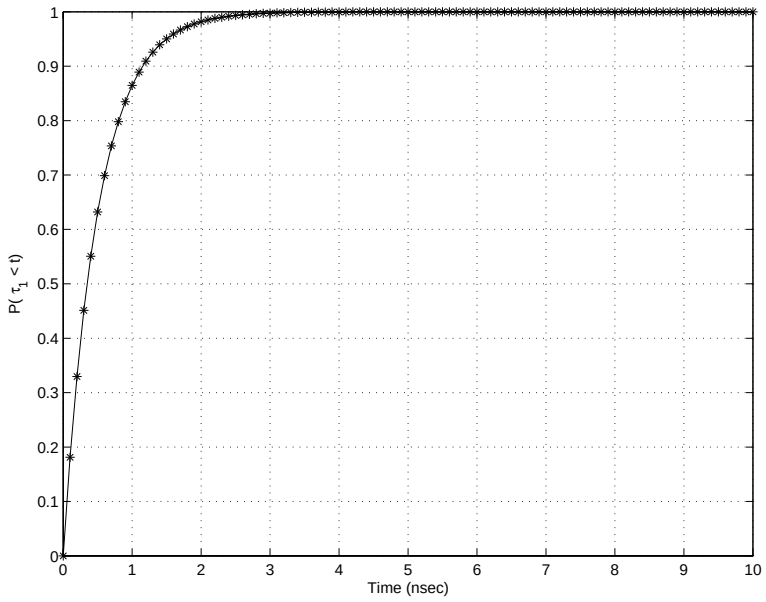

Figure 5.21: Probability for second path to occur before t seconds in the IEEE P802.15 channel model.

Assuming the first arriving path occurs at time zero, the probability of the second path occurring before T seconds is displayed in Figure 5.21, by numerically evaluating Equation (5.38). The probability of the path occurring before $T = 7T_w$ (or 3.5 nanoseconds) is equal to 0.9991. We are therefore almost guaranteed that the second path is within 7 cells of the first path. It remains to see if this path exceeds the threshold.

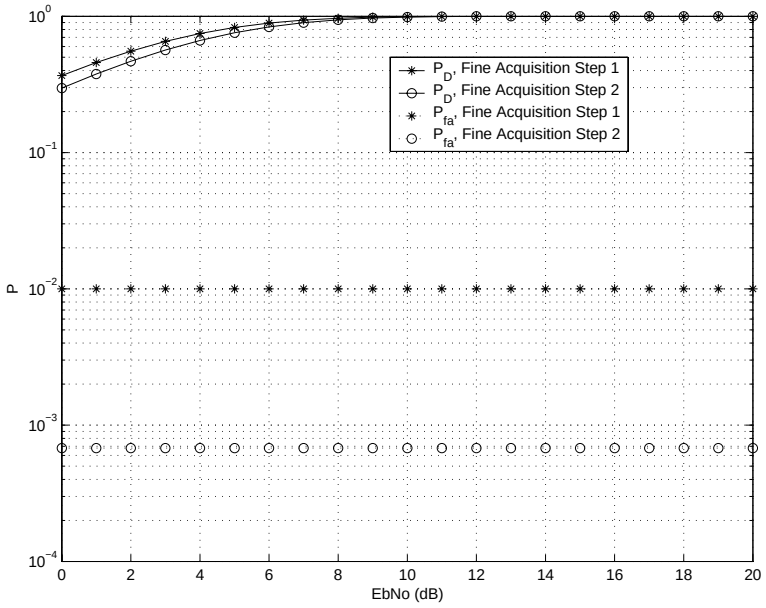

Figure 5.22: Probabilities of false alarm and detection before and after second step in fine acquisition.

The probabilities of path detection and false alarm before and after the second step of fine acquisition are obtained by numerically evaluating Equations (5.35) and (5.43) (Figure 5.22). Notice that the probability of false alarm is reduced by more than an order of magnitude, while the probability of detecting the first path only decreases slightly, especially for high SNR. Since the H_0 cells are independent, and neighboring H_1 cells exhibit high correlation due to the clustering effect, the probability of detecting an H_0 cell drops significantly, while the probability of detecting the first H_1 cell remains nearly constant. Note that $\frac{E_p}{N_0}$ in Figure 5.22 refers to the *total* pulse energy to noise ratio, that is, the energy of all the multipath components. The energy in the first arriving path is only a fraction of the total energy, and therefore the *effective* path energy to noise ratio is much smaller than $\frac{E_p}{N_0}$.

5.9 Case Study: Acquisition for a Ranging Application

The performance of the acquisition scheme in a ranging application is tested as follows. For a specific channel profile, the timing error for traditional acquisition (no fine stage) and the proposed scheme are mapped to a distance error, based on $d = v.t$, where v is the speed of light, and d and t are the range and timing errors respectively. In a first experiment, 32 different channel profiles are examined. The system is first tested for

the high SNR case (Figure 5.23). Notice that the ranging error caused by locking into an arbitrary multipath in the traditional acquisition stage is drastically reduced when the proposed scheme is applied. In fact, the mean ranging error (calculated over all simulated channel profiles) is reduced from 1.47 meters to less than 5 centimeters. For a more realistic setting where $\frac{E_p}{N_0} = 15$ dB and N_c=64 (Figure 5.24), the error is reduced from 2.35 meters to around 40 centimeters. Note that E_p is the total energy in all multipath components; only a fraction of this energy is contained in the LOS path.

Additional simulations are carried to illustrate the importance of the fine acquisition stage. The timing error is simulated for three systems: A system employing coarse acquisition only, a system employing coarse acquisition plus the first step of the fine acquisition stage (no H_0 cell segregation), and the proposed system (coarse acquisition, plus two-step fine acquisition). 542 different channel profiles are examined, and the results are averaged over multiple noise realizations. The system is tested for $\frac{E_p}{N_0} = 15\ dB$ (Figure 5.25, where only the ranging errors for the first 180 profiles are displayed, for clarity). First, notice that locking onto an arbitrary multipath after the coarse acquisition stage leads to a relatively large error. The average range error for the first system is 108.27 centimeters. Also, notice that the first step of the fine acquisition stage leads to unacceptable error, because acquisition is erroneously locking into an H_0 cell in the reduced uncertainty region. The mean absolute error for that system is 387.85 centimeters. Finally, note that the error is drastically reduced when the second step of fine acquisition is applied. H_0 cells are efficiently segregated by exploiting the clustered nature of the multipath. The mean ranging error for the proposed model is 45.3 centimeters.

5.9.1 Optimization of Parameter c

The performance of the fine acquisition stage is highly dependent on the choice of parameter c. In fact, on one hand, for very small values of c, the period t_0 (against which the distance between consecutive surviving cells is tested) drops below the average multipath inter-arrival time, and detection of the LOS component is missed, causing large ranging errors. On the other hand, if c is too large, the probability of false alarm in (5.35) grows, and the likeliness of locking on a noise cell increases.

In the case of perfect knowledge of the system's parameters (such as transmit power, noise power, and the

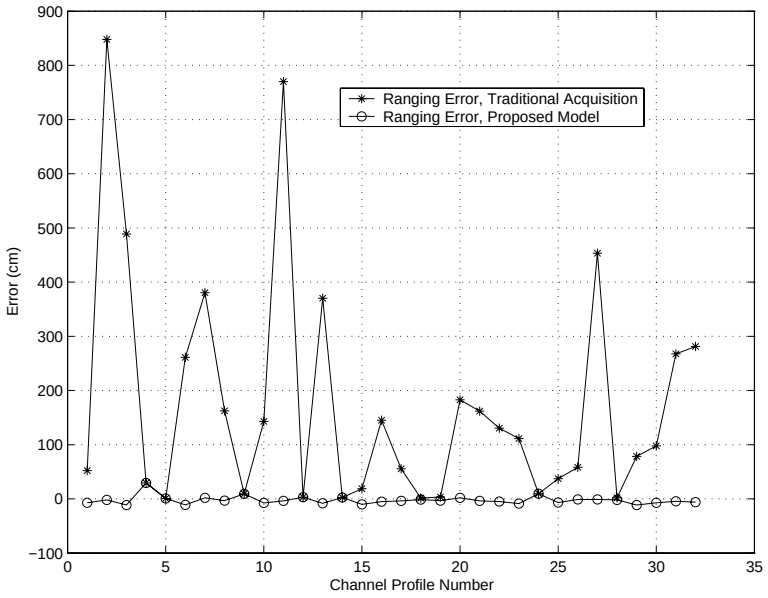

Figure 5.23: Performance of fine acquisition stage in ranging. High SNR Case. 32 real measured channel profiles are used.

channel's statistical properties), the optimal value of c may be numerically evaluated. In absence of such knowledge, a training stage is required. The details of the training stage are not discussed here; we rather rely on a generic training method which showcases the effect of c on the ranging error. The procedure is as follows. For a specific set of system parameters, the acquisition algorithm is applied for different values of c, and the ensuing ranging errors are recorded. The experiment is averaged over a large number of channel realizations. The optimal value of c is the one which minimizes the average ranging error.

Simulations are run for the four basic channel types CM1, CM2, CM3 and CM4 (see simulation results in section 5.7, and the results are plotted in Figures 5.26, 5.27, 5.28 and 5.29, respectively. Note the presence of an optimal c for all four cases. Also, note that the optimal value varies across channel models, which is expected, since the design of c largely depends on the statistical properties of the channel.

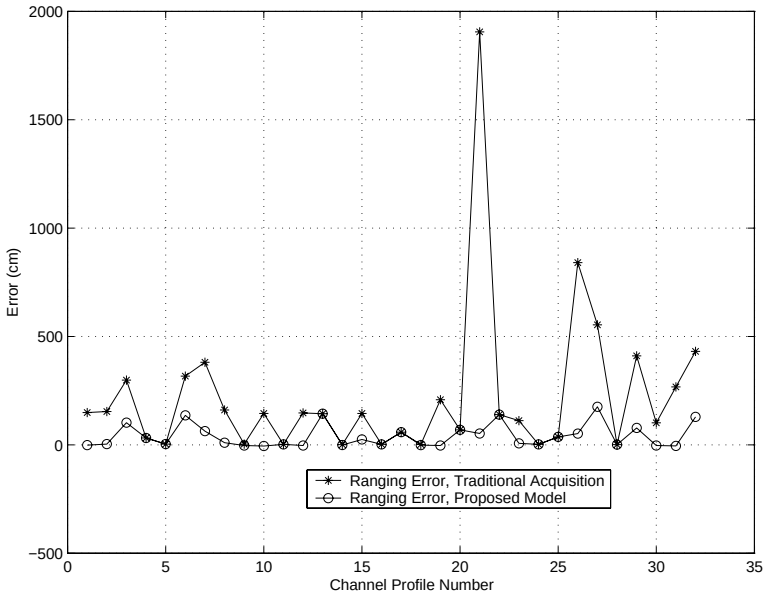

Figure 5.24: Performance of Fine Acquisition in ranging. $N_c = 64$. $\frac{E_p}{N_0} = 15$ dB. 32 real measured channel profiles are used.

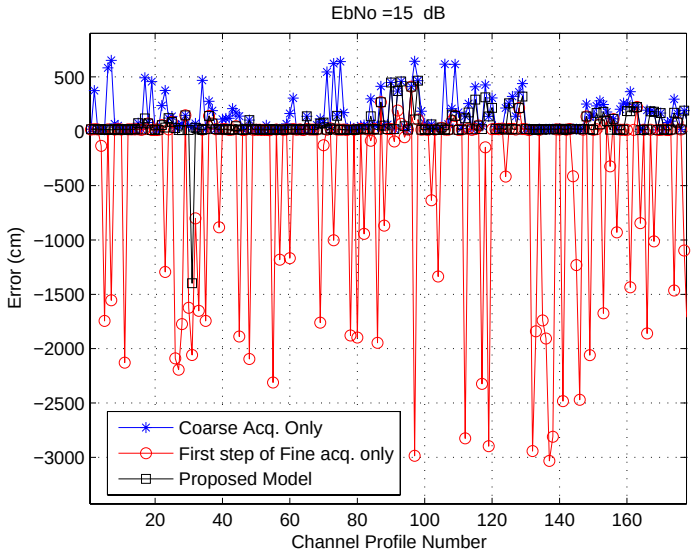

Figure 5.25: Performance of Fine Acquisition in ranging. $N_c = 64$. $\frac{E_p}{N_0} = 15$ dB. 542 real measured channel profiles are used.

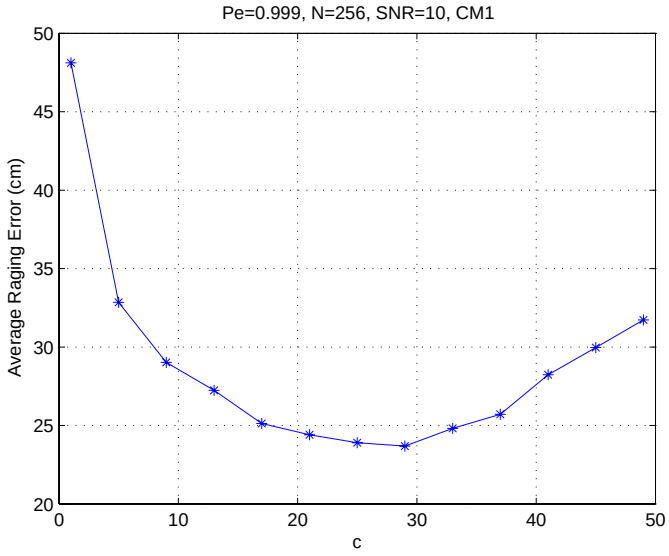

Figure 5.26: $\bar{T}_{acq}$ versus c. P_e=0.999, SNR = 10 dB (relative to entire received signal power), $N_c = 256$. CM1.

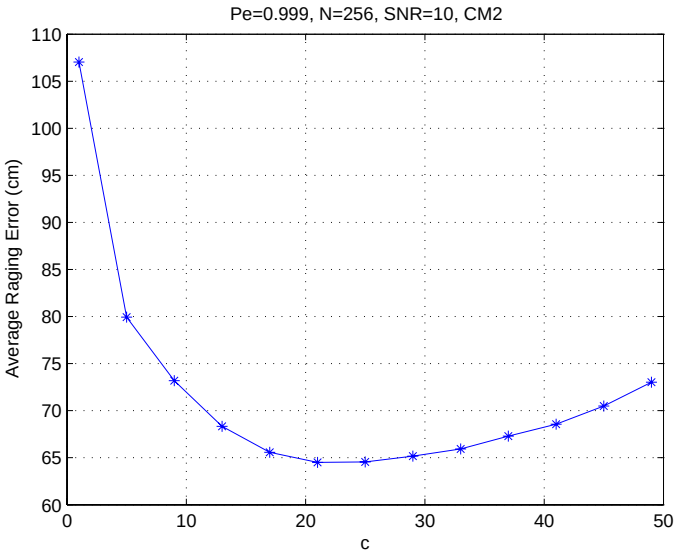

Figure 5.27: $\bar{T}_{acq}$ versus c. P_e=0.999, SNR = 10 dB, $N_c = 256$. CM2.

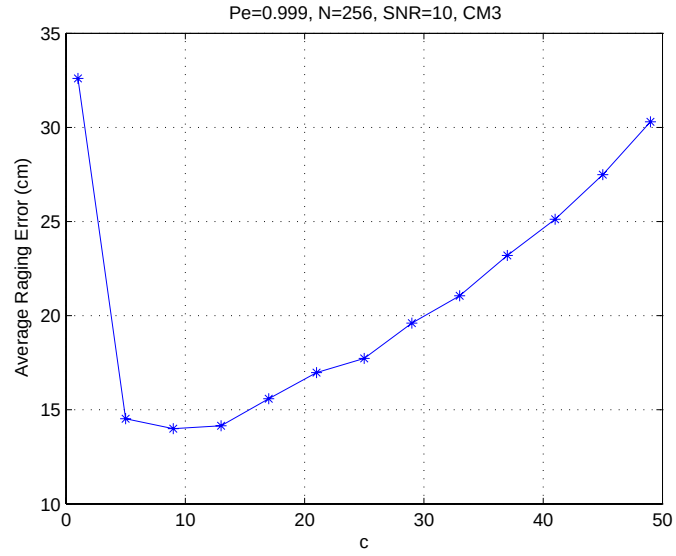

Figure 5.28: $\bar{T}_{acq}$ versus c. P_e=0.999, SNR = 10 dB, $N_c = 256$. CM3.

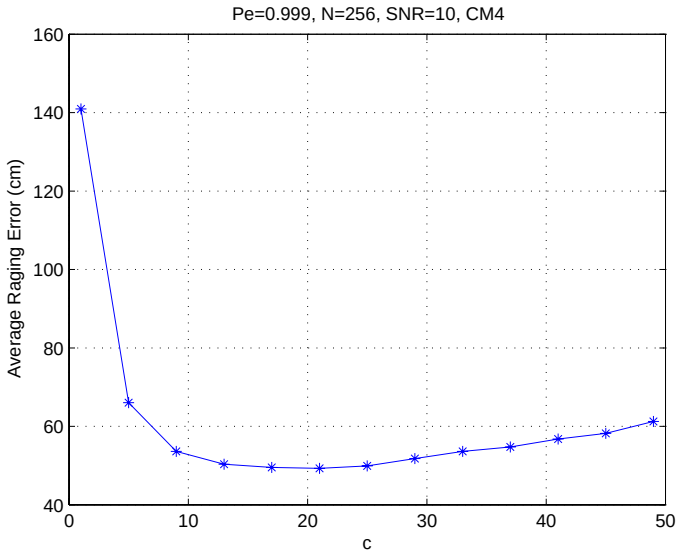

Figure 5.29: $\bar{T}_{acq}$ versus c. P_e=0.999, SNR = 10 dB, $N_c = 256$. CM4.

5.10 Case Study: Acquisition for a Pilot-Assisted Receiver

5.10.1 Probability of Error in Presence of Timing Error

The impact of coarse acquisition on UWB communications is less intuitive than its impact on ranging. In this section, we illustrate the effect of acquisition error on UWB communications and the effectiveness of the proposed model by employing the pilot-assisted receiver (studied in section 3.8) as an example. Recall that the main limitation of the pilot-assisted receiver is their reliance on a noisy template, which results in a "noise-cross-noise" term [35] after correlation. A large number of pilot symbols is required to limit this effect.

In the following discussion, it is assumed that the pilot-assisted template is obtained by despreading the length-N_c acquisition preamble after acquisition is terminated. Since the training sequence is formed of N_c noisy copies of the received signal, the template is constructed by coherently adding these copies. No additional channel estimation overhead is thus required.

Assume that the real symbol delay is 0, and the delay estimated by the coarse acquisition stage is $\hat{\tau}$. Then, the preamble will not sum coherently on the interval $[0, \hat{\tau}]$, and its amplitude will be divided by N_c, due to the spreading gain. The correlator template $h(t)$ can be written as:

$$h(t) = \begin{cases} -\frac{1}{N_c}\sqrt{E_p}v(t) + n_p(t), & 0 \le t \le \hat{\tau} \\ \sqrt{E_p}v(t) + n_p(t), & \hat{\tau} \le t \le T_f \end{cases} \tag{5.44}$$

where $v(t) = \sum_{l=1}^{L} \alpha_l w(t - \tau_l)$ is the *received* pulse shape, and $n_p(t)$ is a zero-mean white Gaussian noise random process with PSD $\frac{N_0}{2N_c}$. Now, assuming binary bipolar data modulation, the received data signal is:

$$r_d(t) = \sqrt{E_p} \sum_{j=-\infty}^{\infty} b_j v(t - jT_f) + n_d(t) \tag{5.45}$$

where $n_d(t)$ is zero-mean white Gaussian noise with PSD $\frac{N_0}{2}$, and $b_j = \pm 1$ are the data bits. Since the noise-cross-noise term overwhelms performance in the absence of a front-end bandlimiting filter ([49], also see section 3.8), we assume that the data and template signals pass through a bandpass filter of bandwidth

W and center frequency f_c before correlation is performed. Let $R_{nd}(\tau)$ and $R_{np}(\tau)$ be the autocorrelation functions of $n_d(t)$ and $n_p(t)$ after filtering, respectively. Then:

$$R_{n_d}(\tau) = N_o W sinc(W\tau) cos(2\pi f_c \tau). \tag{5.46}$$

$$R_{n_p}(\tau) = \frac{N_o}{N_c} W sinc(W\tau) cos(2\pi f_c \tau). \tag{5.47}$$

Let g_k be the decision statistic corresponding to bit b_k. Then,

$$\begin{aligned} g_k = \int_0^{T_f} h(t).r_d(t + kT_f + \hat{\tau})dt = \int_{\hat{\tau}}^{T_f} \left[\sqrt{E_p}v(t) + n_p^{'}(t)\right].\left[b_k\sqrt{E_p}v(t) + n_d^{'}(t)\right]dt \\ + \int_0^{\hat{\tau}} \left[-\frac{\sqrt{E_p}}{N_c}v(t) + n_p^{'}(t)\right].\left[b_{k+1}\sqrt{E_p}v(t) + n_d^{'}(t)\right]dt \end{aligned} \tag{5.48}$$

where $n_p^{'}(t)$ and $n_d^{'}(t)$ are the filtered versions of $n_p(t)$ and $n_d(t)$, respectively. The distortion caused by the filter on $v(t)$ is neglected. g_k can be expressed as:

$$\begin{aligned} g_k &= E_p b_k \int_{\hat{\tau}}^{T_f} v^2(t)dt - \frac{1}{N_c}E_p b_{k+1}\int_0^{\hat{\tau}} v^2(t)dt + \int_0^{T_f} n_d^{'}(t).n_p^{'}(t)dt + \sqrt{E_p}b_k\int_{\hat{\tau}}^{T_f} v(t)n_p^{'}(t)dt \\ &+ \sqrt{E_p}b_{k+1}\int_0^{\hat{\tau}} v(t)n_p^{'}(t)dt + \sqrt{E_p}\int_{\hat{\tau}}^{T_f} v(t)n_d^{'}(t)dt - \frac{1}{N_c}\sqrt{E_p}\int_0^{\hat{\tau}} v(t)n_d^{'}(t)dt \end{aligned} \tag{5.49}$$

By noting that b_k and b_{k+1} are independent (and thus the effect of the second term on the right hand side of the equality is averaged out statistically), and that the last term on the right hand side of the equality is negligible because of the spreading gain, we can write:

$$\begin{aligned} g_k &\approx E_p b_k \int_{\hat{\tau}}^{T_f} v^2(t)dt + \int_0^{T_f} n_d^{'}(t).n_p^{'}(t)dt + \sqrt{E_p}b_k\int_{\hat{\tau}}^{T_f} v(t)n_p^{'}(t)dt \\ &+ \sqrt{E_p}b_{k+1}\int_0^{\hat{\tau}} v(t)n_p^{'}(t)dt + \sqrt{E_p}\int_{\hat{\tau}}^{T_f} v(t)n_d^{'}(t)dt \end{aligned} \tag{5.50}$$

Assuming $b_k = 1$ without loss of generality, the mean value of g_k is given by:

$$\mu_g = E_p \int_{\hat{\tau}}^{T_f} v^2(t)dt. \tag{5.51}$$

After some tedious but straightforward calculations, the total variance of g_k is found to be:

$$\sigma_g^2 = \frac{N_o^2}{N_c} Z_1\left(0, T_f\right) + E_p N_o \frac{1}{N_c}\left[Z_2\left(\hat{\tau}, T_f\right) + Z_2\left(0, \hat{\tau}\right)\right] + E_p N_o Z_2\left(\hat{\tau}, T_f\right) \tag{5.52}$$

where:

$$Z_1\left(\tau_1, \tau_2\right) \;=\; W^2 \int_{\tau_1}^{\tau_2} \int_{\tau_1}^{\tau_2} sinc^2(W(t-\lambda)) cos^2(2\pi f_c(t-\lambda)) dt d\lambda \tag{5.53}$$

$$Z_2\left(\tau_1, \tau_2\right) \;=\; W \int_{\tau_1}^{\tau_2} \int_{\tau_1}^{\tau_2} v_0(t) v_0(\lambda) sinc(W(t-\lambda)) cos(2\pi f_c(t-\lambda)) dt d\lambda. \tag{5.54}$$

It can be shown that g_k can be approximated by a Gaussian random variable [35]. Then, the probability of bit error can be expressed as:

$$P_e = Q\left(\frac{\mu_g}{\sqrt{\sigma_g^2}}\right) = Q\left(\sqrt{\frac{E_p}{N_o} . \frac{\left[\int_{\hat{\tau}}^{T_f} v^2(t) dt\right]^2}{\left(\frac{N_c E_p}{N_o Z_1(0,T_f)}\right)^{-1} + \frac{(N_c+1) Z_2(\hat{\tau}, T_f) + Z_2(0,\hat{\tau})}{N_c}}}\right) \tag{5.55}$$

The probability of error of the iterative data-aided version of the pilot-assisted system (studied in section 3.8) may be derived along similar lines, and is found to be:

$$p_{n,\tau} = Q\left(\sqrt{\frac{E_p}{N_o} . \frac{\left(1-2p_{n-1}\right)^2 \left[\int_{\hat{\tau}}^{T_f} v^2(t) dt\right]^2}{\left(\frac{N_d E_p}{N_o Z_1(0,T_f)}\right)^{-1} + \left[\frac{1}{N_d} + \left(1-2p_{n-1}\right)^2\right] Z_2\left(\hat{\tau}, T_f\right) + \frac{Z_2(0,\hat{\tau})}{N_d}}}\right) \tag{5.56}$$

where N_d is the number of data symbols per frame, and p_n and p_{n-1} are the probabilities of error for the n^{th} and $(n-1)^{th}$ iterations, respectively.

Notice that the numerator in both error probability expressions decreases with increasing $\hat{\tau}$. The symbol energy in the interval $[0, \hat{\tau}]$ is lost. Moreover, the noise-cross-noise term X_1 is independent of $\hat{\tau}$. Thus, in the presence of acquisition error, the energy capture of the pilot-assisted receiver drops, while the degradation brought by X_1 remains the same. Simulation results will show that the loss in energy capture is critical if traditional acquisition methods are used, and performance is overwhelmed by the noise-cross-noise term. It

will also be shown that the proposed acquisition method significantly increases energy capture by decreasing $\hat{\tau}$, thus bringing performance close to the perfect synchronization case.

5.10.2 Simulation Results

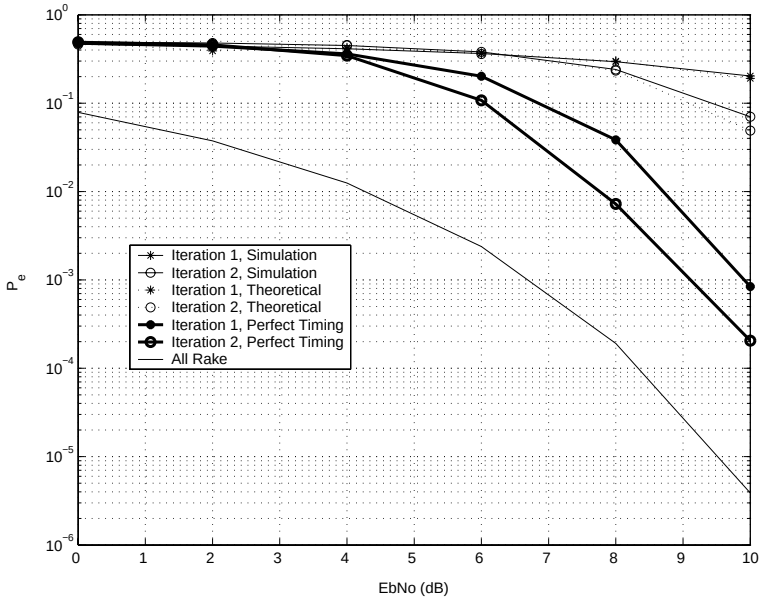

Figure 5.30: Data-aided iterative receiver. $N_p = 10$. $N_d = 100$. Timing Error = 16 nsec. Symbol length = 80 nsec.

The communication systems tested in this section are the traditional and data-aided pilot-assisted receivers from section 3.8. The probability of error performance for an arbitrary NLOS channel profile with an initial timing error of 16 nsec is simulated and compared to the theoretical expression (Equation (5.56)) in Figure 5.30. Note that the simulated and theoretical curves match with negligible error. Also, note the severe performance degradation brought by the initial timing error.

The performance for the generic pilot-assisted receiver based on a template generated after acquisition using only coarse acquisition and two-stage acquisition is simulated with $N_c = 256$ (Figure 5.31). Notice that traditional acquisition results in a significant performance degradation in bit error probability (about 4 dB compared to the perfect synchronization case), because a substantial part of the symbol energy is not captured by the template. Most of this energy is gathered by applying fine acquisition. In fact, performance after fine acquisition is within half a dB from theoretical performance assuming perfect timing.

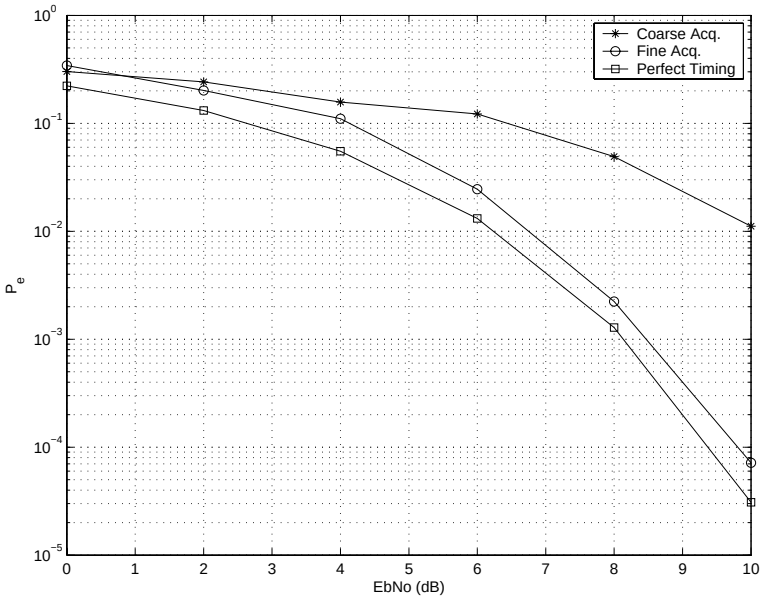

Figure 5.31: Performance of pilot-assisted receiver in presence of acquisition error. $N_c = 256$.

5.11 Tracking for UWB Receivers

Tracking of UWB systems has received little research attention compared to acquisition, and is usually based on the application of traditional SS methods. The most popular investigated tracking method is the delay-lock loop, also called the early-late gate [61][86].

The early-late gate is formed of two correlators, matched to the transmit pulse shape. One correlator starts integrating δ seconds before the estimated delay (initially obtained from acquisition), while the other correlator starts integrating δ seconds after the estimated delay. The early-late gate exploits the symmetry properties of the signal (or code) autocorrelation function. In fact, the autocorrelation function of any pulse is even-symmetric around its maximum. With perfect synchronization, the output of the matched-filter can be viewed as the autocorrelation function sampled at its peak. Therefore, if the estimated delay is correct, the outputs of the early and late branches must be equal in the absence of noise. If the delay is off, however, the branches will give different values. The tracker fixes the delay depending on these values: If the late sample is greater than the early sample, the delay is increased. Else, it is reduced.

The early-late gate was initially analyzed for LOS scenarios in AWGN. The operation of the early-late circuit in the more realistic multipath channel has also received some interest, specifically in the context of SS Rake

receivers. The effect of multipath fading on tracking for a Rake receiver is studied in [81] and [82]. It is shown that as the number of fingers increases, the increase in energy capture is counter-balanced by the error increase in parameter estimation in the tracking stage, and a performance ceiling is observed for a specific number of fingers. Many efforts have concentrated on developing modified Rake tracking circuits with interference mitigation or cancellation capability, where the combined effect of multipath on tracking is treated as unwanted interference (see [116], [117], [118] and [119] for example). Although these references discuss SS systems, their findings may be applied to tracking for UWB Rake receivers, since the problem's framework is essentially the same, except that more interference should be expected for UWB systems, because of the rich multipath channel structure.

Analysis of tracking specifically applied to UWB has received limited attention lately. The effect of time jitter on the classical early-late gate tracking circuit for a UWB receiver is investigated in [120], and the performance of delay and phase-locked-loops applied to UWB monocycles is studied in [121]. However, both works do not take the effect of multipath into consideration. The effect of multipath on UWB tracking is analyzed in [122], where it is assumed that the tracking loop is already locked on the first arriving multipath component at the start of the tracking process. In that case, the effect of multipath interference is found to be negligible. The same assumption is made in [123], where it is assumed that the circuit is already locked on the line of sight (LOS) component, and the effect of multipath is ignored.

In order for the traditional early-late method to work properly, coarse synchronization must provide a good estimate of the timing delay. For SS systems, the delay must be within a chip of the correct time. For UWB systems, the delay must be within one transmit pulse duration of the correct time. This assumption is suitable for UWB Rake receivers where acquisition provides a good estimate of the delay of the multipath component corresponding to each fingers, and a delay-lock loop with interference cancellation capability such as the ones studied in [116]-[119] are applied. However, the assumption is highly problematic for UWB pilot-based receivers in dense multipath, where the objective of synchronization is to detect the LOS component. In fact, as we have already seen, the LOS path might be severely attenuated compared to other paths. Detection of the LOS component is thus problematic. It is likely that the multipath component detected by the acquisition stage is tens of nanoseconds away from the start of the signal due to the large channel delay

spread. In this case, the classical early-late algorithm would lock on that selected multipath, and would fail in correcting the large delay error, resulting in significant energy loss, and thus unacceptable performance degradation, as studied in section 5.10.

The difference in tracking for Rake and pilot-assisted receivers may be formulated in another fashion. On one hand, tracking for a Rake receiver with F fingers is equivalent to the continuous estimation of F delays corresponding to F separate multipath components. An error in the estimation of one delay results in the loss of energy in the corresponding finger. On the other hand, the tracking circuit of the pilot-assisted receiver must estimate a single delay (corresponding to the LOS component). A large error in the estimation of that delay results in a proportionally large error in template estimation and signal detection, which potentially leads to severe loss in energy capture (the reader is referred to section 5.10 for a mathematical formulation of this argument).

The main limitation of standard tracking techniques applied to UWB pilot-assisted receivers in dense multipath is that they are based on the correlation of the received signal with a local stored reference matched to the *transmit* pulse shape. Delay estimation is based solely on the energy available in the LOS component. Most of the received energy is effectively squandered. An alternative and more efficient method is to use the *received* pulse shape rather than the transmit pulse shape as the tracker's template. This strategy parallels the signal detection method used for the pilot-assisted receiver, where the received pulse shape was used as a template for the correlator for signal detection. Such an algorithm is presented in the next section.

5.12 Proposed Tracking System

We use the notation used in section 5.10. Assume that the acquisition error $\hat{\tau}$ is much larger than the pulse width T_w ($\hat{\tau} > nT_w$, where n is a positive integer). A traditional tracking circuit based on the transmit pulse shape (such as the early-late gate [61]) would lock into the multipath component that is in the vicinity of the estimated delay, and would not be able to track the LOS component. In this section, we propose a modified tracking algorithm which will correct such a delay error.

The algorithm is presented in Figure 5.32. Consider the following two intervals:

- The interval $[kT_f + \hat{\tau} - \Delta\tau, kT_f + \hat{\tau}]$ (modulated by data bit b_k), termed the kth early interval.

- The interval $[(k+1)T_f + \hat{\tau}, (k+1)T_f + \hat{\tau} + \Delta\tau]$ (modulated by data bit b_{k+1}), termed the kth late interval.

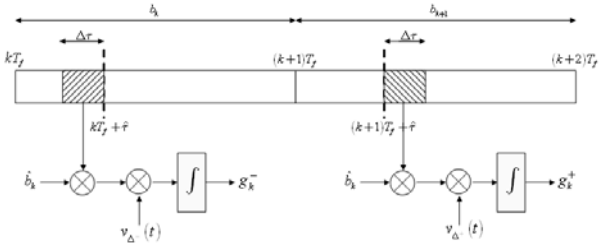

Figure 5.32: Tracking algorithm diagram.

The algorithm produces two "mini-metrics" g_k^- and g_k^+ which measure the energy content of the kth early and the kth late interval, respectively. An early metric G^- and a late metric G^+ are then computed by summing the mini-metrics of all early and late intervals. The timing delay is modified based on the magnitude of the difference in energy $G = G^- - G^+$.

g_k^- and g_k^+ are generated as follows. First, data modulation is removed by multiplying both intervals by $\hat{b}_k$, where $\hat{b}_k$ is the current estimate of b_k (note that $\hat{b}_k = b_k$ with probability $P_{e,\hat{\tau}}$ given by (5.55)). The early and late intervals are then respectively multiplied by an early and late "mini-template" and integrated.

The early "mini-template" is estimated by coherently adding the demodulated early intervals $[\hat{\tau} - \Delta\tau + kT_f, \hat{\tau} + kT_f]$, $0 \le k \le N_d - 1$:

$$v_{\Delta_-}(t) = \frac{1}{N_d} \sum_{k=0}^{N_d-1} \hat{b}_k r\left(t + kT_f + N_c T_f\right). \tag{5.57}$$

The late mini-template is likewise defined on $[\hat{\tau}, \hat{\tau} + \Delta\hat{\tau}]$ as:

$$v_{\Delta_+}(t) \quad = \quad \frac{1}{N_d} \sum_{k=1}^{N_d} \hat{b}_{k-1} r\left(t + kT_f + N_c T_f\right). \tag{5.58}$$

Then:

$$g_k^- = \hat{b}_k \int_{\hat{\tau}-\Delta\tau}^{\hat{\tau}} r(t + N_c T_f + kT_f) v_{\Delta^-}(t) dt \tag{5.59}$$

$$g_k^+ = \hat{b}_k \int_{\hat{\tau}}^{\hat{\tau}+\Delta\tau} r(t + N_c T_f + (k+1)T_f) v_{\Delta^+}(t) dt. \tag{5.60}$$

The early and late metrics are given by:

$$G^- = \frac{1}{N_d} \sum_{k=0}^{N_d-1} g_k^- \tag{5.61}$$

$$G^+ = \frac{1}{N_d - 1} \sum_{k=0}^{N_d-2} g_k^+. \tag{5.62}$$

If $G = G^- - G^+$ exceeds a pre-defined positive threshold Ψ, then the symbol delay is decreased by a time step $\delta\tau$. If $G < -\Psi$, the delay is increased by $\delta\tau$. Else, it is assumed that the intervals do not contain sufficient energy, and the delay is not modified[¶].

In this work, the algorithm is deployed iteratively. Let $\hat{\tau}_i$ be the estimated symbol delay at the ith iteration. A new template $\hat{v}_{\hat{\tau}_i}$ is estimated based on the new timing delay:

$$\hat{v}_{\hat{\tau}_i}(t) = \frac{1}{N_d} \sum_{k=0}^{N_d-1} \hat{b}_k r^{'}(t + kT_f + N_c T_f + \hat{\tau}_i),\ 0 \le t \le T_f. \tag{5.63}$$

Then, new bit estimates are generated based on $\hat{v}_{\hat{\tau}_i}(t)$. The decision metric G is recalculated, and the delay is fixed accordingly. Note that since the iterative template estimation employs N_d data symbols, the effect of the noise-cross-noise term (see section 3.8) is reduced as more bits are estimated correctly (since $N_d >> N_c$ in general).

The system's metric statistics are derived in the next section.

5.13 Tracking System Analysis

The early mini-template $v_{\Delta_-}(t)$ can be written as:

$$v_{\Delta_-}(t) = \frac{\sqrt{E_p}}{N_d} \sum_{k=0}^{N_d-1} \hat{b}_k b_k v\,(t) + n_d^{'}(t). \tag{5.64}$$

[¶]Note that Ψ, $\delta\tau$ and $\Delta\tau$ are system parameters set by the system engineer. The optimal parameter values depend on the operating SNR point and channel statistics.

where $n_d^{'}(t)$ is a filtered Gaussian noise process with pre-filtered PSD $\frac{N_0}{2N_d}$. For N_d large enough, we can write:

$$s_{\Delta_-}(t) \approx (1 - 2P_{e,\hat{\tau}}) \sqrt{E_p} v(t) + n_d^{'}(t) \tag{5.65}$$

where $P_{e,\hat{\tau}}$ is given by (5.55).

Following a similar approach, and since b_{k-1} and b_k are independent, $v_{\Delta_+}(t)$ may be written as[‖]:

$$v_{\Delta_+}(t) \approx n_{d2}^{'}(t), \tag{5.66}$$

where $n_{d2}^{'}(t)$ is filtered Gaussian noise with pre-filtered PSD $\frac{N_0}{2N_d}$.

The kth early mini-statistic can be written as:

$$\begin{aligned} g_k^- &= E_p \hat{b}_k b_k (1 - 2P_{e,\hat{\tau}}) \int_{\hat{\tau}-\Delta\tau}^{\hat{\tau}} v^2(t)dt + \sqrt{E_p} \hat{b}_k b_k \int_{\hat{\tau}-\Delta\tau}^{\hat{\tau}} v(t) n_d^{'}(t)dt \\ &+ \sqrt{E_p} \hat{b}_k (1 - 2P_{e,\hat{\tau}}) \int_{\hat{\tau}-\Delta\tau+kT_f}^{\hat{\tau}+kT_f} n^{'}(t) v(t - kT_f) dt + \hat{b}_k \int_{\hat{\tau}-\Delta\tau+kT_f}^{\hat{\tau}+kT_f} n^{'}(t) n_d^{'}(t - kT_f)dt. \end{aligned} \tag{5.67}$$

The mean of g_k^- is given by:

$$\mu_{g^-} = E_p E\left[\hat{b}_k b_k (1 - 2P_{e,\hat{\tau}}) \int_{\hat{\tau}-\Delta\tau}^{\hat{\tau}} v^2(t)dt\right] + E\left[\hat{b}_k \int_{\hat{\tau}-\Delta\tau+kT_f}^{\hat{\tau}+kT_f} n^{'}(t) n_d^{'}(t - kT_f)dt\right]. \tag{5.68}$$

Note that μ_{g^-} contains a non-zero mean noise term, because the noise in the early template is partially correlated with the noise in the data symbol. The mean is found to be:

$$\mu_{g^-} = E_p (1 - 2P_{e,\hat{\tau}})^2 \int_{\hat{\tau}-\Delta\tau}^{\hat{\tau}} v^2(t)dt + \frac{N_o W}{N_d} \Delta\tau. \tag{5.69}$$

In a similar fashion, the mean of the kth late mini-statistic is:

$$\mu_{g^+} = \frac{N_0 W}{N_d} \Delta\tau. \tag{5.70}$$

[‖]Note that $v_{\Delta_+}(t)$ is a noise-only template because $\hat{\tau} > 0$. In the case $\hat{\tau} < 0$, $v_{\Delta_-}(t) \approx n_d^{'}(t)$.

Note that if $\Delta\tau$ is increased, the observation interval is increased and more signal energy is captured, but more noise is integrated into the metrics.

Note that based on (5.67), g_k^{-2} may be written as the product of two expressions, each formed of the sum of four integrals. The variance of g_k^{2-} may then be computed by evaluating the expected value of each of the resulting 16 elements. The details of the derivation are not included for brevity, and the variance is found to be:

$$\begin{aligned}\sigma_{g-}^2 &= E_p^2\left(1-2P_{e,\hat{\tau}}\right)^2 S^2 + \frac{2}{N_d}E_p.S.\left(1-2P_{e,\hat{\tau}}\right)^2 N_0 X_2^- + \frac{E_p}{N_d}N_0 X_2^- + \frac{2E_p}{N_d}\left(1-2P_{e,\hat{\tau}}\right)^2 N_0 X_2^- \\ &+ E_p\left(1-2P_{e,\hat{\tau}}\right)^2 N_0 X_2^- + \frac{1}{N_d^2}X_3^- + N_0^2\frac{N_d-1}{N_d^2}X_1^- - \mu_{g^-}^2 \end{aligned} \tag{5.71}$$

where S, X_1^-, X_2^- and X_3^- are defined as:

$$\begin{aligned} S &= \int_{\hat{\tau}-\Delta\tau}^{\hat{\tau}} v^2(t)dt \\ X_1^- &= Z_1\left(\hat{\tau}-\Delta\tau,\hat{\tau}\right) \\ X_2^- &= Z_2\left(\hat{\tau}-\Delta\tau,\hat{\tau}\right) \\ X_3^- &= E\left[\int_{\hat{\tau}-\Delta\tau+kT_f}^{\hat{\tau}+kT_f}\int_{\hat{\tau}-\Delta\tau+kT_f}^{\hat{\tau}+kT_f} n'^2(t)n'^2(\lambda)dtd\lambda\right] \end{aligned}$$

and $Z_1\left(\tau_1,\tau_2\right)$ and $Z_2\left(\tau_1,\tau_2\right)$ are defined by (5.53) and (5.54), respectively. In a similar fashion, the variance of the late mini-statistic is:

$$\sigma_{g+}^2 = \frac{1}{N_d}E_pN_0X_2^+ + \frac{1}{N_d^2}X_3^+ + N_0^2\frac{N_d-1}{N_d^2}X_1^+ - \left[\frac{N_oW}{N_d}\Delta\tau\right]^2. \tag{5.72}$$

where:

$$\begin{aligned} X_1^+ &= Z_1\left(\hat{\tau},\hat{\tau}+\Delta\tau\right), \\ X_2^+ &= Z_2\left(\hat{\tau},\hat{\tau}+\Delta\tau\right). \\ X_3^+ &= X_3^-. \end{aligned}$$

Note that the individual mini-statistics g_k^-, $0 < k < N_d - 1$ are not independent, because they are obtained using the same noisy template. The expected value of the product of two arbitrary early mini-statistics g_i^- and g_j^- is found to be:

$$\begin{aligned} E\left[g_i^- g_j^-\right] &= E_p^2\left(1-2P_{e,\hat{\tau}}\right)^4 S^2 + \frac{2}{N_d}E_p\left(1-2P_{e,\hat{\tau}}\right)^2 SN_0W\Delta\tau + \frac{3}{N_d}E_p\left(1-2P_{e,\hat{\tau}}\right)^2 N_0X_2^- \\ &+ \left(\frac{N_0W\Delta\tau}{N_d}\right)^2. \end{aligned} \tag{5.73}$$

The variance of G^- is then:

$$\sigma_{G^-}^2 = \frac{\sigma_{g-}^2}{N_d} + \left(1-\frac{1}{N_d}\right)E\left[g_i^- g_j^-\right] - \left(1-\frac{1}{N_d}\right)\mu_{G^-}^2. \tag{5.74}$$

Using a similar analysis, the variance of G^+ is:

$$\sigma_{G^+}^2 = \frac{\sigma_{g+}^2}{N_d} + \frac{N_d-1}{N_d}\left[\left(\frac{N_0W\Delta\tau}{N_d}\right)^2 + \left(\frac{N_0X_4^+}{N_d}\right)^2\right] - \frac{N_d-1}{N_d}\mu_{G^+}^2 \tag{5.75}$$

where

$$X_4^+ = W\int_{\hat{\tau}}^{\hat{\tau}+\Delta\tau}\int_{\hat{\tau}}^{\hat{\tau}+\Delta\tau} sinc(W(t-\lambda))cos(2\pi f_c(t-\lambda))dtd\lambda.$$

Recall that the final statistic is $G = G^- - G^+$. The mean of G is equal to the sum of the means of G^- and G^+ which is equal to:

$$\mu_G = E_p\left(1-2P_{e,\hat{\tau}}\right)^2 S. \tag{5.76}$$

Since G^- and G^+ are independent, the variance of G is the sum of their respective variances:

$$\begin{aligned} \sigma_G^2 &= \frac{\sigma_{g-}^2}{N_d} + \left(1-\frac{1}{N_d}\right)E\left[g_i^- g_j^-\right] - \left(1-\frac{1}{N_d}\right)\mu_{G^-}^2 + \frac{\sigma_{g+}^2}{N_d} + \frac{N_d-1}{N_d}\left[\left(\frac{N_0W\Delta\tau}{N_d}\right)^2 + \left(\frac{N_0X_4^+}{N_d}\right)^2\right] \\ &- \frac{N_d-1}{N_d}\mu_{G^+}^2. \end{aligned} \tag{5.77}$$

The probability that the timing delay is adjusted in the correct direction is then equal to:

$$P\left(G > \Psi\right) = \frac{1}{2} erfc\left(\frac{\Psi - \mu_G}{\sqrt{2\sigma_G^2}}\right). \tag{5.78}$$

5.14 Tracking Simulation Results

The theoretical expressions of the algorithm's statistics are first tested for $N_p = 50$ and $N_d = 100$. The expressions for the mean values of g_k^- and g_k^+ given respectively by (5.69) and (5.70) are tested by simulation in Figure 5.33. The expressions for their second moment given by (5.71) and (5.72) are tested in Figure 5.34. Finally, the second moments of G^- and G^+ given by (5.74) and (5.75) are tested in Figure 5.35. Note that the theoretical expressions match simulation results with negligible error.

The performance of the proposed system is then showcased for $N_c = 64$ and $N_d = 512$ and displayed in Figure 5.36. First, note that the presence of a 16 nsec acquisition error results in a performance degradation of 3 dB compared to the perfect synchronization case. Moreover, note that the theoretical probability of error expressions given by (5.55) matches the simulation results. The performance of the receiver with the iterative tracking algorithm is also shown, where 5 iterations per frame are performed before a bit decision is made. Note that the tracker corrects the timing error. Moreover, the system outperforms a pilot-assisted system with $N_p = 64$, because the improved template is iteratively estimated based on the 512 data symbols, which drastically reduces the effect of the noise-cross-noise term. In fact, at moderate SNR values, few bits errors occur, and performance converges to a traditional pilot-assisted receiver with $N_c = 512$ and perfect synchronization.

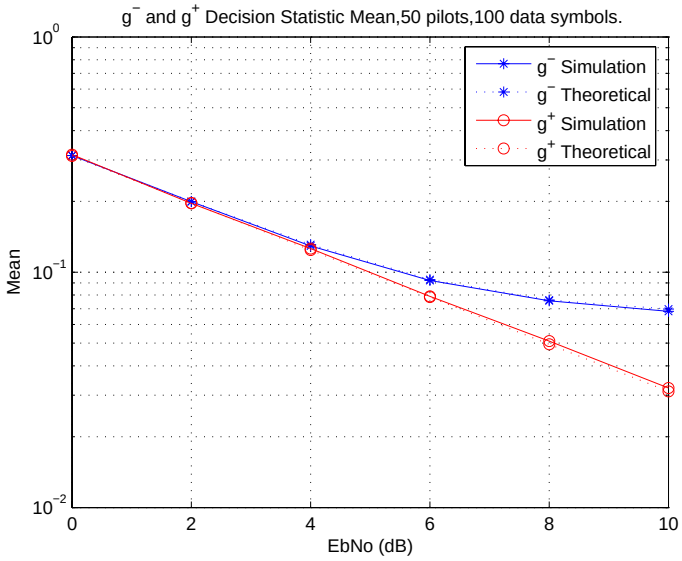

Figure 5.33: g^- and g^+ Mean. $N_c = 50$. $N_d = 100$

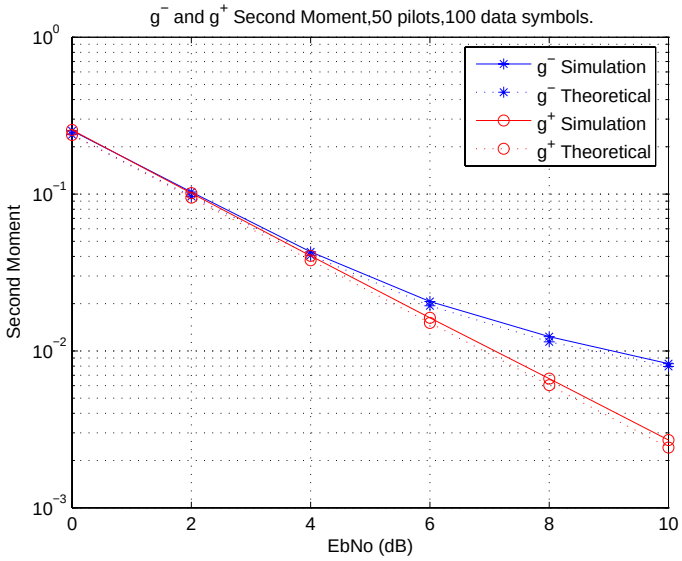

Figure 5.34: g^- and g^+ second moments. $N_c = 50$. $N_d = 100$

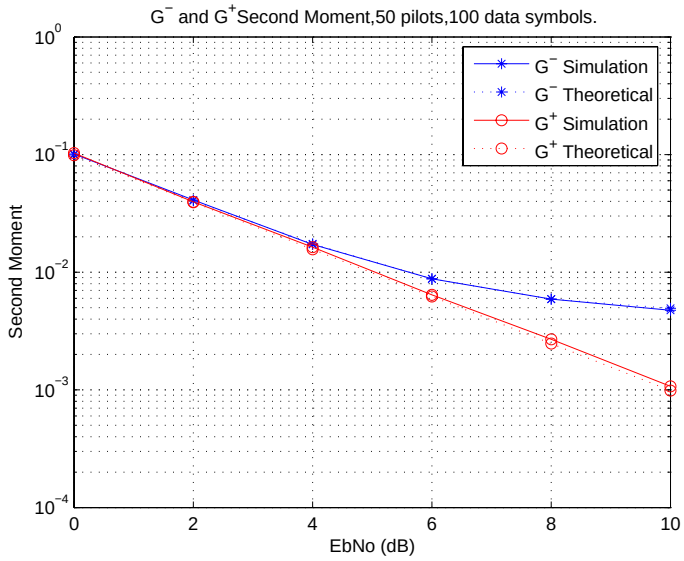

Figure 5.35: G^- and G^+ second moments. $N_c = 50$. $N_d = 100$.

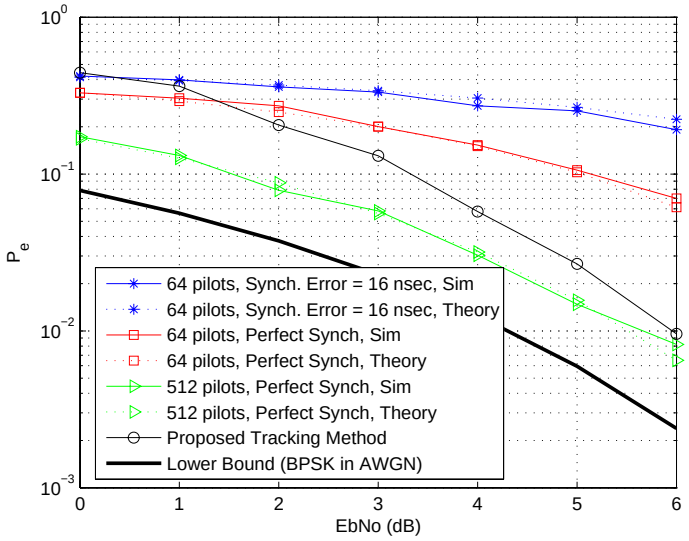

Figure 5.36: Proposed system performance. $N_c = 64$. $N_d = 512$.

5.15 Conclusions

This chapter presents a novel two-stage UWB acquisition algorithm for dense multipath channels. The algorithm takes advantage of the clustered multipath structure to reduce acquisition time and to robustly resolve the earliest arriving path, even when it is severely attenuated. The coarse acquisition phase is shown to perform much better than traditional serial search, and only cause slight increase in mean acquisition time compared to the most efficient acquisition search technique in the literature, in return for a much simpler search mechanism. The effect of the fine acquisition stage is illustrated using the realistic UWB P802.15 indoor channel model. The impact of acquisition error on a pilot-assisted receiver is derived, and the performance improvement brought by employing the proposed acquisition scheme is highlighted. The proposed scheme is validated by simulation based on actual channel measurements for both ranging and communication applications. The inclusion of fine acquisition is shown to yield a significant reduction in ranging error compared to traditional acquisition. Moreover, it increased symbol energy capture for the pilot-assisted receiver, therefore resulting in a performance that approaches the perfect synchronization case. A tracking algorithm for pilot-assisted receivers based on a modified early-late gate approach is also presented. The tracking circuit assumes that coarse synchronization locked into an arbitrary multipath component. The correlation template is based on the received pulse shape rather than the transmit pulse shape. The algorithm is deployed iteratively and is able to correct relatively large timing errors. A statistical analysis of the method is included along with simulation results which validate the theoretical expressions and illustrate system performance.

Chapter 6

NBI Mitigation in Dense Multipath

6.1 Introduction and Motivation

UWB systems must share their large bandwidth with other co-existing narrowband (NB) systems. UWB signals will thus encounter interference from various surrounding sources. UWB will also potentially affect many NB systems. The interference caused by UWB on NB systems is an important issue. One of the biggest concerns is the impact of UWB on GPS systems, since GPS is used in critical air traffic applications. For this reason no UWB transmissions are currently allowed in the GPS spectrum. Since the majority of UWB's energy is outside the NB system's bandwidth, the UWB interference seen by a typical NB system is expected to be minor. Moreover, the FCC power mask is specifically designed to limit this interference. Several research efforts have characterized and studied the impact of UWB on traditional existing systems (see [124] or [130] for example).

NB interference (NBI) seen by UWB systems is a more critical issue. In fact, even though UWB signals may enjoy a high spreading gain due to their large bandwidth, stringent FCC power restrictions (-41.3 dBm/MHz in the 3.1GHz-10.6GHz range) make them susceptible to strong NBI, which can severely degrade performance. The extent of performance degradation depends on the number, power and spatial distribution of the interferers relative to the UWB signal. NBI might be tens of dB stronger than the UWB signal, and can completely overwhelm the receiver front end. Severe NBI could thus render the acquisition process impossible.

Front end interference mitigation techniques must be therefore applied, which makes many traditional SS interference mitigation methods inapplicable, because they require synchronization prior to NBI mitigation. The subject of NBI mitigation in UWB systems has only recently started to receive significant research interest. Some methods to mitigate NBI for UWB systems have been discussed, many of which are based on SS techniques ([136] and [137] for example).

In this chapter, a novel NBI mitigation technique for UWB systems based on multiple receive antennas is proposed. The method takes advantage of the great immunity to fading that UWB signals exhibit when compared to narrowband signals [19, 144, 145, 146]. In fact, in indoor environments, whereas the total captured UWB energy varies only slightly over a relatively small area, the NBI energy level tends to vary wildly. This leads to a selection diversity (SD) scheme where the signal corresponding to the receive antenna with the *least* measured power is selected. The rationale behind this choice is the following: The UWB signal power is approximately constant from antenna to antenna, while the interference power effectively varies independently from antenna to antenna (when the multipath angle spread is high), following a specific distribution depending on the channel characteristics. Thus, any increase in received power level is due to more NBI power. Therefore, the effective received signal-to-interference ratio (SIR) is maximized by selecting the antenna with the lowest measured power (Figure 6.1). This is a potentially attractive method, since it does not assume signal synchronization or knowledge of the NBI's spectral content prior to interference mitigation. Moreover, it does not require high sampling rates at the receiver's front end. The technique was first suggested and briefly discussed in [144]. A mathematical framework for the proposed NBI mitigation scheme, which was not included in [144], is introduced in this chapter. Performance is discussed for both classical Rayleigh and Ricean NBI fading, which together cover a wide range of scenarios. Moreover, the method is extended to two other diversity techniques, equal gain combining (ECG), and maximum ratio combining (MRC). Results from this chapter have been published in [147] and [148].

6.2 List of Contributions and Publications

The major contributions of this chapter are:

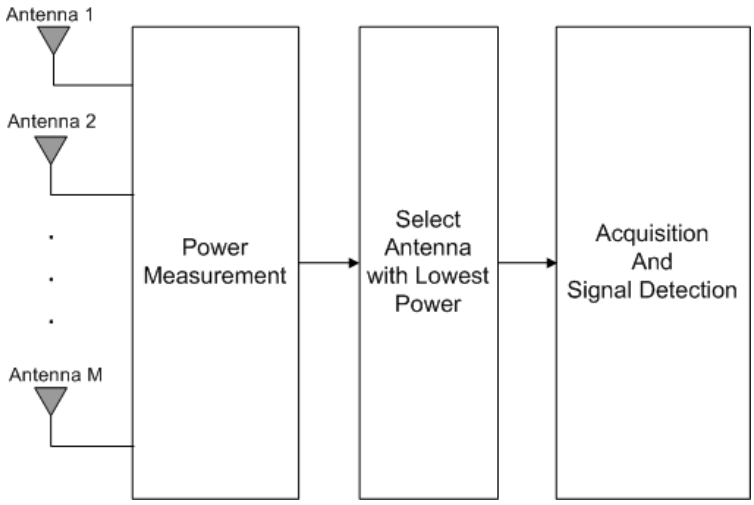

Figure 6.1: Proposed SD NBI mitigation receiver.

- A mathematical formulation of a proposed NBI mitigation model, based on multiple antennas, which achieves diversity by exploiting the difference between NBI and UWB spatial fading properties.
- A derivation of the probability of error for the proposed system for a perfect receiver (where the correlator template is matched to the received UWB pulse shape) as well as for a Rake receiver with a limited number of fingers, under Rayleigh and Ricean NBI fading.
- A derivation of the improvement in effective SIR brought by the use of multiple antennas, for Rayleigh and Ricean NBI fading.

A list of relevant publications is included for reference.

- J. Ibrahim and R.M. Buehrer, "NBI Mitigation for UWB Systems Using Multiple Antenna Selection Diversity," *to appear, IEEE Transactions on Vehicular Technology,* 2007.
- J. Ibrahim and R.M. Buehrer, "A UWB Multiple Antenna System for NBI Mitigation under Rayleigh and Ricean Fading, *Proc. 2006 ICC, 2006.*
- J. Ibrahim and R.M. Buehrer, "A Novel NBI Suppression Scheme for UWB Communications Using Multiple Receive Antennas," *Proc. 2006 RWS, 2006.*

- J. Ibrahim, B. Donlan, and R.M. Buehrer, "Interference Rejection Techniques for UWB Systems," *Embedded Systems Conference*, 2005.

- S. Venkatesh, J. Ibrahim and R.M. Buehrer, "A New Model for Ultra Wideband Indoor NLOS Channels," in *Proc. 2004 Antennas and Propagation Society Conference*, 2004.

- S. Venkatesh, J. Ibrahim, R.M. Buehrer and D.R. McKinstry, "A Spatio-temporal Channel Model for Ultra-Wideband Indoor NLOS Communications," *under review, IEEE Transactions on Communications.*

6.3 Chapter Organization

The rest of this chapter is organized as follows. Previous work in NBI mitigation applied to UWB is included in section 6.4. Spatial energy variation characteristics of NB and UWB signals are discussed in section 6.5. It is shown that while UWB energy remains almost constant over a local area, NB energy incurs large variations. Spatial diversity gains are thus possible, where NBI mitigation is performed by judiciously combining received signals from different locations in a small area. Such a diversity system, based on multiple antennas, is mathematically formulated in section 6.6. NBI is assumed to undergo either flat Rayleigh or Ricean fading, and this choice is analytically justified. SD is discussed in section 6.7, and the probability of error of a system employing M receive antennas and SD is derived for both NBI Rayleigh and Ricean fading. Analysis is first applied to the general Rake receiver employing F fingers, then for the ideal receiver (a perfect Rake or All-Rake receiver), where perfect channel knowledge is assumed. It is shown that doubling the number of antennas potentially results in a 3-dB performance boost for the Rayleigh case. Less substantial gains are seen for the Ricean case. These theoretical results are further checked through simulation. Section 6.8 derives the effective SIR gain brought by this method under both fading scenarios. EGC and MRC are introduced and analyzed in the context of the ideal receiver in section 6.9*. EGC is shown to perform similarly to SD for NBI Rayleigh fading. EGC is superior to SD for Ricean fading. MRC provides additional gains at the cost of increased complexity. Simulation and numerical results are included

*Note that, in this work, the MRC weights are calculated and set to maximize the output SIR. More details on the weight setting procedure is included in section 6.9

in section 6.10. In addition to providing validation of the theoretical findings of the previous sections, the systems performance is compared to the Rake MMSE receiver, which is the most popular NBI mitigation technique available in the literature. Finally, section 6.11 concludes this chapter.

6.4 Previous Work on NBI Mitigation for UWB systems

NBI mitigation for UWB systems has lately received some research interest. An analysis of the effect of tone jammers on UWB systems is presented in [125]. The effect of partial-band interference on UWB is analyzed in [126]. In [127], the effect of NBI on direct sequence-based impulse radio is derived, where NBI is modeled as the sum of sinusoidal signals with variable power and frequency. The performance of a generalized Rake receiver in the presence of MAI and NBI is analyzed in [8]. The impact of NBI on DS-UWB, as well as single and multi-carrier multi-band UWB is discussed in [128] and [129]. The effect of NBI in the GSM and UMTS/WCDMA bands on UWB is studied in [130]. It is shown by simulation that performance degradation is most severe when the NBI bandwidth overlaps with the UWB nominal center frequency. Various pulse shaping methods which introduce nulls in the UWB spectrum where NBI occurs are investigated in [131][132][133][134]. However, these methods assume knowledge of the NBI spectrum. NBI mitigation based on optimization of the PPM parameter Δ is suggested in [135], along with two other methods, based on passing the UWB signal trough a notch filter, and on a MMSE Rake receiver, respectively. NBI mitigation based on the MMSE Rake is also studied in [136] and [137]. In [138], NBI is modeled by a sine wave of unknown amplitude, frequency and phase, and these three parameters are first estimated, then the reconstructed NBI wave is subtracted from the received signal. A spectral-encoded system for NBI mitigation is introduced in [139], where spectral nulls are introduced in the UWB spectrum using SAW devices. The use of SAW filters for transform-domain processing is also suggested in [140]. Another technique is suggested in [140], where NBI is digitally estimated, and an RF estimate is produced to perform the NBI in the analog domain (also studied in [141]).

6.5 Spatial Energy Variation of UWB and NBI Signals

A number of indoor NLOS UWB measurements were taken as part of a campaign conducted at Virginia Tech within the context of the DARPA NETEX (NETworking in EXtreme environments) program. The details of the measurement campaign can be found in section 2.5 and the references therein.

Measurements were taken at multiple locations in an indoor office environment. Consider a specific location, or position, and define its position-set as all the impulse responses recorded at that position. Measurements were grouped into separate position-sets each consisting of 49 channel impulse responses. Each position-set holds measured channel impulse responses at 49 uniformly distributed points in a 1 m^2 local area. For a specific position-set, the total energy captured by a receiver is measured and recorded. The 49 energy-capture values are then divided by the mean energy-capture value over the position-set. Energy averaging is performed because we are interested in the energy variation around the mean value, and not in the mean value itself. The procedure is repeated over all position-sets, and data from all position-sets is analyzed. The histogram of the total energy captured by a receiver over a 1 m^2 spatial grid at multiple locations for a pulse width of 500 psec is shown in Figure 6.2. The variance of the captured energy was found to be only 0.0035. Thus, the total energy capture may be assumed to be constant over this local area emphasizing the low spatial fading of UWB signals. While we base our technique on results from [19], it should be noted that the lack of spatial fading for UWB is a well documented phenomenon (see [32] and [142] for example).

In another experiment, separate transmissions of NBI and UWB signals over NLOS channels were simulated based on actual channel measurements [145]. Two UWB monocycles of different duration (250 psec and 2 nsec) were employed. The received energy content of the NBI and the UWB signal over a 70 cm linear segment was recorded and appears in Figure 6.3. Note that the energy over multiple distance values is normalized such that it has unit mean over the segment. The received NBI energy varies wildly over the linear region as compared to the received energy of the UWB signal. Further, the 250 psec UWB pulse shows less variation in energy across the grid than the 2 nsec pulse due to the presence of more resolvable paths (*i.e.*, larger bandwidth). Thus, in terms of total received energy, UWB signals exhibit great immunity to fading when compared to narrowband signals. We would like to exploit this unique characteristic of UWB

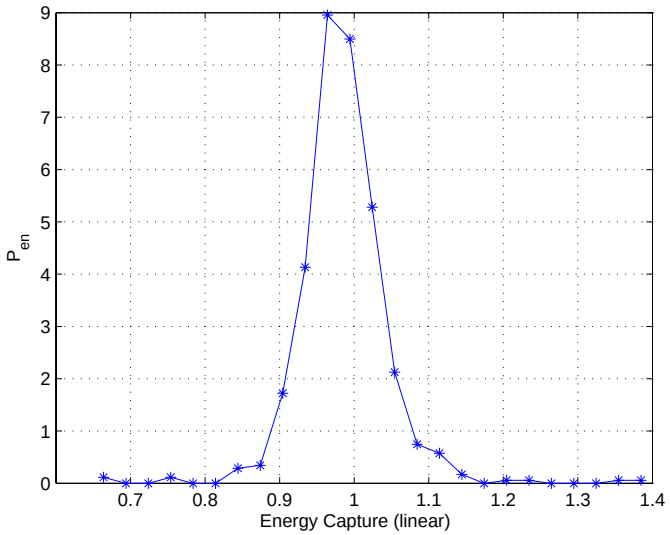

Figure 6.2: Histogram of the normalized received UWB signal energy over a 1 m^2 area. Perfect receiver.

signals in our NBI mitigation system.

In a multiple receive antenna system, the total measured UWB power can thus be assumed nearly constant from antenna to antenna, whereas the NBI power is not. This leads to our proposed method. In conventional SD systems, diversity is achieved by feeding the signal with highest average received power to the demodulator. This is effective due to the fact that the noise power is constant from antenna to antenna while the desired signal varies, and thus the signal with the greatest received power is most likely to have the largest *desired* signal power. In the proposed interference diversity system, the weakest signal is chosen to be fed to the demodulator. This can be explained as follows. Assuming adequate antenna separation in a multipath environment, the UWB signal power is approximately constant across antennas while the interference power varies independently from antenna to antenna, according to a certain statistical distribution. The independence of NBI fading assumes a large multipath angular spread (which is typical for an indoor environment) and that the distance between adjacent antennas is greater than $\frac{\lambda}{2}$, where λ is the wavelength of the NBI signal. Thus, an increase in the SIR of the system is equivalent to less interference power and consequently lower overall received power.

Note that, in the proposed model, the antenna with the lowest power is selected and then signal detection is performed, based on a decision statistic obtained at the output of a correlator-receiver. In the case of

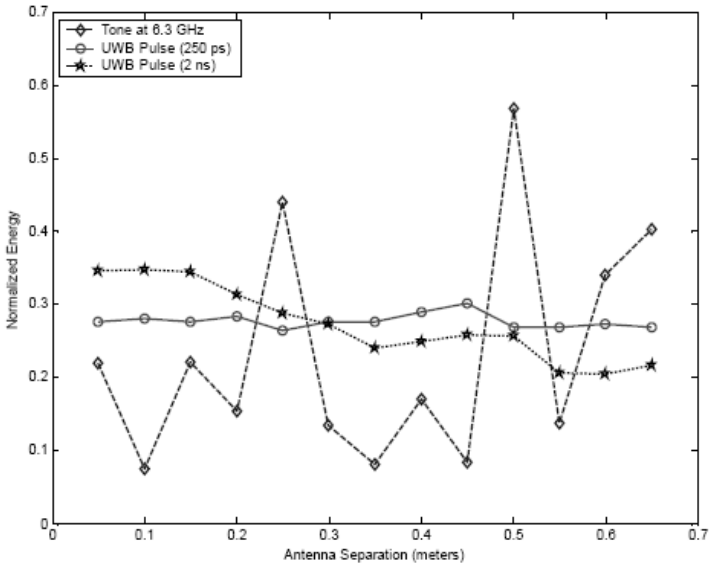

Figure 6.3: Received signal energies at different antenna separations.

perfect channel knowledge (*i.e.* the desired received pulse shape is known, or equivalently a perfect Rake with infinite resources is used), the entire UWB signal energy is captured, and the desired UWB component in the decision statistic is constant across all antennas (since it is a direct function of the total energy capture). However, if only a subset of the multipath components delays and amplitudes is available or the receiver complexity is limited, a more realistic Rake receiver structure (with a limited number of fingers) is used, and only a fraction of the available energy is captured. In this case, more UWB energy variation may be expected across antennas in the decision statistic. The energy capture for a Rake receiver employing F fingers was thus also analyzed using the same procedure for Figure 6.3. Note that it is assumed that the position of the F strongest multipath components is known. It is shown that the Rake energy level varies more significantly than the total energy capture case. For example, the energy variance for a 10-finger Rake when normalized to unit mean is equal to 0.0273, compared to a variance of 0.0035 for the perfect energy capture case. However, the energy variance is still relatively small compared to the NBI. Moreover, it was found that the energy capture, d, across multiple antennas may be approximated by a Laplace random variable (Figure 6.4) with distribution given by:

$$f_d(x) = \frac{1}{\sigma_{d_F}\sqrt{2}} e^{-\frac{\sqrt{2}|x-\bar{d}_F|}{\sigma_{d_F}}} \tag{6.1}$$

where $\bar{d}_F$ is the average energy capture, $\sigma^2_{d_F}$ is the energy capture variance, and $|.|$ is the absolute value operator. A Kolmogorov-Smirnov statistical goodness of fit test was performed to test the Laplace distribution hypothesis, and the hypothesis passed the test for 5, 10, 15 and 20 fingers (Table 6.1). Thus we will use a Laplacian model for the captured Rake received energy with a variance dependent on the number of Rake fingers[†].

We now briefly describe the proposed model in Figure 6.1 in the light of the above discussion. A power measurement device first measures the *total* power of the signals at each of the M receive antennas. Let P_j be the measured power at the j^{th} antenna. In the next section, we will show that P_j may be expressed as the sum of the UWB total received power (which may be assumed to be constant across antennas, based on the discussion in this section), the noise power, and the NBI received power. The signal corresponding to the minimum measured power is selected. Acquisition, modulation and signal detection are then performed on the selected signal. If a perfect Rake receiver is employed, complete energy capture is achieved, and the desired UWB component d in the correlator decision statistic may be assumed constant across antennas. If a Rake receiver with F fingers is used, the desired component of the decision statistic is modeled by a Laplacian random variable with mean $\bar{d}_F$ and variance $\sigma^2_{d_F}$, where $\bar{d}_F$ and σ_{d_F} depend on F. Thus, antenna selection is based on the entire received signal power whereas data detection depends on some fraction of the received power based on the receiver structure used. The next section formulates a mathematical model for this system.

It is important to note that the proposed method assumes slow NBI fading. That is, the NBI fading coefficients on the receiver antennas remain constant during the power measurement-data detection cycle. This is a valid assumption for indoor environments, where the coherence time is estimated at around 30 msec for low mobility environments [143].

[†]Note that the Laplacian model $f_d(x)$ is clearly an approximation, since the Laplacian distribution extends to negative x. However, for small σ_{d_F}, the ensuing error is negligible. Alternatively, we may use a truncated Laplacian distribution (only defined for positive x)

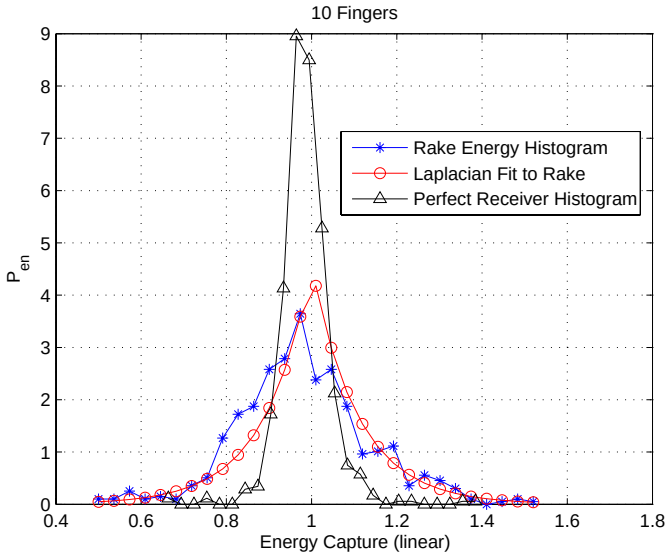

Figure 6.4: Normalized received UWB signal energy over a 1 m^2 area. 10-Finger Rake receiver.

Receiver	$\sigma^2_{d_F}$	*Test statistic*	*Passed Test?*
Rake, F=5	0.0439	0.0548	YES
Rake, F=10	0.0273	0.0454	YES
Rake, F=15	0.0199	0.0540	YES
Rake, F=20	0.0155	0.0477	YES

Table 6.1: Kolmogorov-Smirnov test for Laplacian Fit of Rake receiver energy capture. 580 sample points. Significance level = 0.05. Test threshold = $\sqrt{-\frac{1}{2\times 580} log\left(\frac{0.05}{2}\right)} = 0.0564$

6.6 General System Model

We assume a UWB system with one transmit antenna and M ($M \geq 1$) receive antennas. For mathematical simplicity, we assume perfect synchronization between the transmitter and receiver antennas [‡]. The UWB system employs binary PAM modulation, and is corrupted by an NBI signal $s_{NBI}(t)$ with center frequency f_c. The transmitted UWB signal can be written as:

$$s(t) = \sqrt{E_p} \sum_{i=-\infty}^{\infty} b_i w(t - iT_f) \tag{6.2}$$

where $b_i = \pm 1$ is the i^{th} data bit, $w(t)$ is the unit-energy UWB transmit pulse of duration T_w, and E_p is the transmit pulse energy. The transmit and receive antenna transfer functions are assumed to be included in

[‡]Note that synchronization between different antennas is not required for the SD system. However, synchronization prior to NBI mitigation is required for EGC and MRC, since these two techniques are based on the combination of decision statistics from different antennas.

$w(t)$. T_f is the symbol duration time ($T_f >> T_w$). We assume that T_f is longer than the channel maximum delay spread, so that any ISI effects may be ignored. Note that the same analysis may be applied to any UWB modulation technique.

We restrict our analysis to the time interval $[0, T_f]$ for ease of notation. The received signal corresponding to bit b_0 at the j^{th} receiver antenna can be written as:

$$r_j(t) = b_0\sqrt{E_p}w(t) * h_{j,d}(t) + s_{NBI}(t) * h_{j,NBI}(t) + n(t) \tag{6.3}$$

where $h_{j,d}(t)$ is the channel between the UWB transmitter and j^{th} receive antenna, $h_{j,NBI}(t)$ is the channel between the NBI transmitter and j^{th} receive antenna, and $n(t)$ is white Gaussian noise with power spectral density $\frac{N_0}{2}$.

Let $s_{l,NBI}(t)$ be the equivalent low-pass signal of $s_{NBI}(t)$. We can write:

$$s_{NBI}(t) = Re\left[s_{l,NBI}(t)e^{j2\pi f_c t}\right]. \tag{6.4}$$

The received bandpass signal at the j^{th} antenna can be written as:

$$r_{NBI}(t) = \sum_n \beta_{j,n}(t)\, s_{NBI}(t - \tau_{j,n}(t)) \tag{6.5}$$

where $\beta_{j,n}(t)$ and $\tau_{j,n}(t)$ are the time-varying amplitude and delay of the n^{th} multipath component of $h_{j,NBI}$, respectively. Then:

$$r_{NBI}(t) = \sum_n \beta_{j,n}(t)\, Re\left[s_{l,NBI}(t - \tau_{j,n}(t))e^{j2\pi f_c(t-\tau_{j,n}(t))}\right]. \tag{6.6}$$

Therefore:

$$r_{NBI}(t) = Re\left[\left(\sum_n \beta_{j,n}(t)\, s_{l,NBI}(t - \tau_{j,n}(t))e^{-j2\pi f_c\tau_{j,n}(t)}\right).e^{j2\pi f_c t}\right]. \tag{6.7}$$

The lowpass equivalent of the received signal is therefore:

$$r_{l,NBI}(t) = \sum_n \beta_{j,n}(t)\, s_{l,NBI}(t - \tau_{j,n}(t)) e^{-j2\pi f_c \tau_{j,n}(t)}. \tag{6.8}$$

We assume that the transmitted NBI is a continuous wave (CW) tone with power P_I, center frequency f_c and phase Θ:

$$s_{NBI}(t) = \sqrt{2P_I} cos\left(2\pi f_c t + \Theta\right). \tag{6.9}$$

Note that, due to UWB's very large bandwidth, any narrowband interferer may be approximated by (6.9). Consequently, $s_{l,NBI}(t) = \sqrt{2P_I} e^{j\Theta}$, and:

$$r_{l,NBI}(t) = \sqrt{2P_I} \sum_n \beta_{j,n}(t)\, e^{-j(2\pi f_c \tau_{j,n}(t) + \Theta)}. \tag{6.10}$$

Let $\phi_{j,n}(t) = 2\pi f_c \tau_{j,n}(t) + \Theta$. Then:

$$r_{l,NBI}(t) = \sqrt{2P_I} \sum_n \beta_{j,n}(t)\, e^{-j\phi_{j,n}(t)}. \tag{6.11}$$

In indoor environments characterized by dense multipath, there exist a large number of identically distributed paths, and the central limit theorem applies. $r_{l,NBI}(t)$ may then be modeled as a complex Gaussian random variable. Assuming slow fading (quasi-static channel), we may write:

$$r_{l,NBI}(t) = A + jB, \tag{6.12}$$

where A and B are Gaussian random variables. In the classical case of Rayleigh fading, A and B are zero-mean Gaussian random variables. Then:

$$r_{NBI}(t) = Re\left[(A + jB)\, e^{j2\pi f_c t}\right] \tag{6.13}$$

which gives:

$$r_{NBI}(t) = Acos\left(2\pi f_c t\right) - Bsin\left(2\pi f_c t\right) \tag{6.14}$$

$$r_{NBI}(t) = \sqrt{A^2+B^2}\left[\frac{A}{\sqrt{A^2+B^2}}cos\left(2\pi f_c t\right) - \frac{B}{\sqrt{A^2+B^2}}sin\left(2\pi f_c t\right)\right]. \tag{6.15}$$

Thus:

$$r_{NBI}(t) = \alpha_j cos\left(2\pi f_c t + \phi_j\right) \tag{6.16}$$

where $\alpha_j = \sqrt{A^2+B^2}$ and $\phi_j = tan^{-1}\left(-\frac{B}{A}\right)$. In the case of Rayleigh fading, α_j is a Rayleigh random variable, and ϕ_j is a uniform random variable on $[-\pi, \pi]$. In case a strong specular component exists between the NBI transmitter and the UWB receiver antenna, α_j is modeled by a Ricean random variable [57].

$r_j(t)$ can then be written as:

$$r_j(t) = b_0\sqrt{E_p}w_{rx}(t) + \alpha_j\sqrt{2P_I}cos(2\pi f_c t + \phi_j) + n(t) \tag{6.17}$$

where $w_{rx}(t) = w(t) * h_{j,d}(t)$ is the received UWB pulse shape. We assume that the NBI undergoes a frequency-nonselective, slowly fading channel. ϕ_j is a random phase offset uniformly distributed over $[-\pi, \pi]$, which models the randomness in the time of arrival of the NBI signal, relative to the UWB signal. We shall analyze NBI under both Rayleigh and the more general Ricean fading. In case of Rayleigh fading, the multiplicative term α_j is modeled by a Rayleigh random variable with pdf:

$$f_{\alpha_j}(\alpha) = \frac{\alpha}{\sigma^2}e^{-\frac{\alpha^2}{2\sigma^2}}, \quad \alpha \geq 0 \tag{6.18}$$

where σ depends on the average NBI received power.

In case of Ricean fading, the pdf of α_j is given by:

$$f_{\alpha_j}\left(\alpha\right) = \frac{\alpha}{\sigma^2}e^{-\frac{s^2+\alpha^2}{2\sigma^2}}I_0\left(\alpha\frac{s}{\sigma^2}\right), \quad \alpha \geq 0 \tag{6.19}$$

where I_0 is a modified Bessel function of the first kind, and s is the noncentrality parameter. The ratio of the LOS to the NLOS power is defined as $K = \frac{s^2}{2\sigma^2}$.

6.6.1 Power Measurement

Recall that the SD algorithm is based on selecting the signal corresponding to the antenna with lowest measured power. The measured power from the j^{th} antenna in the interval $[0, T_f]$ can be written as:

$$\begin{aligned} P_j &= \frac{1}{T_f}\int_0^{T_f} r_j^2(t)dt \\ P_j &= \frac{E_p}{T_f}\int_0^{T_f} w_{j,rx}^2(t)dt + \frac{2}{T_f}\alpha_j^2 P_I \int_0^{T_f} cos^2\left(2\pi f_c t + \phi_j\right)dt + \frac{2\sqrt{E_p}b_0}{T_f}\int_0^{T_f} w_{j,rx}(t)n(t)dt \\ &\quad + \frac{2\sqrt{2P_I E_p}}{T_f} b_0 \alpha_j \int_0^{T_f} w_{j,rx}(t).cos\left(2\pi f_c t + \phi_j\right)dt + \frac{2\alpha_j\sqrt{2P_I}}{T_f}\int_0^{T_f} n(t)cos\left(2\pi f_c t + \phi_j\right)dt \\ &\quad + \frac{1}{T_f}\int_0^{T_f} n^2(t)dt. \end{aligned} \tag{6.20}$$

Note that, if the power is averaged over multiple bits, $E\left[b_0\right]=0$ [§]. Moreover, we assume that signals are passed through a band-limiting filter prior to power measurement, where the filter bandwidth W is large enough not to cause distortion to the UWB signal and to the NBI signal [¶]. Then, since noise is zero-mean, P_j may be approximated by:

$$P_j \approx \frac{E_p}{T_f}\int_0^{T_f} w_{j,rx}^2(t)dt + \frac{2}{T_f}\alpha_j^2 P_I \int_0^{T_f} cos^2\left(2\pi f_c t + \phi_j\right)dt + N_0 W. \tag{6.21}$$

Therefore:

$$P_j \approx \frac{E_p}{T_f}\int_0^{T_f} w_{j,rx}^2(t)dt + N_0 W + \frac{\alpha_j^2 P_I}{T_f}\int_0^{T_f}\left(1 + cos\left(4\pi f_c t + 2\phi_j\right)\right)dt. \tag{6.22}$$

[§]It can easily be shown that the variance of the third and fourth terms on the ride hand side in (6.20) is proportional to $\frac{1}{N}$, where N is the number of bits over which power is averaged. The number of bits required for adequate estimation depends on the strength of the NBI, but 10 to 20 bits should be sufficient to effectively limit the term's effect.

[¶]The design of such a filter is beyond the scope of this paper. We note however that the filter is essential for limiting noise power.

Assuming $4\pi f_c T_f$ is large (a valid assumption considering UWB's operating range), then we can write [147][148]:

$$P_j \approx \frac{E_p}{T_f}\int_0^{T_f} w_{j,rx}^2(t)dt + N_0 W + \alpha_j^2 P_I. \tag{6.23}$$

Thus, the measured power P_j is the sum of the *total* received UWB power (which is constant from antenna to antenna as seen in section 6.5), the noise power, and the NBI power $\alpha_j^2 P_I$, where $\alpha_j^2,\ 1 \leq j \leq M$ are independent random variables whose distributions depend on the type of NBI fading (Rayleigh or Ricean). This means that the signal with lowest NBI power corresponds to the signal with lowest measured power, as expected. Note that the analysis assumes slow NBI fading, *i.e* the fading coefficients α_j are assumed constant during the process.

It is important to note that the power measurement procedure is independent of the type of correlator used. That is, the signal with lowest measured power is selected for both the perfect correlator (matched to the UWB received pulse shape) and the Rake receiver, since signal selection is done prior to demodulation and detection, and is based on total received power.

6.6.2 Antenna Decision Statistic

We assume that a correlator is applied at the receiver after the signal corresponding to the lowest measured power is selected. The template of the correlator is given by:

$$y_0(t) = \sum_{f=1}^{F} \gamma_f w(t - \tau_f). \tag{6.24}$$

In the case of perfect knowledge of $h_{j,d}(t)$, γ_f and τ_f are set to the amplitude and delay of the f^{th} multipath component of $h_{j,d}(t)$. Then, $y_0(t)$ is matched to the received pulse shape $w_{j,rx}(t)$, and F is equal to the number of multipath components L. The same template structure may be used if a more realistic Rake receiver is employed, where γ_f and τ_f are the weight and delay of the f^{th} Rake finger, respectively, and $F \leq L$.

The decision statistic corresponding to the j^{th} antenna after correlation can be written as:

$$r_j = \sqrt{E_p} b_0 d_j + i_j + n_j \tag{6.25}$$

where:

$$\begin{aligned} d_j &= \int_0^{T_f} y_0(t) w_{j,rx}(t) dt & (6.26)\\ i_j &= \alpha_j \sqrt{2P_I} \int_0^{T_f} y_0(t) cos(2\pi f_c t + \phi_j) dt & (6.27)\\ n_j &= \int_0^{T_f} y_0(t) n(t) dt. & (6.28) \end{aligned}$$

Based on the discussion from section 6.5, we study two receiver cases:

- In the case of perfect knowledge of $h_{j,d}(t)$, perfect energy capture is achieved. The UWB power is then constant over all antennas, and consequently $d_j = \bar{d}$, $\forall j$. This case is equivalent to a perfect Rake receiver which can resolve *all* the available channel multipath components. In other words, $y_0(t) = w_{j,rx}(t)$.
- If a Rake receiver with F fingers is employed, only a fraction of the total available energy is captured, and d_j is no longer assumed to be constant across the M antennas, but rather follows a Laplace distribution with mean $\bar{d}_F$ and variance $\sigma^2_{d_F}$, where $\bar{d}_F$ and σ_{d_F} depend on F.

Moreover, the interference component i_j can be written as:

$$i_j = \sqrt{2N_I} \left[a\alpha_j cos\phi_j - b\alpha_j sin\phi_j \right] \tag{6.29}$$

where:

$$\begin{aligned} a &= \sqrt{\frac{1}{T_w}} \int_0^{T_f} y_0(t) cos(2\pi f_c t) dt & (6.30)\\ b &= \sqrt{\frac{1}{T_w}} \int_0^{T_f} y_0(t) sin(2\pi f_c t) dt & (6.31)\\ N_I &= P_I T_w & (6.32) \end{aligned}$$

where N_I may be interpreted as the interferer's one-sided power density, as defined in [61][‖].

6.7 Selection Diversity Probability of Error

6.7.1 Rayleigh Fading

In this section, we derive the probability of error expression for the proposed system when a Rake receiver with F fingers is employed in the presence of NBI Rayleigh fading. The result may be easily extended to the perfect energy capture case (All-Rake), as will be seen.

Assume that the signal corresponding to the m^{th} antenna is selected. The decision statistic may be written as:

$$r_m = \sqrt{E_p} b_0 d_m + i_m + n_m \tag{6.33}$$

with:

$$i_m = \sqrt{2N_I}\left[a\alpha_m cos\phi_m - b\alpha_m sin\phi_m\right] \tag{6.34}$$

where α_m and ϕ_m are the NBI Rayleigh fading term and phase at the m-th antenna, respectively.

Based on the power measurement derivation in the previous section, the antenna selection mechanism is equivalent to selecting the minimum of M independent, identically distributed (i.i.d) random variables α_1^2, α_2^2, ... α_M^2. Then, based on classical order statistics [149], the distribution of α_m is given by:

$$f_{\alpha_m}(\alpha) = M\left[1 - F_{\alpha_j}(\alpha)\right]^{M-1} f_{\alpha_j}(\alpha) \tag{6.35}$$

where $F_{\alpha_j}(\alpha)$ is the CDF of α_j. For Rayleigh fading, we get:

$$f_{\alpha_m}(\alpha) = \frac{M}{2\sigma^2}\alpha e^{-\frac{M\alpha^2}{2\sigma^2}}. \tag{6.36}$$

Thus, α_m is also a Rayleigh random variable, where σ^2 is replaced by $\frac{\sigma^2}{M}$.

Now, let $z = \alpha_m cos\phi_m$ and $w = \alpha_m sin\phi_m$. Note that the power measurement process is not affected by the

[‖]Here, the interference's contribution to the decision statistic is expressed as a function of N_I rather than P_I to make the notation consistent with classical jammer analysis in the literature.

phase, and ϕ_m remains uniformly distributed over $[-\pi, \pi]$. Using the basic Jacobian method [114], the joint distribution of z and w is found to be:

$$f_{z,w}(z,w) = \frac{M}{2\pi\sigma^2} e^{-\frac{M\left(z^2+w^2\right)}{2\sigma^2}}. \tag{6.37}$$

z and w are thus uncorrelated, jointly Gaussian random variables. Consequently, z and w are independent, zero-mean Gaussian random variables with equal variance $\frac{\sigma^2}{M}$. Thus, i_m is also a zero-mean Gaussian random variable, with variance:

$$\sigma_I^2 = 2N_I E\left[(az - bw)^2\right] = 2N_I\left(a^2 + b^2\right)\frac{\sigma^2}{M}. \tag{6.38}$$

Note that the power selection process does not affect the distribution of d_m (since power is measured before modulation and detection, and is based on total received power). In other words, d_m is selected *randomly* from a group of M i.i.d Laplace random variables. Then, the pdf of d_m is given by:

$$f_{d_m}(x) = \frac{1}{\sigma_{d_F}\sqrt{2}} e^{-\sqrt{2}\frac{|x-\bar{d}_F|}{\sigma_{d_F}}}. \tag{6.39}$$

Assume $b_0 = -1$. Then, a bit error occurs if $r_m > 0$, or:

$$-\sqrt{E_p} d_m + i_m + n_m > 0. \tag{6.40}$$

Equivalently:

$$\frac{d_m}{i_m + n_m} < \frac{1}{\sqrt{E_p}}. \tag{6.41}$$

Let $Z = \frac{d_m}{i_m+n_m}$. It is trivial to show that n_m is a zero-mean Gaussian random variable with variance $\sigma_N^2 = \frac{N_0}{2}$. Then, the CDF of Z is given by [114]:

$$F_Z(z) \quad = \quad c_z \int_{y=0}^{\infty} \int_{x=0}^{zy} e^{-\frac{\sqrt{2}|x-\bar{d}_F|}{\sigma_{d_F}} - \frac{y^2}{2\sigma_T^2}} dxdy \tag{6.42}$$

where $c_z = \frac{1}{2\sigma_{d_F}\sigma_T\sqrt{\pi}}$ and $\sigma_T^2 = \sigma_I^2 + \sigma_N^2$. From (6.41), the probability of error is equal to $F_Z\left(\frac{1}{\sqrt{E_p}}\right)$.

The CDF of Z may be expressed as:

$$F_Z(z) = \frac{1}{\sigma_{d_F}\sqrt{2}} \frac{1}{\sqrt{2\pi\sigma_T^2}} \int_{y=0}^{\infty} \int_{x=0}^{zy} e^{-\frac{\sqrt{2}|x-\bar{d}_F|}{\sigma_{d_F}}} e^{-\frac{y^2}{2\sigma_T^2}} dxdy. \tag{6.43}$$

Then, we may write:

$$\begin{aligned} F_Z(z) = \frac{1}{\sqrt{2}\sigma_d} \frac{1}{\sqrt{2\pi\sigma_T^2}} \Bigg[& \int_{y=0}^{\frac{\bar{d}}{z}} e^{-\frac{y^2}{2\sigma_T^2}} \int_{x=0}^{zy} e^{\frac{\sqrt{2}(x-\bar{d})}{\sigma_d}} dxdy + \int_{y=\frac{\bar{d}}{z}}^{\infty} e^{-\frac{y^2}{2\sigma_T^2}} \int_{x=0}^{\bar{d}} e^{\frac{\sqrt{2}(x-\bar{d})}{\sigma_d}} dxdy \\ & + \int_{y=\frac{\bar{d}}{z}}^{\infty} e^{-\frac{y^2}{2\sigma_T^2}} \int_{x=\bar{d}}^{zy} e^{-\frac{\sqrt{2}(x-\bar{d})}{\sigma_d}} dxdy \Bigg] \end{aligned} \tag{6.44}$$

which is equivalent to:

$$\begin{aligned} F_Z(z) = \frac{1}{2} \frac{1}{\sqrt{2\pi\sigma_T^2}} \Bigg[& \int_{y=0}^{\frac{\bar{d}_F}{z}} e^{-\frac{y^2}{2\sigma_T^2}} \left[e^{\frac{\sqrt{2}(zy-\bar{d}_F)}{\sigma_{d_F}}} - e^{-\frac{\sqrt{2}\bar{d}_F}{\sigma_{d_F}}} \right] dy + \int_{y=\frac{\bar{d}_F}{z}}^{\infty} e^{-\frac{y^2}{2\sigma_T^2}} \left[1 - e^{-\frac{\sqrt{2}\bar{d}_F}{\sigma_{d_F}}} \right] dy \\ & + \int_{y=\frac{\bar{d}_F}{z}}^{\infty} e^{-\frac{y^2}{2\sigma_T^2}} \left[1 - e^{\frac{\sqrt{2}(\bar{d}_F-zy)}{\sigma_{d_F}}} \right] dy \Bigg]. \end{aligned} \tag{6.45}$$

Re-ordering elements, we get:

$$F_Z(z) = \frac{1}{2} \frac{1}{\sqrt{2\pi\sigma_T^2}} \left[\int_0^{\frac{\bar{d}_F}{z}} e^{-\frac{y^2}{2\sigma_T^2} + \frac{\sqrt{2}(zy-\bar{d}_F)}{\sigma_{d_F}}} dy + 2\int_{\frac{\bar{d}_F}{z}}^{\infty} e^{-\frac{y^2}{2\sigma_T^2}} dy - e^{-\frac{\sqrt{2}\bar{d}_F}{\sigma_{d_F}}} \int_0^{\infty} e^{-\frac{y^2}{2\sigma_T^2}} dy - \int_{\frac{\bar{d}_F}{z}}^{\infty} e^{-\frac{y^2}{2\sigma_T^2} + \frac{\sqrt{2}(\bar{d}_F-zy)}{\sigma_{d_F}}} dy \right]. \tag{6.46}$$

Moreover:

$$F_Z(z) = Q\left(\frac{\bar{d}_F}{z\sigma_T}\right) - \frac{1}{4} e^{-\frac{\sqrt{2}\bar{d}_F}{\sigma_{d_F}}} + \frac{1}{2} \frac{1}{\sqrt{2\pi\sigma_T^2}} \left[\int_0^{\frac{\bar{d}_F}{z}} e^{-\frac{y^2}{2\sigma_T^2} + \frac{\sqrt{2}(zy-\bar{d}_F)}{\sigma_{d_F}}} dy - \int_{\frac{\bar{d}_F}{z}}^{\infty} e^{-\frac{y^2}{2\sigma_T^2} + \frac{\sqrt{2}(\bar{d}_F-zy)}{\sigma_{d_F}}} dy \right]. \tag{6.47}$$

We thus get the following expression:

$$\begin{aligned} F_Z(z) = Q\left(\frac{\bar{d}_F}{z\sigma_T}\right) - \frac{1}{4} e^{-\frac{\sqrt{2}\bar{d}_F}{\sigma_{d_F}}} + \frac{1}{2} e^{\frac{z^2\sigma_T^2}{\sigma_{d_F}^2} - \frac{\sqrt{2}\bar{d}_F}{\sigma_{d_F}}} \left[Q\left(\frac{-\sqrt{2}z\sigma_T}{\sigma_{d_F}}\right) - Q\left(\frac{\bar{d}_F}{z\sigma_T} - \frac{\sqrt{2}z\sigma_T}{\sigma_{d_F}}\right) \right] \\ - \frac{1}{2} e^{\frac{z^2\sigma_T^2}{\sigma_{d_F}^2} + \frac{\sqrt{2}\bar{d}_F}{\sigma_{d_F}}} Q\left(\frac{\bar{d}_F}{z\sigma_T} + \frac{\sqrt{2}z\sigma_T}{\sigma_{d_F}}\right). \end{aligned} \tag{6.48}$$

Then:

$$P_e = Q\left(\sqrt{\frac{E_p\bar{d}_F^2}{\sigma_T^2}}\right) - \frac{1}{4}e^{-\frac{\sqrt{2}\bar{d}_F}{\sigma_{d_F}}} + \frac{1}{2}e^{\frac{\sigma_T^2}{E_p\sigma_{d_F}^2}-\frac{\sqrt{2}\bar{d}_F}{\sigma_{d_F}}}\left[Q\left(\frac{-\sqrt{2}\sigma_T}{\sqrt{E_p\sigma_{d_F}^2}}\right) - Q\left(\frac{\sqrt{E_p}\bar{d}_F}{\sigma_T} - \frac{\sqrt{2}\sigma_T}{\sqrt{E_p\sigma_{d_F}^2}}\right)\right] - \frac{1}{2}e^{\frac{\sigma_T^2}{E_p\sigma_{d_F}^2}+\frac{\sqrt{2}\bar{d}_F}{\sigma_{d_F}}}Q\left(\frac{\sqrt{E_p}\bar{d}_F}{\sigma_T} + \frac{\sqrt{2}\sigma_T}{\sqrt{E_p\sigma_{d_F}^2}}\right). \quad (6.49)$$

Note that, in case of full energy capture (which is equivalent to a perfect Rake receiver with complete knowledge of the desired received UWB pulse shape), the desired component of the decision statistic may be assumed constant, as demonstrated in section 6.5. Equivalently, $\sigma_d = 0$, and the probability of error becomes:

$$\begin{aligned} P_e &= Q\left(\sqrt{\frac{E_p\bar{d}^2}{\sigma_T^2}}\right) = Q\left(\sqrt{\frac{E_pM\bar{d}^2}{2N_I\left(a^2+b^2\right)\sigma^2 + \frac{N_0}{2}}}\right) \\ &= Q\left(\sqrt{M \times SIR_{SD}}\right) \end{aligned} \quad (6.50)$$

where $SIR_{SD} = \frac{E_p\bar{d}^2}{2N_I(a^2+b^2)\sigma^2+\frac{N_0}{2}}$ is the SIR at the output of the correlator. Thus, for the perfect Rake receiver, we expect a 3-dB performance gain in the probability of error every time we double the number of antennas M. Moreover, simulation results will show that the gain in the case of the traditional Rake receiver is also practically equal to 3-dB for a moderate number of fingers, because of the negligible UWB energy variation across antennas ($\sigma_d^2 \approx 0$).

6.7.2 Ricean Fading

The probability of error for the NBI Ricean fading case may be obtained following the same analysis performed for Rayleigh fading. However, the calculations are more cumbersome, and the obtained expressions do not always provide intuitive understanding of the gains yielded by the proposed system. We include the basic strategy for the derivation of P_e, and note the fundamental results.

Keeping with the notation of the previous section, and based on (6.35), the distribution of the selected

interference fading parameter after SD for Ricean fading is given by:

$$f_{\alpha_m}(\alpha) = \frac{M}{\sigma^2} Q_1^{M-1}\left(\frac{s}{\sigma}, \frac{\alpha}{\sigma}\right) e^{-\frac{s^2+\alpha^2}{2\sigma^2}} I_0\left(\alpha \frac{s}{\sigma^2}\right) \tag{6.51}$$

where $Q_1(.)$ is the generalized Marcum's Q function.

The Jacobian method used for Rayleigh fading yields complex expressions for the Ricean case, because the random variables are no longer Gaussian. We thus follow a different approach for obtaining P_e. Note that i_m may be written as:

$$i_m = R\alpha_m sin\left(\phi_m + \Gamma\right) \tag{6.52}$$

where $\Gamma = tan^{-1}\left(\frac{-a}{b}\right)$ and $R = \sqrt{2N_I\left(a^2+b^2\right)}$. The distribution of $\beta_m = Rsin\left(\phi_m + \Gamma\right)$ is given by [114]:

$$f_{\beta_m}(\beta) = \frac{1}{\pi\sqrt{R^2-\beta^2}}, |\beta| < R. \tag{6.53}$$

Similar to previous section, the probability of error is given by:

$$P_e = \int_{\alpha=0}^{\infty}\int_{\beta=-R}^{R}\int_{n=-\alpha\beta}^{\infty}\int_{x=0}^{\frac{\alpha\beta}{\sqrt{E_p}}} f_d(x) f_{n_m}(n) f_{\alpha_m}(\alpha) f_{\beta_m}(\beta) dx\ dn\ d\alpha\ d\beta \tag{6.54}$$

which may be written as:

$$P_e = \frac{M}{\pi\sigma^2}\sqrt{\frac{1}{\pi N_0}}\int_{\alpha=0}^{\infty}\int_{\beta=-R}^{R}\int_{n=-\alpha\beta}^{\infty}\int_{x=0}^{\frac{\alpha\beta}{\sqrt{E_p}}} e^{-\frac{\sqrt{2}|x-\bar{d}_F|}{\sigma_{d_F}}} e^{-\frac{n^2}{N_0}} \frac{1}{\sqrt{(R^2-\beta^2)}} \alpha Q_1^{M-1}\left(\frac{s}{\sigma}, \frac{\alpha}{\sigma}\right) e^{-\frac{s^2+\alpha^2}{2\sigma^2}}$$
$$.I_0\left(\alpha\frac{s}{\sigma^2}\right) dx\ dn\ d\alpha\ d\beta. \tag{6.55}$$

In the case of full energy capture ($\sigma_d = 0$), and ignoring thermal noise (the case where performance is strictly limited by high-power NBI), the probability of error becomes:

$$P_e = \int_{\frac{\sqrt{E_p}\bar{d}}{R}}^{\infty}\int_{-R}^{-\frac{\sqrt{E_p}\bar{d}}{\alpha}} f_{\alpha_m}(\alpha) f_{\beta_m}(\beta) d\alpha d\beta. \tag{6.56}$$

After some manipulation, we get:

$$P_e = \frac{M}{\pi\sigma^2}\int_{\frac{\sqrt{E_p}\bar{d}}{R}}^{\infty}\left(sin^{-1}\left(\frac{-\sqrt{E_p}\bar{d}}{Rx}\right)+\frac{\pi}{2}\right)xQ_1^{M-1}\left(\frac{s}{\sigma},\frac{x}{\sigma}\right)e^{-\frac{s^2+x^2}{2\sigma^2}}I_0\left(x\frac{s}{\sigma^2}\right)dx. \quad (6.57)$$

Numerical evaluation of (6.57) shows that P_e drops with increasing M. However, the diversity gains are less substantial as compared to the Rayleigh fading case. Moreover, the gain deteriorates for increasing power ratio $K = \frac{s^2}{2\sigma^2}$.

6.8 Diversity SIR Improvement

We have studied the system gain from a probability of error point of view in the previous section. We now formulate the improvement in effective SIR provided by the SD method. Specifically, we are interested in the average SIR required to guarantee a target probability of error. It will be shown that the required SIR drops with increasing number of antennas. Analysis is provided for both Rayleigh and Ricean fading.

6.8.1 Rayleigh Fading

Let's first consider NBI Rayleigh fading. In this case, the interference energy at the j^{th} antenna, $I_j = |\alpha_j|^2$ (where P_I is subsumed into the random variable for notational simplicity), over a local area, is central Chi-square distributed with 2 degrees of freedom, and may be expressed as:

$$f_{I_j}(x) = \frac{1}{\overline{I}}e^{-\frac{x}{\overline{I}}} \quad (6.58)$$

where $\overline{I}$ is the average interference energy. Let $\bar{S}$ be the average UWB signal energy over the local area. Then, based on the arguments in section 6.5, the UWB energy may be approximated by a constant $\bar{S}$ (since power measurement is performed prior to demodulation and detection), and the distribution of the SIR at the j^{th} antenna, $\chi_j = \frac{\overline{S}}{I_j}$ may be written as:

$$f_{\chi_j}(\chi) = f_{I_j}\left(\frac{\overline{S}}{\chi}\right)\left|\frac{d}{d\chi}\left(\frac{\overline{S}}{\chi}\right)\right| = \frac{\overline{\chi}}{\chi^2}e^{-\frac{\overline{\chi}}{\chi}} \quad (6.59)$$

where $\overline{\chi} = \frac{\overline{S}}{\overline{I}}$ is the average SIR.

The CDF of the SIR can then be easily shown to be:

$$F_{\chi_j}(\chi) = e^{-\frac{\overline{\chi}}{\chi}}. \tag{6.60}$$

Consider a diversity array with M receive antennas, *i.e.* M independent fading channel realizations (from the NBI perspective). Let the instantaneous SIR in each branch be χ_i. The pdf of χ_i is given by (6.59). The probability that a single branch has an instantaneous SIR less than or equal to some threshold χ is $e^{-\frac{\overline{\chi}}{\chi}}$. Since the diversity branches are independent, the probability that all M independent diversity branches receive signals which are simultaneously less than or equal to some specific SIR threshold χ is:

$$P_M(\chi) = \left(\Pr\left[\chi_i \leq \chi\right]\right)^M = e^{-\frac{M\overline{\chi}}{\chi}}. \tag{6.61}$$

The probability that at least one branch exceeds χ is then:

$$P_S(\chi) = 1 - e^{-\frac{M\overline{\chi}}{\chi}}. \tag{6.62}$$

Assume that we require at least one branch to exceed χ with a probability p (where $1-p$ an be interpreted as an outage probability). Then, assuming the average SIR is equal to $\overline{\chi}$, the required number of antennas is:

$$M = \left\lceil \frac{\chi}{\overline{\chi}} log\left(\frac{1}{1-p}\right) \right\rceil \tag{6.63}$$

where $log(x)$ is the natural logarithm of x, and $\lceil . \rceil$ is the ceil operator. Equivalently, with a fixed M, the required $\overline{\chi}$ would be:

$$\overline{\chi} \geq \frac{\chi}{M} log\left(\frac{1}{1-p}\right). \tag{6.64}$$

Note that the required $\bar{\chi}$ drops directly with increasing M.

6.8.2 Ricean Fading

Assume that the NBI goes through Ricean fading. The energy $I = |\alpha_j|^2$ is now distributed following a noncentral Chi-square distribution with 2 degrees of freedom:

$$f_I(x) = \frac{1}{2\sigma^2} e^{-\frac{s^2+x}{2\sigma^2}} I_0\left(\sqrt{x}\frac{s}{\sigma^2}\right). \tag{6.65}$$

Again, let $\chi = \frac{\overline{S}}{I}$ be the SIR. Then, using the same method as for Rayleigh fading, we get:

$$f_\chi(\chi) = \frac{\bar{S}}{2\sigma^2}\frac{1}{\chi^2} e^{-\frac{s^2+\frac{\bar{S}}{\chi}}{2\sigma^2}} I_0\left(\sqrt{\frac{\bar{S}}{\chi}}\frac{s}{\sigma^2}\right). \tag{6.66}$$

The CDF may then be written as:

$$F_\chi(\chi) = \int_0^\chi \frac{\bar{S}}{u^2}\frac{1}{2\sigma^2} e^{-\frac{s^2+\frac{\bar{S}}{u}}{2\sigma^2}} I_0\left(\sqrt{\frac{\bar{S}}{u}}\frac{s}{\sigma^2}\right) du. \tag{6.67}$$

Let $v = \frac{\bar{S}}{u}$. A basic change of variable gives:

$$F_\chi(\chi) = \int_{\frac{\bar{S}}{\chi}}^\infty \frac{1}{2\sigma^2} e^{-\frac{s^2+v}{2\sigma^2}} I_0\left(\sqrt{v}\frac{s}{\sigma^2}\right) dv. \tag{6.68}$$

Using the well known formula for the CDF of a Ricean distribution, we get:

$$F_\chi(\chi) = Q_1\left(\frac{s}{\sigma}, \frac{\sqrt{\frac{\bar{S}}{\chi}}}{\sigma}\right). \tag{6.69}$$

Following the same analysis for Ricean fading, and based on Equation (6.69), the probability that at least one branch exceeds χ is:

$$P_S(\chi) = 1 - \left[Q_1\left(\frac{s}{\sigma}, \frac{\sqrt{\frac{\bar{S}}{\chi}}}{\sigma}\right)\right]^M. \tag{6.70}$$

Assume that we require at least one branch to exceed χ with a probability p. Then, after some manipulation, we get:

$$M = \left\lceil \frac{log\left(\frac{1}{1-p}\right)}{log\left(Q_1^{-1}\left(\frac{s}{\sigma}, \frac{\sqrt{\frac{\bar{S}}{\chi}}}{\sigma}\right)\right)} \right\rceil . \tag{6.71}$$

Note that $\bar{I} = s^2 + 2\sigma^2$. Also, recall that $K = \frac{s^2}{2\sigma^2}$. Then, after straightforward manipulation, (6.71) may be written as:

$$M = \left\lceil \frac{log\left(\frac{1}{1-p}\right)}{log\left(Q_1^{-1}\left(\sqrt{2K}, \sqrt{2\left(K+1\right)\frac{\bar{\chi}}{\chi}}\right)\right)} \right\rceil . \tag{6.72}$$

If $K = 0$, it is easy to show that (6.72) degenerates to (6.63), which corresponds to the Rayleigh fading case. Moreover, for $K \to \infty$, we distinguish two cases:

- If $\chi < \bar{\chi}$, then $\lim_{K\to\infty} Q_1\left(\sqrt{2K}, \sqrt{2\left(K+1\right)\frac{\bar{\chi}}{\chi}}\right) \to 0$, and $M = 1$ satisfies (6.72).
- If $\chi > \bar{\chi}$, then $\lim_{K\to\infty} Q_1\left(\sqrt{2K}, \sqrt{2\left(K+1\right)\frac{\bar{\chi}}{\chi}}\right) \to 1$, and $M > \infty$ (in other words, no solution exists).

The above observation is intuitive. Indeed, as K grows, Ricean fading is dominated by the deterministic, non-variable LOS component. For $K \to \infty$, the NBI power is constant across antennas ($\chi = \bar{\chi}$), and all diversity gains vanish.

The proof is now included for completeness. Let's define D as:

$$D = Q_1\left(\sqrt{2K}, \sqrt{2\left(K+1\right)\frac{\bar{\chi}}{\chi}}\right).$$

Let $Z = \frac{\bar{\chi}}{\chi}$. Then, D may be written as:

$$D = Q_1\left(\sqrt{2K}, \sqrt{2ZK + 2Z}\right).$$

Suppose $Z > 1$. Then, $\sqrt{2K} < \sqrt{2ZK + 2Z}$. Then, based on [150],

$$D \leq e^{-\frac{(\sqrt{2ZK+2Z} - \sqrt{2K})^2}{2}}.$$

It is trivial to show that:

$$\lim_{K\to\infty} \frac{\left(\sqrt{2ZK+2Z}-\sqrt{2K}\right)^2}{2} = \lim_{K\to\infty} K\left(\sqrt{Z}-1\right)^2 = \infty.$$

Then, since $D \geq 0$, $\lim_{K\to\infty} D = 0$, and consequently:

$$\lim_{K\to\infty} \frac{log\left(\frac{1}{1-p}\right)}{log\left(Q_1^{-1}\left(\sqrt{2K}, \sqrt{2\left(K+1\right)\frac{\bar{\chi}}{\chi}}\right)\right)} = 0.$$

Thus, if $Z > 1$, $M = 1$ satisfies (6.72) as $K \to \infty$.

Now, suppose $Z < 1$. Then, there exists a value K_0 such that, for $K > K_0$, $\sqrt{2K} > \sqrt{2ZK+2Z}$. Then, based again on [150], for $K > K_0$:

$$1 - \frac{1}{2}\left[e^{-\frac{(\sqrt{2K}-\sqrt{2ZK+2Z})^2}{2}} - e^{-\frac{(\sqrt{2K}+\sqrt{2ZK+2Z})^2}{2}}\right] \leq D.$$

It is trivial to show that:

$$\lim_{K\to\infty} 1 - \frac{1}{2}\left[e^{-\frac{(\sqrt{2K}-\sqrt{2ZK+2Z})^2}{2}} - e^{-\frac{(\sqrt{2K}+\sqrt{2ZK+2Z})^2}{2}}\right] = 1.$$

Then, since $D \leq 1$, $\lim_{K\to\infty} D = 1$, and consequently:

$$\lim_{K\to\infty} \frac{log\left(\frac{1}{1-p}\right)}{log\left(Q_1^{-1}\left(\sqrt{2K}, \sqrt{2\left(K+1\right)\frac{\bar{\chi}}{\chi}}\right)\right)} = \infty.$$

Thus, if $Z < 1$, no value of M satisfies (6.72) as $K \to \infty$.

Simulation results will show that, although performance improves with increasing M, the gains are less substantial than the Rayleigh case.

6.9 Other Combining Techniques

In this section, we describe two additional combining methods: EGC and MRC. These methods may not be practical for the studied system, since they pose complexity issues, and require synchronization between different antennas, which might not be achievable prior to NBI mitigation. Nonetheless, their analysis is useful, since they provide a valuable comparison benchmark for the proposed SD method. We restrict the analysis to the perfect receiver (all-Rake) case.

6.9.1 Equal Gain Combining

Rayleigh Fading

In EGC, diversity is achieved by simply averaging the signals from different antennas (and therefore their equivalent decision statistics). Assuming the data bit is 1, The EGC decision statistic can be written as:

$$r_{EGC} = \frac{1}{M}\sum_{k=1}^{M} r_k = \sqrt{E_p}d + \frac{1}{M}\sum_{k=1}^{M} i_k + n_{EGC} = \sqrt{E_p}d + i_{EGC} + n_{EGC}. \tag{6.73}$$

where n_{EGC} is a zero-mean Gaussian random variable with variance $\frac{N_0}{2}$. From section 6.7, we know that i_k is a zero-mean Gaussian random variable with variance $2N_I\left(a^2+b^2\right)\sigma^2$, $\forall\ k$ (see section 6.7). Therefore, i_{EGC} is a zero-mean Gaussian random variable with variance $2N_I\left(a^2+b^2\right)\frac{\sigma^2}{M}$. Thus it is simply shown that performance of EGC for this receiver is identical to that of SD and is given by Equation (6.50).

Ricean Fading

The decision statistic for EGC under NBI Ricean fading is given by (6.73). Obtaining a statistical distribution of the interference term i_{EGC} is not straightforward, because the terms i_k, $\forall\ k$ are characterized by a relatively complex distribution. However, since $i_{EGC} = \frac{1}{M}\sum_{k=1}^{M} i_k$, and the individual terms of the sum are independent, the pdf of i_{EGC} may be written as:

$$f_i(x) = f_{j_1}(x) * f_{j_2}(x) * f_{j_3}(x) ... * f_{j_M}(x) \tag{6.74}$$

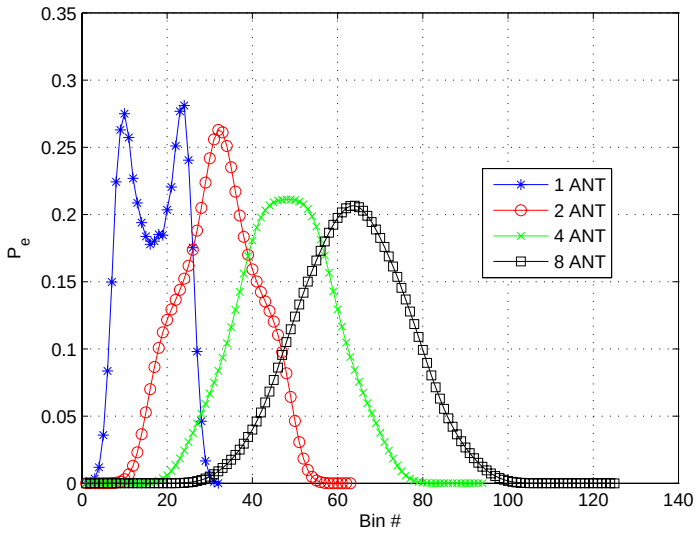

Figure 6.5: Probability density function for EGC decision statistic under Ricean fading for 1, 2, 4 and 8 antennas. K=3. Plots shifted for clarity. Gaussian approximation is acceptable for $M \geq 2$.

where $j_k = \frac{i_k}{M}$, and $f_{j_k}(x)$ is the PDF of j_k.

Note that j_k, $\forall$ k are i.i.d Gaussian random variables. Therefore, for a sufficient number of antennas, the central limit applies, and i may be approximated by a Gaussian random variable. In fact, numerical evaluation of $f_i(x)$ for different antenna numbers suggests that the Gaussian approximation may be applied with negligible error for a small number of antennas: Figure 6.5 shows that the PDF shape converges to the Gaussian shape very fast for increasing M. Figure 6.6 provides the decision metric's PDF along with its Gaussian fit (a Gaussian distribution with equal mean and variance). The PDF is practically Gaussian for $M \geq 2$. The probability of error is then given by Equation (6.50). Simulation results will show that this approximation results in negligible error.

6.9.2 Maximum Ratio Combining

In MRC, individual weights are assigned to each antenna. Neglecting thermal noise, The weights are selected to maximize the system SIR. Assuming the data bit is 1, the MRC decision statistic can be written as:

$$r_{MRC} = \sum_{k=1}^{M} c_k r_k = \sqrt{E_p} d \sum_{k=1}^{M} c_k + \sum_{k=1}^{M} c_k i_k \tag{6.75}$$

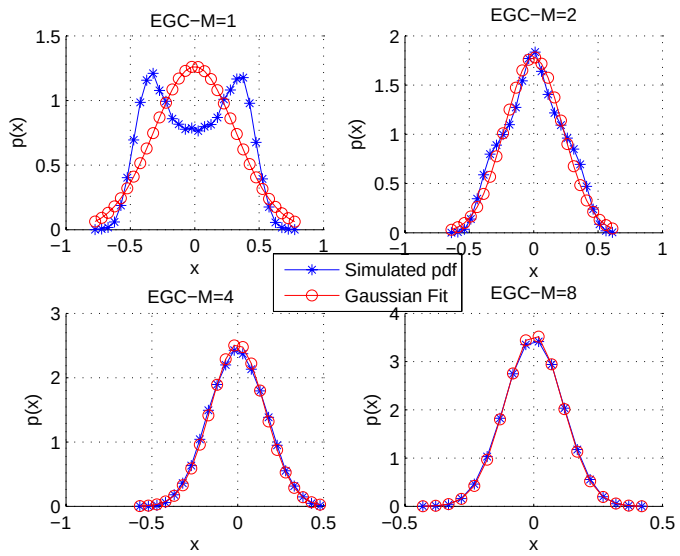

Figure 6.6: Probability density function for EGC decision metric under Ricean fading for 1, 2, 4 and 8 antennas. K=3. Gaussian fit provided. Gaussian approximation is acceptable for $M \geq 2$.

where c_k is the weight of the k^{th} antenna. We define the SIR as:

$$SIR = \frac{E_p d^2 \left(\sum_{k=1}^{M} c_k\right)^2}{\sum_{i=1}^{M} c_i^2 P_i} \tag{6.76}$$

where P_i is the interference power seen by the i^{th} antenna. We find the optimal weight c_j by partial differentiation. We get:

$$\frac{\delta SIR}{\delta c_j} = E_p d^2 \frac{num}{\left(c_j^2 P_j + \sum_{i \neq j} c_i^2 P_i\right)^2} \tag{6.77}$$

where:

$$num = 2\left(c_j + \sum_{i \neq j} c_i\right)\left(c_j^2 P_j + \sum_{i \neq j} c_i^2 P_i\right) - 2c_j P_j \left(c_j + \sum_{i \neq j} c_i\right)^2 \tag{6.78}$$

Setting $num = 0$ and solving for c_j, we get:

$$c_j = \frac{\sum_{i \neq j} P_i c_i^2}{P_j \sum_{i \neq j} c_i}, \quad 1 \leq j \leq M. \tag{6.79}$$

Notice that the optimal weight for the j^{th} antenna is inversely proportional to the j^{th} antenna power, and proportional to a linear combination of the other antennas powers: On one hand, as the j^{th} power grows, the j^{th} decision statistic becomes less reliable, and is thus weighted down. On the other hand, when the other powers grow, more weight is given to the j^{th} antenna.

Let's take the case of 2 antennas. We get $c_1 = \frac{P_2}{P_1} c_2$ and $c_2 = \frac{P_1}{P_2} c_1$. By forcing $c_1 + c_2 = 1$, we get $c_1 = \frac{P_2}{P_1+P_2}$ and $c_2 = \frac{P_1}{P_1+P_2}$.

6.10 Simulation Results

A simulation of the proposed system using UWB 2-PAM modulation was carried out based on actual NLOS channel measurements recorded at MPRG. For a thorough analysis of the channel characterization, the reader is referred to section 2.5 and the references therein. Measurements are grouped in separate position-sets of 49 channel impulse responses. Each position-set holds measured channel impulse responses at 49 uniformly distributed points in a 1 m^2 local area. In the simulation, M channel impulse responses from the same position-set are selected randomly and assigned to the M receive antennas. The simulation is averaged over a large number of channel realizations by repeating the procedure over multiple position-sets. NBI is modeled by a 1 GHz tone (which is near the middle of the UWB band), and is assumed to undergo independent Rayleigh or Ricean fading over M receive antennas. Power measurements are averaged over multiple bits, such that (6.23) holds. A 500 psec UWB Gaussian transmit pulse is used. The symbol duration T_f is equal to 80 nsec, which is longer than the channel maximum delay spread.

Figure 6.7 displays the performance of SD versus signal-to-noise-plus-interference (SINR) under Rayleigh fading when perfect channel knowledge and full energy capture is available (*i.e.* a perfect Rake receiver which captures all the available multipath components). Here, SINR is defined as the signal-to-noise-plus-interference ratio at the output of the correlator. As expected, performance matches the theoretical expression of (6.50). Doubling the number of antennas yields a 3-dB gain.

Performance of the proposed SD system applied to a 20-finger Rake receiver employing MRC combining is tested for NBI Rayleigh fading in Figure 6.8. The performance is plotted for simulation results, theoretical results assuming a Laplacian distribution for the desired signal component (6.49), and theoretical results

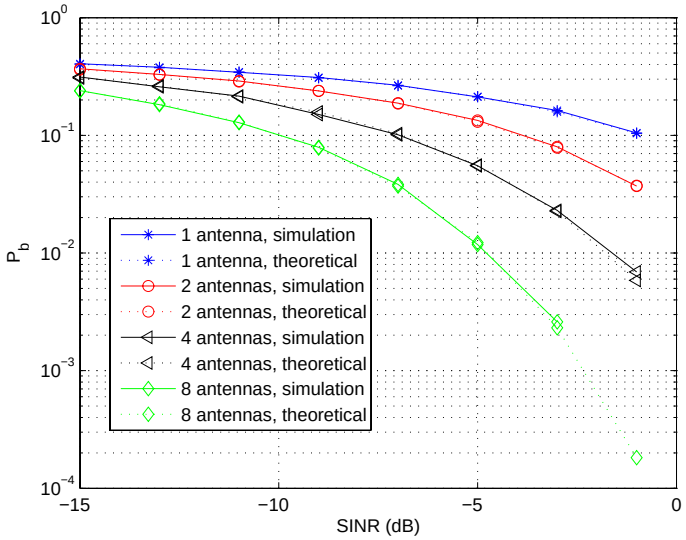

Figure 6.7: SD under NBI Rayleigh Fading. Perfect energy capture. 1, 2, 4 and 8 antennas.

assuming constant energy capture (6.50). Notice that, at low SINR values, diversity gains are practically equal to 3-dB when doubling M, and that (6.49) and (6.50) yield almost the same performance. The variation in energy capture across antennas is negligible compared to the variation of the interference energy, and gains are similar to the full energy capture case. However, for high SIR values, the energy capture variation impacts performance, and the simulated probability of error is closer to (6.49). At high SINR, the performance is more heavily influenced by the fluctuation in UWB energy. Note that since SIR is measured at the output of the correlator, the average Rake energy capture $\bar{d}_F$ is incorporated into SIR. In other words, we are interested in the variance of the energy over a local area, and not in its mean value**. Also, it is important to note the distinction between the SD process applied at the power selection level, and the MRC process which occurs at the Rake finger combination level; the two processes are independent and must not be confused. Finally, note that similar diversity gains are observed for a Rake receiver with a smaller number of fingers (10 fingers, or 5 fingers).

Performance for Ricean fading ($K = 5$) under SD and complete energy capture is displayed in Figure 6.9. It is assumed that performance is limited by high-power NBI, and Gaussian noise is neglected. Notice that the simulation results match the theoretical expression in (6.57). Moreover, for a specific number of antennas

**The Rake average energy capture is an important issue for a practical system, but here we are only interested in the diversity gains achievable by our system.

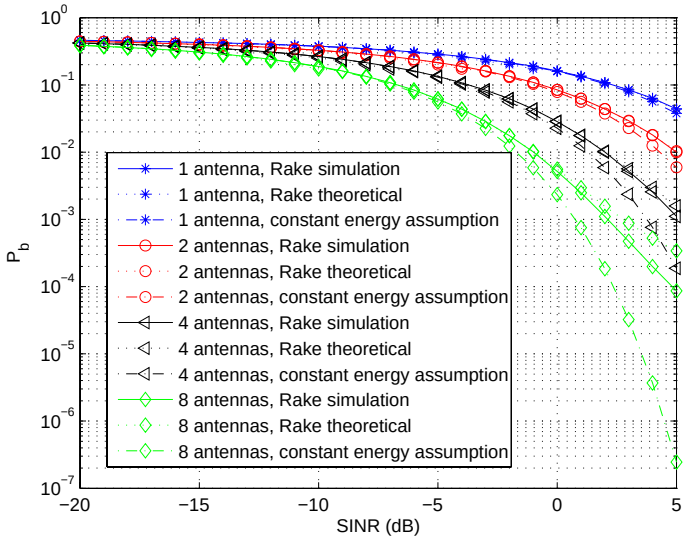

Figure 6.8: SD under NBI Rayleigh Fading. 20-Finger Rake. 1, 2, 4 and 8 antennas.

M, Ricean fading yields a higher probability of error compared to Rayleigh fading. Less diversity gains are observed when increasing the number of antennas (1-2 dB when doubling M). This is an intuitive result, since the NBI power does not vary much across antennas compared to the Rayleigh case, because of the dominant deterministic LOS power component, and thus less diversity gains are achievable.

Figure 6.10 compares the performance of SD and EGC under Rayleigh fading. Perfect channel knowledge is assumed at the receiver, and the effect of thermal noise is ignored. As expected, performance of both methods is similar, and matches that of Equation (6.50). Doubling the number of antennas yields a 3-dB gain. Figure 6.11 compares performance of MRC and ECG (and consequently SD) with perfect channel knowledge. Notice that MRC consistently outperforms ECG by about 1 to 2 dB, by individually optimizing the weights of the received antennas.

Performance for EGC and SD under Ricean fading with perfect channel knowledge are compared in Figure 6.12. Notice that Ricean EGC outperforms Ricean SD, and performance is similar to that of Rayleigh fading for 2 or more antennas. The decision statistic may be approximated as Gaussian for $M \geq 2$, as suggested in section 6.9, which explains this result.

MRC and EGC performance under Ricean fading with perfect channel knowledge are compared in Figure 6.13. Notice that gains brought by MRC vanish as the factor K increases. This is an intuitive result, since,

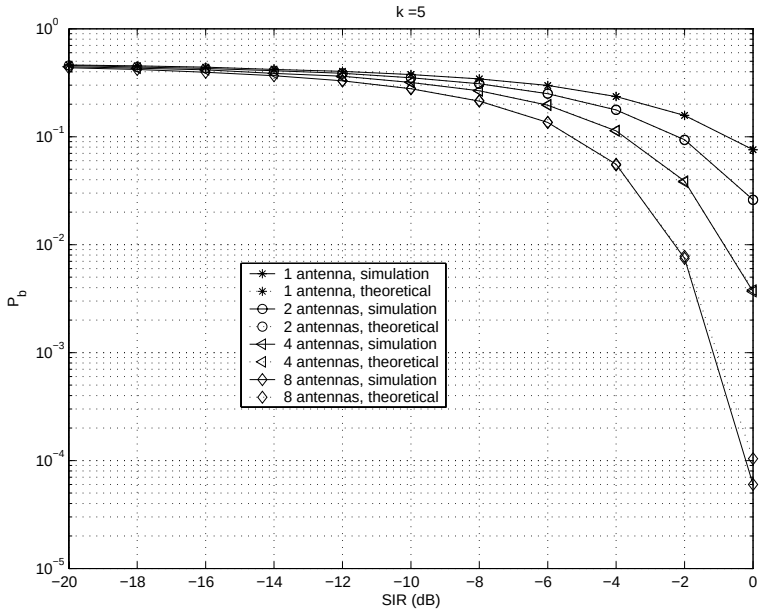

Figure 6.9: SD performance under NBI Ricean Fading. Perfect energy capture. $K = 5$.

as K grows, the constant LOS component dominates NBI. The NBI power then varies less across different antennas, and the MRC weighting factors are approximately equal to the same value. At the extreme case of pure LOS NBI, all antennas are weighted equally, and the system converges to EGC.

The effect of increasing the power in the Ricean LOS component under full energy capture is illustrated in Figure 6.14. Performance degrades with increasing K at low SIR, because of the diminishing diversity gains. At high SIR, the dominant LOS component becomes negligible compared to the UWB power, and the performance of the receiver is better with Ricean fading compared to Rayleigh fading ($K = 0$). As $K \to \infty$, the probability of error curve tends to a step function, where $P_e = 0.5$ at SIR < 0 dB, and $P_e = 0$ at SIR $>$ 0 dB. However, note that we are more concerned with performance at low SIR, since practical UWB systems will normally operate in the low SIR region.

The performance of a 20-finger Rake receiver under Ricean fading ($K = 5$) for high-power NBI is shown in Figure 6.15. Notice that the diversity gains are limited compared to the Rayleigh fading case (around 1-dB when M is doubled), because of the dominating LOS interference component.

The proposed system applied to a 20-finger Rake receiver is compared to a 20-tap MMSE receiver in Figure 6.16. The MMSE receiver is the most popular NBI mitigation technique in the literature. The MMSE receiver has the structure of a Rake receiver, but the individual finger weights (or filter taps) are computed

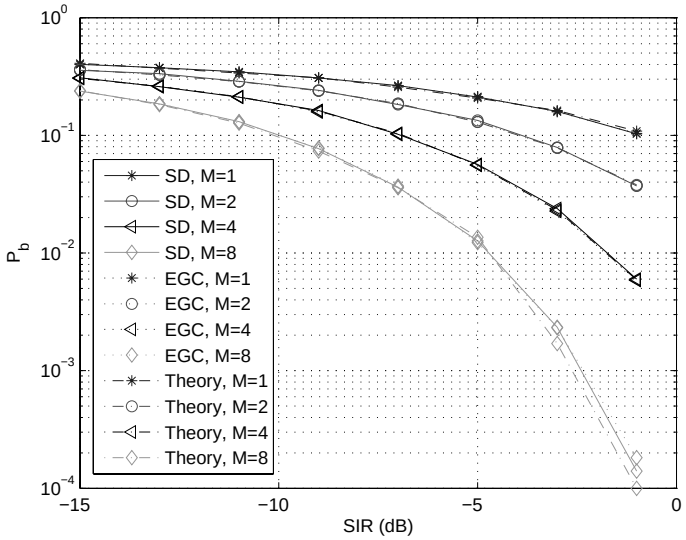

Figure 6.10: SD and EGC under NBI Rayleigh Fading. 1, 2, 4 and 8 antennas.

to minimize the mean square error instead of maximizing the energy capture [137]. In this simulation, it was assumed that the MMSE receiver has complete knowledge of the NBI's center frequency as well as the NBI average received power, which are not needed for our proposed system. The SIR is fixed at -10 dB, and performance is studied for varying SNR. Notice that the MMSE receiver outperforms the proposed receiver by about 2-dB when $M = 8$. With $M = 16$, the proposed receiver performs practically the same as the MMSE receiver. Note that the MMSE receiver is substantially more complex than the proposed receiver (it requires the inversion of a 20×20 covariance matrix), and simply provides a performance benchmark in the context of this work.

The probability $P_S(\chi)$ of at least one antenna SIR exceeding a threshold χ (see (6.62)) is plotted versus χ in Figure 6.17. Rayleigh fading is assumed, with an average antenna SIR of 5 dB. For a fixed $P_S(\chi)$, the threshold χ increases by 3 dB when the number of antennas is doubled. $P_s(\chi)$ is plotted for Ricean fading (with the same average antenna SIR) in Figure 6.18. The power ratio K is equal to 5. First, note that for a fixed χ, Ricean fading yields a lower (worse) $P_S(\chi)$ compared to Rayleigh fading. Second, the gains seen from increasing M are less substantial (about 1 dB when doubling the number of antennas). Due to the deterministic Ricean LOS power component, the SIR varies less across different antennas, and less diversity gains are possible. This is illustrated in Figure 6.19, where performance degrades for larger K. As K grows,

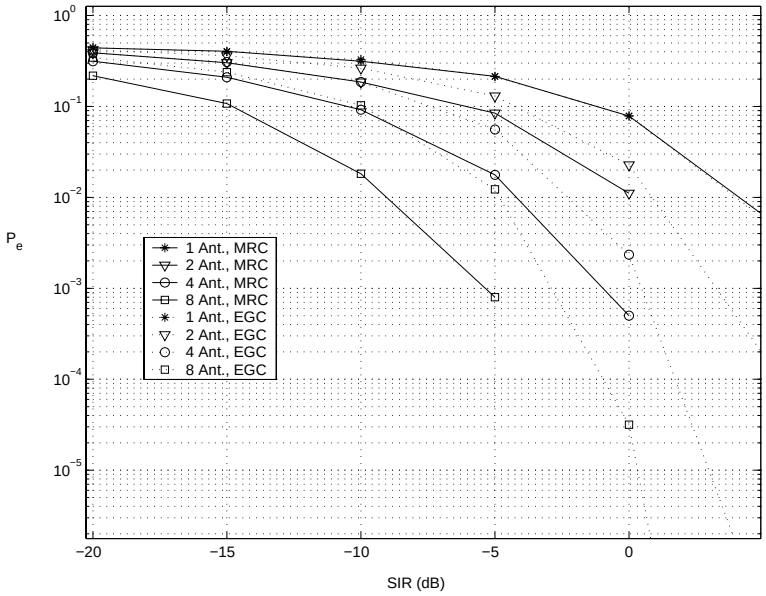

Figure 6.11: MRC and EGC under NBI Rayleigh Fading. 1, 2, 4 and 8 antennas.

the interference power across antennas becomes constant, and all diversity gains vanish.

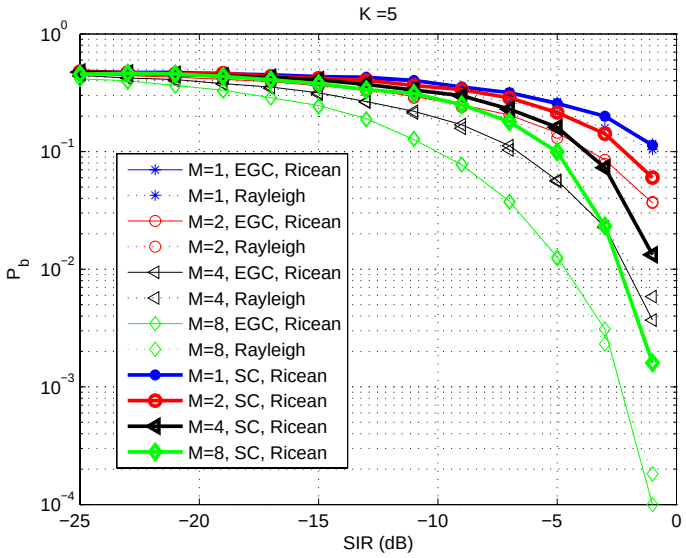

Figure 6.12: SD and EGC performance under NBI Ricean fading for varying M.

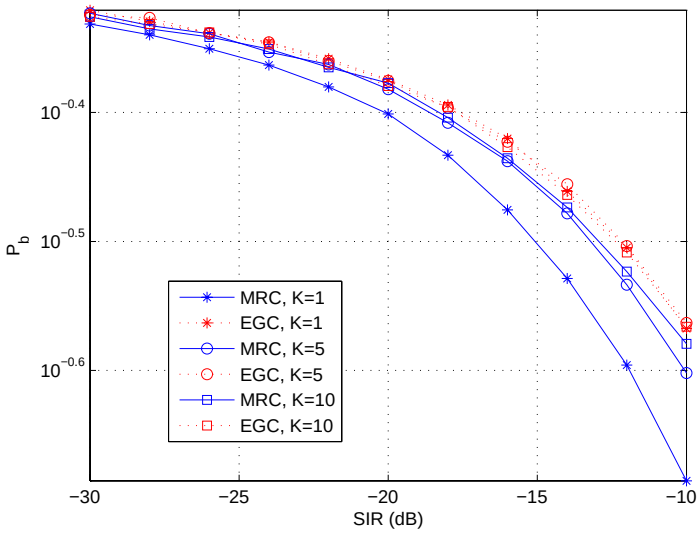

Figure 6.13: MRC and EGC performance under NBI Ricean fading for varying K. $M = 2$.

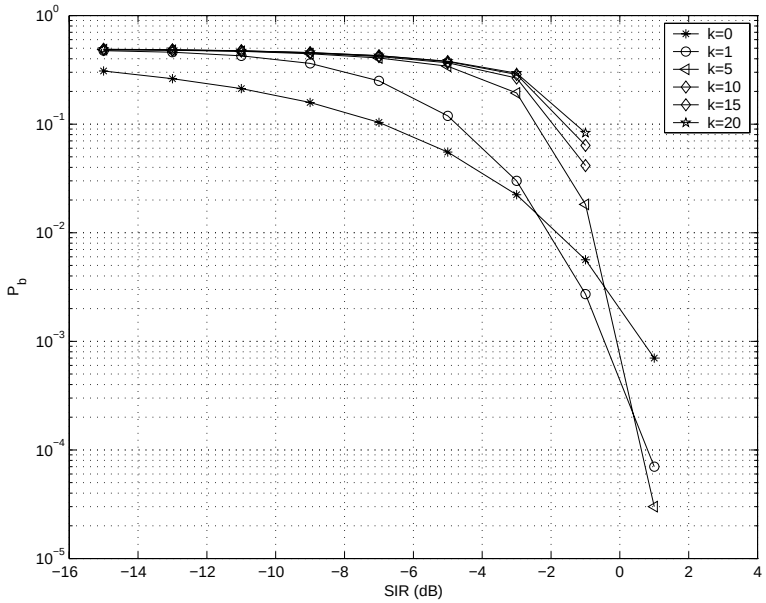

Figure 6.14: SD Performance under NBI Ricean Fading for varying K. M=4. Perfect energy capture.

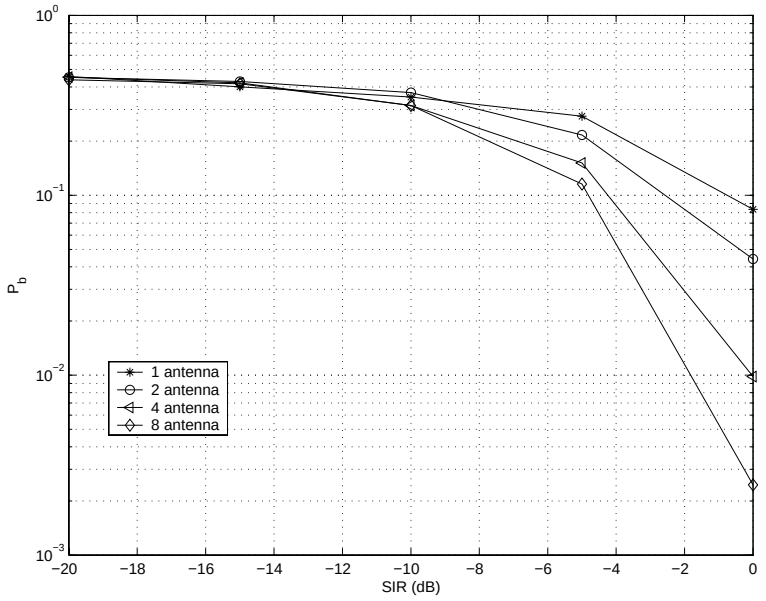

Figure 6.15: SD performance under NBI Ricean Fading. 20-Finger Rake. $K = 5$.

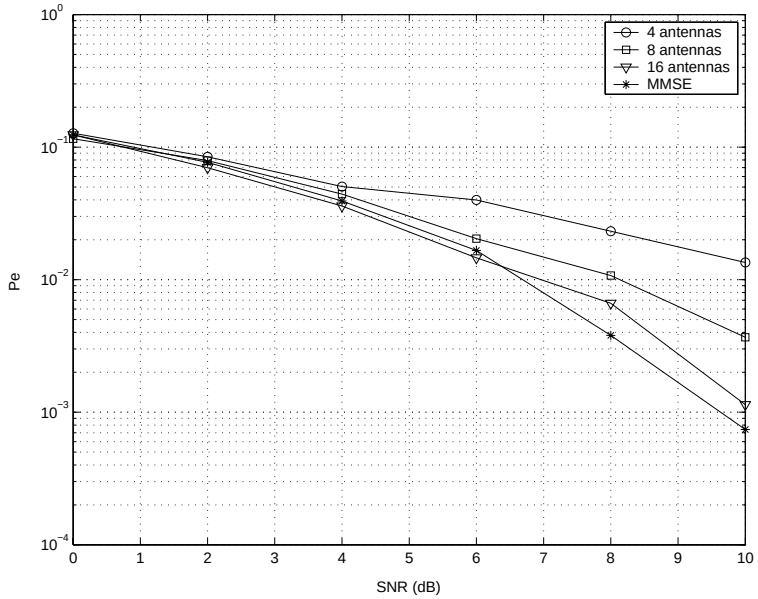

Figure 6.16: Proposed system versus MMSE receiver. 20-Finger Rake. Rayleigh fading.

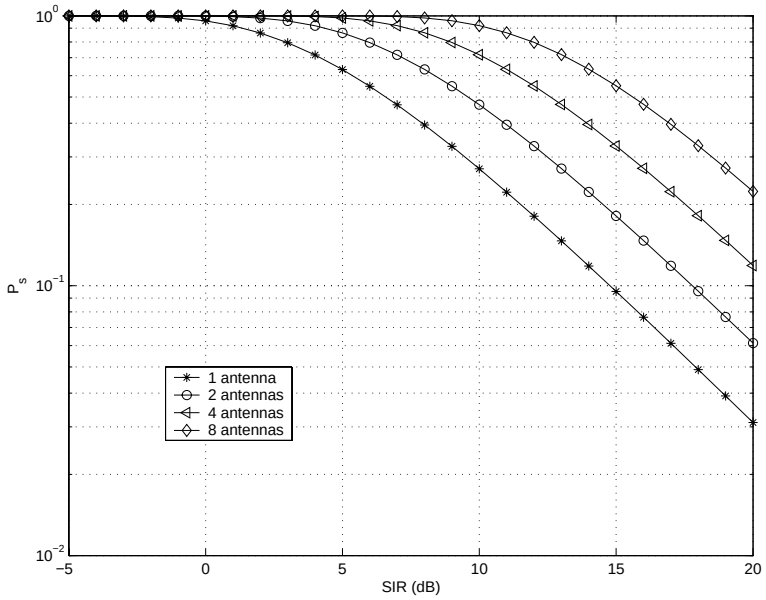

Figure 6.17: $P_S(\chi)$ (Probability that at least one antenna SIR exceeds χ) vs. χ for different number of antennas. Rayleigh fading. Average SIR = 5 dB.

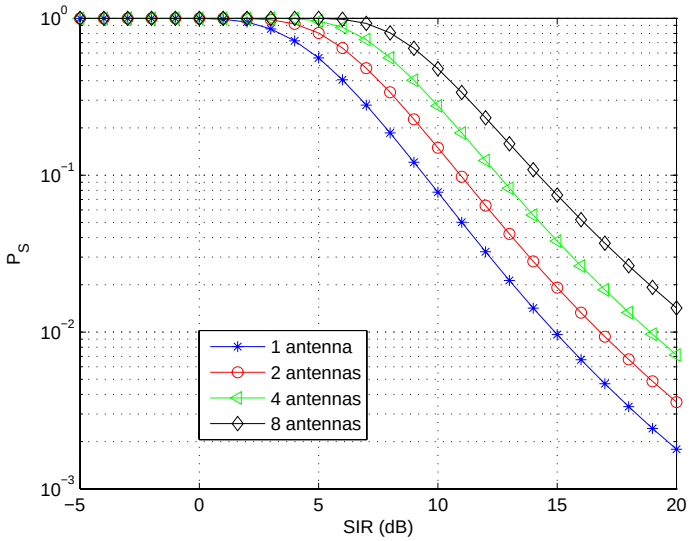

Figure 6.18: $P_S(\chi)$ vs. χ for different number of antennas. Ricean fading. $K = 5$. Average SIR =5 dB.

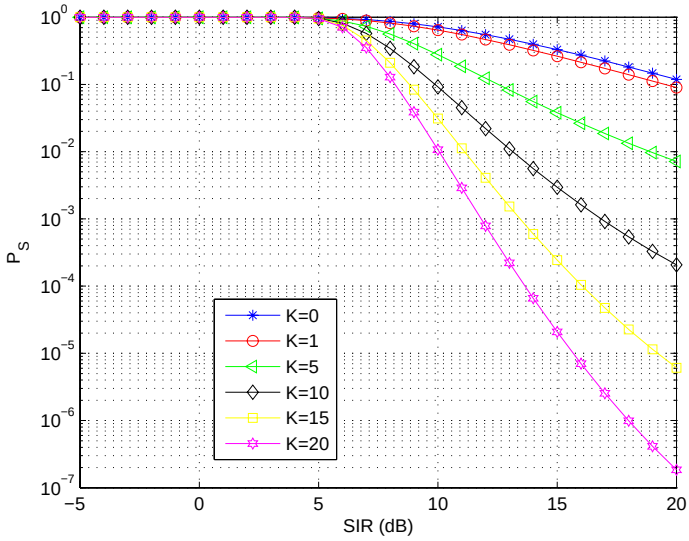

Figure 6.19: $P_S(\chi)$ vs. χ for different K. Average SIR =5 dB. $M = 4$.

6.11 Conclusions

This chapter presents a novel NBI mitigation scheme for UWB based on multiple receive antennas, where UWB's low spatial fading characteristics are exploited to mitigate NBI. This method has relatively low complexity, and does not assume synchronization prior to NBI cancellation. NBI diversity is studied under NBI Rayleigh and Ricean fading. SD, EGC and MRC techniques are considered. Probability of error expressions are derived for SD for both perfect (full) energy capture and partial energy capture. SD and EGC are shown to yield a potential 3-dB performance gain when the number of antennas is doubled for the Rayleigh fading case. Additional gains are observed for MRC. Gains are less substantial for the Ricean fading case, because Ricean NBI fading provides less variation to exploit through diversity, but can still provide some benefit. EGC outperforms SD for the Ricean fading case, because the EGC decision statistic is smoothened out by the averaging EGC operation, and approaches a Gaussian random variable, which is less detrimental to performance. MRC provides negligible gains compared to EGC in extreme Ricean fading scenarios.

Chapter 7

Conclusions and Recommended Future Work

7.1 Research Synthesis

This document presented research work conducted for UWB signal detection, synchronization, and NBI mitigation in dense multipath. The challenges posed in these three areas were discussed. Traditional solutions were analyzed and their limitations were identified. New algorithms, specifically tailored for dense multipath channels, were proposed.

Multipath is traditionally treated as a nuisance. Methods are usually devised to limit its effects, or remedy its damages. However, when attempting to discern intersections between the various proposed algorithms in this report, an interesting pattern immerges, which may define the underlying philosophy of this research. In fact, in most cases, multipath is not viewed as a limitation, but rather as a resource which may be exploited to our advantage. For example, the sequence optimization receiver achieves very high energy capture by treating the available multipath components as potential degrees of freedom. Judicious manipulation of these degrees of freedom (in this case, sequence optimization which forces multipath components to combine constructively at the receiver) potentially leads to efficient, high-performance algorithms. The two-stage acquisition process takes advantage of the existence of multiple H_1 cells to reduce acquisition time. Moreover, it uses the clustered

multipath structure to more robustly detect the LOS component. In the proposed interference mitigation scheme, dense multipath again plays to our advantage, since it causes low UWB and high NBI spatial energy fading, and thus creates diversity which may be utilized. From this viewpoint, multipath is transformed from an inconvenience to a potential asset. Going further, it would be interesting to establish a framework where it is possible to compare the performance of the proposed algorithms in dense multipath to the performance of traditional methods *in the absence* of multipath. Taking acquisition as an example, it has been already established that jump-phase search outperforms serial search in dense multipath. However, it is interesting to also note that jump-phase search in a dense multipath environment would outperform serial search in an environment deprived of multipath, since serial search would process half the available cells on average, while jump-phase search would process less cells, depending on the number of available H_1 cells.

7.2 Contributions and Publications

The main contributions of this research are listed below:

- An accurate characterization of existing/traditional signal detection approaches for UWB systems in dense multipath channels.
- A proposed iterative data-aided, pilot-assisted receiver with forward-error correction, which reduces the training overhead required by traditional TR receivers, and achieves high performance gains, by exploiting the synergy between improved channel estimation and coding gain.
- A proposed sequence optimization receiver, which exploits the dense multipath structure and achieves very high energy capture and efficient interference mitigation by forcing coherent combining of a large number of multipath components at the output of the receiver.
- A mathematical formulation for a general indoor UWB acquisition model, where the effect of dense multipath and the existence of multiple H_1 cells (which is usually neglected in the literature) are explicitly included.
- A proposed two-stage acquisition approach, which achieves fast acquisition and maintains reasonable complexity by uniformly spreading the delays corresponding to the multipath components over the

timing uncertainty region, and provides robust timing estimate by taking advantage of the clustered nature of multipath, even when the LOS component is severely attenuated.

- A proposed UWB tracking algorithm which utilizes the dense multipath structure to achieve robust continuous tracking of the LOS component or other multipath component.

- A NBI mitigation technique, based on multiple antennas, which exploits the low spatial fading of UWB signals relative to NBI signals to achieve "interference diversity". A complete characterization of this approach is also provided for various levels of multipath fading and receiver implementations.

Relevant publications resulting from this work are also listed for reference:

- Co-author, *An Introduction to Ultra Wideband Communication Systems,* Chapter 6, Receiver Design Principles, edited by Jeffrey H. Reed, Prentice Hall, 2005.

- J. Ibrahim, R. Menon, and R.M. Buehrer, "UWB Signal Detection Based on Sequence Optimization" *IEEE Communications Letters,* pp. 228-230, vol. 10, issue 4, April 2006.

- J. Ibrahim and R.M. Buehrer, "Two-Stage Acquisition for UWB in Dense Multipath," *IEEE Journal on Selected Areas in Communication,* vol. 24, issue 4, part I, pp. 801-807, April 2006.

- J. Ibrahim and R.M. Buehrer, "NBI Mitigation for UWB Systems Using Multiple Antenna Selection Diversity," *to appear, IEEE Transactions on Vehicular Technology,* 2007.

- S. Venkatesh, J. Ibrahim, R.M. Buehrer and D.R. McKinstry, "A Spatio-temporal Channel Model for Ultra-Wideband Indoor NLOS Communications," under review, *IEEE Transactions on Communications.*

- J. Ibrahim and R.M Buehrer, "A Modified Tracking Algorithm for UWB Pilot-Assisted Receivers," in *Proc. 2006 ICUWB,* September 2006.

- J. Ibrahim and R.M. Buehrer, "A UWB Multiple Antenna System for NBI Mitigation under Rayleigh and Ricean Fading," in *Proc. 2006 ICC,* vol. 10, pp. 4751-4756, June 2006.

- J. Ibrahim and R.M. Buehrer, "A Novel NBI Suppression Scheme for UWB Communications Using Multiple Receive Antennas," in *Proc. 2006 RWS,* pp. 507-510, January 2006.
- J. Ibrahim, R. Menon, and R.M. Buehrer, "UWB Sequence Optimization for Enhanced Energy Capture and Interference Mitigation," in *Proc. 2005 MILCOM,* vol.4, pp. 2086-2092, October 2005
- J. Ibrahim and R.M. Buehrer, "Two-Stage Acquisition for UWB in Dense Multipath," in *Proc. 2005 MILCOM,* pp. 1898-1904, vol.3, October 2005.
- R. Menon, J. Ibrahim, and R.M. Buehrer, "UWB Signal Detection Based on Sequence Optimization," in *Proc. 2005 WirelessComm,* vol.2, pp. 1231-1236, June 2005.
- J. Ibrahim and R.M. Buehrer, "A Data-Aided Iterative UWB Receiver with LDPC," in *Proc. 2005 VTC Fall,* vol. 1, pp. 33-37, June 2005.
- J. Ibrahim, B. Donlan, and R.M. Buehrer, "Interference Rejection Techniques for UWB Systems," in *Embedded Systems Conference,* 2005.
- S. Venkatesh, J. Ibrahim and R.M. Buehrer, "A New Model for Ultra Wideband Indoor NLOS Channels," in *Proc. 2004 Antennas and Propagation Society Conference*, 2004.

7.3 Recommendation for Future Work

This research has presented various physical layer algorithms which exploit UWB's characteristics in dense multipath. When evaluating the algorithms, emphasis was put on system performance metrics, such as probability of error, acquisition time and timing error. Although the computational complexity of the major UWB receiver structures was tackled in this work for comparison purposes, an in-depth study of the hardware implementation of the studied algorithms is beyond the scope of this research effort.

Efficient digital implementations will be critical for proper operation of synchronization, signal detection and NBI mitigation for UWB devices. Digital realizations of the proposed algorithms are required to harness their full potential. Any realistic UWB transceiver will be hindered by the inherently high required sampling rate. Power consumption, efficient ADC resolutions and memory requirements are other critical design challenges

(the reader is referred to [80] for an in-depth analysis of these issues).

Although the design of low-cost, low-complexity UWB transceivers has received some research interest lately (see [151] for a study of monobit UWB receivers for example), the implementation of such affordable devices is still largely an open and crucial research issue upon lies which the full potential deployment of the technology.

Bibliography

[1] C. Fowler, J. Entzminger, and J. Corum, "Report: Assessment of Ultra-Wideband (UWB) Technology," OSD/DARPA Ultra-Wideband Radar Review Panel, R-6280, 1990.

[2] "Revision of Part 15 of the Commission's Rules Regarding Ultra-Wideband Transmission Systems," First note and Order, Federal Communications Commission, ET-Docket 98-153, Adopted February 14, 2002, released April 22, 2002. Available: http://www.fcc.gov/Bureaus/Engineering_Technology/Orders/2002/fcc02048.pdf.

[3] L. Yang and G.B. Giannakis, "Ultra-wideband communications: an idea whose time has come," *Signal Processing Magazine,* vol. 21, issue 6, pp. 26-54, November 2004.

[4] R. Scholtz, "Multiple Access with Time-Hopping Impulse Modulation," *Proc. 1993 MILCOM,* vol. 2, pp. 447-450, 1993.

[5] J. H. Reed, *An Introduction to Ultra Wideband Communication Systems,* NJ: Prentice Hall, 2005.

[6] M. Welborn, T. Miller, J. Lynch, and J. McCorkle, "Multi-User Perspectives in UWB Communication Networks," *Proc. 2002 UWBST,* 2002.

[7] V. S. Somayazulu, "Multiple Access Performance in UWB Systems Using Time Hopping vs. Direct Sequence Spreading," *Proc. 2002 WCNC,* vol. 2, pp. 522-525, March 2002.

[8] J.R. Foerster, "The performance of a direct-sequence spread ultrawideband system in the presence of multipath, narrowband interference, and multiuser interference," *Proc. 2002 UWST,* pp. 87-91, 2002.

[9] F. Ramirez-Mireles and R. A. Scholtz, "Wireless Multiple-Access Using SS Time-Hopping and Block Waveform Pulse Position Modulation, Part 1: Signal Design," *Proc. 1998 ISITA Symposium*, October 1998.

[10] F. Ramirez-Mireles and R. A. Scholtz, "Wireless Multiple-Access Using SS Time-Hopping and Block Waveform Pulse Position Modulation, Part 2: Multiple- Access Performance," *Proc. 1998 ISITA Symposium*, October 1998.

[11] F. Ramirez-Mireles and R. A. Scholtz, "Multiple-Access with Time Hopping and Block Waveform PPM Modulation," *Proc. 1998 ICC*, vol. 2, pp. 775-779, 1998.

[12] T.S. Rappaport, *Wireless Communications: Principles and Practice,* 2nd ed., Upper Saddle River, NJ: Prentice Hall, 2002.

[13] G.L. Turin, D. Clapp, T.L. Johnson, S.B. Fine, and D. Lavry, "A statistical model of urban multipath propagation," *Transactions on Vehicular Technology,* vol. VT-21, pp. 1-9, February 1972.

[14] H. Suzuki, "A statistical model for urban radio propagation," *Transactions on Communications,* vol. COM-25, no. 7, pp. 673-680, July 1977.

[15] H. Hashemi, "Impulse response modeling of indoor radio propagation channels," *IEEE Journal on Selected Areas in Communications,* vol. 11, no. 7, pp. 967-978, September 1993.

[16] H. Hashemi, "The indoor radio propagation channel," *Proceedings of the IEEE,* vol. 81, no. 7, pp. 943-968, July 1993.

[17] W.H. Tranter, K.S. Shanmugan, T.S. Rappaport, and K. Kosbar, *Communication Systems Simulation with Wireless Applications,* NJ: Prentice Hall, 2004.

[18] D.R. McKinstry and R.M. Buehrer, "UWB small scale channel modeling and system performance," *Proc. 2003 VTC-Fall,* vol. 1, pp. 6-10, October 2003.

[19] R.M. Buehrer, A. Safaai-Jazi, W.A. Davis and D. Sweeney, "Ultra-wideband Propagation Measurements and Modeling," *Final Report, DAPRA NETEX Program*, Virginia Polytechnic Institute and State University, Electrical and Computer Engineering, available at http://www.mprg.org/people/buehrer/ultra/darpa-netex.shtml, 2004.

[20] R.M. Buehrer, W.A. Davis, A. Safaai-Jazi, and D. Sweeney, "Characterization of the ultra-wideband channel", *Proc. 2003 UWBST*, pp. 26-31, November 2003.

[21] D.R. McKinstry, "Ultra-wideband small scale channel modeling and its application to receiver design," Masters Thesis, Dept. of Electrical and Computer Engineering, Virginia Tech, Blacksburg, VA, 2003.

[22] Liu Yang, "The applicability of the tap-delay line channel model to ultra wideband,", Masters Thesis, Dept. of Electrical and Computer Engineering, Virginia Tech, Blacksburg, VA, 2004.

[23] A. A. Saleh and R.A. Valenzuela, "A statistical model for indoor multipath propagation," *Journal on Selected Areas in Communications,* vol. SAC-5, no.2, pp. 128-137, February 1987.

[24] IEEE P802.15-02/368r5-SG3a, "Channel Modeling Sub-committee Report Final, November 18, 2002.

[25] S. Venkatesh, J.Ibrahim and R.M. Buehrer, "A New 2-Cluster Model for Indoor UWB Channel Measurements," *Proc. AP-S International Symposium and UNSC/URSI National Radio Science Meeting*, June 2004.

[26] S. Venkatesh, J.Ibrahim and R.M. Buehrer, "A New 2-Cluster Model for Indoor UWB Channel Measurements,"submitted to *Transactions on Communications,* June 2004.

[27] M.Z. Win and R.A. Scholtz, "Energy capture vs. correlator resources in ultra-wide bandwidth indoor wireless communications channels," *Proc. 1997 MILCOM,* vol. 3, pp. 1277-1281, November 1997.

[28] M.Z. Win and R.A. Scholtz, "On the energy capture of ultrawide bandwidth signals in dense multipath environments," *IEEE Communications Letters,* vol.2, Issue 9, pp. 245 - 247, September 1998.

[29] M.Z. Win, G. Chrisikos, and N. R. Sollenberger, "Impact of spreading bandwidth and diversity order on the error probability performance of RAKE reception in dense multipath channels," *Proc. 1999 WCNC*, vol. 3, pp. 1558 - 1562, September 1999.

[30] M.Z. Win and Z.A. Kostic , "Impact of spreading bandwidth on RAKE reception in dense multipath channels," *Journal on Selected Areas in Communications*, vol. 17, issue 10, pp. 1794 - 1806, October 1999.

[31] M.Z. Win, G. Chrisikos, and N. R. Sollenberger, "Performance of RAKE reception in dense multipath channels: implications of spreading bandwidth and selection diversity order," *Journal on Selected Areas in Communications,* vol. 18, issue 8, pp. 270 - 274, August 2000.

[32] M.Z. Win and R.A. Scholtz, "Characterization of ultra-wide bandwidth wireless indoor channels: a communication-theoretic view," *IEEE Journal on Selected Areas in Communications,* vol. 20, issue 9, pp. 1613-1627, December 2002.

[33] J.R. Foerster, "The effects of multipath interference on the performance of UWB systems in an indoor wireless channel ," *Proc. 2001 VTC Spring*, vol. 2, pp. 1176 - 1180, May 2001.

[34] D. Cassioli, M.Z. Win, F. Vatalaro, and A.F. Molisch, "Performance of low-complexity RAKE reception in a realistic UWB channel", *Ptoc. 2002 ICC,* vol. 2, pp. 763-767, April-May 2002.

[35] J.D. Choi and W.E. Stark, "Performance of ultra-wideband communications with suboptimal receivers in multipath channels," *Journal on Selected Areas in Communications,* vol. 20, issue 9, pp. 1754 - 1766, December 2002.

[36] J.D. Choi and W.E. Stark, "Performance analysis of RAKE receivers for ultra-wideband communications with PPM and OOK in multipath channels," *Proc. 2002 ICC,* vol. 3, pp. 1969 - 1973, May 2002.

[37] J.D. Choi and W.E. Stark, "Performance of UWB communications with imperfect channel estimation," *Proc. 2003 MILCOM*, vol. 2, pp. 915-920, October 2003.

[38] M.A. Rahman, S. Sasaki, J. Zhou, and H. Kikuchi, "On Rake Reception of Ultra Wideband Signals over Multipath Channels from Energy Capture Perspective," *IEICE Trans. Fundamentals,* vol. E88-A, no. 9, pp. 1-11, September 2005.

[39] R. Hoctor and H. Omlinson, "Delay-hopped transmitted-reference RF communications," *Proc. 2002 UWBST,* pp. 265-269, May 2002.

[40] N. Van Stralen, A. Dentinger, K. Welles, R. Gaus, R. Hoctor, and H. Tomlinson, "Delay hopped transmitted reference experimental results," *Proc. 2002 UWBST,* pp. 93-98, May 2002.

[41] J. D. Choi and W. E. Stark, "Performance of autocorrelation receivers for ultra-wideband communications with PPM in multipath channels," *Proc. 2002 UWBST,* pp. 213-217, May 2002.

[42] W.M. Gifford and M.Z. Win, "On transmitted-reference UWB communications," *Proc. 2004 Asilomar,* vol. 2, pp. 1526 - 1531, 2004.

[43] L. Yang and G. B. Giannakis, "Optimal pilot waveform assisted modulation for ultra-wideband communications," *Proc. 2002 Asilomar,*, vol. 1, pp. 733-737, November 2002.

[44] Yi-Ling Chao and R.A Scholtz, "Optimal and suboptimal receivers for ultra-wideband transmitted reference systems," *Trans. 2003 GLOBCOM,* vol. 2, pp. 759 - 763, December 2003.

[45] S. Franz, and U. Mitra, "On optimal data detection for UWB transmitted reference systems," *Trans. 2003 GLOBCOM,* vol. 2, pp. 744-748, December 2003.

[46] Y. Chao and R.A. Scholtz, "Novel UWB transmitted reference schemes," *Trans. 2004 Asilomar*, vol. 1, pp. 652 - 656, 2004.

[47] Y. Chao, "Optimal integration time for UWB transmitted reference correlation receivers ," *Trans. 2004 Asilomar,* vol. 1, pp. 647-651, 2004.

[48] Y. and R.A. Scholtz, "Weighted correlation receivers for ultra-wideband transmitted reference systems," *Proc. 2004 GLOBECOM*, vol. 1, pp. 66 - 70, 2004.

[49] J. Ibrahim and R.M. Buehrer, "A data-aided iterative UWB receiver with LDPC," *Proc. 2005 VTC-Fall,* 2005.

[50] R. Menon, J. Ibrahim, and R.M. Buehrer, "UWB signal detection based on sequence optimization," *PROC. 2005 WIRELESSCOM,* June 2005.

[51] J. Ibrahim, R. Menon, and R.M. Buehrer, "UWB sequence optimization for enhanced energy capture and interference mitigation," *Proc. 2005 MILCOM*, vol.4, pp. 2086-2092, October 2005.

[52] J. Ibrahim, R. Menon, and R.M. Buehrer, "UWB signal detection based on sequence optimization for dense multipath channels," *Communications Letters,* vol.10, issue 4, pp. 228-230, April 2006.

[53] R. Qiu, J.Q. Zhang, and Nan Guo, "Detection of Physics-Based Ultra-Wideband Signals Using Generalized RAKE With Multiuser Detection (MUD) and Time-Reversal Mirror," *Journal on Selected Areas in Communications,* vol. 24, no. 10, pp. 724-730, April 2006.

[54] N. Guo, R.C. Qiu, and B.M. Sadler, "An ultra-wideband autocorrelation demodulation scheme with low-complexity time reversal enhancement," in *Proc. 2005 MILCOM,* vol. 5, pp. 3066-3072, October 2005.

[55] M.Z. Win and R.A. Scholtz, "Impulse radio: how it works," *Communications Letters*, vol. 2, issue 2, pp. 36-38, Feb. 1998.

[56] M.Z. Win and R.A. Scholtz, "Ultra-wide bandwidth time-hopping spread-spectrum impulse radio for wireless multiple-access communications, " *Transactions on Communications*, vol. 48, issue 4, pp. 679 - 689, April 2000.

[57] J. G. Proakis, *Digital Communications*, NY: McGraw-Hill, 2001.

[58] F. Ramirez-Mireles, "On the performance of ultra-wide-band signals in Gaussian noise and dense multipath," *Transactions on Vehicular Technology,* vol. 50, issue 1, pp. 244 -249, Jan. 2001.

[59] X. Huang and Y. Li, "Performances of impulse train modulated ultra-wideband systems," *Proc. 2002 ICC,* vol. 2, pp. 758 - 762, 2002.

[60] L. Ge, G. Yue, and S. Affes, "On the BER performance of pulse-position-modulation UWB radio in multipath channels ," *Proc. 2002 UWBST,* vol. 13, issue 8, pp. 231 - 234 , May 2002.

[61] M.K. Simon, J. Omura, R. Scholtz, and K. Levitt, *Spread Spectrum Communications*, MD: Computer Science Press, 1985.

[62] A.J. Viterbi, *CDMA Principles of Spread Spectrum Communication*, MA: Addison-Wesley, 1995.

[63] T.J. Richardson, M.A. Shokrollahi, and R.L Urbanke "Design of capacity-approaching irregular low-density parity-check codes," *Transactions on Information Theory,* vol. 47, issue 2, pp. 619637, February 2001.

[64] S. B. Wicker, *Error Control Systems,* Prentice Hall, 1995.

[65] L. W. Couch, *Digital and Analog Communication Systems,* Prentice Hall, 2001.

[66] R. Esmailzadeh and M. Nakagawa, "Pre-RAKE diversity combination for direct sequence spread spectrum communications systems Communications" *Proc. 1993 ICC,* vol. 1, pp. 463-467, May 1993.

[67] R. Esmailzadeh, E. Sourour, and M. Nakagawa, "Pre-RAKE diversity combining in time-division duplex CDMA mobile communications," *Transactions on Vehicular Technology,* vol. 48 , issue 3 , pp. 795-801, May 1999.

[68] S. Imada and T. Ohtsuki, "Pre-RAKE diversity combining for UWB systems in IEEE 802.15 UWB multipath channel", *Proc. UWBST 2004,* pp. 236 - 240, May 2004.

[69] K. Usuda, H. Zhan, and M. Nakagawa, "Pre-Rake performance for pulse based UWB system in a standardized UWB short-range channel," *Proc. 2004 WCNC*, vol. 2 , pp. 920 - 925, March 2004.

[70] M. Jun and T. Oh, "Performance of pre-rake combining time hopping UWB system," *Transactions on Consumer Electronics,* vol. 50, issue 4, pp. 1033 - 1037 , November 2004.

[71] B.M. Sadler and A. Swami, "On the performance of episodic UWB and direct-sequence communication systems," *Transactions of Wireless Communications,* vol. 3, issue 6, pp. 2246-2255, November 2004.

[72] T. Strohmer, M. Emami, J. Hansen, G. Papanicolaou, and A.J. Paulraj, "Application of time-reversal with MMSE equalizer to UWB communications," *Proc. 2004 GLOBCOM,* vol. 5, pp. 3123-3127, 2004.

[73] Di Wu, P. Spasojevic, and I. Seskar, "Multipath beamforming for UWB: channel unknown at the receiver," *Proc. 2002 Asimolar,* vol. 1, pp. 599-603, November 2002.

[74] J. Wang, M.Zhao, S. Zhou, and Y. Yao, "A novel multipath diversity scheme in TDD-CDMA systems," *Proc. 1999 RWC,* pp. 77 - 79, August 1999.

[75] R. Irmer, A. Noll Barreto, and G. Fettweis, "Transmitter Precoding for Spread-Spectrum Signals in Frequency-Selective Fading Channels," *Proc. 2001 3GWireless*, pp. 939-944, May 2001.

[76] G. H. Golub and C. F. Van Loan, *Matrix Computations,* Johns Hopkins Series in the Mathematical Sciences, Johns Hopkins University Press, 3rd edition, 1996.

[77] G. Strang, *Linear Algebra and Its Applications,* Harcourt Brace Jovanovich College Publishers, San Diego, CA, 3rd edition, 1988.

[78] Z. Xu, "Perturbation Analysis for Subspace Decomposition with Applications in Subspace-Based Algorithms," *Transactions on Signal Processing*, vol. 50, no. 11, pp. 2820-2830, November 2002.

[79] T. Weng, T. S. Huang, and N. Ahuja, "Motion and structure from two perspective views: Algorithms, error analysis, and error estimation," *Transactions on PAMI*, vol. 11, no. 5, pp. 451-476, 1989.

[80] C. Anderson, "A Software Defined Ultra Wideband Transceiver Testbed for Communications, Ranging, and Imaging," PhD Dissertation, Virginia Polytechnic Institute and State University, Electrical and Computer Engineering, 2006.

[81] R.E. Ziemer, B.R. Vojcic, L.B. Milstein, and J.G. Proakis, "Effects of carrier tracking in RAKE reception of wide-band DSSS in Rician fading," *Transactions on Microwave Theory and Techniques,* vol. 47, issue 6, part 1, pp. 681-686, June 1999.

[82] R.E. Ziemer and L.B. Milstein, "Comments on Carrier tracking in RAKE reception of wide-band DSSS in Ricean fading," *Transactions on Microwave Theory and Techniques,* vol. 49, issue 10, part 1, pp. 1822-1823, October 2001.

[83] A. R. Forouzan, M. Nasiri-Kenari, and J. A. Salehi, "Performance analysis of time-hopping spread-spectrum multiple-access systems: Uncoded and coded schemes," *Transactions on Wireless Communications,* vol. 1, pp. 671681, October 2002.

[84] A.R. Forouzan, and M. Abtahi, "Application of convolutional error correcting codes in ultrawideband M-ary PPM signaling," in *IEEE Microwave and Wireless Components Letters,* vol. 13, issue 8, pp. 308 -310, August 2003.

[85] U. Mengali and A.N. D'Andrea, *Synchronization Techniques fir Digital Receivers,* Plenum Press, New York, 1997.

[86] R.M. Buehrer, Synchronization of Spread Spectrum Signals, *ECE 5984 Class Notes*, Virignia Tech, ECE Dep., Spring 2004.

[87] R.L. Peterson, R.E. Ziemer, and D.E. Broth, *Introduction to Spread Spectrum Communications,* Prentice Hall, NJ, 1995.

[88] J. Lee and R.A. Scholtz, "Ranging in a dense multipath environment using an UWB radio link," *Journal on Selected Areas in Communications,* vol. 20, issue 9, pp. 1677-1683, December 2002.

[89] G.E. Corazza, "On the MAX/TC criterion for code acquisition and its application to DS-SSMA systems," *Transactions on Communications,* vol.44, issue 9, pp. 1173-1182, September 1996.

[90] B.B. Ibrahim and A.H. Aghvami, "Direct sequence spread spectrum matched filter acquisition in frequency-selective Rayleigh fading channels," *IEEE Journal on Selected Areas in Communications,* vol.12, issue 5, pp. 885-890, June 1994.

[91] J. Iinatti and M. Latva-aho, "Matched filter acquisition for CDMA systems in multipath channels," *Proc. 1998 GLOBCOM,* vol. 6, pp. 3449-3454, November 1998.

[92] J. Linatti, "Performance of DS code acquisition in static and fading multipath channels," *Proceedings in Communications,* vol. 147, Issue 6, pp. 355-360, December 2000.

[93] M. Katz, J. Iinatti, and S. Glisic, "Two-dimensional code acquisition in fixed multipath channels," *Proc. 2000 VTC-Fall,* vol. 5, pp. 2317-2324, December 2003.

[94] O. Shin and K.B. Lee, "Utilization of multipaths for spread-spectrum code acquisition in frequency-selective Rayleigh fading channels," *Transactions on Communications,* vol. 49, issue 4, pp. 734-743, April 2001.

[95] A.L. Garrett and D.L. Noneaker, "Multipath acquisition for RAKE reception in DS packet-radio systems," *Proc. 1998 MILCOM,* vol.3, pp. 837 - 841, October 1998.

[96] S. Glisic and M.D. Katz, "Modeling of the code acquisition process for RAKE receivers in CDMA wireless networks with multipath and transmitter diversity," *Journal on Selected Areas in Communications,*, vol.19, issue 1, pp. 21 - 32, January 2001.

[97] Saravanan Vijayakumaran and T.F. Wong, "Equal gain combining for acquisition of UWB signals," *Proc. 2003 MILCOM,* vol. 2, pp. 880-885, October 2003.

[98] S. Aedudodla, S. Vijayakumaran, and T.F. Wong, "Rapid ultra-wideband signal acquisition," *Proc. 2004 WCNC,* vol. 2, pp.1148-1153, March 2004.

[99] E.A. Homier and R.A. Scholtz, "Rapid acquisition of ultra-wideband signals in the dense multipath channel," *Proc. 2002 UWBST,* pp.105-109, May 2002.

[100] E.A. Homier, "Synchronization of ultra-wideabnd signals in the dense multipath channel," PhD Dissertation, University of Southern California, Los Angeles, 2004.

[101] E.A. Homier and R.A. Scholtz, "A Generalized Signal Flow Graph Approach for Hybrid Acquisition of Ultra-Wideband Signals," *International Journal of Wireless Information Networks,* vol. 10, number 4, pp. 179-191, Oct. 2003.

[102] J. Oh, S. Yang, and Y. Shin, "A rapid acquisition scheme for UWB signals in indoor wireless channels," *Proc. WCNC*, vol.2, pp. 1143-1147, March 2004.

[103] Y. M. F. Chin, B. Kannan, and S. Pasupathy, "Acquisition performance of an ultra wide-band communications system over a multiple-access fading channel," *Proc. 2002 UWBST,*, pp. 99-103, May 2002.

[104] L. Yang and G.B. Giannakis, "Blind UWB timing with a dirty template," *Proc. 2004 ICASSP*, vol. 4, pp. 509-512, May 2004.

[105] L. Yang and G.B. Giannakis, "Low-complexity training for rapid timing acquisition in ultra wideband communications," *Proc. 2003 GLOBECOM*, vol. 2, pp. 769 - 773, December 2003.

[106] Z. Tian, Liuqing Yang, and G.B. Giannakis, "Symbol timing estimation in ultra wideband communications," *Proc. 2002 Asilomar,* vol. 2, pp. 1924 - 1928, 3-6 Nov. 2002.

[107] L. Yang, Zhi Tian, and G.B. Giannakis, "Non-data aided timing acquisition of ultra-wideband transmissions using cyclostationarity," *Proc. 2003 ICASSP*, vol. 4, pp. 121-124, April 2003.

[108] I. Maravic, M. Vetterli, and K. Ramchandran, "High resolution acquisition methods for wideband communication systems," *Proc. 2003 ICASSP,* vol.4, pp. 133-136, April 2003.

[109] I. Maravic, M. Vetterli, and K. Ramchandran, "Channel estimation and synchronization with sub-Nyquist sampling and application to ultra-wideband systems," *Proc. 2004 ICASSP,* vol.5, pp. 381-384, May 2004.

[110] C. Carbonelli, U. Mengali, and U. Mitra, "Synchronization and channel estimation for UWB signals," *Proc. 2003 GLOBCOM,* vol.2, pp. 764-768, December 2003

[111] S. Gezici, E. Fishler, H. Kobayashi, H.V. Poor, and A.F. Molisch, "A rapid acquisition technique for impulse radio Communications," in *Proc. 2003 PRCCS,* vol. 2, pp. 627 -630, August 2003.

[112] A. Polydoros and C. Weber, "A Unified Approach to Serial Search Spread-Spectrum Code Acquisition–Part I: General Theory," *IEEE Transactions on Communications,* vol. 32, issue 5, pp. 542-549, May 1984.

[113] A. Polydoros and C. Weber, "A Unified Approach to Serial Search Spread-Spectrum Code Acquisition–Part II: A Matched-Filter Receiver," *Transactions on Communications,* vol. 32, issue 5, pp. 550-560, May 1984.

[114] A. Papoulis and S.U. Pillai, *Probability, Random Variables ans Stochastic Processes* NY: McGraw Hill, 2002.

[115] J. Linatti, "Robust method for threshold setting in a DS/DS-CDMA code acquisition," in *Proc. 1996 ICUPC,* vol. 1, pp. 145-153, 1996.

[116] W. Sheen and C.H. Tai, "A noncoherent tracking loop with diversity and multipath interference cancellation for direct-sequence spread-spectrum systems," *Transactions on Communications,* vol. 46, issue 11, pp. 1516-1524, November 1998.

[117] G. Fock, J. Baltersee, P. Schulz-Rittich, and H. Meyr, "Channel tracking for RAKE receivers in closely spaced multipath environments," *Journal on Selected Areas in Communications,* vol. 19, issue 12, pp. 24202431, December 2001.

[118] J. Lin, "A modified PN code tracking loop for direct-sequence spread-spectrum communication over arbitrarily correlated multipath fading channels," *Journal on Selected Areas in Communications,* vol. 19, issue 12, pp. 2381 - 2395, December 2001.

[119] M. El-Tarhuni and A. Ghrayeb, "A robust PN code tracking algorithm for frequency selective Rayleigh-fading channels," *Transactions on Wireless Communications,* vol. 3, issue 4, pp. 1018-1023, July 2004.

[120] W.M. Lovelace and J.K. Townsend, "The effects of timing jitter and tracking on the performance of impulse radio," *IEEE Journal on Selected Areas in Communications,* vol. 20, issue 9, pp. 1646-1651, Dec. 2002.

[121] C. Chui and R.A. Scholtz, "Optimizing tracking loops for UWB monocycles," *Proc. 2003 GLOBECOM,* vol. 1, pp. 425-430, Dec. 2003.

[122] C. Chui and R.A. Scholtz, "Tracking UWB monocycles in IEEE 802.15 multipath channels," *Proc. 2003 Asilomar,* vol.2, pp. 1761-1765, Nov. 2003.

[123] S. Farahmand, Xiliang Luo, and G. B. Giannakis, "Demodulation and Tracking With Dirty Templates for UWB Impulse Radio: Algorithms and Performance," *IEEE Transactions on Vehicular Technology,* vol. 54, no. 5, pp. 1595-1608, Sept. 2005.

[124] A.H. Light, "NETEX Task 1: Measured effects of UWB emitters on existing narrownband military receivers," *Proc. 2003 UWBST,* pp. 10-14, November 2003.

[125] J.D. Choi and W.E. Stark, "Performance analysis of ultra-wideband spread-spectrum communications in narrowband interference," *Proc. 2002 MILCOM,* vol. 2, pp. 1075 - 1080, October 2002.

[126] L. Zhao, A.M. Haimovich and H. Grebel, "Performance of ultra-wideband communications in the presence of interference," *Journal on Selected Areas in Communications,* vol. 20, issue 9, pp. 1684-1691, Dec. 2002.

[127] L. Piazzo and F. Ameli, "Performance analysis for impulse radio and direct-sequence impulse radio in narrowband interference," in *Transactions in Communications,* vol. 53, issue 9, pp. 1571-1580, September 2005.

[128] L. Yang and G.B. Giannakis, "Unification of ultra-wideband multiple access schemes and comparison in the presence of interference," *Proc. 2003 Asilomar,* vol.2, pp. 1239-1243, 2003.

[129] L. Yang and G.B. Giannakis, "A general model and SINR analysis of low duty-cycle UWB access through multipath with narrowband interference and rake reception," *Transactions on Wireless Communications,* pp. 1818-1833, vol. 4, issue 4, July 2005.

[130] M. Hamalainen, V. Hovinen, R. Tesi, J. Iinatti, and M. Latva-aho, "On the UWB system coexistence with GSM900, UMTS/WCDMA, and GPS," in *Journal on Selected Areas in Communications,* pp. 1712-1721, vol. 20, issue 9, December 2002.

[131] M.S. Iacobucci, M.G. Di Benedetto, and L. De Nardis, "Radio frequency interference issues in impulse radio multiple access communication systems," *Proc. 2002 UWBST*, pp. 293-296, 2002.

[132] A. Taha and K.M. Chugg, "A theoretical study on the effects of interference UWB multiple access impulse radio," *Proc. 2002 Asilomar,* vol.1, pp. 728 - 732, 2002.

[133] W. Tao, W. Yong and C. Kangsheng, "Analyzing the interference power of narrowband jamming signal on UWB system," *Proc. 2003 PIMRC,* vol. 1, pp. 612-615, 2003.

[134] Z. Luo, H. Gao, Y. Liu, and J. Gao, "A new UWB pulse design method for narrowband interference suppression," *Proc. 2004 GLOBECOM,* vol. 6, pp. 3488 - 3492, 29, 2004.

[135] X. Chu and R.D. Murch, "The effect of NBI on UWB time-hopping systems," *Transactions on Wireless Communications,* vol.3, issue 5, pp. 1431-1436, Sept.2004.

[136] I. Bergel, E. Fishler, and H. Messer, "Narrowband interference suppression in time-hopping impulse-radio systems," *IEEE UWBST*, pp. 303 - 307, May 2002.

[137] N. Boubaker and K.B. Letaief, "A low complexity MMSE-RAKE receiver in a realistic UWB channel and in the presence of NBI," *Proc. 2003 WCNC,* vol. 1, pp. 233-237, March 2003.

[138] E. Baccarelli, M. Biagi, and L. Taglione, "A novel approach to in-band interference mitigation in ultra wideband radio systems," *Proc. 2002 UWBST*, pp. 297 - 301, May 2002.

[139] C.R.C.M. da Silva and L.B. Milstein, "Spectral-Encoded UWB Communication Systems: Real-Time Implementation and Interference Suppression," *Transactions on Communications,* vol. 53, issue 8, pp. 1391-1401, August 2005.

[140] B. Donlan, "Ultra-wideband narrowband interference cancellation and channel modeling for communications," Masters Thesis, Dept. of Electrical and Computer Engineering, Virginia Tech, Blacksburg, VA, 2005.

[141] D.R. McKinstry and R.M. Buehrer, "LMS analog and digital narrowband rejection system for UWB communications," *Proc. 2003 UWBST*, pp. 91-95, Nov. 2003.

[142] M.Z. Win and R.A. Scholtz, "On the robustness of ultra-wide bandwidth signals in dense multipath environments," *IEEE Communications Letters,* vol. 2, issue 2, pp. 51-53, February 1998.

[143] A. F. Molisch, "Time variance for UWB wireless channels," *IEEE P802.15-02/461r0,* Nov. 2002.

[144] V. Bharadwaj, and R.M. Buehrer, "An Interference Suppression Scheme for UWB Signals Using Multiple Receive Antennas," *Communications Letters*, vol. 9, Issue 6, pp. 529 - 531, June 2005.

[145] V. Bharadwaj, "Ultra-Wideband for Communications: Spatial Characteristics and Interference Suppression," Masters Thesis, Dept. of Electrical and Computer Engineering, Virginia Tech, Blacksburg, VA, 2005.

[146] A.H. Muqaibel, "Characterization of Ultra Wideband Communication Channels," PhD Dissertation, Virginia Polytechnic Institute and State University, Electrical and Computer Engineering, 2003.

[147] J. Ibrahim and R.M. Buehrer, "A Novel NBI Suppression Scheme for UWB Communications Using Multiple Receive Antennas," *Proc. 2006 RWS,* pp. 507-510, January 2006.

[148] J. Ibrahim and R.M. Buehrer, "NBI Mitigation for UWB Systems Using Multiple Antenna Selection Diversity," *to appear, Transactions on Vehicular Technologies.*

[149] C. Rose and M.D. Smith, *Order Statistics,* Springer-Verlag, New York, 2002.

[150] M.K. Simon and M.S. Alouini, "Exponential-type bounds on the generalized Marcum Q-function with application to error probability analysis over fading channels," *IEEE Transactions on Communications,* vol. 48, issue 3, pp. 359-366, March 2000.

[151] S. Hoyos, B. Sadler and G. Arce, "Monobit Digital Receivers for Ultra wideband Communications," *IEEE Transactions on Wireless Communications,* vol.4, issue 4, pp. 1337-1344, July 2005.